Light (anti)nuclei production at the LHC measured in pp collisions at 13 TeV

Produktion leichter (Anti)Kerne am LHC gemessen in pp Kollisionen bei 13 TeV
Zur Erlangung des Grades eines Doktors der Naturwissenschaften (Dr. rer. nat.)
genehmigte Dissertation von Michael Karim Habib aus Ruthweiler
Tag der Einreichung: 16.11.2021, Tag der Prüfung: 15.12.2021
Darmstadt — D 17

1. Gutachten: Prof. Dr. Tetyana Galatyuk
2. Gutachten: Prof. Dr. Anton Andronic

TECHNISCHE
UNIVERSITÄT
DARMSTADT

Light (anti)nuclei production at the LHC measured in pp collisions at 13 TeV
Produktion leichter (Anti)Kerne am LHC gemessen in pp Kollisionen bei 13 TeV

Genehmigte Dissertation von Michael Karim Habib aus Ruthweiler

1. Gutachten: Prof. Dr. Tetyana Galatyuk
2. Gutachten: Prof. Dr. Anton Andronic

Tag der Einreichung: 16.11.2021
Tag der Prüfung: 15.12.2021

Darmstadt — D 17

Abstract

ALICE (A Large Ion Collider Experiment) collected over two billion proton-proton collision events at a center-of-mass energy of 13 TeV during the second running period (from 2016 to 2018) of the Large Hadron Collider (LHC). This rich data sample allows for studies of at this collision energy rarely produced objects, such as light nuclei. In this work, the first multiplicity and transverse-momentum (p_{T}) differential measurement of helium (^{3}He) nuclei and triton (^{3}H) as well as their corresponding antinuclei in proton-proton collisions at the LHC is presented.

The interaction of quarks and gluons, the constituents of all hadrons, is described by quantum chromodynamics (QCD), the theory of the strong interaction. Thus, QCD is the underlying theory of the formation process of light nuclei. In practice, the light nuclei formation in collisions at relativistic energies is modeled using two phenomenological approaches: the statistical hadronization model and the coalescence model. The first expresses the production of all hadrons according to the laws of statistical physics, assuming emission from a medium in local thermal equilibrium. In this approach, the hadron yields are determined by the hadron mass, the chemical freeze-out temperature, the baryon chemical potential, and the system volume. The statistical hadronization model successfully describes the hadron yields over a wide mass range, going from the lowest (a few GeV) to the highest (a few TeV) center-of-mass collision energies. It is effectively applied to small and large systems ranging from e^+e^- to central uranium-uranium collision. The coalescence model, on the other hand, describes the production mechanism of nuclei on the microscopic level. In the simplest version, a nucleus is formed when its constituent nucleons are close in phase space (momentum and spatial distance are small). More sophisticated versions of the coalescence model take the emission source size and the nuclear radius into account. The key parameter of the model is the coalescence parameter B_A, with A being the mass number of the nucleus. Experimentally B_A is accessed as the ratio of the nucleus yield to the product of its constituent nucleon yields. The coalescence model is successfully used to describe and predict the formation of nuclei in relativistic collisions. Additionally, it is systematically used by the astrophysics community to predict antinuclei fluxes originating from collisions of cosmic rays with the interstellar medium.

The ALICE detector at the LHC is perfectly suited to track and identify light nuclei. The identification capability of the ALICE Time Projection Chamber (TPC) allows for excellent separation power in the low-p_{T} region via the measurement of the specific energy loss and it is complemented by a Time-of-Flight (TOF) detector extending the p_{T} reach of the particle identification. Due to being doubly charged the helium nucleus is very well separated via its specific energy loss in the TPC and the measurement can be performed in the $1 \leq p_{\mathrm{T}} \leq 6$ GeV/c interval. The ^{3}H nucleus on other hand is identified using the combined information from TPC and TOF detectors limiting the transverse-momentum reach of the measurement to $1 \leq p_{\mathrm{T}} \leq 2.5$ GeV/c. Additionally, the multiplicity and p_{T} differential (anti)proton spectra serving as important references for light nuclei are measured in a transverse-momentum interval of $0.6 \leq p_{\mathrm{T}} \leq 5$ GeV/c.

In this work, two new data-driven correction methods have been developed, exploiting recent ALICE measurements of the inelastic hadronic interaction cross section. In the first method, the inelastic hadronic interaction cross section implemented in the Monte Carlo simulations, which

are needed for the efficiency and acceptance correction, are reweighted, reducing the systematic uncertainty of this contribution by a factor of three compared to previous analyses. The second method uses the well-known proton inelastic cross section to evaluate the effect of the material budget on the particle spectra when using the TOF detector.

The p_{T}-spectra and the resulting integrated yields obtained in this work are used to study the formation process of light nuclei. Additionally, the p_{T}-spectra of deuterons in pp collisions at a center-of-mass energy of 13 TeV are presented and compared to the proton measurements. To study the light nuclei formation process as a function of the emission source radius, the results obtained in this work are discussed in the context of previously published ALICE results of light nuclei. The integrated deuteron-to-proton and helium-to-proton yield ratios show a smoothly increasing evolution with the event averaged charged-particle multiplicity density ($\mathrm{d}N_{\mathrm{ch}}/\mathrm{d}\eta$), going from pp to central lead-lead collisions. The trend is in both cases described by the statistical hadronization and the coalescence model. However, in the intermediate multiplicity region ($\mathrm{d}N_{\mathrm{ch}}/\mathrm{d}\eta \approx 30$), a tension between the models and the measured helium-to-proton yield ratio is observed. The coalescence parameters B_2 and B_3 follow a decreasing trend with the average charged-particle multiplicity, which is, to first order, described by the latest coalescence models. The coalescence parameters are determined as a function of p_{T}, showing a clear dependence on p_{T}. The p_{T} dependent coalescence parameter is compared to coalescence-model predictions using different nuclear wave functions. Surprisingly, B_2 agrees best with the prediction using the solution of a harmonic oscillator as the wave function, while more sophisticated wave functions (e.g. van Hulthen) do not describe the data. B_3 on the other hand is not predicted using a Gaussian nuclear wave function, which is the only one available at the moment. In the future, this approach can be used to study the nuclear wave function of exotic hyperons.

Additionally, the measurement of the coalescence parameter will give a fundamental baseline for space-bound experiments measuring cosmic antinuclei fluxes. The experiments try to discover physics beyond the standard model via indirect dark matter searches. Antinuclei are one of the most potent probes due to their low background component originating from hadronic interactions in the galaxy. The proper estimate of this component is nevertheless crucial and B_A measurements as presented in this work are therefore essential.

With the third running period of the LHC starting in 2022 a new precision era for light-(anti)nuclei measurements will start. Among many new and exciting opportunities, the measurement of the triton-to-helium yield ratio, which at the moment does not have the necessary precision, will give a defined answer on the underlying nuclei formation process.

Zusammenfassung

Während der zweiten Messperiode (von 2016 bis 2018) des Large Hadron Colliders (LHC) zeichnete ALICE (A Large Ion Collider Experiment) über zwei Milliarden Proton-Proton Kollisionen mit einer Schwerpunktsenergie von 13 TeV auf. Dieser einzigartige Datensatz ermöglicht die Messung seltener Teilchen, wie zum Beispiel leichte Kerne. In dieser Arbeit wird die erste Messung von Helium- (^{3}He) und Tritiumkernen (^{3}H) und ihren entsprechenden Antikernen, in Abhängigkeit von Multiplizität und Transversalimpul (p_{T}), in Proton-Proton Kollisionen am LHC vorgestellt.

Die Wechselwirkung von Quarks und Gluonen, den Bausteinen aller Hadronen, wird durch die Quantenchromodynamik (QCD), die Theorie der starken Wechselwirkung, beschrieben. Somit ist QCD die zugrundeliegende Theorie des Entstehungsprozesses leichter Kerne. In der Praxis wird die Entstehung leichter Kerne in relativistischen Kollisionen in zwei phänomenologischen Ansätzen modelliert: dem statistischen Hadronisierungsmodell und dem Koaleszenzmodell. Das erste Modell nutzt die Gesetze der statistischen Physik, um die Ausbeute aller Hadronen zu beschreiben. Die zugrunde liegende Annahme besagt, dass alle Hadronen dem gleichen Medium, welches sich in lokalem thermischen Gleichgewicht befindet, entstammen. Die Ausbeute der einzelnen Hadronen ist durch die Hadronenmasse, die Temperatur beim chemischen Ausfrieren des Mediums, das baryochemiche Potential und das Systemvolumen bestimmt. Das statistische Hadronisierungsmodell wird erfolgreich verwendet, um die Hadronenausbeuten in einen weiten Massenbereich und einem weiten Kollisionsenergiebereich (von einigen GeV bis zu einigen TeV) verwendet. Es wird sowohl auf kleine Systeme, wie etwa in e^+e^- Kollisionen, als auch auf große Systeme, wie etwa erzeugt in Uran-Uran Kollision, angewendet. Das Koaleszenzmodell hingegen beschreibt den Produktionsmechanismus leichter Kernen auf der mikroskopischen Ebene. In der naivsten Fassung des Koaleszenzmodells entsteht ein Kern, sobald seine Nukleonen sich nahe im Phasenraum befinden, das heißt relativer Impuls und räumlicher Abstand klein sind. Modernere Versionen des Koaleszenzmodells berücksichtigen unter anderem die Größe der Emissionsquelle sowie den Kernradius. Der entscheidende Parameter des Modells ist der sogenannte Koaleszenzparameter B_A, der experimentell als Verhältnis der Kernausbeute zum Produkt der Nukleonenausbeute bestimmt wird. Das Koaleszenzmodell wird erfolgreich verwendet, um die Entstehung leichter Kerne in relativistischen Kollisionen zu beschreiben und vorherzusagen. Darüber hinaus wird es in der Astrophysik systematisch verwendet, um die kosmischen Flüsse von Antikernen vorherzusagen, welche den Kollisionen kosmischer Strahlung mit dem interstellaren Medium entspringen.

Der ALICE-Detektor am LHC ist ausgezeichnet dazu geeignet die Spuren leichter Kerne zu rekonstruieren und diese zu identifizieren. Die Teilchenidentifikation der ALICE Zeitprojektionskammer (TPC) ermöglicht es, mit der Messung des spezifischen Energieverlusts, verschiedene Teilchensorten bei niedrigen Transversalimpulsen voneinander zu separieren. Zusätzlich wird diese durch eine Flugzeitmessung (TOF) ergänzt, welche die Teilchenidentifikation bei höheren Transversalimpulsen ermöglicht. Dank seiner zweifachen Ladung ist der Heliumkern über den Energieverlust in der TPC exzellent separiert und die Messung wurde in dem Intervall $1 \leq p_{\mathrm{T}} \leq 6$ GeV/c durchgeführt werden. Für die Identifikation des ^{3}H-Kerns müssen hingegen die kombinierten Informationen der TPC- und TOF-Detektoren verwendet werden, wodurch

sich das Transversalimpulsintervall der Messung auf $1 \leq p_{\mathrm{T}} \leq 2.5$ GeV/c begrenzt. Zusätzlich werden die (Anti-)Protonenspektren als Funktion des Transversalimpulses und in Abhängigkeit der Multiplizität, in dem Intervall $0.6 \leq p_{\mathrm{T}} \leq 5$ GeV/c, gemessen. Diese dienen als wichtige Referenzen zur Interpretation der Messungergebnisse leichter Kerne.

In dieser Arbeit wurden zwei neue datenbasiere Korrekturmethoden entwickelt, die aktuelle ALICE-Messungen des inelastischen hadronischen Wechselwirkungsquerschnitts verwenden. Die erste Methode gewichtet, basierend auf Messdaten, die in Monte-Carlo-Simulationen, welche für die Effizienz- und Akzeptanzkorrektur benötigt werden, implementierten inelastischen hadronischen Wechselwirkungsquerschnitte. Dies reduziert die systematischen Unsicherheit dieses Beitrags im Vergleich zu früheren Analysen um einen Faktor drei. Die zweite Methode verwendet den bekannten inelastischen Protonenwechselwirkungsquerschnitt, um den Effekt des Detektormaterials auf die Teilchen zu evaluieren, sobald der TOF-Detektor für die Identifikation verwendet wird.

Die in dieser Arbeit erzielten Messergebnisse werden mit früheren bereits veröffentlichten ALICE-Messungen leichter Kerne verglichen. Dies ermöglicht die Untersuchung des Entstehungsprozesses leichter Kerne als Funktion des Emissionsquellenradius. Zusätzlich wird eine Deuteronmessung in pp-Kollisionen bei einer Schwerpunktsenergie von 13 TeV verwendet und mit der Protonenmessung verglichen. Die Verhältnisse der integrierten Ausbeute von Deuteronen zu Proton und Heliumkernen zu Proton steigen stetig mit der durchschnittlichen Kollisionsmultiplizität geladener Teilchen ($\mathrm{d}N_{\mathrm{ch}}/\mathrm{d}\eta$) an. In beiden Fällen wird der Trend durch sowohl das statistische Hadronisierungs- als auch das Koaleszenzmodell beschrieben. Im mittleren Multiplizitätsbereich ($\mathrm{d}N_{\mathrm{ch}}/\mathrm{d}\eta \approx 30$) zeigen sich jedoch Unterschiede zwischen den Modellen und dem gemessenen Verhältnis der Helium-zu-Protonausbeute auf. Die Koaleszenzparameter B_2 und B_3 folgen einem abnehmenden Trend als Funktion der durchschnittlichen Kollisionsmultiplizität, welcher in erster Näherung von aktuellen Koaleszenzmodellen beschrieben wird. Die Koaleszenzparameter als Funktion von p_{T} zeigen einen deutlichen Anstieg mit dem Transversalimpuls. Der p_{T} -abhängige Koaleszenzparameter wird mit Vorhersagen des Koaleszenzmodell unter Verwendung verschiedener nuklearer Wellenfunktionen verglichen. Überraschenderweise stimmt B_2 am besten mit dem Koaleszenzmodell überein, welches einen harmonischen Oszillator als Wellenfunktion verwendet, während komplexere Wellenfunktionen (z.B. van Hulthen) die Daten nicht beschreiben. Der gemessene B_3 Parameter hingegen wird nicht unter Verwendung einer Gaußschen Wellenfunktion beschrieben, welche momentan als einzige zur Verfügung steht. In der Zukunft kann dieser Ansatz unter anderem verwendet werden, um die Wellenfunktion von exotischen Hyperkernen zu untersuchen.

Darüber hinaus liefert der Koaleszenzparameter eine Grundlage um die Messung der Flüsse kosmischer Antikern zu interpretieren. Kosmische Experimente versuchen, mithilfe dieser Messungen Physik jenseits des Standardmodells in Form von dunkler Materie zu entdecken. Antikerne sind aufgrund ihres geringen Hintergrunds, welcher aus hadronischen Wechselwirkungen in der Galaxie stammt, eine besonders gut geeignete Probe. Allerdings ist die richtige Abschätzung des Hintergrunds entscheidend und die B_A-Messung, wie in dieser Arbeit vorgestellt, unerlässlich.

Mit dem Start der dritten Messperiode des LHC im Jahr 2022 wird eine neue Ära der Präzision für die Messung leichter (Anti)Kerne beginnen. Unter anderem wird die Messung des Verhältnisses der Ausbeute von Triton zu Heliumkernen, die derzeit nicht die nötige Präzision erreicht, Aufschluss über den zugrundeliegenden Kernbildungsprozess geben.

Contents

1 Introduction

According to quantum chromodynamics (QCD), which is the theory describing the strong interaction, nuclear matter is believed to undergo a phase transition at very high temperatures and/or densities into a deconfined state, the so-called quark-gluon plasma (QGP). All matter in the universe was likely in such a deconfined state shortly after the big bang for a period of approximately 10 μs. At the Large Hadron Collider (LHC) in ultrarelativistic collisions, the necessary temperatures are reached and a QGP is created. ALICE (A Large Ion Collider Experiment) at the LHC is specifically optimized to measure the properties of the QGP, as well as the phase transition from the QGP state into the hadronic state. In addition, ALICE's unique particle identification and its excellent tracking capabilities allow for a strong proton-proton physics program at the LHC.

1.1 Standard model of particle physics

In the Standard Model, the constituents of matter are quarks and leptons. These are spin one-half particles and thus fermions, which interact by the exchange of spin-1 gauge boson via the electromagnetic, the weak, or the strong interaction. All leptons (e, μ, τ, ν_e, ν_μ, ν_τ, and corresponding antiparticles), do not interact strongly. Quarks (up: u, down: d, strange: s, charm: c, bottom: b, and top: t) on the other hand carry color charges and interact strongly by the exchange of gluons. The gauge boson of quantum electrodynamics (QED) does not carry charge. By contrast, gluons, which are the gauge bosons of quantum chromodynamics (QCD), carry color charges. As a consequence gluon-gluon interactions are possible in QCD. Figure 1.1 summarizes the properties of all the elementary particles of the Standard Model. Very interesting to note is the huge difference in masses for the different quark flavors ranging from a few MeV/c^2 to a hundred MeV/c^2 for u,d, and s up to a few to a hundred GeV/c^2 for c,b, and t. These sets are defined as light and heavy flavors, respectively, with the light-flavor quarks being more abundant. In ordinary matter, quarks are bound into color-neutral mesons ($q\bar{q}$) or baryons (qqq).

Within the Standard Model, three (electromagnetic, weak, and strong) of the four known fundamental interactions are described. Gravity, however, despite being one of the most familiar and well-known interactions, is not included in the Standard Model. In contrast to the other three interactions, gravitation described by Einstein's general relativity approach does not fit into the quantum field picture of the Standard Model. As the gravitational force is almost zero on microscopic scales, it can be neglected in discussions of subatomic particles.

1.2 Strong interaction

In QED the strength of the interaction is given by its coupling constant, also known as the fine-structure constant α. At small momentum transfer (Q^2) α is approximately 1/137, while at very large momentum transfer α increases due to vacuum polarization. Because $\alpha \ll 1$, QED processes can be calculated very precisely using perturbation theories. QED properties like the electron magnetic moment are among the most precisely calculated quantities in physics [3].

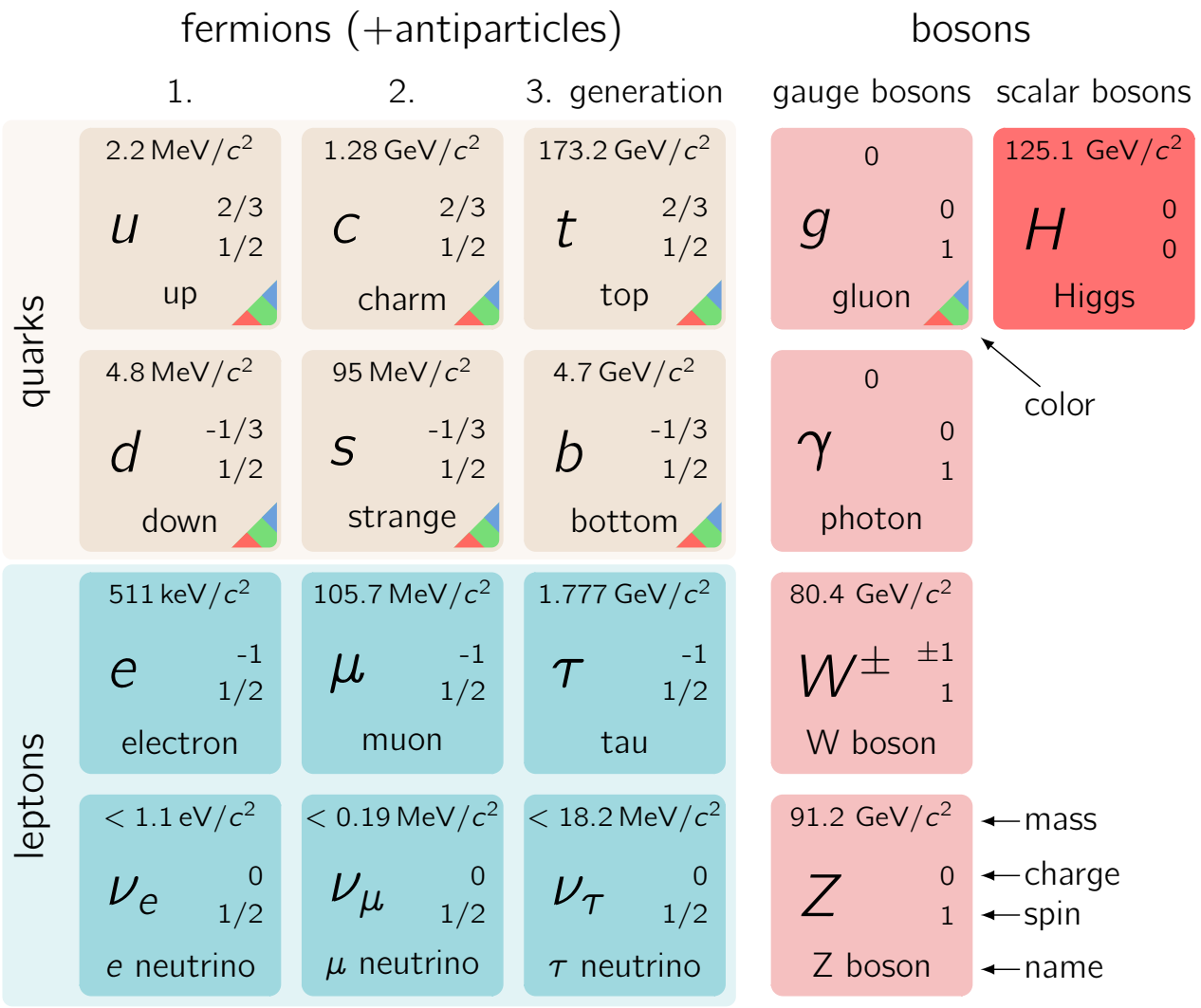

Figure 1.1: Summary table of all Standard Model particles. The particles can be divided into two groups of spin one-half fermions the quarks and the leptons. Additionally, the gauge bosons (s=1) are listed which are the mediators between the fermions. The values are taken from reference [1] and the figure is adopted from reference [2].

The exchange boson of the strong interaction is the gluon, which itself carries a color charge. This leads to one of the fundamental differences between QED and QCD. The QCD coupling constant (α_S) is strongly dependent on momentum transfer (Q^2) and is parameterized in first-order perturbation theory [4] by

$$\alpha_S(Q^2) = \frac{12\pi}{(33-2n_f)\cdot \ln(Q^2/\Lambda^2_{\mathrm{QCD}})}, \tag{1.1}$$

where Λ_{QCD} is the scale below which perturbation theories are not applicable anymore. From lattice QCD calculations Λ_{QCD} is determined to be approximately 200 MeV. n_f is the number of quark flavors. At low momentum transfer the heavy quark flavor component becomes negligible and thus n_f can be simplified and reduced from 6 to 3. The coupling constant is not a physical observable. It is rather a parameter defined within the perturbation theory. Within perturbation theory, however, physical observables can be used to access the strength of the coupling constant

at the momentum transfer of the measurement. This is an active field of research and more information can be found in reference [5]. Figure 1.2 shows a summary of the latest and most precise measurements used to extract α_S as a function of the momentum transfer [6]. In the label, the order of the perturbation theory used to extract α_S is indicated in the parentheses, with NLO standing for Next-to-Leading Order.

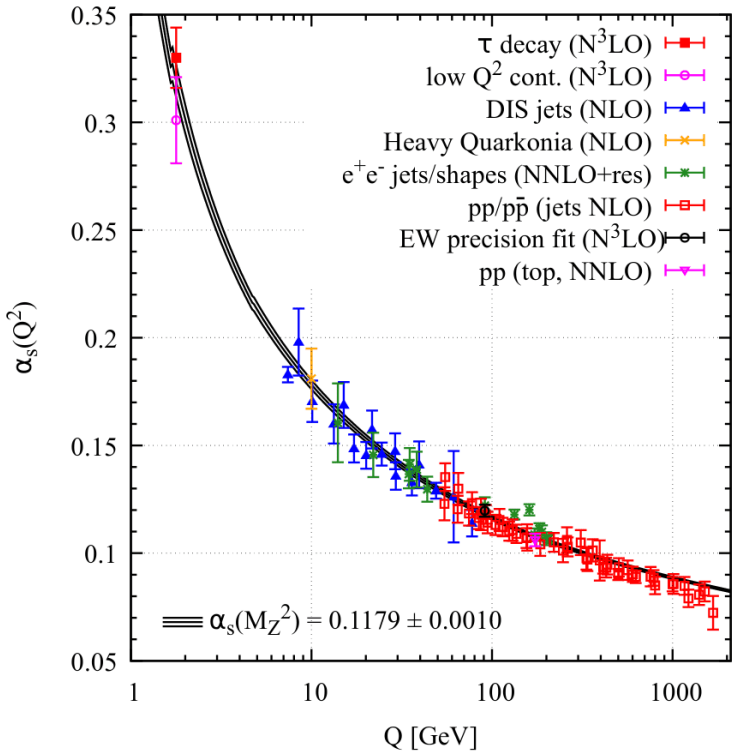

Figure 1.2: Strength of the QCD coupling constant (α_S) as a function of the momentum transfer (Q). The order of QCD perturbation theory used to extract α_S is indicated in the parentheses [6].

In a quark-quark, gluon-quark, or gluon-gluon scattering process at large momentum transfer ($Q^2 \gg \Lambda_{\mathrm{QCD}}$) α_S becomes small. A large momentum transfer results in the resolution of a short distance. These hard scattering processes can be calculated perturbatively, and typically the quark masses can be neglected in such calculations since they are significantly smaller than the momentum transfer. For $Q \to \infty$ the coupling strength approaches zero and eventually, quarks behave like quasi-free particles. This behavior is called asymptotic freedom [7, 8].

At small momentum transfer and long distances, α_S is large ($\alpha_S \to 1$), which results in the confining property of the strong interaction. This can be easily illustrated by looking into the potential of the strong interaction. A phenomenological way of describing the quark-antiquark potential as a function of the distance (r) is given by the Cornell potential [9]

$$V(r) = -\frac{4}{3}\frac{\alpha_S}{r} + \kappa r\,. \tag{1.2}$$

At small distances, the potential behaves like the Coulomb potential, while at large distances the linear term gains in relevance. The first term resembles a single gluon exchange while the second term is typically referred to as the confinement term. The constant κ resembles a string tension between the quark pair. The value of κ is on the order of 1 GeV/fm [10]. When the

distance between a quark pair increases, the energy in the field between the quarks rises until the threshold for the production of a new quark-antiquark pair is crossed. The newly created quarks will hadronize with the original ones into color-neutral baryons and mesons. Therefore, free quarks can never be observed. This process is called confinement. The quark hadronization into color-neutral objects typically happens on the timescale of $1/\Lambda_{\mathrm{QCD}} \approx 1$ fm/c. The top quark is an exception because its weak decay happens on shorter timescales than the hadronization process.

The most sophisticated theoretical description of the quark-quark, quark-gluon, or gluon-gluon interactions at large α_S is provided by lattice QCD. In lattice QCD the QCD Lagrangian is solved numerically with a non-perturbative approach, where the QCD equations are expressed on a discrete space-time lattice using Euclidean space-time.

1.2.1 Parton distribution function

In the 1960s Feynman postulated hypothetical strongly interacting elementary particles called partons [11] as the main constituents of the hadrons. Today we know, that hadrons are made of quarks and gluons and, thus, refer to them as partons. The distribution of the partons inside hadrons shows some interesting effects due to the nature of the strong interaction. The quantum numbers of the valence quarks in a hadron ($\mathrm{q\bar{q}}$ for mesons and qqq for baryons) determine the hadrons species. However, the valence quarks are not the only partons in the hadron. Due to effects like vacuum fluctuations, quark-antiquark pairs are constantly created and destroyed. These so-called sea quarks carry alongside the valence quarks and the gluons a fraction x of the total hadron momentum. The partonic structure of a nucleon was first measured in deep inelastic electron-proton scattering at SLAC in 1968 [12]. The so-called parton distribution functions (PDFs) give the likelihood of finding a parton at a specific momentum fraction in the hadron. Up to now, the most precise measurements of the PDFs, giving insight into the hadronic structure of a proton were performed in electron-proton deep inelastic scattering at DESY [13]. Figure 1.3 shows the proton parton distribution functions at a momentum transfer Q^2 of 10 GeV^2 as a function of the carried momentum fraction. With decreasing momentum fractions, the proton structure becomes dominated by gluons (xg), and the sea quark contribution rises (xS), containing all virtual quark-antiquark pairs. At high momentum fractions ($x \approx 1/3$) on the other hand, the contributions from the valence quarks ($x\mathrm{u}_v$ and $x\mathrm{d}_v$) rise, meaning that a valence quark is carrying a relative large momentum fraction in comparison to a sea quark.

1.3 Matter in extreme conditions

Even though quarks and gluons are confined into hadrons under normal conditions, as a consequence of the asymptotic freedom at high temperatures and pressures strongly interacting matter can undergo a phase transition into a hot and dense state of deconfined quarks and gluons. This state is called the quark-gluon plasma (QGP) [14, 15]. According to the latest research, the phase transition into this deconfined state occurs above a pseudo critical temperature T_{pc}. With our current understanding, it is most likely that shortly after the big bang (≈ 10 ps) the entire universe was in such a deconfined state and it took about 10 µs for the universe to expand and simultaneously cool down below T_{pc} resulting in the hadronization of quarks and gluons into color-neutral states. On Earth, matter under these extreme conditions can only be

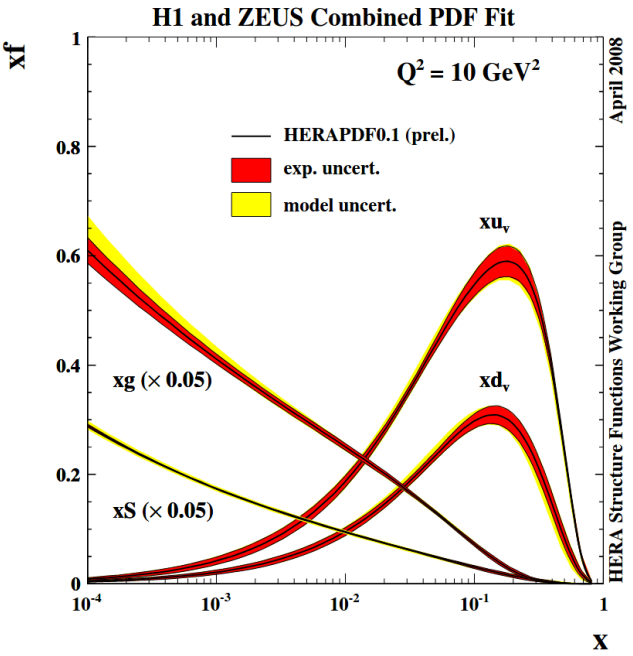

Figure 1.3: Parton distribution functions (PDF) of a proton as at $Q^2 = 10$ GeV^2 as a function of the carried momentum fraction measured at DESY by the HEAR and ZEUS Collaborations [13]. Please note that the sea quark (xS) and gluon (xg) PDFs are scaled by $1/20$.

produced and studied in ultra-relativistic heavy-ion collisions. In heavy-ion collisions, which will be explained in section 1.3.1, the medium does not undergo an equilibrium process like heating and is rather "born" in the deconfined state, due to the very short time scales of a heavy-ion collision (10^{-2} fm/c).

Thermodynamic properties, such as temperature, volume, pressure, and/or chemical potential of a medium are normally expressed in the form of a phase diagram. The phase diagram of strongly interacting matter shows the different states as a function of the temperature (T) and the baryon chemical potential (μ_B). The baryon chemical potential is defined as the energy needed to add a baryon to the system, or in other words, it is given as the net difference of baryons to anti-baryons in a phase-space element. At ordinary temperatures, the baryon chemical potential μ_0 is given as the mass of a nucleon minus the nuclear binding energy ($\mu_0 \approx$ 930 MeV). At LHC energies baryons and anti-baryons are produced in equal amounts. In a system where baryons and anti-baryons are fully balanced $\mu_B = 0$. So for LHC energies, $\mu_B \to 0$ is a good approximation. In figure 1.4 a schematic version of the phase diagram of the strongly interacting matter is shown. The phase transition from a hadron gas to a quark-gluon plasma is indicated with a line starting at $\mu_B = 0$ and $T = 155$ MeV. With increasing chemical potential the critical temperature decreases.

From lattice QCD calculations the order of the transition from the hadron gas to the deconfined state is considered to be of a crossover type at $\mu_B = 0$ and supposed to happen rapidly [16]. For larger net baryon densities the order of the phase transition is not yet known and still under debate. If the phase transition changes from a crossover to a first-order type transition (with non-continuous evolution of the thermodynamic properties at the phase boundary), this would imply the existence of a critical endpoint. The search for the first-order phase transition and

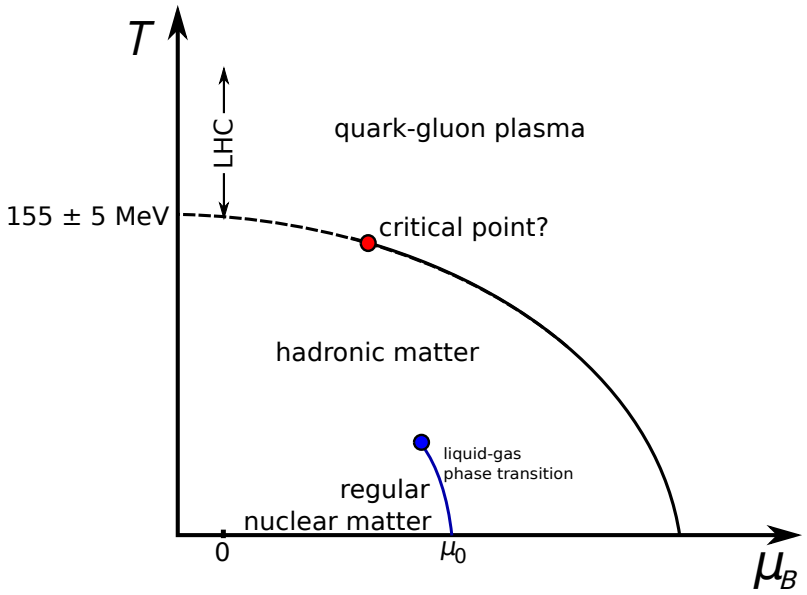

Figure 1.4: A sketch of the phase diagram of the strongly interacting matter.

critical point is one of the main areas of focus for the beam energy scan at the Realistic Heavy Ion Collider (RHIC) with the STAR [17] experiment and future experiments like CBM [18] at FAIR.

The latest theoretical descriptions of the thermodynamic properties of the quark-gluon plasma (like the critical temperature) are provided by lattice QCD. With this approach, the most recent and accurate calculations using using physical quark masses found a pseudo critical temperature of $T_{pc} = 156.5 \pm 1.5$ MeV [19] and $T_{pc} = 158.0 \pm 0.6$ MeV [20], which corresponds to an energy density of approximately 0.4 GeV/fm^3 [21, 22]. Figure 1.5 shows the results of one Lattice calculation using 2+1 quark flavors under the assumption that two light quarks (up and down) have equal mass and the third flavor (strange) is heavier. The normalized pressure $3p/T^4$, energy density ϵ/T^4, and entropy density $3s/4T^3$ are shown as a function of temperature. Additionally, a calculation is shown using the hadron resonance gas (HRG) model [23], which will be further explained in section 1.4.1. As expected, the Lattice and HRG results agree well until the pseudo critical temperature is reached. Because the HRG model does simply has now no knowledge about quarks and gluons the lines start to diverge from the lattice QCD predictions at T_{pc}. The horizontal line corresponds to the Stefan-Boltzmann limit of an ideal non-interacting gas of quarks and antiquarks. Even at high temperatures ($T > 300$ MeV) the energy, entropy, and pressure are far from the ideal gas limit, indicating a substantial interaction between quarks and gluons in the quark-gluon plasma.

1.3.1 Relativistic heavy-ion collisions

Relativistic heavy-ion collisions are a unique tool to experimentally study the quark-gluon plasma and its properties. Figure 1.6 shows the evolution of a relativistic heavy-ion collision in a space-time picture. The left side of the sketch shows the evolution of a collision without the formation of a deconfined strongly interacting medium, which is for example the case in low energy heavy-ion collisions.

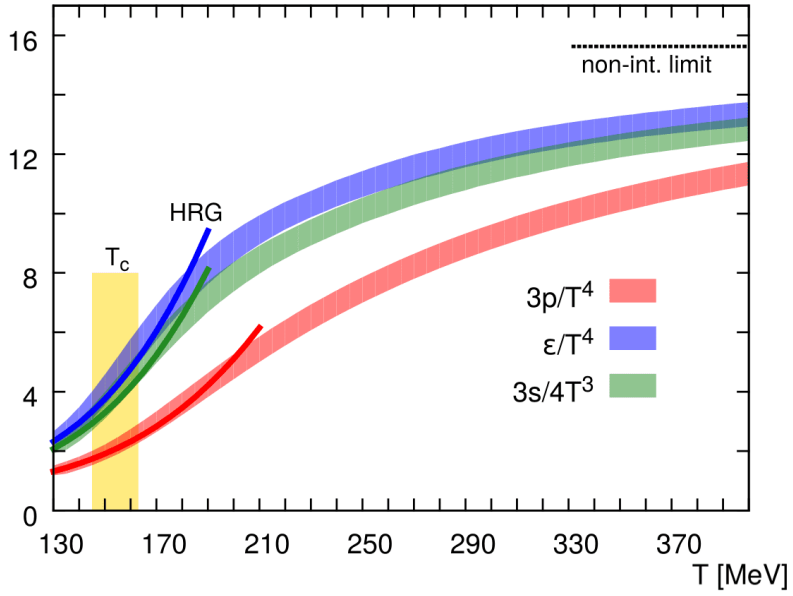

Figure 1.5: Lattice QCD calculations at zero chemical potential of the normalized pressure (p) in red, the energy density (ϵ) in blue, and the entropy density (s) in green as a function of the temperature. The dark lines show the prediction of the hadron resonance gas (HRG) model [23]. The horizontal line at $95\pi^2/60$ corresponds to the Stefan-Boltzmann limit of an ideal gas for the energy density and the vertical band marks the crossover region indicated $T_{pc} = (154 \pm 9)$ MeV. The figure is taken from reference [24].

The right side of the sketch shows the evolution of a heavy-ion collision with the formation of a quark-gluon plasma medium as realized in Pb-Pb collisions at the LHC. The nuclei move in opposite directions along the beamline with nearly the speed of light. They are highly Lorentz contracted, which makes them disc-like in the laboratory frame. Due to the high speed, the nuclei with radius R (in the order of a few fm) are transparent for each other and pass within a timescale of $2R/\gamma c \approx 10^{-2}$ fm/c, which is two orders of magnitude smaller than the typical timescale of the strong interaction $1/\Lambda_{\mathrm{QCD}} \approx 1$ fm/c.

The collision starts at $t = 0$. The first hard scattering processes occur within typical time scales of $t \approx 1/p_{\mathrm{T}} \ll 1/Q_0 \approx 0.1$ fm/c. Here Q_0 is the four-momentum transfer in the parton-parton collision, which produce particles with high transverse momentum p_{T}. These first hard collisions typically produce high-momentum hadrons in the fragmentation process.

Following this, most of the parton-parton collisions occur in the pre-equilibrium phase, typically with lower momentum transfer than the initial scatterings. In this phase the energy density rises rapidly until at $t = \tau_0 \approx 1$ fm/c [26], due to the strong interaction of the partons, the medium reaches (local) thermal equilibrium. Once thermal equilibrium is reached the evolution of the quark-gluon plasma medium can be described by hydrodynamic models.

The system subsequently expands with nearly the speed of light in beam direction and about half the speed of light in the transverse direction which is seen in the form of radial flow in transverse direction. During this expansion, the energy density and temperature of the system fall until T_{pc} is crossed and the deconfined medium of quarks and gluons undergoes a phase transition into a hadron gas. Since the mean free path of the hadrons is smaller than the system size, thermodynamic models can be used to describe the system. The system continues to expand

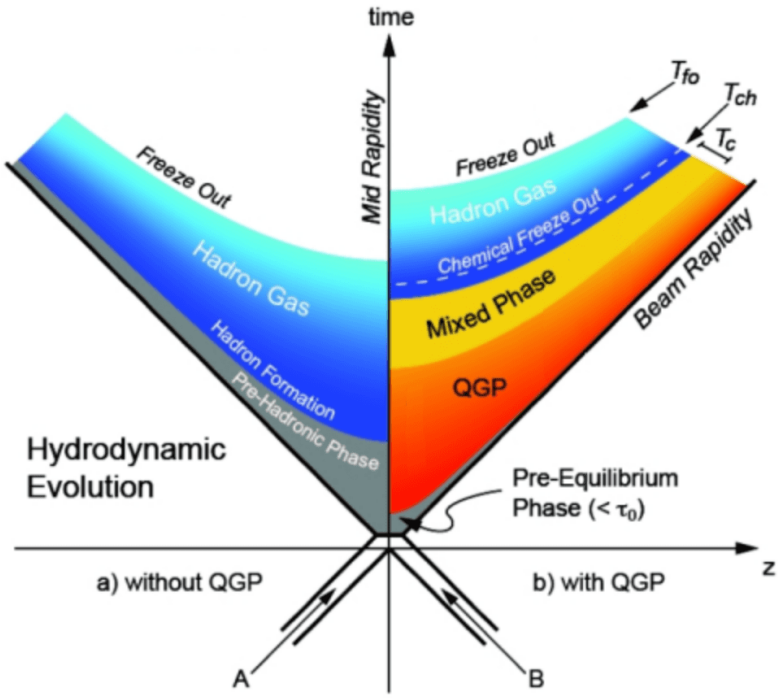

Figure 1.6: A space-time picture of a hadronic collision (left) compared to a heavy-ion collision (right) in the (t,z) plane, showing the evolution of the respective collision [25].

and the mean free path of the hadrons further increases resulting in a decreasing inelastic interaction cross section. Eventually, it becomes zero which stops the occurrence of inelastic collisions. This results in a fixed hadron chemistry. This moment is called chemical freeze-out and it is characterized by the chemical freeze-out temperature T_{ch}. The system expands further and reaches the point where not even elastic scattering between hadrons occurs. This point is called kinetic freeze-out because the momentum distributions do not change anymore.

The geometry of a heavy ion-collision

Due to the extended size of the colliding nuclei, the collision geometry varies for each collision. In heavy-ion physics, the geometry of the collision is expressed using the impact parameter b, which is defined as the distance between the centers of the two colliding nuclei in a plane transverse to the beam axis [27]. So the impact parameter determines the overlap region and, thus, the size of the created volume. It is accessed by comparing the purely geometrical Glauber model [28] to data. In the model, the collision is treated as a binary superposition of nucleon-nucleon collisions. The model defines two collision regions: the overlap region, where nucleons participate in the collision, and the spectator region, where the nucleons do not participate in the collision. A nucleon is called a participant if it undergoes more than one binary collision with the nucleons of the other nucleus. Within the model, the number of participants (N_{part}) and the number of spectators (N_{spec}) are calculated for a given impact parameter under the assumption of a realistic distribution of nucleons inside the nucleus. Additionally, the total number of binary collisions (N_{coll}) are calculated under the assumption that the nucleons follow a straight trajectory. Experimentally, neither impact parameter nor N_{coll}, N_{part}, or N_{spec} can be measured

directly. However, the average charged-particle multiplicity at mid rapidity ($dN_{ch}/d\eta$) and energy deposit in the very forward direction are strongly correlated with the impact parameter and can thus be estimated by comparing these measurements to the Glauber model predictions. N_{coll} can be estimated by using central tracking detectors and the energy deposit in the forward direction. In the case of ALICE, the energy deposit in forward direction is measured by the Zero-Degree-Calorimeters (ZDC) located in the forward direction. Centrality classes are given as percentiles of charged-particle multiplicity, or energy deposit in the ZDC in data and Monte Carlo. A more detailed distribution of the ALICE centrality estimation in Pb-Pb collisions at $\sqrt{s_{NN}} = 2.76$ TeV can be found in reference [27].

1.3.2 Proton-proton collisions

Proton-proton collisions are an interesting tool to study strong interactions. The protons, which are color-neutral objects, interact by the exchange of a colored gluon as they approach another. When the system decouples a gluon is exchanged so that the separated systems stay color neutral. The interaction is typically expressed using the Regge approach [29]. It is a pre-QCD theory, in which colorless particles, called pomerons, containing the quantum numbers of the vacuum are exchanged. Proton-proton collisions are generally classified by the topology of the final state. Inelastic proton-proton interactions are divided into two categories: diffractive and non-diffractive. Feynman diagrams of the different topologies are shown in figure 1.7. If one or both protons dissociate the process is called either single or double diffractive. If both protons remain intact, and the interaction happens between two pomerons the process is called central diffractive. Only around 25% [30] of the collisions belong to the diffractive class. The rest is of the inelastic cross section belongs to the non-diffractive event class, where the interaction happens on the parton level.

The non-diffractive collisions can be divided into two stages: the hard interaction and the underlying event [32]. The hard parton-parton interactions are characterized by a large momentum transfer, which results in high momentum partons, hadronization into high momentum particles in the final state. These processes can be modeled using perturbative QCD. The underlying event on the other hand is characterized by processes such as parton rescattering, initial as well as final state gluon radiation, before and after the collision. These multi parton interactions are predominantly non-perturbative and are modeled using Monte Carlo event generators. The understanding of these processes plays a critical role for many observables in hadron collisions and their precise modeling is vital for the interpretation of the measurements [33]. It is additionally possible to model the hadronic phase of a proton-proton collision using statistical models, which require local thermal equilibrium and local conservation of quantum numbers. This approach will be described in greater detail in section 1.4.2.

One of the main and unexpected discoveries at LHC was the first observation of collectivity in small systems (pp collisions). The measurement of long-range two-particle azimuthal correlations at large pseudorapidity in events with a high charged-particle multiplicity ($\langle dN_{ch}/d\eta \rangle$) showed a correlation over a wide pseudorapidity range ($|\Delta\eta| > 2$) [34]. This observation is referred to as the ridge and was first seen in nucleus-nucleus collisions at RICH [35] and LHC [36]. In high-multiplicity pp collisions, the ridge is interpreted as a result of a collective medium [34].

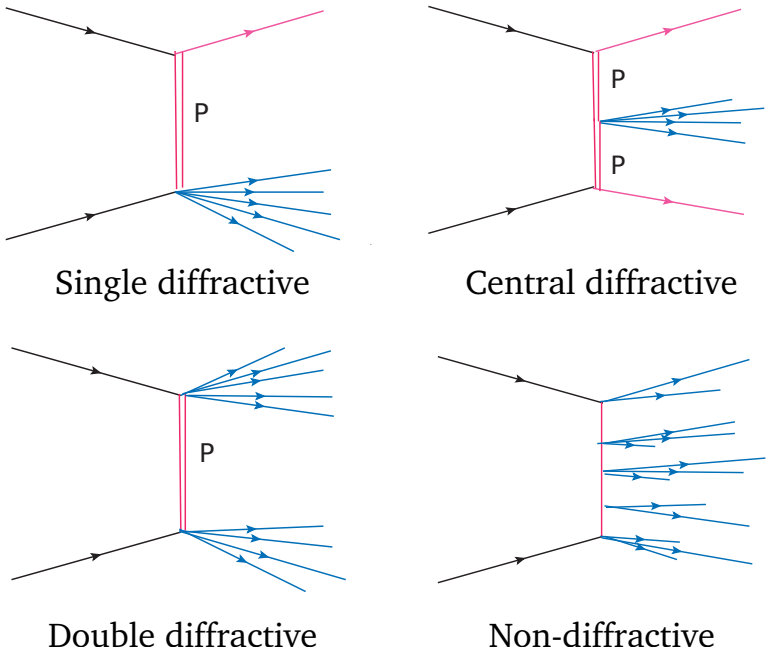

Figure 1.7: Different inelastic event types in pp collisions. The Feynman diagrams show the Pomeron (P) exchange graphs in Regge theory. The figure is adopted from reference [31].

1.3.3 Experimental signatures of a quark-gluon plasma

Because a heavy-ion collision takes less than 10 fm/c [37], the quark-gluon plasma created during its evolution, can not be investigated with external probes directly. Instead, one needs to rely on probes that themselves are created in the collision.

A commonly used technique is the comparison of an observation measured in nucleus-nucleus collisions to the same observable measured in proton-proton collisions. The proton-proton measurement is additionally scaled by the average number of binary nucleon-nucleon collisions $\langle N_{\mathrm{coll}} \rangle$ according to the purely geometrical Glauber model. Under the assumption that the nucleus-nucleus collision is a superposition of many independent nucleon-nucleon collisions, any deviation from unity can be attributed to medium effects which modify the nucleus-nucleus result. This method is known as the nuclear modification factor, here expressed for the number of produced particles per rapidity and transverse momentum as observable

$$R_{\mathrm{AA}} = \frac{\mathrm{d}N_{\mathrm{AA}}/\mathrm{d}y\mathrm{d}p_{\mathrm{T}}}{\langle N_{\mathrm{coll}} \rangle \mathrm{d}N_{\mathrm{pp}}/\mathrm{d}y\mathrm{d}p_{\mathrm{T}}}. \tag{1.3}$$

Over the last few decades, several probes have been suggested to study the QGP. Two examples are quarkonia and jets.

Quarkonia are flavorless mesons with their constituents being heavy quark and antiquark pairs, namely charm and bottom quarks. Due to their large masses, charm and bottom quarks are produced in the initial hard parton-parton scattering and thus expected to experience the full evolution of the QGP medium. In the deconfined medium, the attraction between the quark and the antiquark is supposed to be reduced because of color screening. The idea is based on the concept of Debye screening in an electromagnetic plasma, where the free moving charges

tend to cluster around their opposite charge. This means the heavy (anti-)quarks created in the QGP should be less likely to form a quarkonia state, depending on its binding energy and the temperature of the surrounding system. Especially the J/ψ, the $c\bar{c}$ ground state, was concluded to be an unambiguous signature of quark-gluon plasma formation [38]. As predicted measurements of the J/ψ nuclear modification factor at SPS [39, 40] and RHIC [41, 42] verified the suppression in heavy-ion collisions. However, at LHC energies the physics picture changes. In central Pb-Pb collisions at 2.76 TeV, the J/ψ suppression was found to be weaker in comparison to the measurements performed at lower energies [43]. This observation is explained by the (re)generation of charmonium due to copiously produced charm quarks at high energies [44].

Another method to study the deconfined medium created in the heavy-ion collision uses high transverse-momentum hadrons, with $p_{\mathrm{T}} > 5$ GeV/c. Most high transverse-momentum particles are produced in the hadronization of hard partons, produced in the initial stages of the collision. Thus, these hard scattered partons are expected to experience the evolution of the heavy-ion collision and the QGP medium. When penetrating the medium the partons will interact strongly with it and, thus, lose energy. This effect results in a suppression of high transverse-momentum hadrons and is known as jet quenching. The strength of the suppression is correlated with the transport coefficient of the QGP medium. Experimentally it is accessed by comparing the high transverse-momentum part of the charged particle transverse momentum spectra measured in nucleus-nucleons and pp collisions, using the nuclear modification factor.

One example measurement of the nuclear modification factor of primary charged particles in Pb-Pb collisions is shown in figure 1.8 for central and peripheral collisions [45]. A strikingly similar modification was observed for Xe-Xe collisions [46]. A suppression ($R_{\mathrm{AA}} < 1$) can be observed in the case of central collisions and a less pronounced effect for peripheral collisions, due to the in-medium modification of the transverse momentum spectra. Additionally, the nuclear modification factor, comparing p-Pb collisions to pp collisions (R_{pPb}) is shown. The R_{pPb} serves as an important reference for the nucleus-nucleus system, because no QGP medium should be created in p-Pb collisions and any modification gives access to initial state effects of the lead ions (for example shadowing [47]), which modify the parton distribution functions within the nucleus. As crosscheck, the nuclear modification factor is also measured for particles that do not interact strongly (e.g photon, W boson) [48]. There no suppression is observed ($R_{\mathrm{AA}} = 1$), which validates the binary scaling realized in Glauber model.

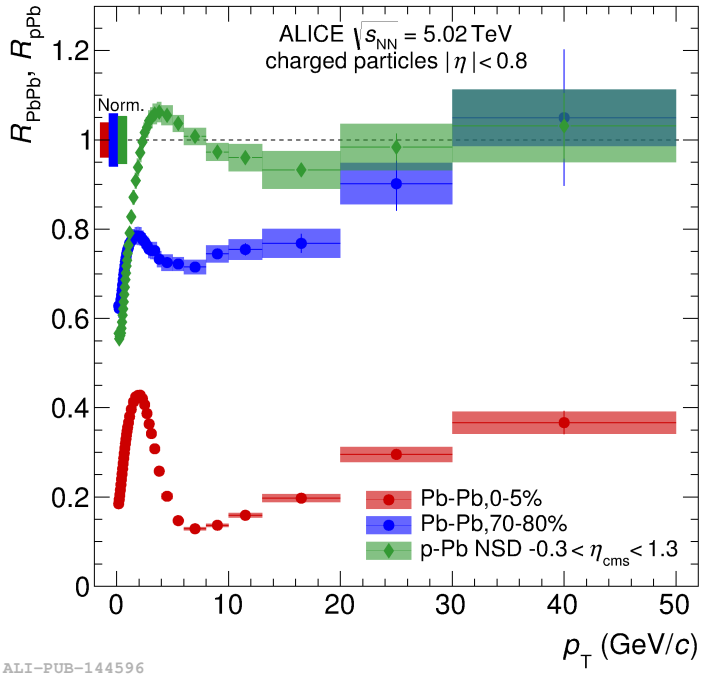

Figure 1.8: Nuclear modification factors in central and peripheral Pb-Pb and p-Pb collisions measured by ALICE [45, 49]

1.4 Light (anti)nuclei production in relativistic collisions

The production mechanism of light (anti)nuclei and (anti)hypernuclei in ultra-relativistic heavy-ion collisions remains still an open and actively discussed topic in the heavy-ion physics community. (Anti-)hypernuclei are composed objects containing at least one strange baryon. An experimentally accessible hypernucleus is the so-called hypertriton, being a bound state of proton, neutron, and Λ. The formation process of neither light (anti)nuclei nor (anti)hypernuclei can be calculated using first principle QCD and, therefore, relies on phenomenological models. Additionally, it is not at all intuitive how such loosely bound objects like light nuclei form in the hot environment of a heavy-ion collision. For comparison, the deuteron binding energy is 2.2 MeV, while the fireball temperature at chemical freeze-out is above 150 MeV. This causes the cross section for a pion-induced deuteron breakup to be remarkably larger than the typical neutron-proton (pseudo-)elastic re-scattering cross section [50, 51]. This picture becomes even more dramatic when looking at the hyperon sector. In the case of the (anti)hypertriton, only an energy of 130 ± 30 keV is needed to remove the Λ from the system. The exact underlying production mechanism of these very loosely bound objects is still under investigation and remains an open question. Nevertheless, two competing models, containing different physics pictures, have been developed over the last decades and both successfully describe the light nuclei yields in ultra-relativistic collisions, namely the statistical hadronization model and the coalescence model.

The statistical hadronization model (SHM) can describe the hadron chemistry of heavy-ion collisions over a wide range of collision energies, particle masses, and nine orders of magnitude in terms of particle abundances [52]. The hadron chemistry of a heavy-ion collision is fixed at chemical freeze-out and typically statistical hadronization models are fitted to the final-state particle abundances in a heavy-ion collision to extract the medium temperature and baryon chemical potential at chemical freeze-out. The statistical hadronization model will be discussed in detail in subsection 1.4.1.

In contrast to that, the coalescence model describes the formation of light (anti)nuclei via the coalescence of baryons, which are close in space, have similar momenta, and matching spins. In the coalescence formalism, the formation of light (anti)nuclei happens during the hadronic phase of the collision. Coalescence models successfully calculate the yields and transverse-momentum spectra of light (anti)nuclei. The latest approaches use a superposition of the nucleon distribution with the wave function of the nucleus employing a Wigner formalism [53]. The coalescence approach will be discussed in detail in subsection 1.4.3.

Previous studies presented in reference [54] found that both models are capable to describe measured light (anti-)nuclei and (anti-)hypernuclei yields and that both approaches agree well in their predictions. However, in reference [53] statistical hadronization model and coalescence model calculations are carried out as a function of the size of the (anti)(hyper)nuclei relative to the size of the particle emitting source, which shows a significant difference between coalescence and thermal model predictions for deuteron, helium-3 nuclei, and hypertriton yields in the intermediate charged-particle multiplicity region. Intermediate charged-particle multiplicities ranging from $10 < \mathrm{d}N_{\mathrm{ch}}/\mathrm{d}\eta < 50$ can be reached using high-multiplicity triggered pp collisions, or in larger systems such as p-Pb collisions. The model predictions as a function of the source size radius are shown in figure 1.9 for deuteron, helium, and hypertriton nuclei. Additionally, reference [55] suggests the helium-to-triton ratio as well as the hypertriton-to-lambda

ratio to be a good probe to test different coalescence pictures. In figure 1.10 the ratios are displayed as a function of charged-particle multiplicity. In the low multiplicity regime, created in minimum bias pp collisions, the measurement is sensitive to the difference predicted from two or three-body coalescence models giving further inside on the coalescence of helium nucleus and triton within the coalescence picture. In the two-body coalescence, a deuteron and a proton form a helium nucleus while in the three-body coalescence the helium nucleus is formed from three baryons instead.

Such models are tested using a large variety of measurements which have been performed by the ALICE Collaboration in the light nuclei sector, reaching up to ^{4}He [56, 57, 58, 59, 60, 61, 62, 63, 64, 65, 66]. Additionally, many studies of light nuclei production are performed at lower energies at BNL (Brookhaven National Laboratory) with measurements of the AGS [67, 68, 69, 70] and at RHIC [71, 72, 73, 74, 75, 76].

1.4.1 Statistical hadronization models

The original idea of describing a system of interacting hadrons within a statistical approach was formulated by Fermi in 1950 who claimed that particles will be released from a small volume and populate the available states according to statistical laws [81]. In 1965, Hagedorn extended that idea and formulated his bootstrap model [23]. He assumed that the interactions of hadrons in the ground state taking part in the thermodynamic evolution can be described by the creation of higher and higher resonance hadron states, also called clusters as if they were non-interacting particles. This led to the conclusion that the hadron mass spectra $\rho(m)$, with $\rho(m)\mathrm{d}m$ yielding the number of excited hadrons in the mass interval from m to $m + dm$, follows an exponential behavior:

$$\rho(m) \propto \frac{1}{m^3} \exp\left(\frac{m}{T_H}\right) \tag{1.4}$$

with T_H being the so-called Hagedorn temperature, which he referred to as the boiling point of hadronic matter beyond which a gas of quarks would form a new state of matter. The first estimate of T_H was around 158 MeV, which is pretty close to the latest Lattice QCD calculation of the phase transition temperature as discussed in section 1.3. Hagedorn's idea was modified so that clusters do not need to be identified with resonance states to decay statistically. Current versions of statistical hadronization models are used to connect experimental observation of the hadron chemistry produced in a relativistic heavy-ion collision with the medium properties at the chemical freeze-out. Very recent studies even use the QCD partition function and draw conclusions on the QCD phase diagram [52]. However, the original assumption that the system produced in a heavy-ion collision behaves like a thermalized medium and can be described using statistical physics is still the same. Thus, the grand-canonical partition function for a particle i in the case of a relativistic ideal gas is given by:

$$\ln Z_{\mathrm{GK}\,i} = \pm g_i \frac{V}{2\pi^2} \int_0^\infty p^2 \ln\left(1 \pm \exp\left(-\frac{\sqrt{m_i^2 + p^2} - \mu_i}{T_{\mathrm{ch}}}\right)\right) \mathrm{d}p \tag{1.5}$$

here $g_i = 2J_i + 1$ is the spin degeneracy factor, V the volume of the emitting source, m_i is the mass of the particle of interest, μ_i the chemical potential, and T_{ch} the temperature of the

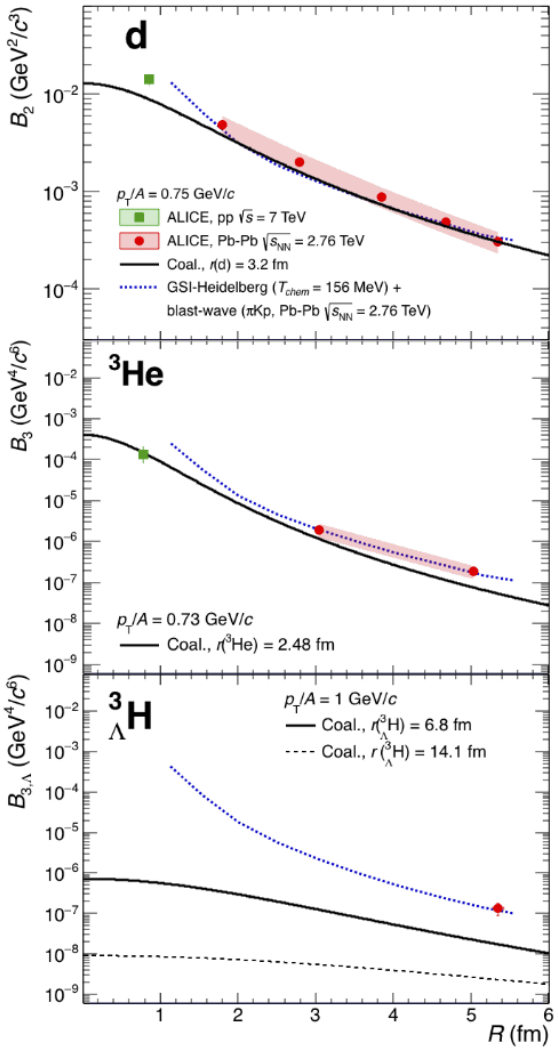

Figure 1.9: The coalescence parameter measured by ALICE for deuteron, ^{3}He, and hypertriton nuclei in pp [59], and Pb-Pb [77, 78] compared to expectations from coalescence and a thermal+blast-wave model as a function of the emission source radius. The figure is taken from reference [53].

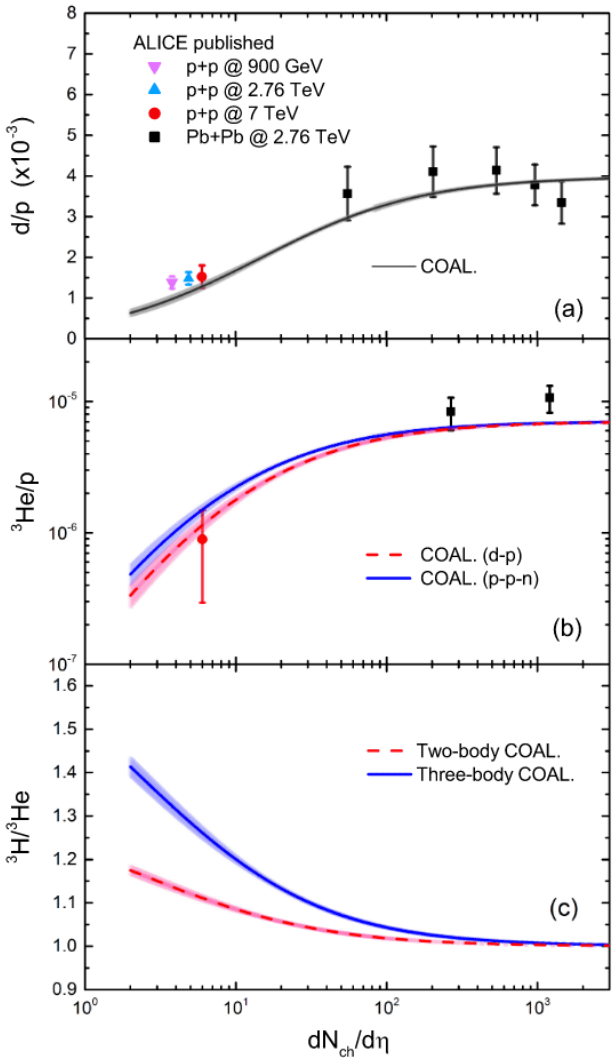

Figure 1.10: Ratio of d-to-p, ^{3}He-to-p and ^{3}H-to-^{3}H integrated yields as a function of multiplicity measured by ALICE [79, 80, 77, 59] compared to two and three-body coalescence predictions. The figure is taken from reference [55].

system. The chemical potential includes four components conserving the baryon (B_i), strange (S_i), isospin (I_3), and charm (C_i) quantum numbers. Note, however, that charm is not thermally produced and a fugacity factor, which will be explained later in this section, is typically used. It can be written as $\mu_i = \mu_B B_i + \mu_S S_i + \mu_{I_3} I_3 + \mu_C C_i$. The positive sign is used according to the Fermi-Dirac statistics of fermions, while the negative sign describes bosons according to the Bose-Einstein statistics. From the partition function, four thermodynamic properties of the medium can be calculated using its partial derivatives.

The pressure is given by

$$P = \frac{\partial (T_{\mathrm{ch}} \ln Z_{\mathrm{GK}})}{\partial V} , \tag{1.6}$$

the energy by

$$E = T_{\mathrm{ch}}^2 \frac{\partial \ln Z_{\mathrm{GK}}}{\partial T_{\mathrm{ch}}} , \tag{1.7}$$

the entropy by

$$S = \frac{\partial (T_{\mathrm{ch}} \ln Z_{\mathrm{GK}})}{\partial T_{\mathrm{ch}}} , \tag{1.8}$$

and the individual particle yield by

$$n_i = \frac{\partial (T_{\mathrm{ch}} \ln Z_{\mathrm{GK}})}{\partial \mu_i} . \tag{1.9}$$

The chemical potentials can be determined from conservation laws, using the initial conditions of the collision. Since the initial colliding nuclei, neither contains net strange nor net charm both quantities have to be net-zero in the final state. Thus, $\sum_i N_i(\mu_s) S_i = 0$ and $\sum_i N_i(\mu_c) c_i = 0$ follows. Equally, the isospin is fixed from the initial conditions and given as $\sum_i N_i(\mu_{I_3}) I_{3_i} = (Z - N)/2$, where Z and N are the proton and neutron numbers of the colliding nuclei. This leaves us with only three free parameters in the partition function: the baryon chemical potential μ_B, the temperature of the system T_{ch}, and the volume of the fireball V. Note that within the statistical hadronization formalism the parameters are at chemical freeze-out, which is the point in time at which the hadron chemistry is fixed. Within such a formalism, these parameters at chemical freeze-out can be accessed by fitting the model to measured particle yields at mid rapidity. However, for each particle i, the feed down from strong and electroweak decays of higher mass resonances has to be included. If one looks specifically at particle yield ratios, the procedure simplifies a bit, because the volume dependence cancels.

The implementation of the statistical hadronization formalism varies slightly between theory groups. Some introduce an additional fugacity factor γ_s which takes care of a potentially incomplete equilibration of strangeness [82]. Each particle's partition function is multiplied by $\gamma_s S_i$, with S_i being the number of strange and antistrange valence quarks. Some others introduce an additional repulsive interaction, due to the radii (r_0) of the hadrons, which can be also interpreted as an exclusion volume [83]. For weak repulsions ($r_0 < 0.3$ fm) this effect mainly decreases particle densities while temperature and baryon chemical potential stay the same.

In heavy-ion collisions, the statistical hadronization models show remarkable agreement with measurements in central Pb-Pb collisions at $\sqrt{s_{\mathrm{NN}}} = 5.02$ TeV as shown in figure 1.11. Here, three different statistical hadronization implementations are compared to the data, namely THERMUS [84], GSI-Heidelberg [52], and statistical hadronization with resonances (SHARE) [85]. For all models, the baryon chemical potential is set to zero, which as mentioned before is very reasonable at LHC energies.

For the calculation in figure 1.11 the exclusion volume is set to $\tau_0 = 0.3$ fm and the fugacity factor is set to $\gamma_S = 1$, for the THERMUS and the GSI-Heidelberg model. In SHARE both of these corrections are not implemented. The models shown in figure 1.11 are fitted to the ALICE measurements and used to predict the abundances for (anti-)^{3}H and (anti-)^{3}He. Overall all three models agree well with the data over nine orders of magnitude in production yields with a chemical freeze-out temperature $T_{\mathrm{ch}} = 153 \pm 2$ MeV. In a more sophisticated study, including also the $A = 3$ nuclei into the interpolation and carefully adjusting the corrections to minimize the χ^2

the GSI-Heidelberg model predicts a chemical freeze-out temperature of $T_{\mathrm{ch}} = 156 \pm 2$ MeV [52]. The largest difference between data and model was found in the observed proton and antiproton yields where the deviation from the experimental results is 2.7σ. In a recent study by the same authors, this effect can be resolved when considering resonant and non-resonant πN and $\pi\pi$N interactions [86].

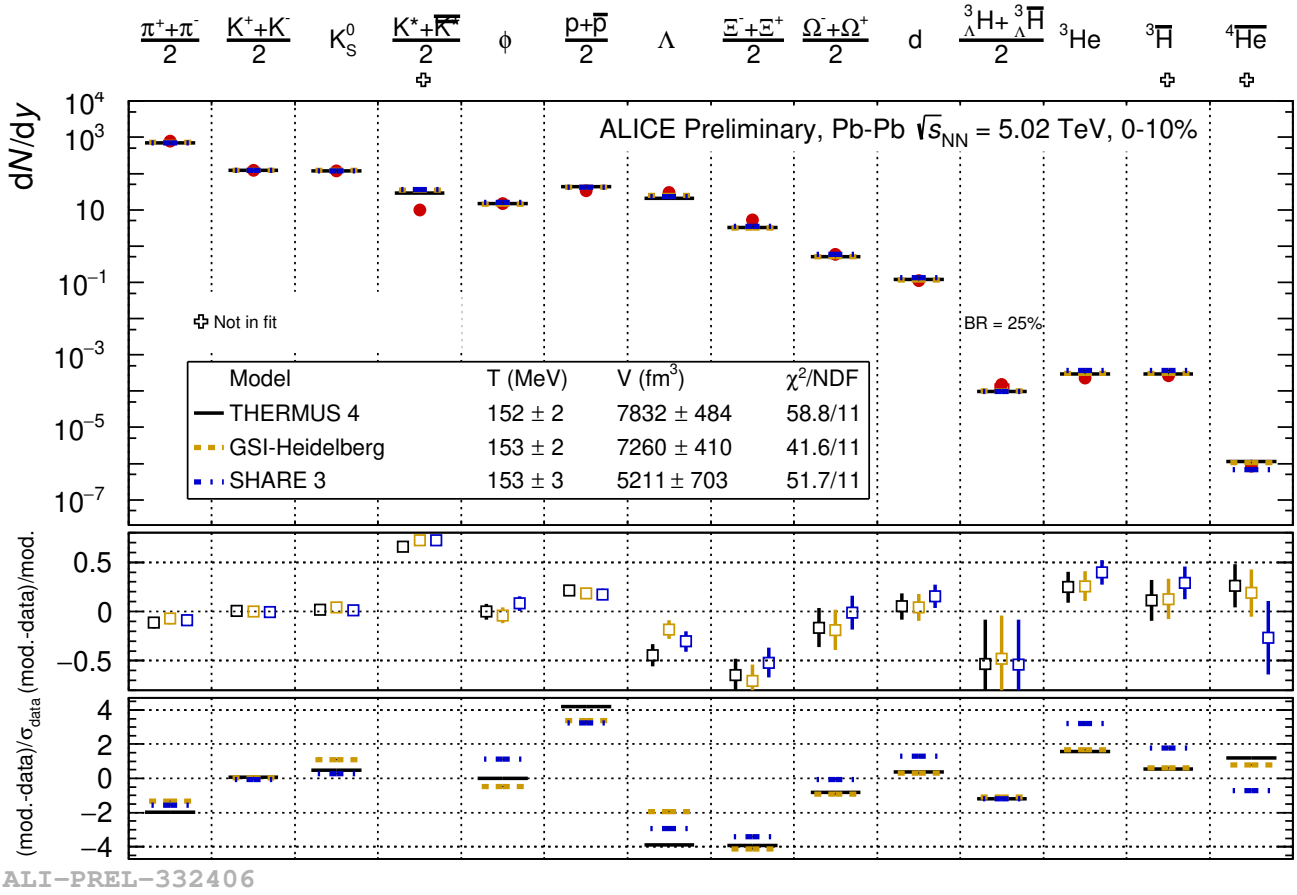

Figure 1.11: Statistical hadronization model fits (THERMUS 4 [84], GSI-Heidelberg [52], SHARE 3 [85]) to integrated particles yields at mid rapidity measured with ALICE in central Pb-Pb collisions. The chemical freeze-out temperatures in all three implementations agree within uncertainties. The middle panel shows the difference between the model and the measurement divided by the model expectation. The lowest panel shows the same difference expressed in terms of uncertainties of the measured ALICE data.

1.4.2 Statistical hadronization models in small systems

The concepts of statistical hadronization can also be extended to small systems like e^+e^-, pp, or p-Pb collisions. Here, however, instead of the grand canonical ensemble, a canonical ensemble has to be applied, because on average conservation of charges is not sufficient in a small system. Instead, the baryon number, electrical charge, and strangeness have to be strictly conserved within the correlation volume V_c. This exact conservation of charges and quantum numbers leads to an effect called canonical suppression of the yields of particles carrying conserved quantities when going from large to small systems [87]. According to references [87, 88, 89], the

mean multiplicities of various particle species can be calculated using the mean multiplicity obtained in the grand canonical approach at the same temperature and volume and the canonical partition function of the hadron resonance gas ($Z(B,Q,S)$). The mean multiplicity is given as

$$\langle n_i \rangle_{\mathrm{C}} = \frac{Z(B-B_i, Q-Q_i, S-S_i)}{Z(B,Q,S)} \langle n_i \rangle_{\mathrm{GK}} \tag{1.10}$$

At the LHC, the particle yields at mid rapidity are the same for particle and antiparticle.
Due to that the canonical ensemble is calculated at vanishing value of $B = 0$. Additionally, strangeness and charged conservation leads to $Q = S = 0$. The canonical statistical model calculation presented in reference [90] takes finite widths of the resonance states into account expressed as Breit-Wigner resonances. In comparison to the grand canonical description, the correlation volume (V_c) becomes another critical parameter in the model next to the chemical freeze-out temperature T_{ch}, the baryon chemical potential μ_B, and the total volume V. A priori the correlation volume is not known and can not be easily accessed. However, in reference [91] the causality of hadron production in high energy collisions is studied, claiming that the production occurs in several causally disconnected regions of finite space-time size. This leads to locally conserved quantum numbers in spatially restricted correlation clusters. On that basis, the authors of reference [87] choose the correlation volume to be between one and three units of rapidity. The same authors argue in a later published article found in reference [92], that the correlation volume can extend up to six units of rapidity. Additionally, they introduced a multiplicity-dependent freeze-out temperature and the strangeness saturation parameter γ_S improving the description of light light hadron yield ratios significantly.

1.4.3 Coalescence models

In contrast to the statistical hadronization model (see section 1.4.1), the coalescence model describes the production mechanism of nuclei on a microscopic level. The first to describe the formation of the deuteron in nuclear collisions using the coalescence picture were Butler and Pearson [93]. The coalescence model says that nucleons that are close in momentum and coordinate space can form a bound state. Such a process is sketched in figure 1.12. After the chemical freeze-out, a pair of independent nucleons in the final state transfer momentum to the rest frame of the system to form a deuteron [94]. Following this idea, the deuteron density observed in a collision should be proportional to the product of the densities of its constituents, namely the neutron and proton. Due to isospin symmetry, the proton and neutron production rates are assumed to be the same in a collision. Thus, the deuteron density should be proportional to the square of the proton density. For heavier nuclei the same principle holds and, therefore, the nuclei spectra are given as:

$$E_{\mathrm{A}} \frac{\mathrm{d}^3 N_{\mathrm{A}}}{\mathrm{d}p_{\mathrm{A}}^3} = B_A \cdot \left(E_{\mathrm{n}} \frac{\mathrm{d}^3 N_{\mathrm{n}}}{\mathrm{d}p_{\mathrm{n}}^3} \right)^{A-Z} \Bigg|_{\vec{p}_{\mathrm{n}} = \frac{\vec{p}_{\mathrm{A}}}{A}} \cdot \left(E_{\mathrm{p}} \frac{\mathrm{d}^3 N_{\mathrm{p}}}{\mathrm{d}p_{\mathrm{p}}^3} \right)^{Z} \Bigg|_{\vec{p}_{\mathrm{p}} = \frac{\vec{p}_{\mathrm{A}}}{A}} \approx B_A \cdot \left(E_{\mathrm{p}} \frac{\mathrm{d}^3 N_{\mathrm{p}}}{\mathrm{d}p_{\mathrm{p}}^3} \right)^{A} \Bigg|_{\vec{p}_{\mathrm{p}} = \frac{\vec{p}_{\mathrm{A}}}{A}} \tag{1.11}$$

with $E_{\mathrm{i}} \frac{\mathrm{d}^3 N_{\mathrm{i}}}{\mathrm{d}p_{\mathrm{i}}^3}$, ($i = \mathrm{A}, \mathrm{p}, \mathrm{n}$) being the invariant yield of the nucleus, the proton, and the neutron, respectively. A and Z are the mass and proton numbers of the nucleus, and B_A is the so-called coalescence parameter.

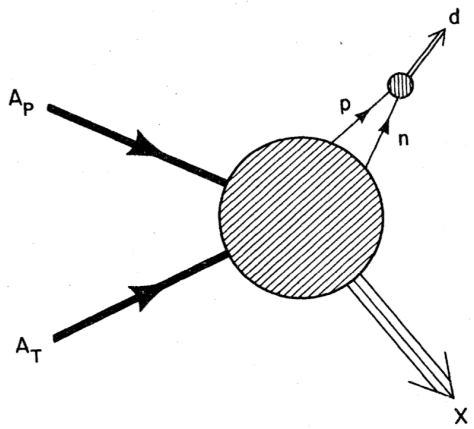

Figure 1.12: Illustration of the simple coalescence production of a deuteron from two independent nucleons [94].

In reference [94], the most basic theoretical description of the coalescence process is formulated, often referred to as "simple coalescence". Here the focus lies only on the momentum dependence while the spatial component is neglected. When one considers a sphere in momentum space with radius p_0 centered at $\vec{p}$, the geometrical probability of finding a nucleon on the sphere is given as:

$$P = \frac{1}{M}\frac{4\pi}{3}p_0^3\gamma\frac{\mathrm{d}^3N}{\mathrm{d}p^3}, \tag{1.12}$$

where $\frac{\mathrm{d}^3N}{\mathrm{d}p^3}$ is the invariant momentum-space density of the nucleons before the coalescence process (under the assumption neutron and proton densities are equal), gamma is the Lorentz factor, M is the mean nucleon multiplicity, and p_0 is the maximum relative momentum difference between the nucleons for coalescence to occur if the nucleons are in the appropriate spin states. To simplify the problem, p_0 is assumed to be momentum independent and needs to be determined by fitting the model to measurements. p_0 is assumed to be in the order of the Fermi motion of the nucleons, which is in the order of $p \approx 250$ MeV/c. The probability of finding A nucleons in the previously defined sphere is

$$P_M(A) = \binom{M}{A}P^A(1-P)^{M-A}. \tag{1.13}$$

Under the assumption that all nucleons which are close enough in momentum space to form a nucleus, the coalescence probability should be given as the probability of finding a nucleus with the mass number A in the sphere. Two further simplifications can be made if $MP \ll 1$, which is the case if the production of a nucleus is a rare process, and if $M \gg 1$, which is the case if many nucleons are produced in the collision. Then $P^A(1-P)^{M-A}$ approximately becomes one and $\frac{1}{M^A}\binom{M}{A} \approx \frac{1}{A!}$. This leads to a nucleus space density with mass number A of:

$$\begin{aligned}\frac{4\pi}{3}p_0^3\gamma_\mathrm{A}\frac{\mathrm{d}^3N_\mathrm{A}}{\mathrm{d}p^3} &= \frac{1}{A!}\left(\frac{4\pi}{3}p_0^3\right)^A\left(\gamma_\mathrm{p}\frac{\mathrm{d}^3N_\mathrm{p}}{\mathrm{d}p^3}\right)^A \\ \gamma_\mathrm{A}\frac{\mathrm{d}^3N_\mathrm{A}}{\mathrm{d}p_\mathrm{A}^3} &= \frac{1}{A^3}\left(\frac{4\pi}{3}p_0^3\right)^{A-1}\frac{1}{A!}\left(\gamma_\mathrm{p}\frac{\mathrm{d}^3N_p}{\mathrm{d}p^3}\right)^A\end{aligned} \tag{1.14}$$

In the coalescence process, the momentum p of the nucleons has to be transfered into to the momentum $p_{\mathrm{A}} = Ap$ of the nucleus, hence the $1/A^3$ factor appears in the equation. The derived equation can now be compared to equation 1.11 to determine the coalescence parameter B_A, using $\gamma = E/m$:

$$B_A = \frac{2J_A+1}{2^A}\frac{1}{A^3}\frac{1}{A!}\left(\frac{4\pi}{3}p_0^3\right)^{A-1}\frac{M_{\mathrm{A}}}{m^A} \tag{1.15}$$

Here M_{A} is the mass of the nucleus and m is the nucleon mass. An additional spin factor of $(2J_A+1)/2^A$ was also added to take the spins of the nucleons and the nucleus into account. As mentioned above, in the simple coalescence picture B_A is momentum independent. Also, the emission source size as well as the size of the produced nucleus, do not enter the formalism. These simplifications disagree with a range of ALICE measurements showing a centrality dependence of B_A in Pb-Pb collisions. One example measured in reference [77] shows the B_3 as a function of transverse momentum in central and peripheral Pb-Pb collisions at $\sqrt{s_{\mathrm{NN}}} = 2.76$ TeV in figure 1.13.

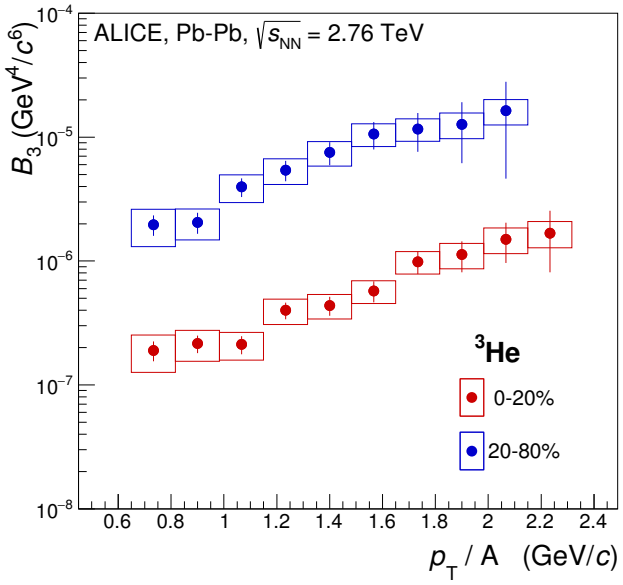

Figure 1.13: The coalescence parameter B_3 as a function of transverse-momentum measured in central and peripheral Pb-Pb collisions at $\sqrt{s_{\mathrm{NN}}}$ = 2.76 TeV with ALICE [77].

1.4.4 Advanced coalescence models

As already mentioned, the simple coalescence approach is not able to capture key features of the measured coalescence parameter (like the p_{T} dependence). However, Scheibl and Heinz expanded the coalescence formalism using a density matrix approach in reference [95]. A recent study [96] picked up that idea and developed it further using hadron-hadron correlations in momentum space measured with ALICE. These developments are usually referred to as "advanced coalescence" models and will be summarized in this section.

A correlation between the source volume and the coalescence parameter was discussed in reference [95]. For a cluster with mass A and spin J_A, this correlation can be expressed as:

$$\frac{B_A}{m^{2(A-1)}} \approx \frac{2J_A+1}{2^A\sqrt{A}}\left(\frac{mR}{\sqrt{2\pi}}\right)^{3(1-A)} \tag{1.16}$$

Note that the equation is evaluated at $p_T = 0$ in the center-of-mass frame of the fireball. The crucial factor is the second one which contains the source radius R. Experimentally, the source radius is accessible via two-particle correlation functions via so-called HBT (Hanbury Brown-Twiss) analysis [97], being a specific case of femtoscopy. In heavy-ion collisions, a wide variety of several different femtoscopy measurements have been studied. Some of them are summarized in figure 1.14. The source created in a Pb-Pb collision has a radius of approximately 4 fm while the one created in a pp collision has a smaller radius around 1 fm. Therefore, equation 1.16 predicts a decrease of the coalescence parameter when going from small to large systems. In

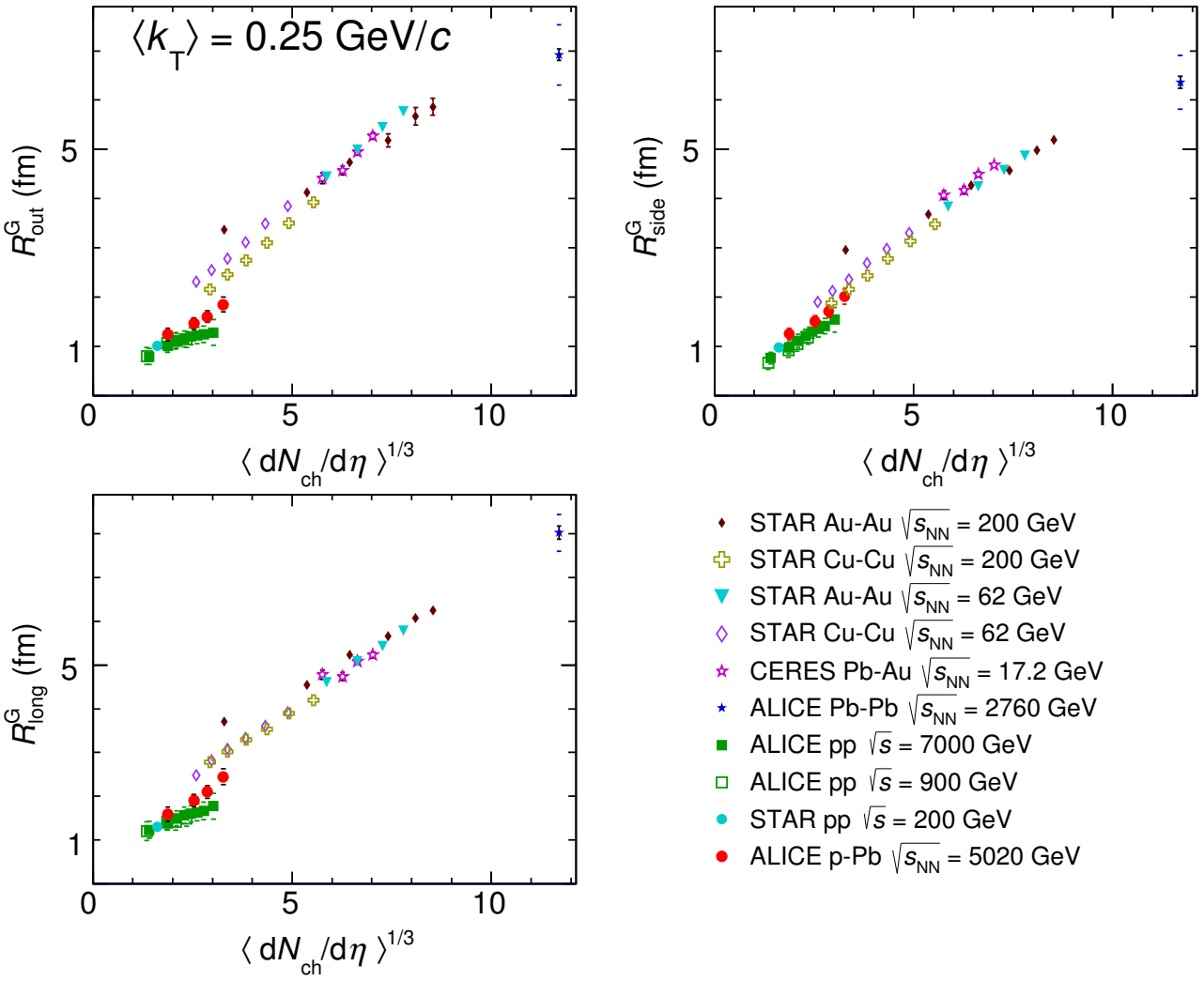

Figure 1.14: Different source radii obtained with femtoscopy techniques, as a function of charged-particle multiplicity density, measured for a wide range of collision systems and center of mass energies. The figure is taken from reference [98].

first order, the source size radius (R) can be related to the average charged-particle multiplicity of the collision using

$$R = a\langle \mathrm{d}N_{\mathrm{ch}}/\mathrm{d}\eta\rangle^{1/3} + b \tag{1.17}$$

as discussed in reference [53], with $a = 0.339$ fm and $b = 0.128$ fm constrained by ALICE data. The source size radius as a function of the $\langle \mathrm{d}N_{\mathrm{ch}}/\mathrm{d}\eta\rangle^{1/3}$ is displayed in figure 1.15.

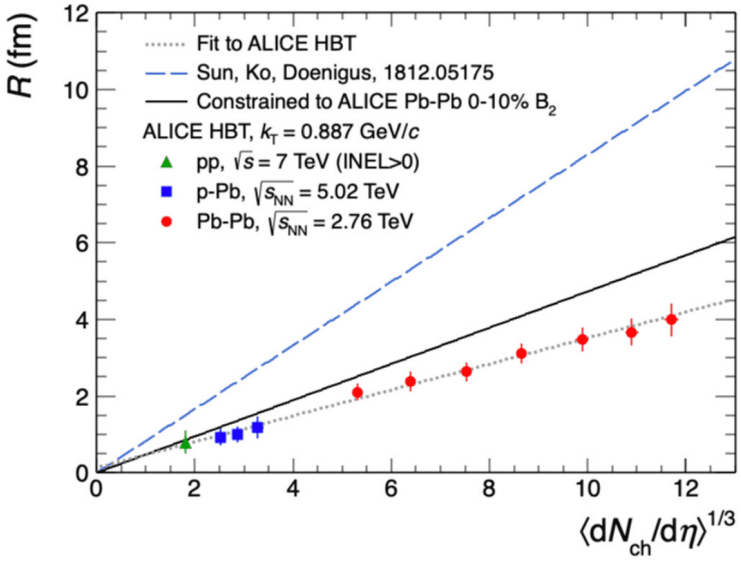

Figure 1.15: Collision source radius as a function of $\langle \mathrm{d}N_{\mathrm{ch}}/\mathrm{d}\eta\rangle^{1/3}$ with three different source size parameterizations. The dotted line is a fit to a set of ALICE femtoscopy measurements [99, 100, 101]. The blue line shows a parametrization used in reference [55]. The black line is a parametrization that is obtained by constraining the source size to the measured B_2 in central Pb-Pb collisions as discussed in reference [53].

In equation 1.16 the deuteron wave function is assumed to be Gaussian. Blum and Takimoto [96] have built upon these results and developed a deuteron coalescence model for a generalized deuteron wave function ($\Phi_{\mathrm{d}}(\vec{r})$), with $\int \mathrm{d}^3 r |\Phi_{\mathrm{d}}(\vec{r})|^2 = 1$. The baseline for their calculation is the assumption that hadronic collisions produce high-excitation states which are characterized by a density matrix ($\hat{\rho}$). The probability of producing any finial state is then given by its projection onto the density matrix. In the case of the deuteron this is:

$$\frac{\mathrm{d}N_{\mathrm{d}}}{\mathrm{d}^3 p_{\mathrm{d}}} = \langle \Psi_{p_{\mathrm{d}}} | \hat{\rho} | \Psi_{p_{\mathrm{d}}} \rangle \tag{1.18}$$

The next crucial input of the model is the two-particle (proton-neutron) bound state wave function $|\Psi_{p_d}\rangle$, which allows for the calculation of the deuteron probability density. For a deuteron with momentum p_{d} in the laboratory frame $|\Psi_{p_d}\rangle$ is given as:

$$\Psi_{p_{\mathrm{d}}}(x_1, x_2) = e^{i\vec{p}_{\mathrm{d}}\cdot\vec{x}} \Phi_{\mathrm{d}}(\vec{r}) \tag{1.19}$$

with the space coordinates $\vec{x} = (\vec{x}_1 + \vec{x}_2)/2$ and $\vec{r} = \vec{x}_1 - \vec{x}_2$. The deuteron density (evaluating equation 1.18) is mainly driven by the two-particle reduced density matrix. Here, an important

simplification is made by assuming the two-particle reduced density matrix can be factorized, which allows for the description of the one particle-densities matrices using Wigner density. The Wigner density links the nuclear wave function to a probability distribution in phase space. The Wigner density of a deuteron $D(\vec{q})$ is given as:

$$D(\vec{q}) = \int \mathrm{d}^3 r |\Phi_d(\vec{r})|^2 e^{-i\vec{q}\cdot\vec{r}} \tag{1.20}$$

with $\vec{q} = \vec{p}_1 - \vec{p}_2$ being the relative momentum of the nucleons. This representation allows for the study of different nuclear wave functions. In the study discussed here a Gaussian wave function was considered, but the equation also allows the input of for example the van Hulthen wave function, very commonly used in nuclear physics.

The second input in the model is the emission source which as discussed before is accurately studied using femtoscopic techniques. The two-particle correlation function in the two-particle rest frame was found to be

$$C_2^{\mathrm{PRF}}(\vec{p}, \vec{q}) = \exp\left(-R_\perp^2 q_\perp^2 - R_\parallel^2 q_\parallel^2\right) \tag{1.21}$$

with $q_\perp$ and $q_\parallel$ being the parallel and transverse momentum component (relative to the beam axis) of the two-particle relative momentum. For a homogeneous source this can be further simplified using $R = R_\perp = R_\parallel$, which leads to:

$$C_2^{\mathrm{PRF}}(\vec{p}, \vec{q}) = \exp\left(-R^2 q^2\right) \tag{1.22}$$

These inputs lead to a final result for the deuteron coalescence parameter for the case of small relative momenta $|\vec{q}| < m$

$$B_2 = \int \mathrm{d}^3 p D(\vec{q}) C_2^{\mathrm{PRF}}(\vec{p}, \vec{q}) \tag{1.23}$$

This is a very interesting result because only two free parameters remain in the calculation of the coalescence parameter. The first is the emission source radius, which is very well constrained by measurements and the second is the deuteron wave function, which contains information about the nuclear structure of a deuteron.

Blum and Takimoto also provide an equation for the coalescence parameter of a nucleus with the mass number A. This calculation, however, is more complex and was, therefore, performed for an $(A-1)$ symmetrical Gaussian wave function and only in the case of a homogeneous emission source. The coalescence parameter as a function of the emission source radius is given as:

$$B_A(R) = \frac{2J_A + 1}{2^A \sqrt{A}} \frac{1}{m^{A-1}} \left(\frac{2\pi}{R^2 + (r_A/2)^2}\right)^{\frac{3}{2}(A-1)} \tag{1.24}$$

with r_A being a nuclear size parameter related to the rms charge radius via $r_{\mathrm{rms}}^2 = \frac{3(A-1)}{2A} r_A^2$. The ^{3}He coalescence parameter as a function of the emission source radius according to equation 1.24 is shown in appendix figure A.1. A fully detailed description of the calculation of the deuteron coalescence parameter as well as the generalized case for a nucleus with A nucleons can be found in reference [96].

1.5 Connection to astrophysical observables

From the observation of the gravitational force between galaxies, the conclusion arises that only 5% of the matter and energy content of our universe contains ordinary matter, described by the Standard Model and a much larger fraction of about 25%, which interacts via the gravitational force must come from an additional source. This unknown source of matter is called dark matter. The remaining 70% is known as dark energy, needed to describe the accelerating expansion of the universe. Especially, the searches for and the theoretical description of dark matter are among the hottest research topics right now. Particle physics, as well as the astrophysics community, have dedicated research programs and experiments trying to discover a potential dark matter candidate. The potential mass range covered in theoretical models spans over many orders of magnitude from 10^{-24} eV/c^2 up to 10^{19} GeV/c^2 which is the Planck scale. One of the most promising candidates is the so-called weakly interacting massive particle (WIMP), which has an expected mass of roughly 100 GeV/c^2. In the models, WIMPs are assumed to be stable, neutral, weakly interacting, and massive particles, which were produced thermally in the early universe. At the LHC, the CMS, ATLAS, and LHCb collaborations did a benchmark study for direct searches of dark matter particles in the LHC Run 2 period in reference [102].

If the WIMP has similar properties as the known standard model particles, they should in principle annihilate with their corresponding antiparticle as schematically shown in figure 1.16. The dark matter annihilation is indicated with question marks because nothing is known about such an interaction. The searches for dark matter candidates using these decay products are referred

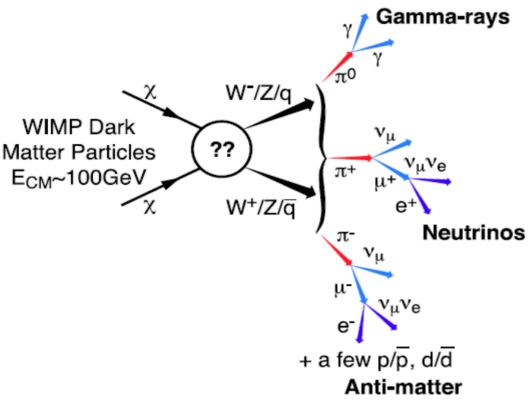

Figure 1.16: Sketch of the possible annihilation of a weakly interacting massive particle into a variety of standard model particles. The figure is taken from reference [103].

to as indirect searches. The most common probes are neutrinos or light antinuclei. Due to the weakly interacting nature of neutrinos, they are measured using huge active volumes on earth like it is realized in the IceCube experiment [104]. The measurement of antinuclei, on the other hand, is straightforward, and there are only a few known background sources. Cosmic antinuclei fluxes, however, can only be measured outside the earth's atmosphere since the antinuclei would annihilate with the matter in the atmosphere. The AMS Collaboration overcomes these constraints by operating the Alpha Magnetic Spectrometer (AMS-02) [105] on the international space station. It is designed to measure and identify cosmic antinuclei fluxes.

With our current knowledge, there is only one antinuclei source in the galaxy. These are antinuclei originating from interactions of cosmic rays, which are mostly protons, with the interstellar

medium, which consists of 90% hydrogen and 10% ^{4}He atoms. Any excess antinuclei yield is a clear sign of new physics. Therefore, antinuclei are often referred to as a "smoking-gun" for indirect dark matter searches. The proper estimate of the background component originating from hadronic interactions in the galaxy, however, plays a critical role. Here two key components enter the equation: first, the production process itself, which is typically described using a coalescence model (see section 1.4.3), and second the propagation of the produced antinuclei through the universe and the solar system.

The LHC is the only machine on earth reaching the needed center-of-mass energies to produce a substantial number of anti-^{3}He. Therefore, the coalescence parameter measurements presented in this work give a fundamental baseline for the production rate of antinuclei originating from known hadronic interaction in space. Additionally, the ALICE Collaboration is planning to constrain the propagation of antinuclei in space by measuring the antinuclei inelastic cross sections as done in reference [106] for antiprotons and antideuterons as also discussed in section 3.5.1.

Figure 1.17 shows the expected flux of antihelium originating from ordinary hadronic interactions as a function of energy. The study was performed in reference [107]. A clear mass ordering between anti-^{3}He and ^{4}He is visible with the second being the even cleaner probe. Additionally, the expected sensitivity of the AMS experiment is indicated using the shaded area. The work done in reference [108] concluded compatible results. During a CERN seminar in 2018, the AMS Collaboration showed preliminary results claiming the measurement of six anti-^{3}He and two anti-^{4}He candidate events in six years of AMS running time [109]. Up to now, the AMS Collaboration did not publish these results in a peer-reviewed journal. Their confirmation, however, would be a major breakthrough significantly impacting cosmology. As shown in figure 1.17, already the observation of the anti-^{3}He events is difficult to reconcile with our current knowledge of the production of antinuclei, but the observation of anti-^{4}He events is nearly excluded. With the antarctic balloon mission GAPS (General AntiParticle Spectrometer), flying at a height of about 37 km and an attitude with small geomagnetic cut-off [110, 111], an independent measurement is planned to start in 2021.

An alternative model used to describe the preliminary AMS observation is the existence of antimatter clouds or stars in the universe [107], which is another exciting explanation. The review in reference [112] summarizes the work done in recent years and presents an implementation of the upcoming antinuclei observation in space-bound experiments.

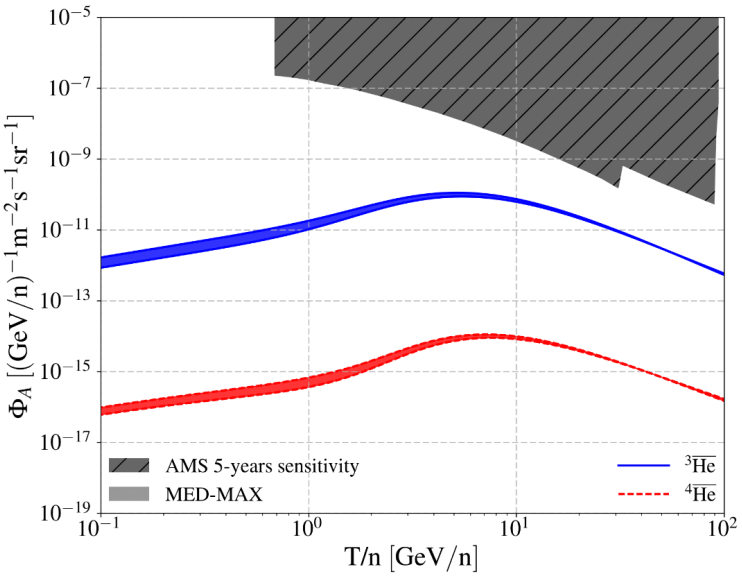

Figure 1.17: The expectation of the AMS secondary antihelium flux, origination from cosmic rays on interstellar medium scattering based on the ALICE measurements of the coalescence parameter published in reference [77]. The figure is taken from reference [107].

2 A Large Ion Collider Experiment at the Large Hadron Collider

2.1 The accelerator complex

The European Organization for Nuclear Research, known as CERN, located in Geneva, Switzerland, is one of the largest particle and nuclear physics laboratories worldwide. It operates various facilities and a unique accelerator complex, offering opportunities for physicists to explore hadron, nuclear, and elementary particle physics on the most fundamental level.

CERN's accelerator complex is a chain of many different accelerator types. Several accelerators serve as a pre-accelerator chain, increasing the beam energy step-wise to a maximum center-of-mass energy of $\sqrt{s} = 13$ TeV for proton beams in its last stage - the Large Hadron Collider (LHC). A systematic drawing of the CERN accelerator complex is shown in figure 2.1.

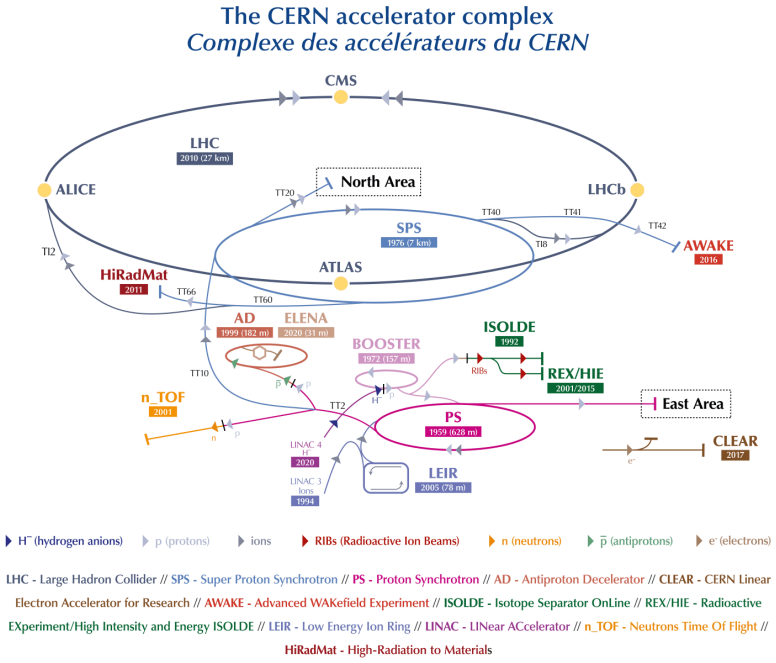

Figure 2.1: Schematic drawing of CERN's accelerator complex [113].

The acceleration chain starts with a proton source, which is essentially a hydrogen bottle where the electrons are stripped off via an electric field.

Linac2 is the first accelerator in the chain. This is a linear accelerator using radiofrequency cavities to reach a beam energy of 50 MeV before the beams are injected into the Proton Synchrotron Booster (PSB). The PSB consists of synchrotron rings layered on top of each other. It accelerates the protons further to a beam energy of 1.4 GeV.

From there, the proton beam is injected into the Proton Synchrotron (PS), which has a circumference of 628 m. This machine is equipped with 277 conventional dipole magnets to keep the beam on its trajectory. It reaches maximum a beam energy of 25 GeV for protons.

CERN's second-largest machine, the Super Proton Synchrotron (SPS) with a circumference of seven km, receives the beam from the PS and further accelerates it up to 450 GeV. The beam is then provided to the Large Hadron Collider (LHC) or the fixed-target experiments in CERN's north area. The SPS uses 1317 conventional electromagnets for bending and focusing the beam.

The final beam acceleration takes place in the world's largest particle accelerator, the Large Hadron Collider [114]. This unique machine with a circumference of approximately 27 km reaches a maximum center-of-mass energy of 13 TeV for proton beams and 5 TeV per nucleon-nucleon pair for lead (Pb) beams. To keep the two traveling beams on their trajectories roughly 1200 superconducting dipole magnets are used, providing a magnetic field of approximately 8 T.

In addition to protons, ions (mostly Pb ions) are accelerated in the CERN complex. They are extracted from a dedicated ion source and are pre-accelerated in the Linac3. Then they are injected into the Low Energy Ion Ring (LEIR) from where they are injected into the PS to then follow the same path as the protons leading finally into the LHC.

At the LHC, four major experiments are located: ATLAS [115], CMS [116], ALICE [117], LHCb [118].

2.2 A Large Ion Collider Experiment

ALICE is an acronym for A Large Ion Collider Experiment. It is one of the four major Large Hadron Collider (LHC) experiments and the one specially designed for studying the QCP and its properties [119].

ALICE is a multi-purpose detector located at Point 2 at the LHC in Saint-Genis (France) at CERN. It comprises 19 different sub-detectors, and a schematic view of the setup is shown in figure 2.2. The whole setup has a volume of 26×16×16 m^3 and a weight of ∼10000 tons.

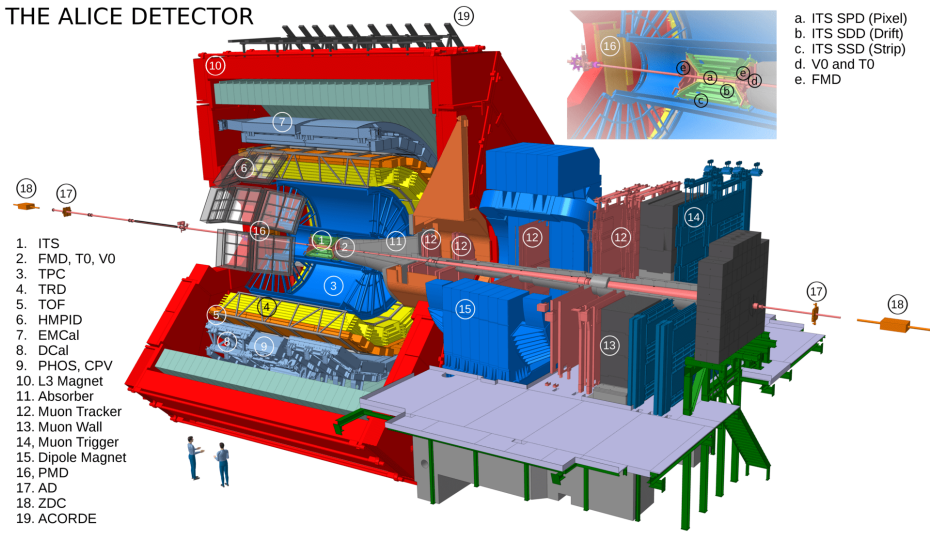

Figure 2.2: Schematic view of the ALICE detector in its Run 2 configuration [120].

The detector can be separated into two parts, a forward spectrometer ($2.5 < \eta < 4$) specialized to measure muons and the central barrel ($-0.8 < \eta < 0.8$) embedded in a huge solenoid providing a magnetic field of up to 0.5 T. The ALICE central barrel is designed to measure Pb-Pb collisions with the highest multiplicities of up to 3000 tracks per unit rapidity, while also

providing excellent tracking capabilities down to a transverse momentum of 100 MeV/c for pions. Additionally, ALICE is very well suited to identify the different particle species produced in the collisions over a wide transverse-momentum range.

To fulfill this task the interplay of the different subdetectors is critical. The function and purpose of the most important detectors employed for this thesis will be described in the following subsections.

2.2.1 Inner Tracking System

The Inner tracking system (ITS) is the innermost detector of the ALICE setup. It consists of 6 cylindrical layers of silicon detectors. They have a hermetic structure and are coaxial with the beam pipe. Going from inner to outer layers these are two Silicon Pixel Detector (SPD), two Silicon Drift Detector (SDD), and two Silicon Strip Detector (SSD), as shown in figure 2.2. The distance to the beam axis is 4 cm for the innermost layer and 43.6 cm for the outermost.

The detector has full azimuthal coverage and a pseudorapidity coverage of $|\eta| \leq 0.9$. Its main purpose is the precise measurement of primary as well as secondary interaction vertices.

The ITS refines the central barrels tracking capabilities close to the interaction point. The four analog SDD and SSD signals can additionally be used for particle identification at low momenta, using the specific energy loss ($\mathrm{d}E/\mathrm{d}x$) in the layers.

2.2.2 Time Projection Chamber

The ALICE Time Projection Chamber (TPC) is the heart of the ALICE experimental setup and serves as the main tracking and particle identification device. The TPC has an inner diameter of 1.2 m, an outer diameter of 5 m, and a length of 5.1 m. The TPC consists of two main parts the gas-filled field cage and the two endplates, which are equipped with read-out chambers. The gas mixture, that can be exchanged, was Ne-CO_2-N_2 (90 parts Ne, 10 parts CO_2, and 5 N_2) in 2017 and Ar-CO_2 (88 parts Ar and 12 parts CO_2) for 2016 and 2018.

A schematic view of the ALICE TPC without readout chambers is shown in figure 2.3. One can see the field cage with the central electrode, which creates a uniform electric field parallel to the beam pipe, by applying a negative electrical voltage of 100 kV at the central electrode and a voltage of 0 V at the endplates. The endplates are split into 18 sectors in the azimuthal direction. In the radial direction, one sector is further divided. The two parts are the so-called inner readout chamber (IROC) and outer readout chamber (OROC). The chambers are Multi-Wire Proportional Chamber (MWPC) with a cathode pad plane for the readout.

A charged particle traveling through the gas loses energy and leaves ionized gas atoms along its trajectory. The filled gas plays a crucial role and Argon or Neon is used because it has a high electron ionization probability when penetrated by charged particles. A detailed description of the energy loss per unit track length ($\mathrm{d}E/\mathrm{d}x$) is given in section 2.2.3.

The ionization electrons are accelerated along the electrical field and constantly interact with the gas molecules. So their motion can macroscopically be described by a constant drift velocity v_D:

$$v_D = a\tau = \frac{eE}{m}\tau = \mu E \tag{2.1}$$

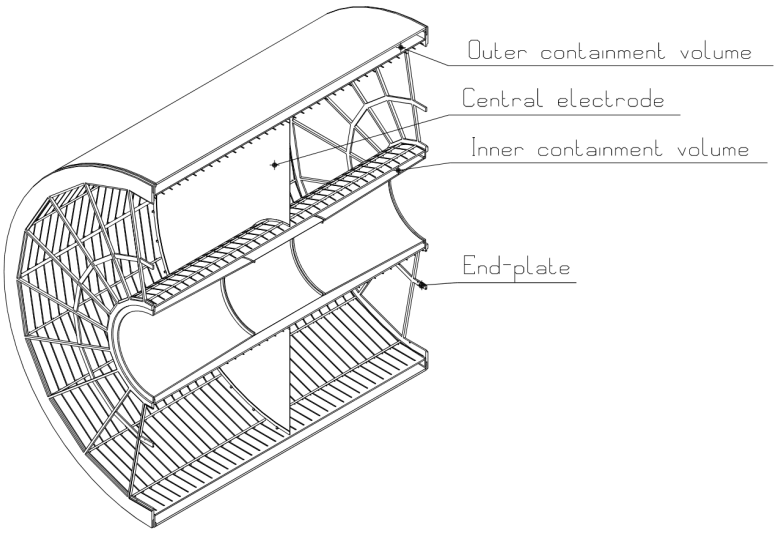

Figure 2.3: Schematic view of the ALICE TPC field cage without readout chambers [121].

e and m are electron charge and mass, respectively, E is the applied electrical field, τ the average time between collisions, and μ the mobility. Due to their much larger mass, ions drift much slower in the opposite direction towards the central electrode.

The electrons reach the MWPCs which exist of three layers of wires and a readout pad. The first layer is the so-called gating grid. The potential of the gating grid can be alternated (closed/opened). The closed gating grid stops new electrons from entering into the amplification region, while also preventing ions from escaping back into the drift volume. A cloud of charged ions escaping into the drift volume can create a noticeable electrical source. This charge distribution disturbs the drift field. The effect is also called space-charged distortion. The other two layers are used to amplify the incoming electron signal by creating an electron avalanche.

The electron avalanche is readout by the pads which have a size of 4×7.5 mm^2 in the IROC and a variable size in the OROC increasing from 6×10 mm^2 at the inner radius to 6×15 mm^2 at the outer radius.

2.2.3 Specific energy loss in the TPC

When a charged particle travels through matter it can trigger different physical processes. The occurrence probability is typically measured in units of path length. It is dependent on the kinematics of the charged particle and the material it is interacting with.

The first process is energy loss, due to inelastic collisions with the atomic electrons in the material. This can be further divided into two cases: hard collisions, where ionization of the material occurs, and soft collisions, in which only the material's electrons are excited. The energy loss in these processes is typically small in comparison to the particle's total energy. The second one is a deflection of the particle due to elastic scattering from nuclei. Here, however, the energy loss is significantly smaller than in the first process and thus negligible. Also, nuclear reactions, bremsstrahlung, Cherenkov radiation, or transition radiation occur. However, these play only a minor role in the ALICE TPC environment [122].

In figure 2.4 the ALICE TPC specific energy loss is displayed. The labeled lines indicated the expected TPC signal for the different species. The figure shows a clear particle separation in the

form of bands for low momentum ($p < 1$ GeV/c), while the lines converge for high momentum ($p > 3$ GeV/c). In the high momentum region the identification can not be done on a track-by-track basis, but when using a Bayesian approach π, K, and p can be identified up to 20 GeV/c. The physics behind the energy loss is described in the next subsection.

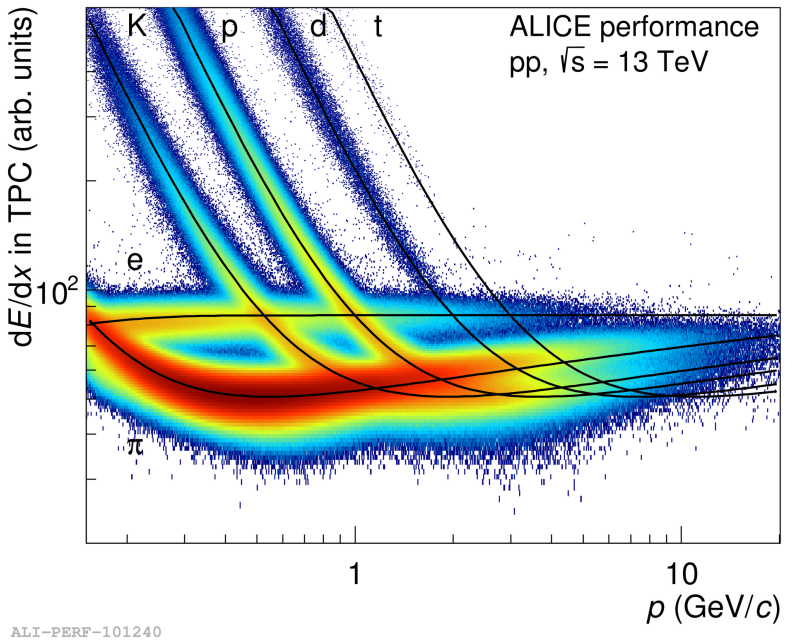

Figure 2.4: Performance plot of the ALICE TPC particle identification capabilities in pp collisions at $\sqrt{s} = 13$ TeV. The specific energy loss (dE/dx) vs. p is shown. The lines indicated the expected signal for the different particle species.

Bethe-Bloch formula

The first studies of energy loss of charged particles in material have been published by Bethe [123] and where later modified by Bloch, Fermi and others. The energy loss is described by:

$$\left\langle \frac{dE}{dx} \right\rangle = \frac{4\pi N e^4}{mc^2} \frac{z^2}{\beta^2} \left(\ln \frac{2mc^2\beta^2\gamma^2}{I^2} - \beta^2 - \frac{\delta(\beta)}{2} \right) \tag{2.2}$$

where e is the elementary charge, mc^2 is the rest mass of the electron, z the charge of the projectile, N the number density of electrons in the matter traversed, β the velocity of the projectile, and I the mean excitation energy of the atom. So for a fixed momentum and known material, the energy loss of a given particle is only dependent on its charge and mass. This can also clearly be seen in figure 2.4.

In figure 2.5 shows the energy loss of muons in copper as function of $\beta\gamma = p/mc$ and the muon momentum. The intermediate part ($\beta\gamma > 0.05$) is described by the Bethe-Bloch formalism. The $\beta\gamma$ representation is used because it is mass (particle species) independent. As $\beta\gamma$ rises the curve falls proportional to $1/\beta^2$ until it goes through the minimum ionization region ($\beta\gamma \approx 4$). After that, the energy loss rises again, in the so-called relativistic rise (described by the logarithmic term). The rise is caused by an increase in maximal transferable energy in each collision.

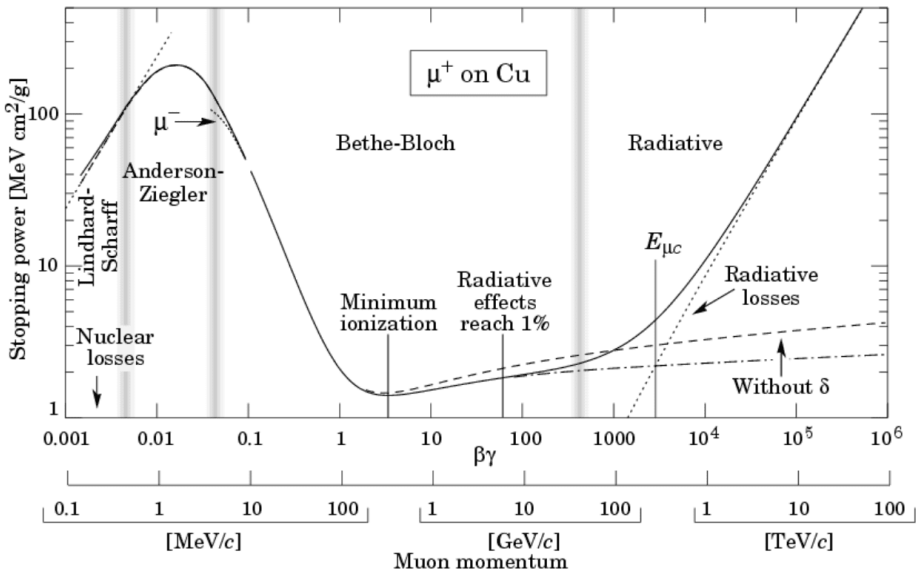

Figure 2.5: Mean energy loss per unit path length (see equation 2.2) for muons (μ^+) in copper as a function of $\beta\gamma$ [1].

Simultaneously the excitation and ionization cross section increase, due to the contraction of the electrical field in the longitudinal direction. The $\delta(\beta)$ term, first introduced by Fermi, corrects the so-called density effect. For large $\gamma\beta$, the surrounding polarized atoms shield the field of the propagating particle. The $\delta(\beta)$ term is material dependent. Looking at figure 2.5, the ALICE TPC mostly operates in the $1 < \beta\gamma < 1000$ regime close to the minimum ionization energy.

2.2.4 Transition Radiation Detector

The Transition Radiation Detector (TRD) [124] surrounds the TPC and also consist of individual 18 segments in ϕ direction. Each segment is built out of MWPCs and radiators and is filled with a Xe-O_2 (85%-15%) gas mixture. The TRD was designed to identify electrons, in an energy regime where the TPC alone is not conclusive, while also providing tracking information to improve the overall track quality. Additionally, the TRD has a relatively fast signal collection and readout, making it a perfect trigger detector. Two configurations allow triggering on high p_T electrons or highly ionizing nuclei. A highly relativistic charged particle ($\gamma > 1000$) traveling through the radiators creates transition radiation in form the of X-rays.

These X-rays are then again absorbed by the high-Z gas and, additionally, the gas is further ionized by the charged particle traveling through the detector. The created electrons are measured by the MWPCs.

2.2.5 Time-of-Flight Detector

The Time-of-Flight (TOF) detector [125] is built of 1593 individual multi-gap resistive plate chambers, divided into 18 sectors. The detector is located at a radial distance of 3.7 m from the interaction point and covers the central barrel ($|\eta| \leq 0.9$).

The detector is used for particle identification by measuring the particle's time of flight t. The mass of the particles with momentum $p = m\beta\gamma$ and track length l can be calculated by:

$$m = p \cdot \sqrt{\left(\frac{t}{l}\right)^2 - 1} \tag{2.3}$$

The TOF multi-gap resistive plate chambers have an intrinsic resolution of approximately 80 ps. The time resolution for particle identification also depends on the t_0 time resolution and, hence, it is given as $\sigma_{\mathrm{TOF}} = \sqrt{\sigma^2_{\mathrm{intr}} + \sigma^2_0}$. For Pb-Pb and pp collisions, time resolutions of $\sigma_{\mathrm{TOF}} = 86$ ps and $\sigma_{\mathrm{TOF}} = 120$ ps, respectively, are reached [125]. In a high multiplicity environment, a 2σ separation for protons and kaons can be achieved up to a momentum of 5 GeV/c. Figure 2.6 shows β measured with the TOF versus particle momentum at the interaction vertex. At $p_{\mathrm{T}} < 3$ GeV/c the TOF PID capabilities start to shine and a clear mass ordering is visible for the different particle species.

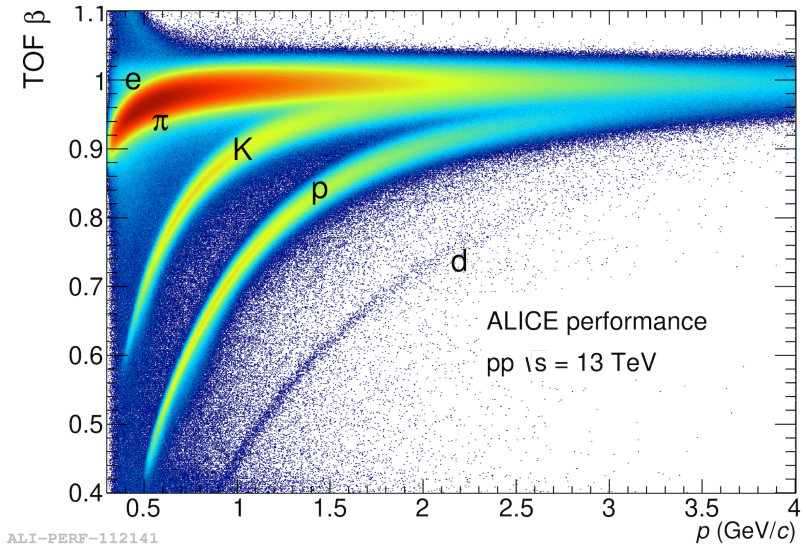

Figure 2.6: TOF particle identification, using velocity β vs. momentum p.

2.2.6 VZero Detector

The VZERO (V0M) detector [126] is used for event triggering (e.g. minimum bias or high multiplicity) and to determine the event multiplicity. The determination of the event multiplicity using the VZERO is detailedly described in section 3.1. It consists of VZERO-A (V0A) covering $2.8 < \eta < 5.1$ and VZERO-C (V0C) covering $-3.7 < \eta < -1.7$. Both have full azimuthal coverage and consist of four rings of plastic scintillators, with eight selections in the azimuthal direction. The 32 channels are read out by optical fibers. V0A is located at a distance of 329 cm from the interaction point and V0C is located at $z = -88$ cm along the beam axis. Due to the detector's very good time resolution, better than one ns, it can be used to discriminate between beam-beam and background beam-gas collisions. Furthermore, it is also used to measure beam luminosity, charged-particle multiplicity, and azimuthal distributions.

2.2.7 Track finding and reconstruction in the central barrel

Track reconstruction describes the process of reconstructing the trajectory of a charged particle traveling through the detector.

This is a very computing-intensive procedure. Therefore it is once performed for a given data period. The physics analysis is performed on the reconstructed data.

The first step in the process (shown in figure 2.7) is the cluster finding in all individual detectors. The raw signals of the detector are combined into clusters. For the TPC, neighboring pad row signals are combined into one cluster, which can also be in different time bins. This can either be done on the stored raw data or online using the High-Level Trigger (HLT). The online clusterization has the big advantage of a smaller data volume which needs to be saved. It comes, however, at the cost of losing access to the raw data.

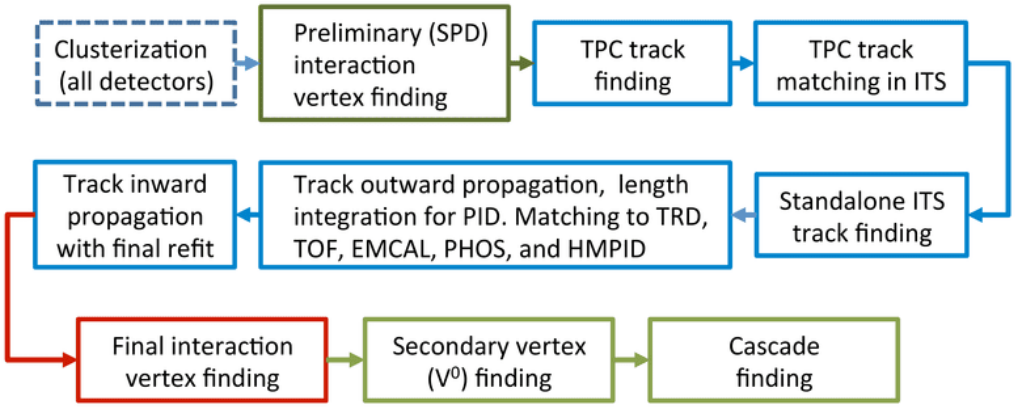

Figure 2.7: Schematic outline of the tracking and reconstruction procedure in ALICE [117].

After that, the track reconstruction can be initiated. First, the event vertex is determined using the two innermost ITS layers, in which individual clusters are combined to tracklets. They are propagated towards the interaction region. The point in space where the track density is largest is assumed to be the event vertex. Track reconstruction is initialized at the outer radius of the TPC, where the track density is the lowest. With 159 pad rows in the TPC, a maximum of 159 clusters can be found per track. TPC track seeds are first constructed using two clusters and the event vertex. Then, the same is done using three clusters. Like this, an iterative procedure is initiated increasing the number of clusters slowly and propagating the track seed inwards. The angle straggling is estimated on an assumed preliminary particle mass, which defines the width of the search window when looking for the next cluster. On the same mass estimate, which is based on the specific energy loss (see section 2.2.3) the particle energy loss to the TPC gas is corrected. To prevent double counting of tracks the fraction of shared clusters is saved by the algorithm. In the later analysis, a selection on the shared cluster per track is applied. Once the TPC inner layer is reached the track seeds are tracked further inwards using the ITS clusters.

ITS tracking follows the same logic. The TPC tracks are tracked from ITS outer radius (with low track density) inwards using an iterative procedure, which updates the track with each step. Since the ITS has only 6 layers, only a maximum of six ITS clusters can be assigned to the track. ITS clusters without matching TPC tracks are used in the ITS stand-alone tracking. This is of

special importance for low momentum particles since they can be stopped in the ITS detector material before reaching the TPC. With the ITS standalone tracking the transverse-momentum reach extends down to 80 MeV/c for pions.

All tracks are refitted in the outward direction with an update of the track and PID at each step. Once the TPCs outer edge is reached, the tracks are matched to ones reconstructed in the TRD as well as to hits in TOF and further detectors like EMCal, PHOS, and HMPID. Finally, the last refit, using TPC, ITS, and TRD detectors, is performed. The fit is started in the outer position and propagated in the inward direction. The so reconstructed tracks are used to determine the final primary vertex.

In the last step, displaced secondary vertices originating from decays of strange particles or cascade decays are assigned to the corresponding tracks.

3 Analysis steps

The analysis aims to measure the transverse-momentum (p_{T}) spectra of primary protons (p), tritons (^{3}H), and helium (^{3}He) and their corresponding antiparticle. The ALICE Collaboration defines primary particles as: "A primary particle is a particle with a mean proper lifetime τ larger than 1 cm/c, which is either a) produced directly in the interaction, or b) from decays of particles with τ smaller than 1 cm/c, restricted to decay chains leading to the interaction" [127]. Within this definition, weak decay products of heavy flavor particles (e.g. Λ_c, D^0) are considered as primary particles.

There are two sources of secondary particles. These are, first particles originating from weak decays with a τ smaller 1 cm, and, secondly, particles originating from secondary interactions with the detector material or the LHC beam pipe. In the second case, the underlying process is the so-called spallation process, in which a nucleus gets hit by a high energy projectile which causes the target nucleus to excite and afterward deexcite via the release of protons, neutrons, or heavier fragments. The spallation process is further explained in section 3.4.

In high energy physics, particle production is usually described as a function of p_{T} and rapidity (y):

$$y = \frac{1}{2}\ln\left(\frac{E+p_z}{E-p_z}\right) \tag{3.1}$$

The rapidity which is Lorenz invariant can not be directly measured with the ALICE detector since it depends on the rest mass of the particle, which is a priory not known. But instead, the particle's relative angle to the beam axis (Θ) and the curvature of the particle in the magnetic field and thus the transverse-momentum component (p_{T}) can be measured. In this case, the pseudorapidity (η) of the particle can be determined which is equal to the rapidity in the limit of large momentum or massless particles.

$$\eta = -\ln\left(\tan\left(\frac{\Theta}{2}\right)\right) = \frac{1}{2}\ln\left(\frac{|\vec{p}|+p_z}{|\vec{p}|-p_z}\right) \tag{3.2}$$

In the rest of the chapter, the analysis strategy will be explained step-by-step, starting with the event selection and the definition of event classes. In the next step, the particle identification using TPC and/or TOF detectors will be explained, and afterward, the different corrections applied to the p_{T} spectra are evaluated. Lastly, sources of systematic uncertainties are described.

3.1 Trigger selection and multiplicity classes

The minimum bias trigger ($\mathrm{MB}_{\mathrm{AND}}$) is defined by requiring hits in V0A as well as V0C detectors in coincidence with a beam crossing. To reduce the contribution from diffractive interactions at least one tracklet in the SPD is required with $|\eta| < 1$. The resulting data sample is called $\mathrm{MB}_{\mathrm{AND}>0}$.

The multiplicity classes are defined by a percentile range which can be expressed as fractional cross section $\Delta\sigma/\sigma_{\mathrm{MB}_{\mathrm{AND}>0}}$, with the total visible cross section (100%) being $\sigma_{\mathrm{MB}_{\mathrm{AND}>0}}$. The

multiplicity percentile values reach from low multiplicity close to 100% to high multiplicity reaching up to 0%. The multiplicity distribution in forward direction is measured by the amplitude of the V0M detectors in each event. The self normalized V0M multiplicity distribution (V0M/⟨V0M⟩) in $\mathrm{MB}_{\mathrm{AND}>0}$ pp collisions at $\sqrt{s} = 13$ TeV is shown in figure 3.1.

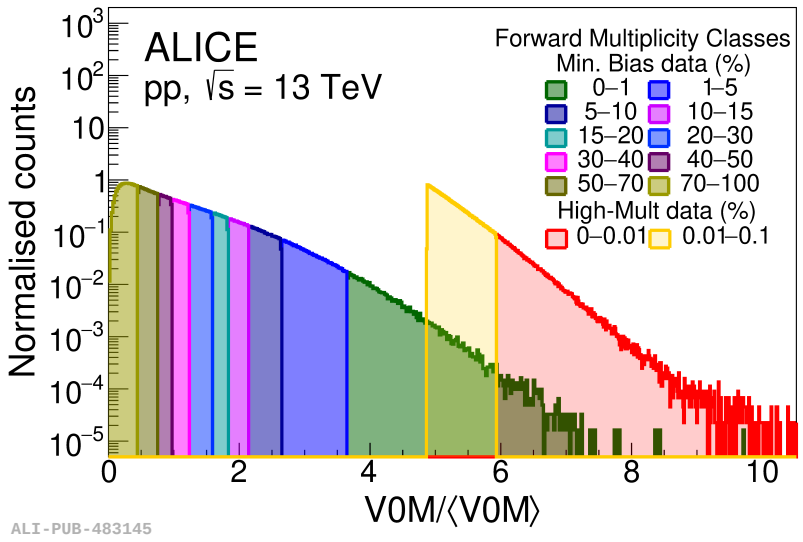

Figure 3.1: Distribution of the V0M amplitude scaled by its average value ⟨V0M⟩ in pp collisions at $\sqrt{s} = 13$ TeV [128].

Additionally, a dedicated V0M high-multiplicity (HM) trigger defined by V0M/⟨V0M⟩ > 4.9 corresponding to $\sigma/\sigma_{\mathrm{MB}_{\mathrm{AND}>0}} < 0.1\%$. This trigger allows the study of pp events in a multiplicity region comparable to p-Pb events and allows for a direct comparison of the two systems. In figure 3.1 also the self normalized V0M multiplicity distribution of the high-multiplicity data sample is shown. Comparing the two distributions the higher reach in multiplicity and, thus, the need for a dedicated trigger in this regime (if one is interested in the highest multiplicity pp events) is visible. The multiplicity reach is up to 10 times higher than the average multiplicity of the minimum bias sample.

Since not every event with an inelastic interaction and at least one particle produced ($\mathrm{INEL}_{>0}$) is triggered the so-called trigger efficiency is corrected. The trigger efficiency, $\epsilon_i^{\mathrm{trig}}$ is strongly multiplicity depended (the higher the event multiplicity the lower the chance of missing the event) and the values for each multiplicity class are quoted in table 3.1. The trigger efficiencies are calculated using PYTHIA 8 with Monash 2013 tune and GEANT3 simulations [128], by taking the ratio of simulated events fulfilling the trigger conditions to the total number of generated events.

To obtain the charged-particle density per pseudorapidity ($\mathrm{d}N_{\mathrm{ch}}/\mathrm{d}\eta$) the measured distributions of tracklets per pseudorapidity ($\mathrm{d}N_{\mathrm{tracklets}}/\mathrm{d}\eta$) is corrected for acceptance and efficiency (α) as well as contamination form tracklets not produced by a primary particle (β). The charged-particle density is calculated by $\mathrm{d}N_{\mathrm{ch}}/\mathrm{d}\eta = \alpha(1-\beta)\mathrm{d}N_{\mathrm{tracklets}}/\mathrm{d}\eta$ [129] and the resulting values for the different analyzed multiplicity classes are listed in table 3.1.

Due to the low production rates of triton and helium-3 all the available LHC Run 2 data, collected in the years 2016, 2017, and 2018 had to be used in the analysis to achieve the best possible statistical precision. The data subsets (runs) have to fulfill the quality criteria, which

	High Multiplicity triggered events				Minimum Bias triggered events		
$\Delta\sigma/\sigma_{\mathrm{MB_{AND>0}}}$	0–0.1%	0–0.01%	0.01–0.05%	0.05-0.1%	0-100%	0-10%	10-100%
ϵ^{trig}	1	1	1	1	0.921 ± 0.030	1	0.914 ± 0.030
$\langle \mathrm{d}N_{\mathrm{ch}}/\mathrm{d}\eta \rangle$	31.53±0.29	35.82±0.33	32.21±0.29	30.13±0.27	6.94 ±0.1	18.68±0.17	5.98±0.05

Table 3.1: Trigger efficiency (ϵ^{trig}) and average charged-particle multiplicity ($\langle \mathrm{d}N_{\mathrm{ch}}/\mathrm{d}\eta \rangle$) corresponding to the forward multiplicity percentile classes ($\Delta\sigma/\sigma_{\mathrm{MB_{AND>0}}}$) [128]. Only the multiplicity classes relevant for this work are listed. Only the systemic uncertainties are shown because the statical uncertainties are negligible.

describe the state of the subdetectors during the run. Only runs with fully operational ITS, V0, TPC, TOF, and T0 detectors are included in the analysis.

Protons, on the other hand, are produced very abundantly at LHC collision energies. So the use of one 2018 running period was sufficient and the "LHC18o" run was chosen. During the LHC18o running period, all for the following analysis important subdetector systems were operational to their fullest potential, according to the ALICE run logbook. The quality of the data was ensured by the ALICE data quality assurance group and also confirmed within the analysis. Additionally, the high-multiplicity trigger was active during the period (which is true for most of 2018) and the period contains a large sample of such high-multiplicity triggered events.

3.1.1 Event selection

Events superimposed with a second collision, so-called pile-up events, are rejected from the analysis. Pile-up is caused by two (or more) collisions happening in the same bunch (called in-bunch pile-up) or two (or more) collisions happening in different bunches and being recorded at the same time (called out-of-bunch pile-up). At first glance, pile-up events appear as individual events in the recorded data. However, they have a distinct signature with more than one primary event vertex. Therefore, pile-up events are excluded by constraining the number of reconstructed vertices to be one. If there is more than one event vertex, the event will be rejected. Additionally, to the ordinary hadron-hadron collisions also beam-gas interaction can occur. These, are due to the kinematics of the collision at very forward or backward rapidity and thus are excluded, by requiring a coincident signal in both V0(A&C) detectors. This condition is fulfilled in the ALICE minimum bias and high-multiplicity trigger setting.

Especially in pp low multiplicity collision, events can be triggered by the V0 detector with only a single track or no track reconstructed in the central barrel. Consequently, only one track contributes to the vertex reconstruction or no vertex can be reconstructed. These events are not used in this analysis.

To minimize beam-induced background the V0 detector time information is correlated with the tracklets and clusters from the SPD detector [117]. To exclude no beam-gas pile-up contamination, only events with a reconstructed vertex position (v_z) within a 10 cm window around the nominal interaction point ($|v_z = 0|$) are selected. This selection is also important to ensure a uniform rapidity distribution, on which the efficiency correction applied later is based.

All event selection criteria reject around 10% of the data of the minimum bias triggered events and around 20% of the high-multiplicity triggered events. The difference lies in the nature of pile-up events which naturally have a higher multiplicity.

In total all used data sets sum up to 1.5 billion MB triggered and selected events and 0.9 billion HM triggered and selected events for the helium analysis. The HM proton sample consists of 13.6 million HM triggered and selected events.

3.1.2 Monte Carlo simulations

Some later applied corrections can not be determined with data-driven approaches and are therefore based on Monte Carlo simulations of the collision and the ALICE detector. The most critical correction dependent on Monte Carlo simulation is the detector acceptance and reconstruction efficiency, see section 3.5. For the study of pp collision, the most commonly used event generator is PYTHIA (version 8) [130]. The most commonly used transport code simulating the detector is GEANT [131]. Within the ALICE Collaboration, two versions of GEANT are used. The latest one is GEANT4 and the older generation is GEANT3.

The simulations are anchored to specific data-taking periods. This allows the most accurate modeling of the detector response in the GEANT transport code. The full detector status is modeled taking also the performance of individual channels into account (for example dead channels) or in the case of the TPC its gas configuration.

In this analysis two Monte Carlo simulations are used anchored to the years 2016, 2017, and 2018 using GEANT3 and GEANT4 as transport codes. Because of the rare production of light nuclei in pp collisions, they are embedded into the simulation. One nucleus is injected into each event following a uniform p_{T} distribution stopping at $p_{\mathrm{T}} = 6$ GeV/c.

Unfortunately, no specific high-multiplicity selected sample is available. However, the detector response might be multiplicity dependent. To verify this, some crosschecks have been performed using a p-Pb HIJING event generator sample, which matches the event multiplicity of high-multiplicity triggered pp collisions. In the Monte Carlo samples, no significant difference for the detector response was found using p-Pb events and minimum bias pp events. Therefore, only the generated minimum bias pp events are used for the further analysis, ensuring the proper representation of the run-dependent detector effects. In total the simulated pp samples using GEANT4 has 30 million and using GEANT3 have 37 million selected events.

3.2 Track selection criteria

To ensure a high track quality as well as a good Monte Carlo description of the tracks, the tracks not fulfilling the selection criteria have to be discarded. The TPC detector is full operational in the rapidity range of $-0.8 < \eta < 0.8$, so only tracks in this η window are used for the analysis. In addition, several detector and reconstruction specific track selection criteria are applied. These will be described in the following. In table 3.2 all applied selection criteria are summarized.

ITS variables		**TPC variables**	
$n_{\text{clu}}^{\text{ITS}}$	≥ 2	$n_{\text{clu}}^{\text{TPC}}$	≥ 70
hit SPD	= any	$n_{\text{clu}}^{\text{TPC}}$ for PID	≥ 50
ITS refit	= true	n_{row}	≥ 70
χ^2_{ITS}	≤ 36	$n_{\text{row}}/n_{\text{findable}}$	≥ 0.8
TOF variables		TPC shared cluster	≤ 0.4
TOF matching window	≤ 10 cm	TPC refit	= true
primary selection		χ^2_{TPC}	≤ 4
reject kinks	= true	**global track selection**	
DCA_{xy}(p)	$\leq 3\sigma$	$\chi^2_{\text{TPC-ITS}}$	≤ 36
$\text{DCA}_{xy}(^3\text{H},^3\text{He})$	≤ 0.15 cm		
DCA_{z}(p)	≤ 1.0 cm		
$\text{DCA}_{z}(^3\text{H},^3\text{He})$	≤ 0.15 cm		

Table 3.2: All track selection criteria applied for the protons, helium and triton analysis.

TPC specific track selection criteria

To ensure good track quality of TPC tracks a fit of the reconstructed tracks is applied and, additionally, a maximum χ^2 per cluster of the fit is required. The χ^2 per cluster is constrained to a maximum value of 4. TPC tracks with high χ^2 per cluster contain most like wrongly assigned clusters or might be even fake tracks, which are tracks being reconstructed falsely by the tracking algorithm without having a particle pass the detector.

The length of a TPC track is directly linked to the number of crossed rows n_{row}, out of the maximum value of 159 pad rows in the TPC. Since not all pad rows leave a signal above the electronics threshold when a charged particle passes, the number of crossed rows is given by the number of all clusters n_{clu} assigned to the track. Additionally, the rows without a signal are added if a cluster in the neighboring pad rows was found.

The number of findable clusters n_{findable} describes the maximum possible number of clusters that could be assigned to a track. This depends on the track parameters. Here, geometrical effects such as the dead areas of the detector as well as the η acceptance are taken into account. Two track-quality criteria are applied, the ratio of $n_{\text{clu}}/n_{\text{findable}}$ and $n_{\text{row}}/n_{\text{findable}}$. The first one is the percentage of found track clusters. The second one gives a similar quantity, but in n_{row} also pad rows are included in which no cluster was found but the neighboring pad row had a cluster. So in other words, it is still the percentage of found track clusters but taking also sub-threshold clusters into account.

The number of tracks sharing a cluster can hint towards fake tracks which might be reconstructed multiple times. Therefore, the fraction of shared clusters is defined as all clusters per track with more than one track assigned divided by the total amount of clusters ($n_{\text{shared}}/n_{\text{clu}}$). The fraction of shared clusters is set to be smaller than 40%.

It is not possible to extract a particle identification (PID) signal, which is given by the total charge, from every cluster, because shared clusters or clusters close to the chamber edges would disturb the PID signal. The clusters close to the boundaries of the chamber can not be used for the PID because the gain is lower in that region due to edge effects. However, this does not disturb the track reconstruction. A minimum number of 50 clusters used for the PID is chosen to ensure a good PID quality.

ITS specific track selection criteria

Similar to the TPC selection, as minimal track quality check a fit for the ITS clusters is performed and, additionally, a maximum χ^2 of the fit per cluster is required. Tracks with wrongly assigned clusters have most likely a large χ^2/cluster and have to be discarded. Furthermore, a minimum amount of clusters associated with each track, out of the six findable ITS clusters (see section 2.2.1), is requested. To suppress the secondary particle contribution and to ensure a good Distance to Closest Approach (DCA) resolution, which will be explained at the end of the section, a selection on the first two ITS layers (the SPD) is applied. The tracks are required to have at least one hit in the SPD (any). Alternatively, also tracks with a hit in the first layer (first) or both layers (both) of the SPD can be chosen. "Any" is the selection criteria with the highest reconstruction efficiency but it comes with worse DCA resolution and higher contamination from secondaries. Especially for the triton and helium analysis where the statistical precision is limited, this is an excellent trade-off.

Additional track selection criteria

The track selection criterion combining the central barrel tracking detectors is the so-called global χ^2 ($\chi^2_{\text{TPC-ITS}}$) cut. The $\chi^2_{\text{TPC-ITS}}$ is calculated from the track parameters and their uncertainties. First, the TPC-constrained track parameters are calculated from a fit to the reconstructed TPC clusters and the primary vertex, which are then compared to the TPC-ITS constrained track parameters calculated from a fit to the reconstructed ITS and TPC clusters and the primary vertex. These TPC-ITS constrained tracks are also called global tracks. With this method, mainly tracks with wrongly assigned ITS clusters or tracks which are scattered in the detector material between ITS and TPC, and thus have a wrongly reconstructed momentum, are removed.

TOF matching

After the completed TPC and ITS tracking, the tracks are propagated through the TRD and then matched with TOF clusters. The matching is done by projecting the TPC tracks on the TOF surface and then searching for a TOF hit within radius r. Due to the very different track densities in the different colliding systems, the radius has to be changed depending on the colliding system. In pp collisions, which have a low track density at mid rapidity, a TOF matching

window with $r = 10$ cm is used. In Pb-Pb collisions on the other hand, which have a high track density at mid rapidity, a $r = 3$ cm TOF matching window is applied. The pp and Pb-Pb collisions matching window radii are tuned to have the maximum efficiency while mismatch probability is kept as low as possible.

Primary selection

A high purity of primary particles can be achieved with a selection on the so-called Distance to Closest Approach (DCA). The DCA is defined as a track's closest distance from the primary event vertex. The radial (xy) and longitudinal (z) components are considered separately because the transverse component of the track is affected by the ALICE magnetic field and hence the DCA_{xy} resolution is p_T dependent, while the DCA_z resolution is unaffected by the magnetic field and, therefore, uniform. Figure 3.2 illustrates DCA_{xy} and DCA_z geometrically. Together they form a cylindric selection window around the primary vertex, which has to be crossed by reconstructed tracks.

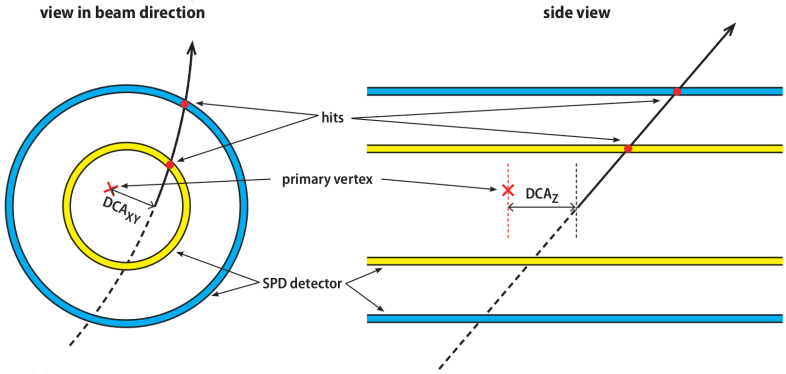

Figure 3.2: Illustration of the transverse (xy) and longitudinal (z) DCA. The figure is taken form reference [132].

With a MC sample of selected primary protons the p_T dependent DCA_{xy} resolution was determined. Such a distribution is shown in figure 3.3. The root-mean-square of the DCA_{xy} distribution in fine transverse-momentum bins was determined and parametrized according to

$$\sigma_{\mathrm{DCA}_{xy}}(p_\mathrm{T}) = a_0 + \frac{a_1}{p_\mathrm{T}^{a_2}}, \tag{3.3}$$

where a_0, a_1, and a_2 are the free parameters. Figure 3.4 shows the DCA_{xy} resolution as function of p_T. At low p_T the DCA_{xy} resolution gets worse due to the increased bending of the tracks in the magnetic field, which causes the track propagation to the nominal interaction point to be less precise.

To select primary particle a 3σ selection in DCA_{xy} was applied in the proton analysis. The helium and triton analyses starts at significantly higher transverse momentum ($p_\mathrm{T} > 1$ GeV/c). In this regime the DCA_{xy} resolution is only weekly p_T dependent. Therefore, a fixed selection of $\mathrm{DCA}_{xy} < 0.15$ cm is sufficient. In the longitudinal direction a $\mathrm{DCA}_z < 0.15$ cm selection was chosen for helium and triton which is approximately equal to five times the resolution in z direction. For the proton analysis a wider $\mathrm{DCA}_z < 1$ cm cut was applied to increase the number

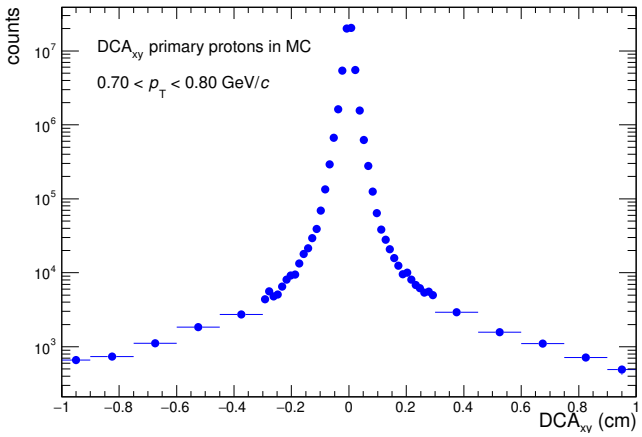

Figure 3.3: DCA$_{xy}$ distribution for primary protons obtained form Monte Carlo in the transverse-momentum range: $0.7 < p_T < 0.8$ GeV/c.

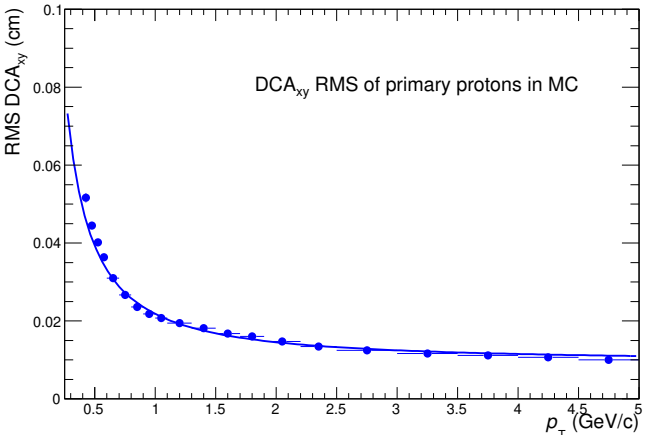

Figure 3.4: DCA$_{xy}$ resolution for primary protons obtained from Monte Carlo.

of secondary particles which is necessary to later corrected with a data-driven method. The cut on the DCA distribution already reduces the number of secondary particles. However, within the selected region, there is still a significant contamination of secondary particles. Section 3.4 discusses the contamination and presents the applied correction methods.

3.2.1 Kink rejection

The topological structure of a kink track is shown in figure 3.5. These are tracks that change direction within the detector. Such a topology is typically caused by a charged particle undergoing a weak decay into a charged and a neutral daughter product in the detector. Thus, the reconstructed track (following the charged particle) seems to have a kink. The search for kinks is done inside the TPC volume during the track reconstruction procedure. Tracks with a kink topology are rejected from the analysis.

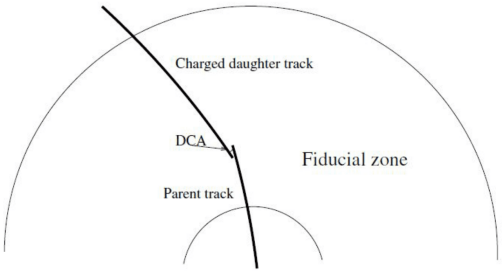

Figure 3.5: Topological signature of charged particles decaying into a charged plus a neural particle, so-called kinks.

3.3 Particle identification

The main device for particle identification is the TPC detector. In section 2.2.3 its working principle and particle identification are explained. The particle identification is based on a charged particle's energy loss by ionization when traveling through the detector gas.

The particle species-specific energy loss in the TPC is calibrated run-by-run by interpolating the e, π, K, and p signals with the Bethe-Bloch equation 2.2 as a function of $\beta\gamma$. The energy loss in the TPC, however, needs to be corrected for the nonuniform η dependence (in the order of up to 10%), which is mainly caused by the diffusion of the charge when the primary electrons drift towards the end caps. Additionally, the event multiplicity-dependent resolution of the $\langle \mathrm{d}E/\mathrm{d}x \rangle$ is taken into account (in the order of 5% for pp collisions and 7% for Pb-Pb collisions). The expected energy loss for heavier particles (e.g. ^{2}H, ^{3}H, ^{3}He) is then extracted by extrapolating the results from the light particle species to the heavier ones. The deviation of the measured energy loss to the expected energy loss of a specific particle species (i) is expressed in terms of the detector resolution $n\sigma^i$:

$$n\sigma^i = \frac{\langle \mathrm{d}E/\mathrm{d}x \rangle_{\text{measured}} - \langle \mathrm{d}E/\mathrm{d}x \rangle^i_{\text{expected}}}{\sigma(\langle \mathrm{d}E/\mathrm{d}x \rangle)} \tag{3.4}$$

For the identification of the helium nuclei, the TPC information is sufficient. This is feasible due to its high charge ($z = 2$), which causes a high energy loss ($\mathrm{d}E/\mathrm{d}x \propto z^2$). For proton and triton, however, the addition of the TOF detector is needed (section 2.2.5) due to overlapping PID signals in the TPC. Figure 2.4 illustrates nicely the contamination with lighter particle species in the TPC for protons and triton above 1 GeV/c and 2 GeV/c ,respectively. A detailed description of the identification and signal extraction for all three particle species is given in the following subsections.

3.3.1 Proton identification

For proton identification, a TPC-only analysis would not be sufficient due to large contamination of the proton TPC signal by lighter particle species for a momentum larger 1 GeV/c (see figure 2.6). To guarantee a high purity of the proton signal over the full p_{T} range ($0.5 < p_{\mathrm{T}} < 4$ GeV/c) in addition to the TPC the TOF detector is used. As shown in figure 2.6 the protons are very nicely separated in the TOF detector.

First, tracks are preselected in the TPC within a 5σ range of the expected TPC signal ($|n\sigma^{\mathrm{p}}_{\mathrm{TPC}}| < 5$). This loose preselection is fully sufficient, because, afterward, for each p_{T} bin the signal is projected into the expected TOF signal ($n\sigma^i_{\mathrm{TOF}}$) plane, where the proton candidates are identified. As done in equation 3.4 for the TPC, $n\sigma^i_{\mathrm{TOF}}$ is defined as the deviation of the measured mass signal to the expected mass signal (see eq. 2.3) for a certain particle (i) and expressed in terms of detector resolution.

The so extracted proton TOF signals are shown in figure 3.6 - 3.8 for three different p_{T} bins.

The TOF signal can be described by a Gaussian function with an exponential tail:

$$\begin{aligned} f(x) &= n \cdot \exp\left(-\frac{1}{2} \cdot \left(\frac{x-\mu}{\sigma^2}\right)\right) && \text{, for } x < \mu + \tau \cdot \sigma \\ &= n \cdot \exp\left(-\tau \cdot \left(\frac{x-\mu-1/2 \cdot \sigma\tau}{\sigma}\right)\right) && \text{, for } x \geq \mu + \tau \cdot \sigma \end{aligned} \tag{3.5}$$

with μ and σ being the mean and the width of the Gaussian function while τ describes the point where the exponential tail starts. The asymmetric tail in the signal is caused by particles passing near the edge of a readout pad which can induce a signal in more than one pad with a consequently worse time resolution [125]. The background, which is caused by lighter particles (mostly kaons) feeding into the signal (see figure 2.6), is described by different functions depending on the p_{T} interval. The higher the p_{T} the larger the contamination and, thus, the more complicated the background shape becomes:

$0.5\ \mathrm{GeV}/c \leq p_{\mathrm{T}} \leq 1.9\ \mathrm{GeV}/c$: Constant function
$1.9\ \mathrm{GeV}/c < p_{\mathrm{T}} \leq 3.0\ \mathrm{GeV}/c$: Exponential function
$3.0\ \mathrm{GeV}/c < p_{\mathrm{T}} \leq 4.0\ \mathrm{GeV}/c$: Exponential plus linear function
$4.0\ \mathrm{GeV}/c < p_{\mathrm{T}} \leq 5.0\ \mathrm{GeV}/c$: Gaussian function with exponential tail

The $n\sigma^{\mathrm{p}}_{\mathrm{TOF}}$ distributions for protons and antiprotons for three example p_{T} bins, with the corresponding interpolations for the integrated multiplicity class 0-0.1% are shown in figure 3.6 - 3.8.

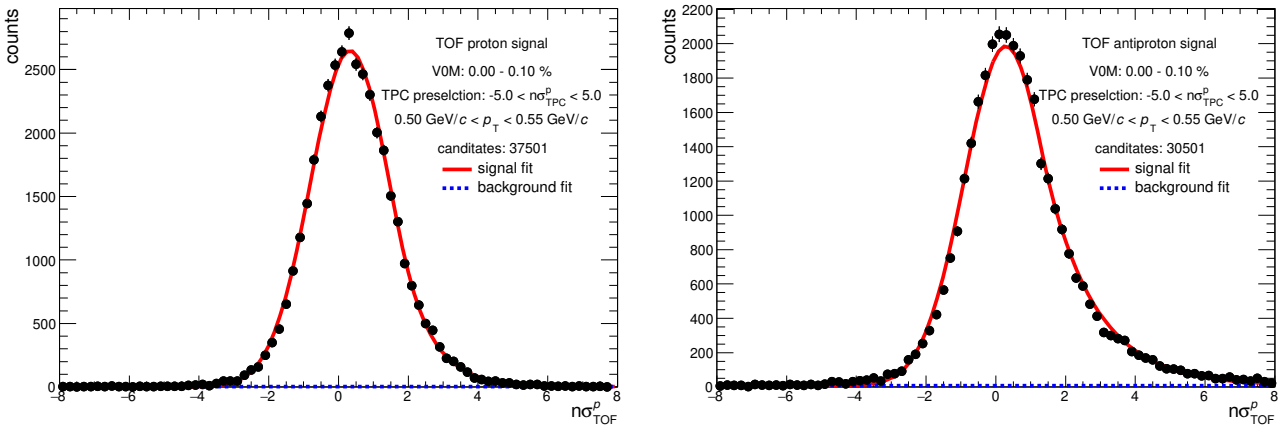

Figure 3.6: Proton TOF signal extraction for the integrated multiplicity class (V0M: 0-0.1%). Protons on the left side and antiprotons on the right. $0.5 \leq p_{\mathrm{T}} < 0.55\ \mathrm{GeV}/c$.

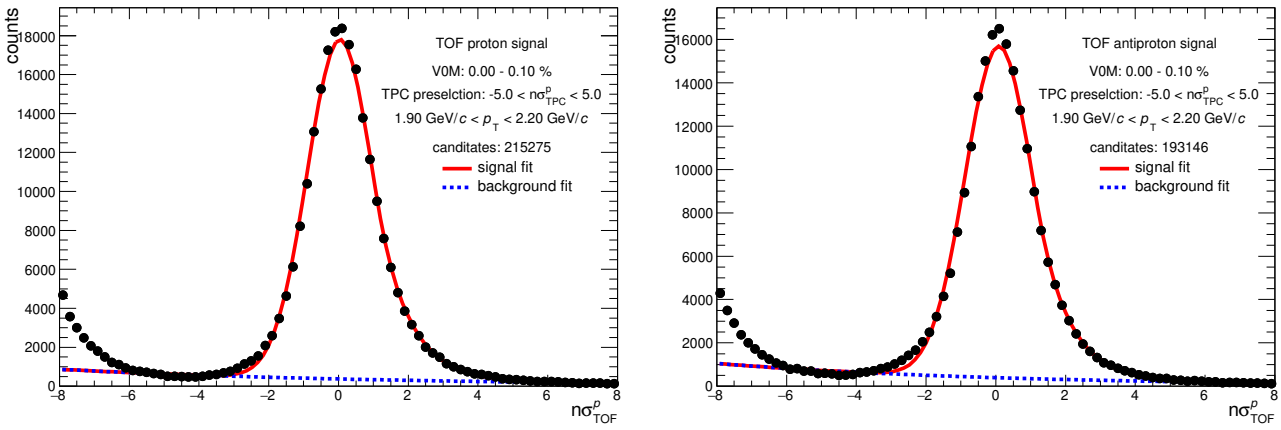

Figure 3.7: Proton TOF signal extraction for the integrated multiplicity class (V0M: 0-0.1%). Protons on the left side and antiprotons on the right. $1.9 \leq p_{\mathrm{T}} < 2.2\ \mathrm{GeV}/c$.

In the last p_{T} bin (4.0 - 5.0 GeV/c) the signal sits on top of a large background, which itself should also follow a Gaussian with exponential tail function (equation 3.5). Therefore this rather complicated function was used to describe the background. When τ is left as a free

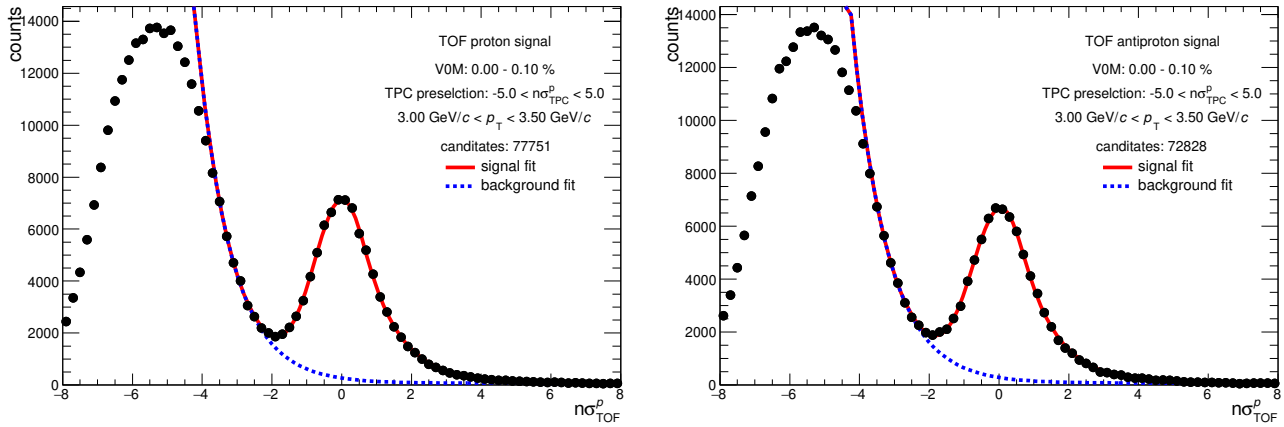

Figure 3.8: Proton TOF signal extraction for the integrated multiplicity class (V0M: 0-0.1%). Protons on the left side and antiprotons on the right. $3.0 \leq p_{\mathrm{T}} < 3.5$ GeV/c.

parameter it converges towards one which is equivalent to the exponential background description. To get a better handle over the systematics, the fit was performed multiple times with a fixed τ. Two extreme cases where chosen as upper and lower limit ($\tau = 0.70$ and $\tau = 2.5$) for the background contamination. The actual contamination is obtained with $\tau = 1.25$. The method is shown for protons and antiprotons in figure 3.9.

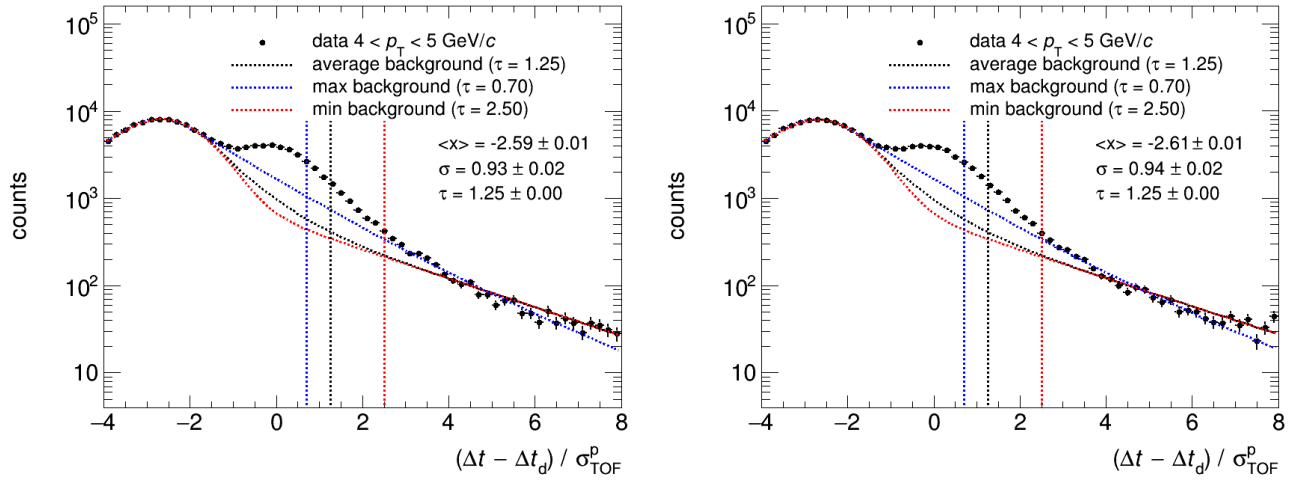

Figure 3.9: TOF signal extraction form integrated multiplicity class (V0M: 0-0.1%). Proton on the left side and antiproton on the right. The transverse-momentum range is $4.0 \leq p_{\mathrm{T}} \leq 5.0$ GeV/c. The background fits are performed multiple times with different settings for the τ parameter. The displayed background fit parameter results (mean $\langle x \rangle$, width σ, τ) are for the average result.

To ensure fit quality the relevant parameters of equation 3.5 are plotted versus p_{T}. The mean ($\langle x \rangle$), the width (σ), and the τ parameter are shown in figure 3.10. In the ideal case, the mean and the width would be zero and one, respectively. However, due to imperfections in the TPC energy-loss calibration one can see small and expected variations, which are negligible in comparison to the total systematic uncertainty. For the multiplicity differential analysis the proton signal extraction is shown for the same example p_{T} bins in the appendix figure B.1, B.2, and B.3.

After the subtraction of the background contribution the proton signal is extracted by bin counting in the $|n\sigma^{\mathrm{p}}_{\mathrm{TOF}}| \leq 3$ interval.

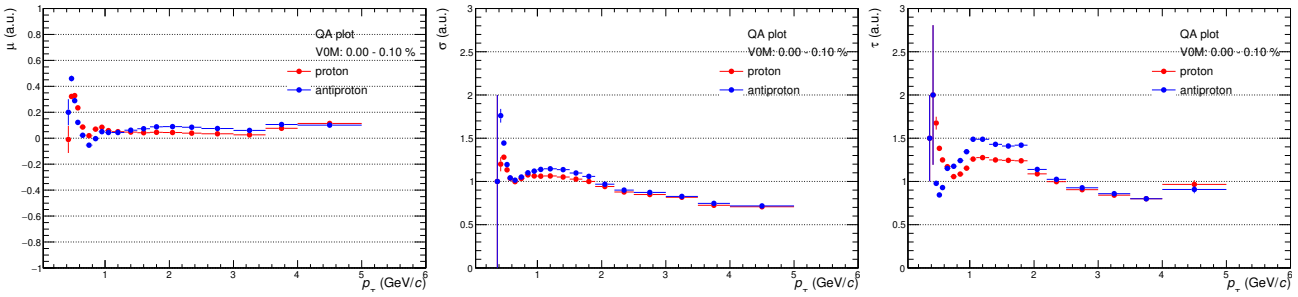

Figure 3.10: Parameter of the Gaussian with exponential tail fit versus p_{T} used for the proton signal extraction. Mean (left), width (middle), and τ parameter (right). In the ideal case the mean and the width would be zero and one, respectively.

3.3.2 Helium identification

As described in section 2.2.3, the energy loss of a particle traveling through matter follows the Bethe-Bloch formalism (see equation 2.2). It is important to note that the particle's energy loss is proportional to its charge squared. This simplifies the identification of helium nuclei because they are the most abundant particles with a charge of two produced at the LHC energies. Hence, the (anti-)^{3}He identification can be done with a TPC-only analysis due to its distinct signal over the full momentum range (see figure 2.4).

As mentioned before the ALICE TPC energy loss is calibrated for each period using e, π, K, and p particles. Unfortunately, due to the low production probability of helium and triton they can not be included in a period-dependent TPC $\mathrm{d}E/\mathrm{d}x$ calibration consistently. Therefore, the expected $\mathrm{d}E/\mathrm{d}x$ signals for helium and triton are obtained by extrapolating the interpolated results from the lighter particles species.

However, this method is not perfect and causes extrapolated TPC PID response for helium to be slightly shifted from the measured mean actual PID signal. This manifests itself in a shift of the mean value from zero. This effect is corrected by measuring the helium PID response in units of $n\sigma$ (see eq. 3.4) and in slices of rigidity ($p/|z|$). Unfortunately, the shift can not be corrected running-period dependent due to the limited statistics in each period. Therefore, the correction was done once and applied to the full data sample. The measured helium PID response follows a Gaussian distribution and it is interpolated with a Gaussian fit function in fine rigidity bins. The mean and the width of these fits give a rigidity-depended distortion from a perfectly calibrated helium PID response. The mean of each Gaussian interpolation is shown in figure 3.11. The obtained distribution was interpolated with a second-order polynomial (also shown in figure 3.11) and the expected helium TPC response was recentered on a track-by-track basis. The recalibration of the width of the expected ^{3}He TPC signal (figure 3.12) suffers from statistical fluctuations. Within the statistical uncertainties the obtained width, which is assumed to be independent of $p/|z|$, agrees with unity. Hence, no reweighting correction to the width of the expected TPC signal was applied.

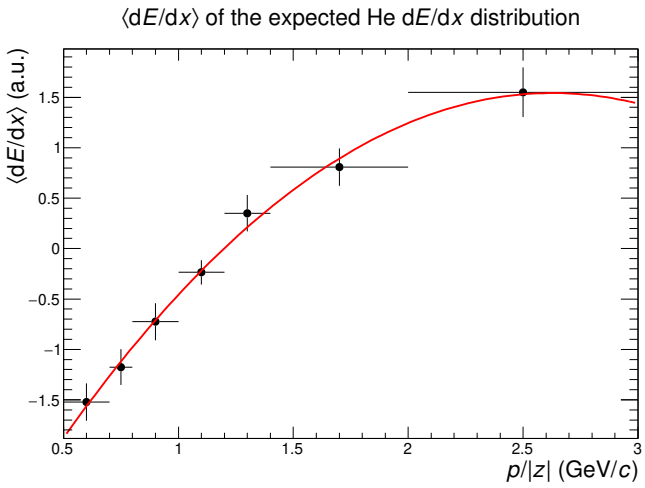

Figure 3.11: Shift of the mean of the expected ^{3}He signal in the TPC, interpolated with a polynomial of second order.

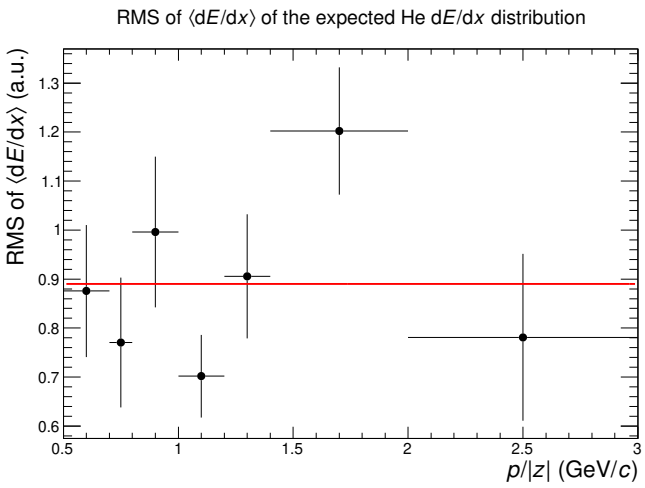

Figure 3.12: Width of the expected ^{3}He signal in the TPC.

The actual signal extraction method is applied after the track-by-track recentering procedure, which is done in fine bins of $p/|z|$. The momentum space needs later to be mapped into transverse-momentum space to extract the physical spectra.

The so extracted ^{3}He TPC signal distribution for particle and antiparticle are shown in figure 3.13 for the integrated minimum bias multiplicity event class and for different ranges of $p/|z|$. In the appendix figure B.4 and B.5 the same plots are depicted for the integrated high-multiplicity triggered event class. For low $p/|z|$ (< 1.25 GeV/c) ^{3}He candidates (not anti-^{3}He) have a significant background contribution, which consists mainly of triton particles, originating form spallation processes.

This contamination is estimated using a combined Gaussian-background and Gaussian-signal function fit. Additionally, a systematic crosscheck is performed using a combined exponential-background and Gaussian-signal function fit. These interpolations are also shown on the left side of figure 3.13. Blue represents the Gaussian-background function and red the exponential background function. The fit parameters of the Gaussian-signal functions are constraint by physical boundary conditions for its mean ($-2 < \mu < 2$) and its width ($0.5 < \sigma < 2$) to ensure the stability of the log-likelihood fit. The multiplicative correction factor (f_{sig}) for the background contamination is determined by integrating the Gaussian (exponential)-background function and dividing it by the total counts in the range $-2 < n\sigma^{^3\text{He}}_{\text{TPC}} < 3$:

$$f_{\text{sig}} = 1 - \frac{\int_{-2}^{+3} \text{BKG}(n\sigma)\text{d}n\sigma}{N_{\text{counts}}} \tag{3.6}$$

The statistical uncertainty from the correction method is propagated by only taking the statistical uncertainty of the background integral ($\frac{\Delta \int \text{BKG}(n\sigma)\text{d}n\sigma}{N_{\text{counts}}}$) into account. The statistical uncertainty of the expected signal on the other hand is not propagated into the multiplicative correction factor to avoid double counting of the uncertainty. The asymmetric selection range of $-2 < n\sigma^{^3\text{He}}_{\text{TPC}} < 3$ was chosen to make the method more robust versus statical fluctuations of the background in the signal-background overlap region.

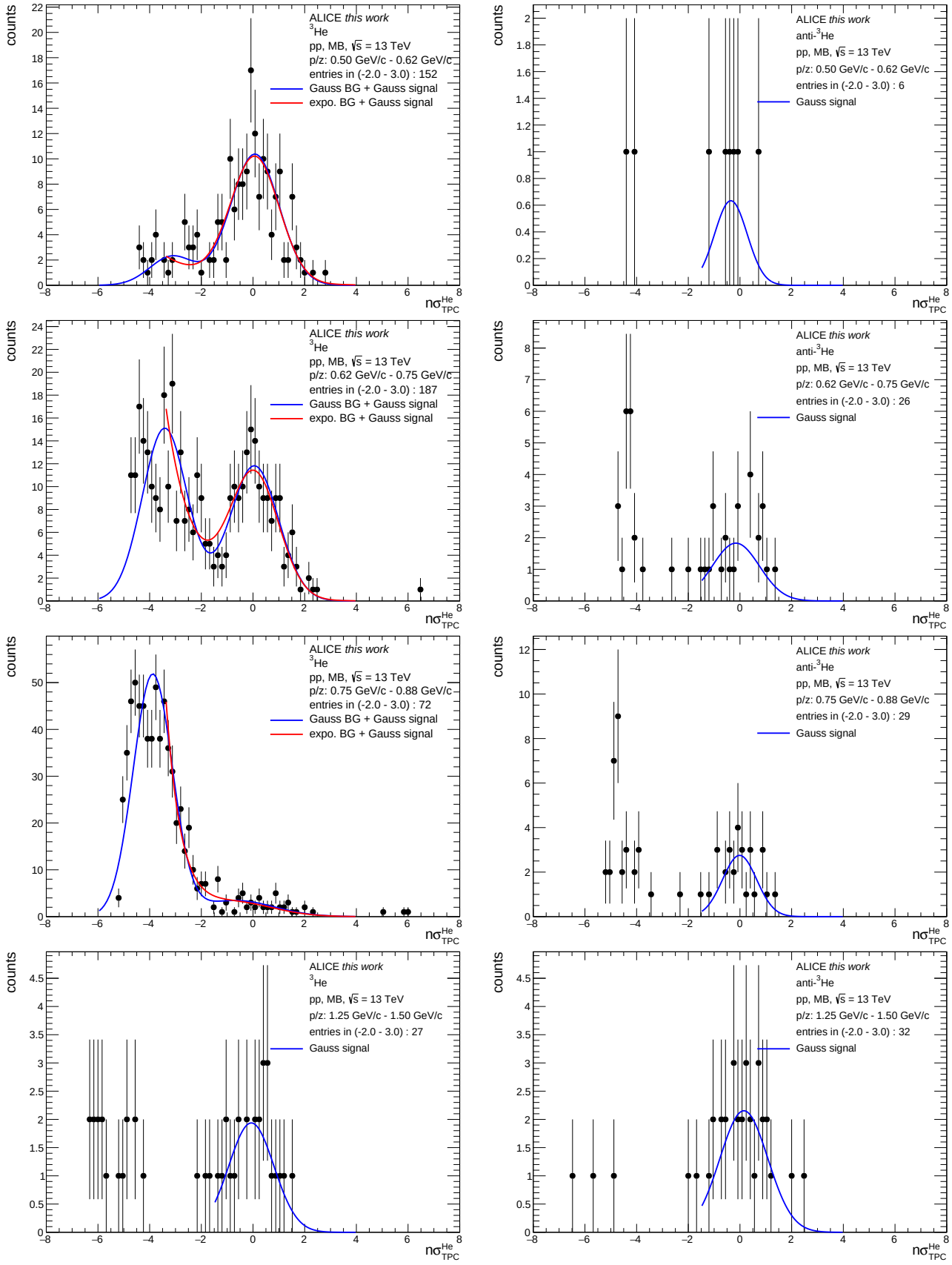

Figure 3.13: TPC signal extraction for ^{3}He (left) and anti-^{3}He (right) for the integrated minimum bias event class, with a signal plus background interpolation. The interpolation is not used for anti-^{3}He.

The right side of figure 3.13 shows the anti-^{3}He distributions with a Gaussian signal fit. The Gaussian signal fit is not used in the later analysis, because the signal is clearly visible. The signal is extracted via bin counting without applying the correction method presented in equation 3.6. Also for ^{3}He with $p/|z| > 1.25$ GeV/c the signal is not contaminated and can be extracted by simple counting. The rigidity-dependent contamination correction factor for ^{3}He is shown in figure 3.14. This contamination correction factor is assumed to be one for anti-^{3}He and for ^{3}He with $p/|z| > 1.25$ GeV/c. The correction factor is the strongest in the $p/|z| \approx 0.8$ GeV/c. This is the area where the ^{3}H distribution has its maximum, while the ^{3}He distribution is already decreasing. The transverse-momentum distributions are extracted following a similar approach

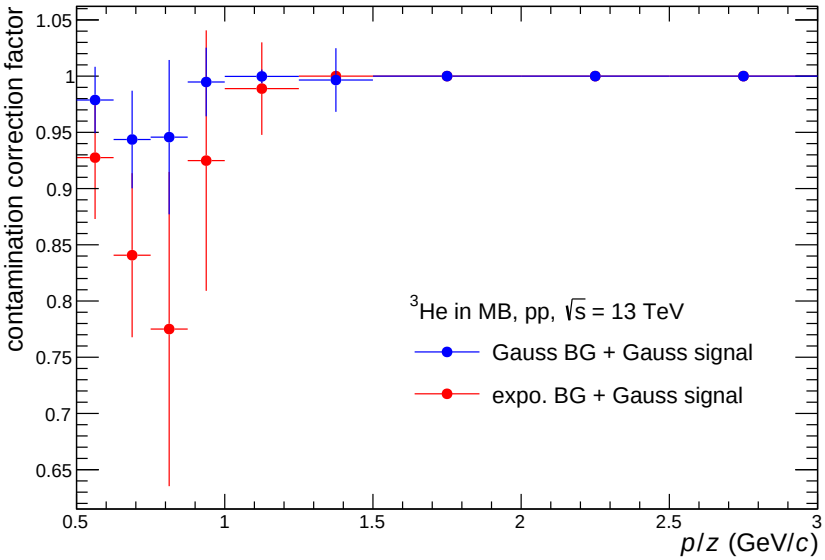

Figure 3.14: Momentum dependent signal contamination correction factor for ^{3}He estimated using a Gaussian or exponential like background function. The correction factor is assumed to be one above 1.25 GeV/c.

and using the previously obtained contamination factor. For the anti-^{3}He nuclei are just selected in a $-2 < n\sigma^{^3\mathrm{He}}_{\mathrm{TPC}} < 3$ window and filled in a transverse-momentum histogram. For ^{3}He the tracks are selected using the same $n\sigma^{^3\mathrm{He}}_{\mathrm{TPC}}$ range. However, the tracks are weighted with the contamination correction factor when filled in the histogram. This is done in four different multiplicity classes within the transverse-momentum intervals of:

MB (V0M: 0-100%):	$1.0\ \mathrm{GeV}/c \leq p_{\mathrm{T}} \leq 5.0\ \mathrm{GeV}/c$
MB (V0M: 0-10%):	$1.0\ \mathrm{GeV}/c \leq p_{\mathrm{T}} \leq 5.0\ \mathrm{GeV}/c$
MB (V0M: 10-100%):	$1.0\ \mathrm{GeV}/c \leq p_{\mathrm{T}} \leq 5.0\ \mathrm{GeV}/c$
HM (V0M: 0-0.1%):	$10.\ \mathrm{GeV}/c \leq p_{\mathrm{T}} \leq 6.0\ \mathrm{GeV}/c$

3.3.3 Triton identification

In comparison to the helium identification, the identification of triton candidates is more challenging, due to tritons carrying only a single charge and being not as cleanly separated in the TPC. The TPC particle identification performance of triton can be seen in figure 2.4. The overlap

with other particle species becomes more notable with increasing momentum and, therefore, the triton PID is separated into two parts: a low-momentum part ($p \leq 2$ GeV/c) where a TPC-only particle identification is applied (similar to the helium identification) and a high-momentum part ($p > 2$ GeV/c) where the triton is identified combining TPC and TOF detectors. Unfortunately, above 2.5 GeV/c the triton signal can not be separated anymore from the background. Overall the triton analysis is quite limited in momentum range and available statistics. For this reason, the recentering of the TPC response, like it was done in the helium analysis, is not feasible. However, the mean shift is not as pronounced as for the helium PID response, because the extrapolation of the expected energy loss works significantly better for charge-one particles.

The TPC-only part of the triton analysis is straightforward because low momentum tritons are well separated in the TPC. The expected TPC triton signal is shown in figure 3.15 in the minimum bias event class, for the two analyzed momentum bins, and for particle and antiparticle. Unfortunately, due to the low production rates, the anti-^{3}H signal contains only around 20 counts. However, the signal is very clean with nearly no background contamination, due to the excellent TPC separation at low momentum. The Gauss interpolations which are shown in figure 3.15 are not used in the later analysis. When filling the p_{T} spectra every track with a momentum smaller 2 GeV/c and within a the selection interval of of $-3 < n\sigma^{^3\mathrm{H}}_{\mathrm{TPC}} < 3$ is considered a tritium nucleus.

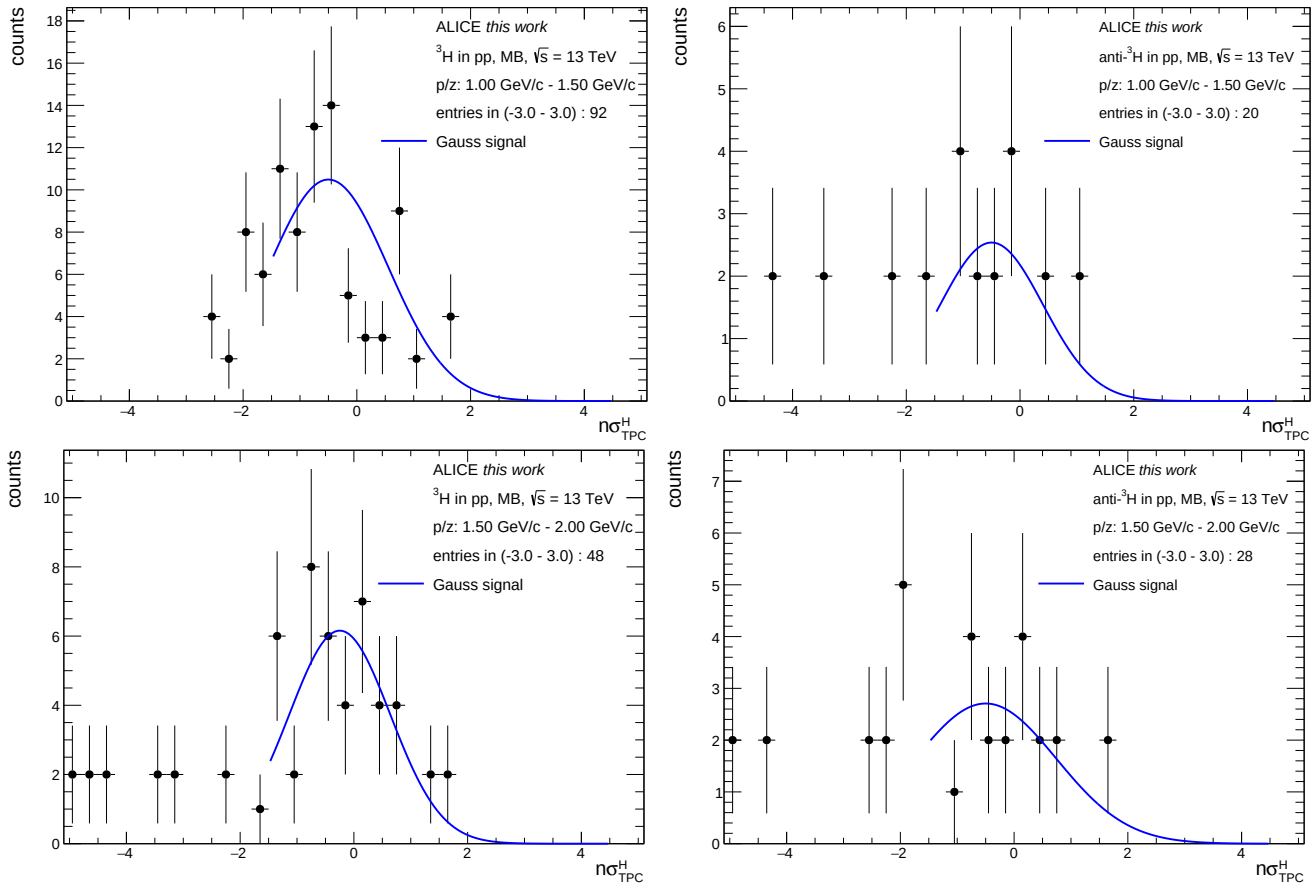

Figure 3.15: TPC-only signal extraction for triton candidates with low momentum ($p \leq 2$ GeV/c) in the minimum bias event class. The left side shows particle while the right one shows antiparticle.

For the high-momentum ($p > 2$ GeV/c) triton particle the identification requires a combination of TPC and TOF detector. First, the tracks are preselected in the TOF with $|n\sigma^{^3\mathrm{H}}_{\mathrm{TOF}}| < 3$. In a second step the triton candidates are filled in a histogram containing the $n\sigma^{^3\mathrm{H}}_{\mathrm{TPC}}$ information. The $n\sigma^{^3\mathrm{H}}_{\mathrm{TPC}}$ distributions are than interpolated with a Gaussian signal function combined with an exponential background function, as shown in figure 3.16 for the momentum interval $2 < p < 2.5$ GeV/c and minimum bias events. Additionally, a Gaussian-signal function was combined with a Gaussian-background function to estimate systematic effects of the chosen background shape. Due to low statistics in the signal region a log likelihood fit is applied.

The signal contamination is estimated by applying equation 3.6. However, the background integration as well as the integration of the histogram is performed in the range $-1 < n\sigma^{^3\mathrm{H}}_{\mathrm{TPC}} < 3$. The asymmetric selection was chosen to minimize the impact of fluctuations in the signal and background overlap region. The signal contamination is around 25% for the exponential background description and around 15% for the Gaussian background description. These factors are again applied as track-by-track weights when filling the p_{T} histograms. The exponential background description is used as the nominal value and the full difference to the Gaussian description is used as a systematic uncertainty. In appendix figure B.6 and B.7 the TPC-only and the TPC-TOF signal extraction for ^{3}H candidates is shown for the integrated high-multiplicity triggered event class.

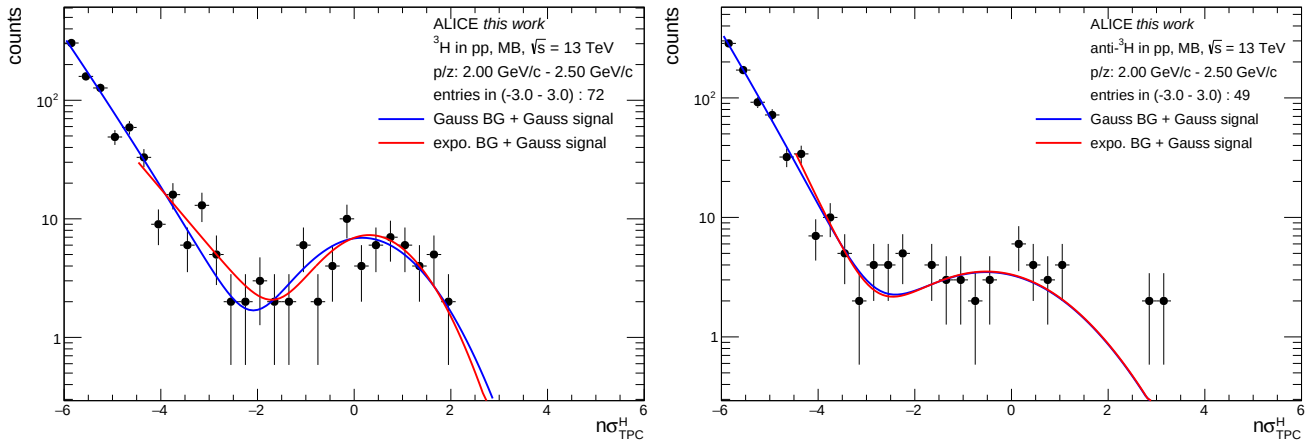

Figure 3.16: Expected TPC triton signal after applying a TOF preselection ($|n\sigma^{^3\mathrm{H}}_{\mathrm{TOF}}| < 3$) for the momentum bin $2 < p < 2.5$ GeV/c in the minimum bias event class. The left side shows particle while the right one shows antiparticle.

3.4 Secondary-particle contamination

As described in section 3.2 a set of track selection criteria, mainly based around the distance to closest approach (DCA), are applied to filter for primary particles. However, these selection criteria only discard a part of the secondary particles and are therefore insufficient.

Secondary particles are originating typically from two different sources. The first one is the production of secondary particles via spallation. Nuclear spallation can occur when a high momentum particle hits a nucleus. The target nucleus is then excited and emits its energy by releasing protons, neutrons, or on rare occasions heavier fragments. This release of fragments happens isotropically in space [133]. The most relevant spallation sources are the beam pipe and the first layers of the ITS. It is important to note that with this mechanism only ordinary matter can be produced, so this contribution does not play a role in the measurement of the antiparticle. The second kind of secondary particle originates from weak decays. The decay products carry a large momentum fraction of their mother particle and, therefore, tend to point in the direction of the primary event vertex.

The difference in the three particle types (primaries, secondaries form weak decay, secondaries form material) DCA_{xy} topologies are shown in the case of protons in figure 3.17. The different shapes of the distributions are used to correct for the secondary-particle contamination. The DCA distribution for each type has a distinct shape. The primary particle DCA distribution is narrow with a sharp peak at zero because all primary particles point back to the primary event vertex. The secondary particles from weak decay have a somewhat compatible DCA shape to the primary particle, however, the peak is significantly broader. The secondary particle DCA distribution originating from interaction with the material has a different shape compared to the other two. The distribution is mostly flat in DCA due to the isotropic nature of spallation processes. The distribution, however, has still a small peak around zero, which is caused by the tracking algorithm favoring tracks pointing back to the ALICE interaction vertex and, thus, associating the wrong cluster. In the innermost layer of the ITS, the track density is the highest. Additionally, very low momentum particles ($p < 100$ MeV/c) never reach further than the first few ITS layers. The tracking algorithm is biased to pick up such clusters so that the tracks point back towards the collision vertex. With the knowledge of the DCA distributions the secondary particle (from weak decay and interaction with the detector material) contamination can be estimated. The contamination is estimated in the various multiplicity classes. In the following the secondary-particle contamination is estimated of the individual particle species.

Secondary-particle contamination for proton

In comparison to the other analyzed particle species, the secondary-particle contamination for proton comes with the advantage of a relatively good knowledge of the spallation process. Thanks to that knowledge, the contamination can be estimated by using a Monte Carlo simulation, generated with PYTHIA [130] and GEANT3 [134]. This Monte Carlo set, however, has no injected nuclei, which would significantly impact the distribution of protons from secondary decay products. Unfortunately, the strange particle yields and, thus, the number of secondary particles from weak decay per collision are not properly described in Monte Carlo. However, the typical shape of the DCA_{xy} distributions are reproduced properly. Therefore, under the assumption of proper DCA_{xy} distributions, the unique shapes for primary, secondary from interaction

with the detector material, and secondary from weak decay, can be used to interpolate the measured DCA_{xy} distribution. This method is called template fits. It is executed using a minimization routine named TFractionFitter [135] which is provided in the ROOT package. The routine needs as input one data distribution and two or more Monte Carlo distributions. The relative fractions of the Monte Carlo templates are added up to match the data and the relative fractions will be adjusted until the χ^2 is minimized. The sum of all fractions needs to be one by construction. The fraction of secondary particles from weak decays plus the ones from material in the relevant DCA_{xy} range give the signal contamination. For antiprotons, the number of secondary particles from the material can be neglected so only two templates are used. The DCA_{xy} distributions in data are obtained by applying a tight PID cut of $|n\sigma_{\mathrm{TOF}}| < 2$ and $|n\sigma_{\mathrm{TPC}}| < 2$ to ensure a clean sample of protons and avoid an overcorrection of possible particle species-dependent effects. This can safely be done because the source of a particle and its PID response are uncorrelated. Additionally, the DCA_z selection window is increased to be $|\mathrm{DCA}_z| < 1$ cm so that more statistics in the tails of the secondary particle distributions is gained. With increasing statistics in the tail of the DCA_{xy} distributions the fits become more stable. As mentioned in section 3.2 the fraction primary particle is calculated p_{T} dependent in the $|\mathrm{DCA}_{xy}| < 3\sigma$ region. The template fits are sensitive to the DCA_{xy} bin granularity because it directly affects the resolution of the shape of the input distribution. Therefore, in the critical region around $\mathrm{DCA}_{xy} = 0$ the bins are chosen to be fine while the tails of the distributions are covered with wider bins to improve the statistical precision. Four different bin settings were studied ranging from fine to coarse, with 64, 45, 31, and 25 bins. Two example p_{T} bins are shown in figure 3.17 for protons (left) and antiprotons (right) for the integrated multiplicity class (0-0.1%) and with 31 DCA_{xy} bins. The left column shows the measured DCA_{xy} for protons in black and the three distributions obtained from Monte Carlo. The previously described shape of the Monte Carlo $\mathrm{DAC}_{\mathrm{xy}}$ distributions for primary particles and secondary particles (form weak decay and from interaction with the detector material) is clearly visible. The material distribution (in magenta) is the flattest out of the three while the primary particle distribution (in green) has a sharp peak at zero as expected. Additionally, with increasing p_{T} the material contribution becomes less relevant. The right side of figure 3.17 shows the measured DCA_{xy} for antiprotons in black and only the two interpolated Monte Carlo templates for primary particles in green and secondary particles from decays in red. For both protons and antiprotons, the fit results are displayed in gray, and agree, especially in the most relevant region of $|\mathrm{DCA}_{xy}| < 0.2$ cm well with the measured distributions. The fit results in terms of relative fractions for two bin granularities of 64 and 31 and the integrated V0M multiplicity 0-0.1% are shown in figure 3.18 and 3.19. The left-hand side shows the proton while the right-hand side the antiproton results. The individual contributions are encoded using the same color scheme: green for primary particles, red for secondary particles form weak decays, and magenta for secondary particles from interaction with the material. Starting at around 70% at 0.5 GeV/c the primary particles contribute 90% from 3 GeV/c. Nearly 30% of the proton signal at 0.5 GeV/c are contaminated by secondary particles while from 3 GeV/c onwards the contamination is less than 10%. The secondary protons form interaction with the detector material play only a minor role of less than 5% at low momentum and are completely negligible for p_{T} larger 2 GeV/c. In a few cases, the fit failed and exchanged the two secondary particle contributions (discontinuity in the magenta and red curves for $p_{\mathrm{T}} > 2.5$ GeV/c) which, however, does not affect the results since the primary particle fraction stays the same.

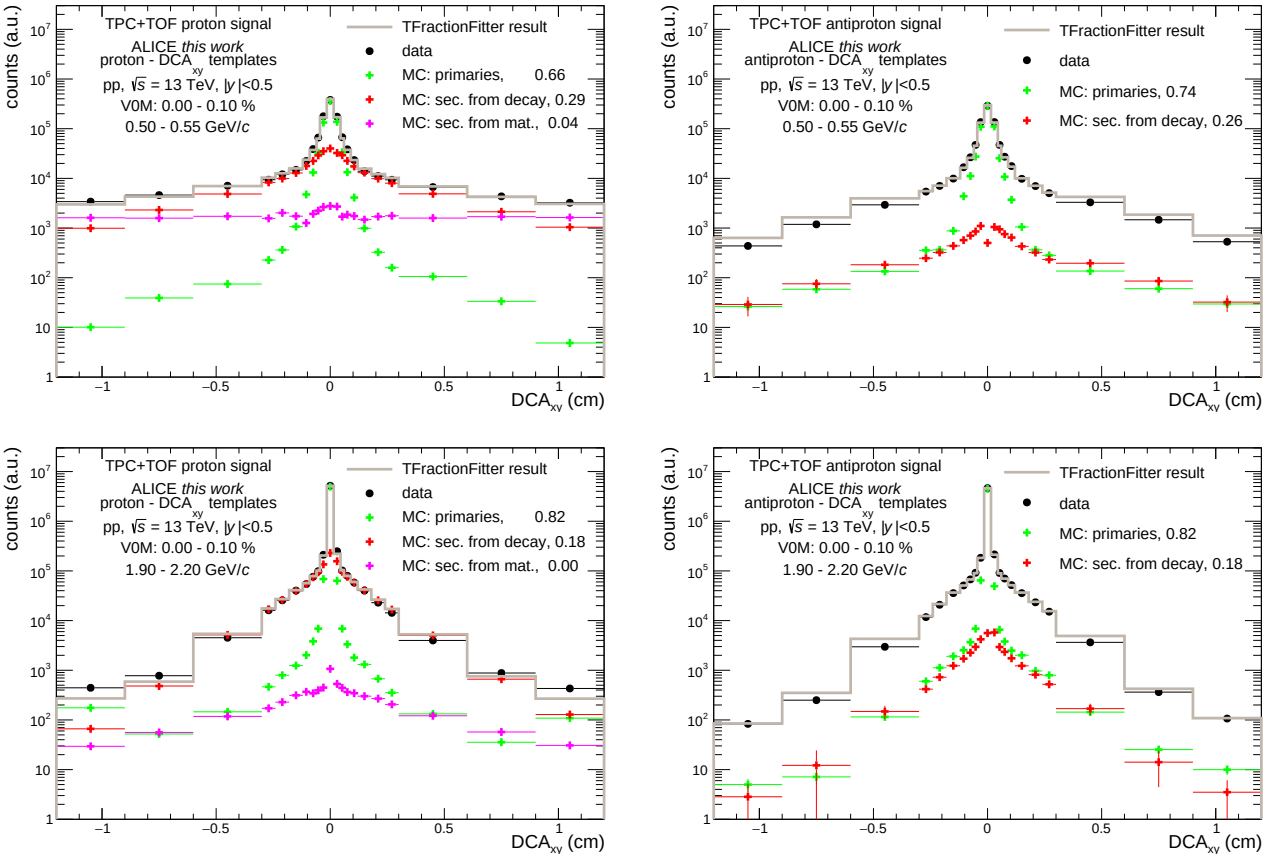

Figure 3.17: DCA_{xy} template fits for protons (left) and antiprotons (right) in the V0M multiplicity class 0-0.1%. The DCA_{xy} bin granularity is 31.

While the fractions in figure 3.18 with a DCA_{xy} bin granularity of 64 and the fractions in figure 3.19 with a DCA_{xy} bin granularity 31 follow the same pattern a small difference in the order of 2 to 5% is noticeable. The same is true for the additionally analyzed bin granularity settings of 25 and 45. The later applied correction to the transverse-momentum spectra is calculated using the mean of the four different bin granularity settings with their standard deviation used as a systematic uncertainty. This correction factor for the multiplicity interval V0M 0-0.1% with the corresponding uncertainties is shown for protons and antiprotons in figure 3.20. The same technique was also applied in the three analyzed V0M multiplicity intervals (0-0.01%, 0.01-0.05%, and 0.05-0.1%) and the corresponding corrections factors are shown in appendix figure B.8. The primary proton fraction is only minimally affected by multiplicity (less than 1%). This is expected because the corresponding multiplicity does not differ much going form the lowest ($\langle \mathrm{d}N/\mathrm{d}\eta \rangle = 30.1 \pm 0.3$) to the highest multiplicity class ($\langle \mathrm{d}N/\mathrm{d}\eta \rangle = 35.8 \pm 0.3$). Therefore, the integrated multiplicity class, which uses the most statistics and has the most stable results, is used to correct all multiplicity differential results.

Secondary-particle contamination for helium nuclei

The secondary ^{3}He contamination needs to be estimated with a different method than the DCA template fits. Due to the rare production of secondary ^{3}He in spallation processes a huge simu-

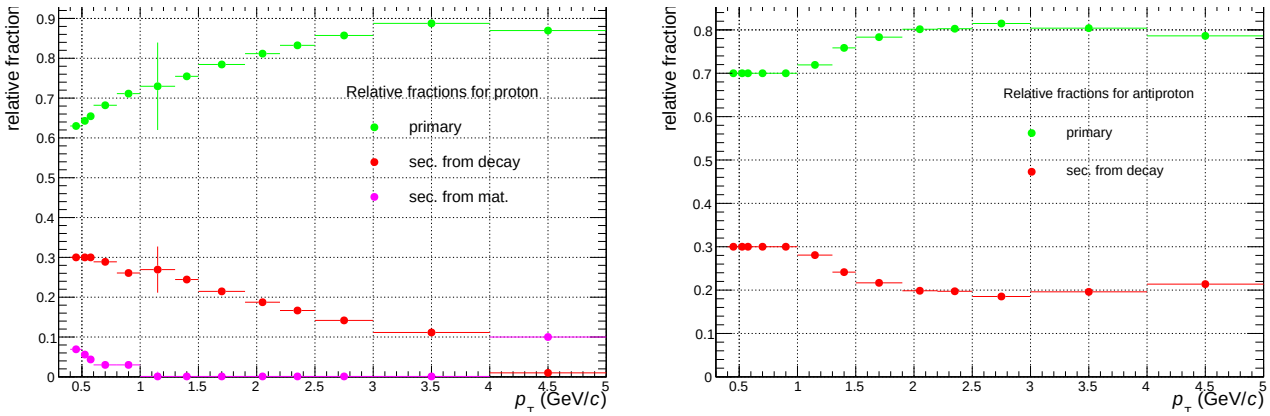

Figure 3.18: Fractions of secondary protons (from weak decay in red and from material in magenta) for protons (left) and antiprotons (right) in the V0M multiplicity interval 0-0.1%. The DCA_{xy} template fits are performed with a bin granularity of 64.

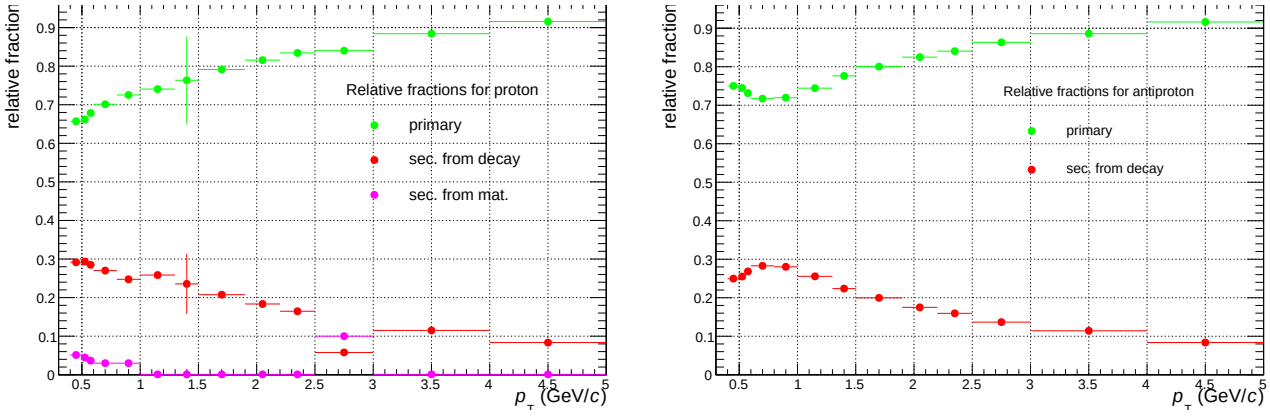

Figure 3.19: Fractions of secondary protons (from weak decay in red and from material in magenta) for protons (left) and antiprotons (right) in the V0M multiplicity interval 0-0.1%. The DCA_{xy} template fits are performed with a bin granularity of 31.

lated Monte Carlo sample would be needed. To put it in perspective in the 40 million analyzed Monte Carlo events not a single ^{3}He from a spallation process was found while the same sample contains 300000 protons originating from spallation. It is also important to note that the contamination of secondary ^{3}He from weak decays can be neglected. The only particle decaying weakly into (anti-)^{3}He as measured with ALICE is the hypertriton ($^3_\Lambda\mathrm{H} \rightarrow {}^3\mathrm{He} + \pi^-$). The following three arguments justify the neglection of the $^3_\Lambda$H contamination:

- In first order the lifetime of $^3_\Lambda$H is compatible with the lifetime of the free lambda (Λ) which is about 260 ps [1]. So most $^3_\Lambda$H decay outside the applied tight DCA selection window.
- The $^3_\Lambda$H decays only with a branching ratio of 25% into a ^{3}He and a pion [136].
- Coalescence models predict a ratio of $^3_\Lambda$H to ^{3}He of about 25% at $\mathrm{d}N_{\mathrm{ch}}/\mathrm{d}\eta = 30$ [137], which decreases to less than 10% with decreasing multiplicity.

Because there is no anti-^{3}He produced in spallation processes the anti-^{3}He signal can not be contaminated by secondary particles from spallation.

For ^{3}He the amount of secondary particles from spallation processes is estimated via a likelihood fit of the DCA distributions in bins of p_{T}. The ^{3}He candidates, which fulfill $|n\sigma^{\mathrm{He}}_{\mathrm{TPC}}| < 2$, are

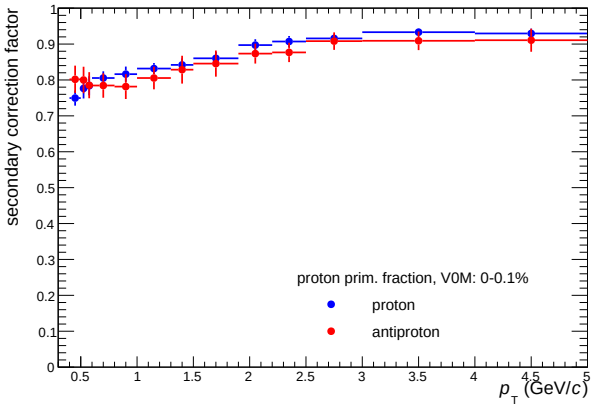

Figure 3.20: Secondary correction factor in the V0M multiplicity interval 0-0.1% with its systematic uncertainties for protons (blue) and antiprotons (red).

projected into their DCA distribution. The PID selection window is on purpose chosen to be small to keep the contamination by other particle species as minimal as possible. One example DCA_{xy}-DCA_zdistribution for ^{3}He in the p_T range (1.5 - 2.0 GeV/c) is shown in figure 3.21.
The DCA distribution is assumed to have a Gaussian signal peak, while various functions for the background distributions were considered, namely a Gaussian, a parabola, and a constant function. However, all of these assume a rather flat background below the signal peak. Additionally, to further constrain the fit, the correlation between DCA_{xy} and DCA_z is used and the fits are performed in two dimensions. The three background functions are assumed to be point symmetric around (DCA_{xy}, DCA_z)=(0, 0) and they are:

$$f_\mathrm{BKG}^\mathrm{Gauss}(\mathrm{DCA}_{xy},\mathrm{DCA}_z) = a_0 \exp\left(-\frac{1}{2}\left(\frac{\mathrm{DCA}_{xy}^2}{a_1^2}+\frac{\mathrm{DCA}_z^2}{a_2^2}\right)\right) \tag{3.7}$$

$$f_\mathrm{BKG}^\mathrm{parabol}(\mathrm{DCA}_{xy},\mathrm{DCA}_z) = a_0 - a_1\cdot\mathrm{DCA}_{xy}^2 - a_2\cdot\mathrm{DCA}_z^2 \tag{3.8}$$

$$f_\mathrm{BKG}^\mathrm{const}(\mathrm{DCA}_{xy},\mathrm{DCA}_z) = a_0 \tag{3.9}$$

To verify the stability of the two dimensional fits, the same procedure was performed exploiting only the DCA_{xy} projection, while requiring the candidates to fulfill $|\mathrm{DCA}_z| < 0.15$ cm. The distributions for different p_T regions were interpolated with the three different background functions 3.7, 3.8, and 3.9, with $\mathrm{DCA}_z = 0$. The DCA_{xy} with the corresponding interpolations is shown in figure 3.22 for the p_T interval 1.5 - 2.0 GeV/c and the integrated MB data sample. A correction factor c_prim is calculated as a multiplicative factor and it is applied to the spectra later:

$$c_\mathrm{prim} = 1 - \frac{\int_{-0.15}^{0.15}\int_{-0.15}^{0.15} f_\mathrm{BKG}\left(\mathrm{DCA}_{xy},\mathrm{DCA}_z\right)\,\mathrm{dDCA}_{xy}\,\mathrm{dDCA}_z}{N_\mathrm{counts}} \tag{3.10}$$

The statistical error is propagated by only taking the background integral error into account. The six different correction factors using different background functions and being performed in one or two dimensions are shown in figure 3.23. The two-dimensional interpolation with

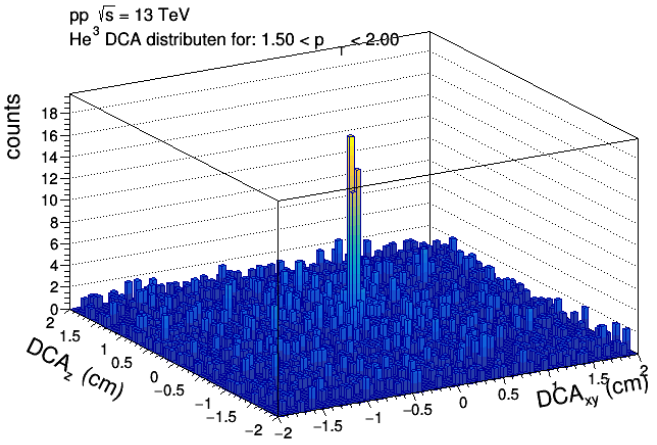

Figure 3.21: The correlation between DCA_{xy} and DCA_z for ^{3}He candidates.

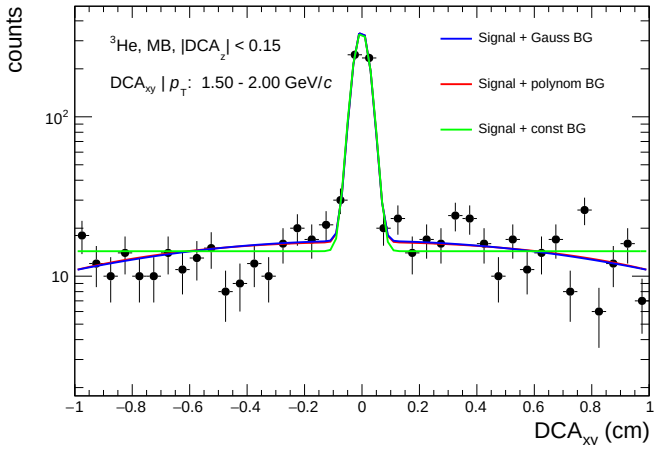

Figure 3.22: DCA_{xy} distribution of ^{3}He candidates with a required $|DCA_z| < 0.15$ cm. The data is interpolated with three different background shapes to estimate the secondary-particle contamination.

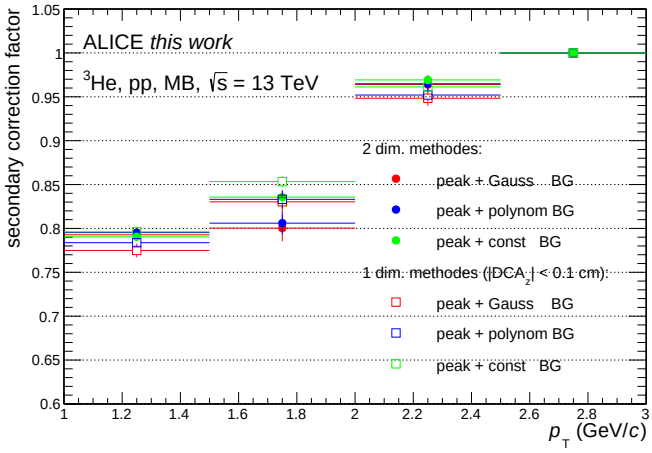

Figure 3.23: p_T-dependent ^{3}He secondary-particle contamination estimated with different background assumptions shown for the MB (V0M 0-100%) data set.

a Gaussian background shape is used as the baseline for the later correction while the other trails give an estimate of the systematic uncertainties. The results for the HM (V0M 0-0.1%) triggered data sample is shown in appendix figure B.9. Only a small multiplicity dependence is observed within the same trigger class. To improve statistical precision only the corresponding integrated result is used as a correction factor. Additionally, for both multiplicity classes, in the transverse-momentum range of $1 < p_T < 1.5$ GeV/c the raw yield of primary ^{3}He overshoots the raw count of primary anti-^{3}He by a factor up to three, even though the fits are stable. This is a clear sign that the assumption of a flat secondary DCA distribution below the signal does not hold in the $1 < p_T < 1.5$ GeV/c region and, therefore, in these bins the ^{3}He measurement is discarded and only the anti-^{3}He results are used, which are not contaminated by secondary helium nuclei.

Secondary-particle contamination for triton

As for the ^{3}He spectra, the hypertriton decay feeds into the (anti-)^{3}H ($^3_\Lambda$H $\rightarrow ^3$H + π^0) and contaminates the measurement. This contribution, however, is expected to be negligible following the same three arguments as in the ^{3}He case. This time, however, the cause is even stronger since the branching ratio is roughly half compared to the ^{3}He decay channel [136].

The same procedure as described for the ^{3}He nuclei was applied to estimate the secondary-particle contamination from spallation processes. Only the preselection criterion was adjusted and candidates with $|n\sigma^H_{\mathrm{TPC}}| < 2$ and $|n\sigma^H_{\mathrm{TOF}}| < 2$ are filled into the DCA distributions. The three Gauss like signal and background functions (equation 3.7 to 3.9) were used to estimate the secondary-particle contamination, by interpolating the two-dimensional DCA_{xy} and DCA_z distribution. Additionally, the one-dimensional projection in the DCA_{xy} plane is interpolated with the same functions and $\mathrm{DCA}_z = 0$. The DCA_{xy} distribution with its corresponding interpolations is shown in figure 3.24 for the integrated MB event class and the transverse-momentum interval $1.5 < p_{\mathrm{T}} < 2$ GeV/c. The resulting p_{T}-dependent secondary-particle contamination of the ^{3}H signal is shown in figure 3.25 for the integrated MB event class. The figure shows the primary fraction estimated with the different methods. The interpolation using the two-dimensional Gaussian background shape is the baseline and the other functions give an estimate for systematic effects. The results for the HM (V0M 0-0.1%) triggered data sample is shown in appendix figure B.10. In the transverse-momentum range of $1 < p_{\mathrm{T}} < 1.5$ GeV/c the same effect as in the ^{3}He analysis was observed. The raw yield of primary ^{3}H overshoots the raw yield of primary anti-^{3}H by a factor up to three, for both multiplicity classes. Since the fits are stable, this clearly shows that the assumption of a flat secondary DCA distribution below the signal is not valid in the $1 < p_{\mathrm{T}} < 1.5$ GeV/c region for ^{3}H. Therefore, in the transverse-momentum range $1 < p_{\mathrm{T}} < 1.5$ GeV/c the ^{3}H measurement is discarded and only the anti-^{3}H result is used.

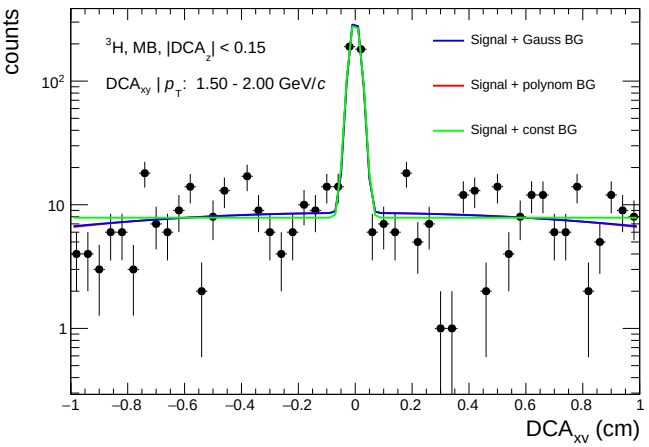

Figure 3.24: DCA_{xy} distribution of ^{3}H candidates with a required $|\mathrm{DCA}_z| < 0.1$ cm. The data is interpolated with three different background shapes to estimate the contamination.

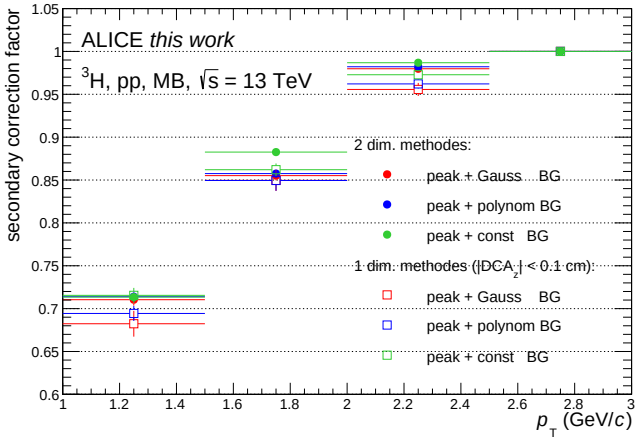

Figure 3.25: p_{T}-dependent ^{3}H secondary-particle contamination estimated with different background assumptions shown for the MB (V0M 0-100%) data set.

3.5 Tracking efficiency and acceptance

Not all primary particles produced in the collision are tracked by the detector. Some do not pass the applied track quality selection criteria, and some do not reach the tracking detectors due to hadronic interactions, energy loss in the detector material, detector dead zones, or simply detector acceptance. Therefore, the particle spectra have to be corrected for the detector tracking efficiency and acceptance. The efficiencies are calculated with a Monte Carlo model using the PYTHIA event generator with a GEANT4 transport model simulating the realistic ALICE detector material. The GEANT4 transport is anchored to specific run setups of ALICE and, therefore, takes run-dependent effects like dead-channels maps into account. The transverse-momentum dependent efficiencies are calculated by the ratio of reconstructed to the generated tracks within the rapidity interval $|y| < 0.5$:

$$\epsilon(p_{\mathrm{T}}) = \frac{N^{\mathrm{rec}}_{\mathrm{prim}}(p^{\mathrm{rec}}_{\mathrm{T}})}{N^{\mathrm{gen}}_{\mathrm{prim}}(p^{\mathrm{gen}}_{\mathrm{T}})} \tag{3.11}$$

The reconstructed tracks are obtained by selecting only as primary flagged particles in the Monte Carlo simulation and applying the same track selection criteria (see table 3.2) as in the analysis of the measured data sample. For the denominator, all primary particles in the Monte Carlo sample in the relevant rapidity interval are counted. The detector efficiency for (anti)protons, (anti)helium, and (anti)triton are shown in figure 3.26, 3.27, and 3.28, respectively. Year dependent differences of the tracking efficiencies are displayed in figure 3.26 for protons, where a small but clear shift (order of 2%) is visible. In the anchored Monte Carlo productions the appropriate event normalization is taken into account. Therefore, for the (anti)helium and (anti)triton efficiencies using Monte Carlo samples linked to different years can be merged and no reweighting is needed. For the proton analysis, only data from 2018 is used. In that case, the efficiency correction is purely based on the 2018 anchored Monte Carlo simulation.

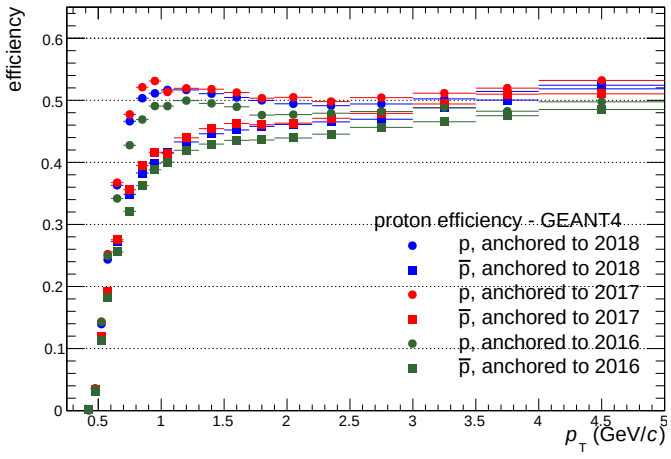

Figure 3.26: (Anti)proton tracking efficiency for the different running periods recorded in the years 2016, 2017, and 2018.

Due to the absorption of antimatter for all particle species, the antiparticle track reconstruction efficiency is a few percent lower than the corresponding particle efficiency. For all three particle species, the efficiency rises rapidly at low p_{T} and then starts to saturate. This typical shape is due

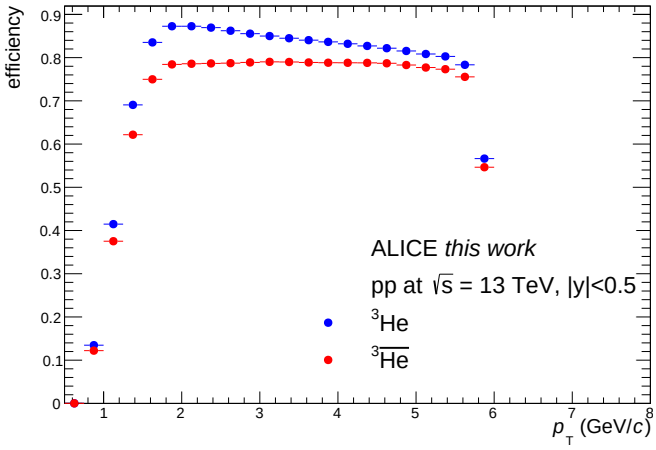

Figure 3.27: (Anti)helium tracking efficiency (ϵ) averaged over all periods in the years 2016, 2017, and 2018.

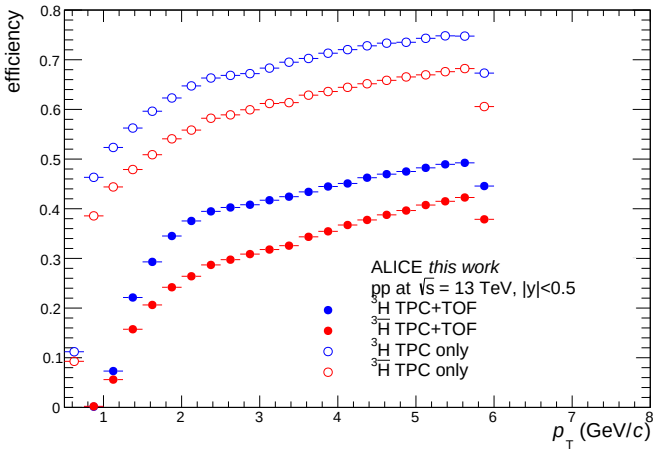

Figure 3.28: (Anti)triton tracking efficiency (ϵ) averaged over all periods in the years 2016, 2017, and 2018. The full symbols represent the efficiency obtained requiring a signal in the TPC and TOF detectors while the open symbols do not require a TOF signal.

to energy loss, which causes low-momentum particles to lose even more energy and eventually stop in the detector.

In figure 3.28 the effect caused by the inclusion of the TOF detector is nicely visible, as depicted with the full symbols. When compared to the open symbols, which require only the TPC detector, the efficiency drops by nearly a factor two. This means a large fraction of particles gets lost in the TRD detector material, which has to be passed on the way from the TPC to the TOF detector. Partially the particles get scattered in the TRD so that TPC and TOF tracks can not be matched and partially the particles get absorbed in the TRD detector. Another way to illustrate the effect is the material budged which amounts to around 10% from the primary vertex to the inner TPC, while the TRD has a material budget of about 25%.

The helium and the triton efficiency drop for $p_{\mathrm{T}} = 6$ GeV/c which is unphysical. This is caused by the p_{T} distribution of the Monte Carlo input. The nuclei are injected with a flat momentum distribution, which stops at $p = 6$ GeV/c. The presented analysis is only insignificantly affected by this because the (anti)triton analysis ends at 2.5 GeV/c and the minimum bias triggered (anti)helium analysis at 5 GeV/c. Only the high-multiplicity triggered (anti)helium analysis reaches to 6 GeV/c. To avoid edge effects, the efficiency is assumed to be constant in p_{T} from 5.5 GeV/c onwards.

3.5.1 Hadronic interaction cross section

(Anti)particles passing through material constantly interact with it and are if the material is thick enough eventually stopped. These processes are modeled in the GEANT4 transport code, and the main quantity representing the absorption rate is the inelastic interaction cross section σ_I. The efficiency correction covers this effect for the most part. However, GEANT4 does not represent the inelastic cross sections perfectly. Therefore, a variety of measurements of the

proton inelastic cross section [138, 139, 140, 141] as well as recent ALICE measurements for the ^{2}H and ^{3}He inelastic cross section [106] are used to reweight the GEANT4 model predictions.
The number of particles being absorbed when penetrating through a material with the thickness Δx can be expressed by:

$$N = N_0 \exp\left(-\frac{\Delta x}{\lambda_I}\right) \tag{3.12}$$

where N_0 is the total number of incoming particles and λ_I is the interaction length. The interaction length can be further expressed by:

$$\lambda_I = \frac{M}{\rho N_A \sigma_I} \tag{3.13}$$

with M being the molar mass of the target, ρ its density, N_A the Avogadro constant, and σ_I the inelastic cross section.
In a simplified picture, the detector efficiency can be expressed by the ratio of outgoing to incoming particles, which is schematically displayed in figure 3.29. This leads to:

$$\begin{aligned} \epsilon = \frac{N}{N_0} &= \exp\left(-\frac{\Delta x}{\lambda_I}\right) \\ &= \exp\left(-\frac{\Delta x \rho N_A \sigma_I}{M}\right) \end{aligned} \tag{3.14}$$

The uncertainty of the efficiency ($\Delta\epsilon$) originating from the inelastic cross section uncertainty ($\Delta\sigma_I$) is given by:

$$\begin{aligned} \Delta\epsilon &= \left|\frac{\delta\epsilon}{\delta\sigma_I}\right| \Delta\sigma_I \\ &= \frac{-\Delta x \rho N_A \sigma_I}{M} \cdot \exp\left(\frac{-\Delta x \rho N_A \sigma_I}{M}\right) \cdot \Delta\sigma_I \\ &= \frac{\Delta x}{\lambda_I} \frac{\Delta\sigma_I}{\sigma_I} \cdot \epsilon \end{aligned} \tag{3.15}$$

which can be expressed as a relative uncertainty for the efficiency:

$$\frac{\Delta\epsilon}{\epsilon} = \frac{\Delta x}{\lambda_I} \frac{\Delta\sigma_I}{\sigma_I} \tag{3.16}$$

The relative uncertainty on the efficiency is, therefore, proportional to the relative uncertainty on the hadronic interaction cross section.
In the following the inelastic hadronic interaction cross sections implemented in GEANT4 are going to be compared to measurements, intending to extract a data-driven correction to the GEANT4 efficiency. To simplify the method, however, the GEANT4 predicted momentum dependence of the hadronic interaction cross section is assumed to be properly represented. With this assumption, the momentum-dependent GEANT4 model prediction is scaled by a constant (c) and interpolated to the existing measurements of the hadronic interaction cross sections. Once the scaling constant is determined a new simulation with the appropriated scaled hadronic

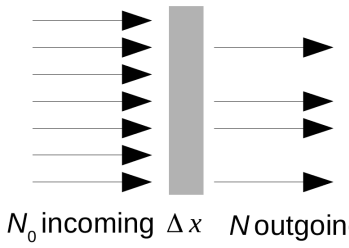

Figure 3.29: Absorption of N_0 particles traveling through a Δx thick material.

interaction cross sections can be rerun. From this, the effect of the hadronic interaction cross sections on the efficiency correction can be determined. The relative uncertainty on the efficiency is obtained following equation 3.16.

Since the proton inelastic cross section is measured for many different targets and, thus, most likely properly described in GEANT4 the method can be verified. Figure 3.30 shows the measured inelastic proton cross sections taken from references [138, 139, 140, 141] with the interpolated GEANT4 parametrization. The rescaling factor is the only free parameter in the model and figure 3.31 displays it as a function of the χ^2/NDF, which has its minimum (best agreement) at 0.993. As described in reference [1] a one σ deviation corresponds to a change in χ^2/NDF of 1.0. This leads to an uncertainty of 0.035 on the rescaling factor. The proton-nucleus inelastic

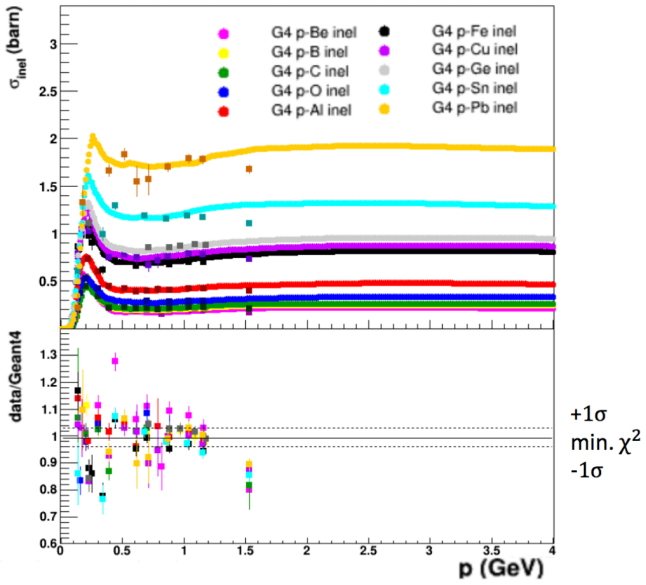

Figure 3.30: The inelastic proton–nucleus cross sections measured in various reaction systems [138, 139, 140, 141] compared to the GEANT4 prediction.

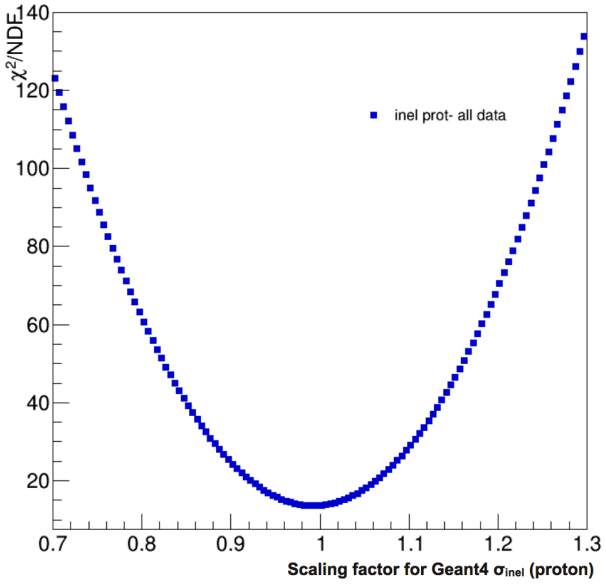

Figure 3.31: The χ^2/NDF as a function of the combined fits rescaling factor.

cross section implemented in GEANT4 is now scaled by 0.993 ± 0.035 and the reconstructed proton spectra are determined. For this purpose, a simplified model of the ALICE detector is applied. In the model, the ALICE detector only exists of stacks of material with a thickness given by the average over the azimuthal angle φ. Two specific reconstruction scenarios are studied:

- Particles travel through ITS and TPC and are reconstructed in both detectors

- Particles travel through ITS, TPC, TRD, and TOF and are reconstructed in ITS, TPC, and TOF detectors

Since GEANT4 described proton-nucleus inelastic cross sections very well the relative change in the reconstructed spectra, the resulting efficiency rescaling factor, and its corresponding uncertainty are very small. For the TPC-ITS scenario, the rescaling factor is momentum independent and has a value of $c = 1.0002 \pm 0.0016$. For the second scenario (inclusion of the TOF detector) the rescaling factor is also momentum independent and has a value of $c = 1.0009 \pm 0.0052$. Since these factors are small they are neglected in the proton analysis.

The same study was applied for antiprotons, for which also several measurements of the inelastic antiproton cross section on various targets are available in references [142, 143, 144, 145, 146]. In figure 3.32 the measured antiproton nucleon cross sections with their GEANT4 parameterizations are shown. Figure 3.33 displays the χ^2per degrees of freedom as a function of the corresponding GEANT4 rescaling factor. For antiprotons, this value has its minimum at 0.913 ± 0.048. This shows that the antiproton nucleus inelastic cross section is slightly overestimated by GEANT4. To see the full impact on the antiproton spectra, a full ALICE simulation

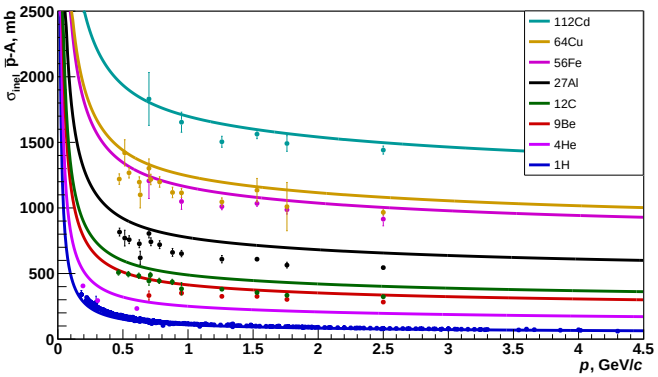

Figure 3.32: The inelastic antiproton–nucleus cross sections measured in various reaction systems [142, 143, 144, 145, 146] compared to the GEANT4 prediction.

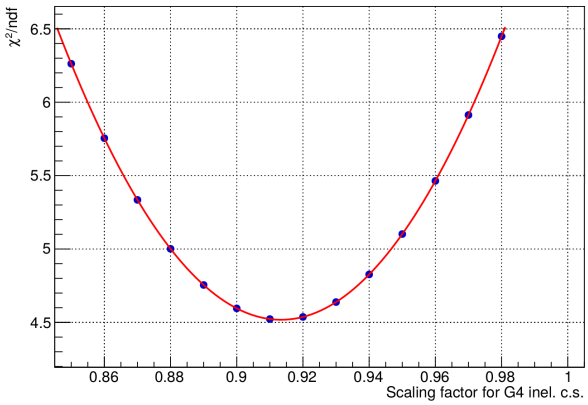

Figure 3.33: The χ^2/NDF as a function of the combined fits rescaling factor.

was used in which the antiproton nucleon inelastic cross section was rescaled accordingly. The impact on the antiproton efficiency can be seen in figure 3.34. Two cases were studied: tracking with ITS and TPC as well as tracking with ITS, TPC, and TOF. Both cases are shown in figure 3.34 with $p_T < 0.7$ GeV/c being the TPC and ITS only part and $p_T > 0.7$ GeV/c being the ITS, TPC, and TOF study. Additionally, in figure 3.34 a one σ uncertainty band is displayed (in red) which is propagated following equation 3.16. The constant ITS-TPC standalone study correction factor is not further used in this analysis and is only shown for completeness because the proton analysis presented in this work uses the ITS, TPC, and TOF detectors for the full momentum range.

To explore the effect of the (anti)helium nucleus inelastic cross section on the reconstruction efficiency a similar study was performed. It is based on an ALICE preliminary measurement of the antihelium inelastic cross section performed in Pb-Pb collisions at 5.02 TeV by measuring the antihelium absorption in the TRD detector. In figure 3.35 the measured cross section is

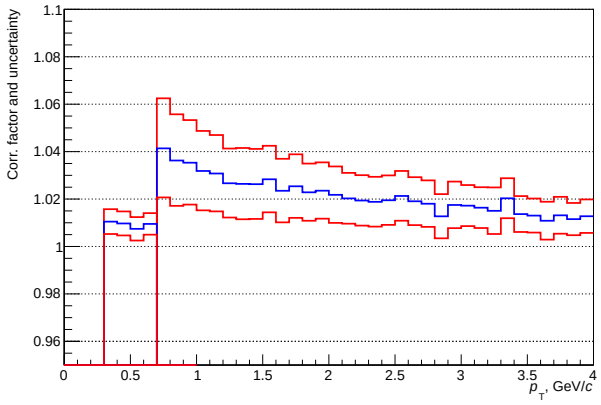

Figure 3.34: Antiproton efficiency correction factor in blue with a one σ uncertainty band in red, due to the imperfectly described antiproton nucleon inelastic cross section. For $p_T < 0.7$ GeV/c the efficiency is calculated with ITS and TPC which results in a nearly constant factor of $c = 1.009 \pm 0.005$, while for $p_T > 0.7$ GeV/c ITS, TPC, and TOF are used.

compared to perdition from default GEANT4. Under the assumption of a proper prediction momentum dependence, the GEANT4 prediction is interpolated to the measurement using the same minimization method as described for (anti)protons. The best description is found for a scaling factor of $C = 0.83 \pm 0.07$. To determine the effect on the antihelium reconstruction efficiency, the cross section is scaled in GEANT4, and simulation of the antihelium propagation thaw parameterizarough the ALICE detector is performed.

The ratio to the default GEANT4 efficacies once using only the TPC and once using TPC and TOF detectors is calculated and interpolated with a power-law parameterization as a function of p_T. The power-law parameterization is applied as a correction to the default GEANT4 efficiency and is shown in figure 3.36. The correction is maximal 5% at low transverse momentum and is reduced to 2% for high p_T. The propagated uncertainties are indicated with the dashed lines and amount maximal 2% at low transverse momentum.

The same studies were done for ^{3}He and lead to a nearly p_T independent correction factor of less than one percent as shown in figure 3.36, with a systematic uncertainty of less than 0.5%.

Neither the ^{3}H nor the anti-^{3}H efficiencies were corrected for such effects because the effect is negligible in comparison to the total systematic uncertainties for ^{3}H, while for anti-^{3}H no measurement of the inelastic cross section is available.

3.5.2 TRD material budget correction

Particles that reach the TOF detector have to pass the TRD detector, in which they can be absorbed via inelastic collisions. As discussed in the previous section (see equation 3.14) the inelastic scattering has a direct effect on the reconstruction efficiency. This effect is dependent on the inelastic hadronic cross section and the properties of the traversed material (e.g. Δx, ρ). Unfortunately, the TRD material is not precisely known and, hence, not perfectly modeled in the Monte Carlo simulations. Therefore, this effect is estimated for (anti)protons based on recant ALICE studies [106]. In reverence [106], the measured TPC-TOF matching efficiency ($r_{\text{TRD-mat}}$) for a clean proton sample originating from Λ decays is compared to GEANT3 and GEANT4

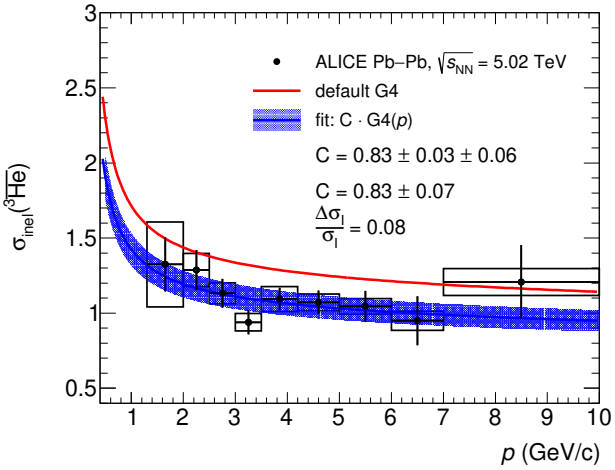

Figure 3.35: Inelastic antihelium cross section measured by ALICE and compared to predictions from default GEANT4. When GEANT4 is scaled by $C = 0.83$ a good description of the data is found as indicted with the blue band.

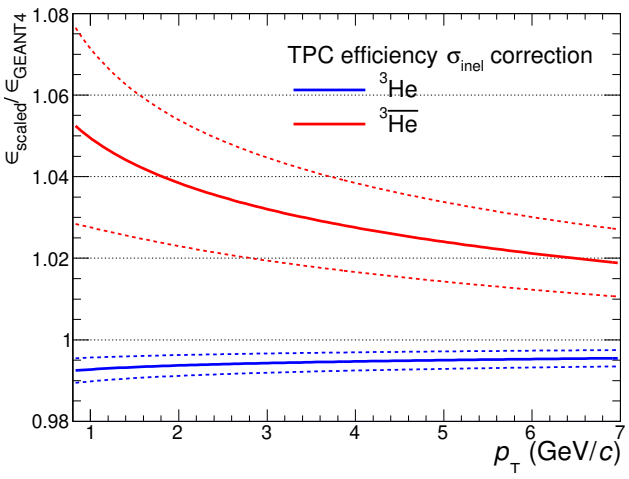

Figure 3.36: Correction factors to the default GEANT4 TPC efficiencies of helium (blue) and antihelium (red) due to the mismatch of the inelastic hadronic interaction cross section in data and Monte Carlo. The dashed lines indicate the uncertainty band on the correction factors.

Monte Carlo simulations. The result can be seen in figure 3.37. Under the assumption of a properly described inelastic cross section in GEANT4 (which is valid protons; see section 3.5.1), the data to Monte Carlo ratio in the lower panel gives a good estimate of the unknown TRD material budget contribution to the efficiency. However, the measurement is performed in bins of the momentum at the inner wall of the TPC (p_{TPC}), while the spectra in this work are measured in p_{T} bins. Therefore, an unfolding from $r_{\text{TRD-mat}}(p_{\mathrm{TPC}})$ to $r_{\text{TRD-mat}}(p_{\mathrm{T}})$ is applied to the ratio. The p_{TPC}-p_{T} correlation matrix ($M(p_{\mathrm{TPC}}, p_{\mathrm{T}})$) is obtained from a Monte Carlo sample and it is shown in figure 3.38. The unfolding is done with a matrix multiplication following:

$$r_{\text{TRD-mat}}(p_{\mathrm{T}}) = M(p_{\mathrm{TPC}}, p_{\mathrm{T}}) \cdot r_{\text{TRD-mat}}(p_{\mathrm{TPC}}) \tag{3.17}$$

The unfolded data to GEANT4 ratio is then applied as a correction factor to the (anti)particle reconstruction efficiency if the TOF detector is required. The result obtained using the GEANT3 transport code is used to estimate the method's systematic uncertainty. The full difference between GEANT4 and GEANT3 is taken as systematic uncertainty.

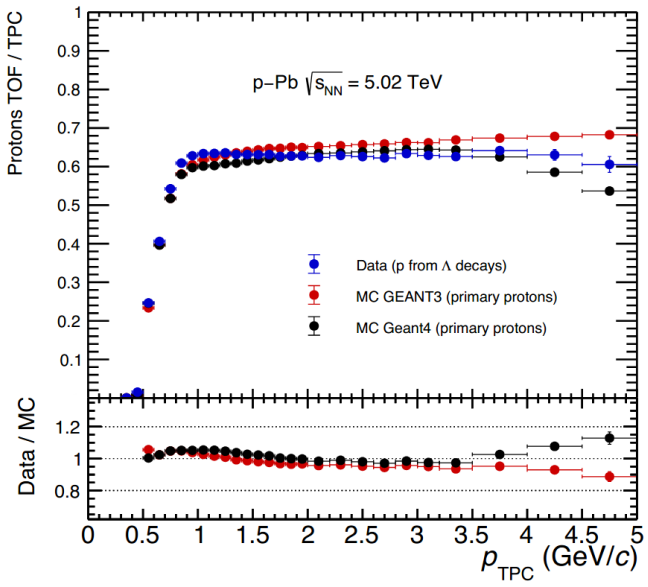

Figure 3.37: Effect of the TRD material budget obtained from the matching efficiency between TPC and TOF in data and Monte Carlo (GEANT3 and GEANT4) as a function of the momentum at the inner wall of the TPC (p_{TPC}).

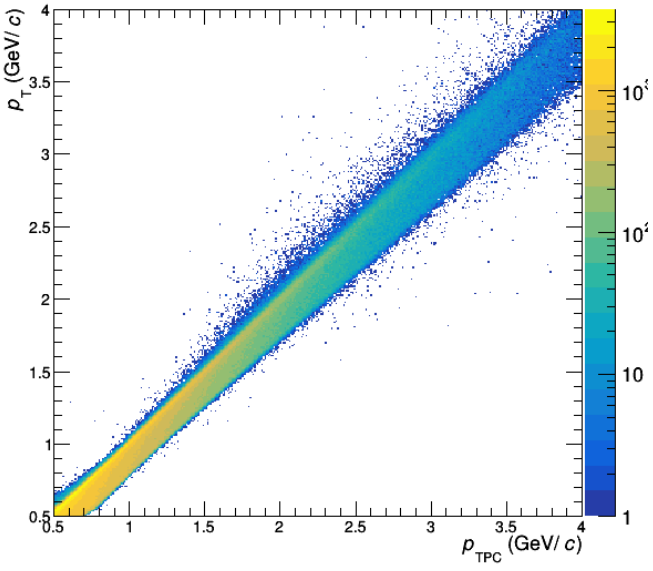

Figure 3.38: Correlation between p_{TPC} and p_{T} form Monte Carlo simulations. This matrix is used for an unfolding procedure on the TRD material budget correction.

3.6 Systematic uncertainties

All known sources of systematic uncertainty for the different particle species were studied. These are track selection criteria, particle identification, secondary-particle contamination, hadronic interaction cross section, detector material budget, ITS-TPC matching, and ${}^{3}_{\Lambda}\mathrm{H}$ feed down for the ${}^{3}\mathrm{He}$ analysis. Additionally, for the MB V0M: 0-100% and 10-100% event class a normalization uncertainty of 3% is considered coming from the trigger efficiency. All other systematic uncertainties are only weakly dependent on the multiplicity class and are, therefore, only calculated in the integrated MB (V0M: 0-100%) and HM (V0M: 0- 0.1%) multiplicity classes. The single contributions are treated fully as uncorrelated and, hence, the total systematic uncertainty for each species and multiplicity class is calculated as the square root of the quadratic sum of all single contributions, which are listed in table 3.3. To give an even better overview of

Source	$p_{\mathrm{T}} = 1.5$ GeV/c			$p_{\mathrm{T}} = 4$ GeV/c	
	p ($\overline{\mathrm{p}}$)	${}^{3}\mathrm{He}$ (${}^{3}\overline{\mathrm{He}}$)	${}^{3}\mathrm{H}$ (${}^{3}\overline{\mathrm{H}}$)	p ($\overline{\mathrm{p}}$)	${}^{3}\mathrm{He}$ (${}^{3}\overline{\mathrm{He}}$)
Track selection	3%	14% (10%)	14% (10%)	3%	10% (7%)
Signal extraction	<1%	13% (<1%)	<1%	5%	<1%
Material budget	1%	2%	2%	1%	2%
Hadronic interaction	1% (2%)	1% (3%)	9% (6%)	1% (2%)	(1%)
ITS–TPC matching	2%	2%	2%	2%	2%
TPC–TOF matching	3%	-	3%	3%	-
Total	6% (7%)	22% (12%)	20% (17%)	7% (8%)	10%

Table 3.3: Summary of the main contributions to the systematic uncertainties for all particle species under study at $p_{\mathrm{T}} = 1.5$ GeV/c and at $p_{\mathrm{T}} = 4$ GeV/c. Values in parentheses refer to antiparticles. If they are not quoted, the systematic uncertainty is the same for particles and antiparticles.

the systematic uncertainties they depicted for the proton p_{T} spectra estimated in the integrated high-multiplicity triggered event class in figure 3.39 and for antiprotons in figure 3.40. In black the total systematic uncertainty is shown while the individual contributions are color coded. The same is shown in figure 3.41 and 3.42 for (anti-)${}^{3}\mathrm{He}$ and in figure 3.43 and 3.44 for (anti-)${}^{3}\mathrm{H}$ in the integrated minimum bias event class. The figure for the high-multiplicity triggered event class in the case of (anti-)${}^{3}\mathrm{He}$ and (anti-)${}^{3}\mathrm{H}$ are in the appendix in figure B.11 to B.14.

3.6.1 Track selection systematic uncertainty

The systematic uncertainty studies on the track selection are based on the mismatch between the track parameter distributions in data and Monte Carlo. Therefore, the variables are typically varied simultaneously in data and Monte Carlo within a range in which both distributions match reasonably well. In figure 3.45 mismatch between data and Monte Carlo of $n_{\mathrm{ITS}}^{\mathrm{clus}}$, χ^2_{ITS}, and χ^2_{TPC} is shown for charged particles in p-Pb collisions. The difference will cause the corrected p_{T} spectra to change when varying the selection criteria. Most of the track selection criteria (see table 3.2) are strongly correlated with each other, e.g. if a track has more clusters in the TPC typically the number of crossed rows and the number of clusters used for PID increases. This

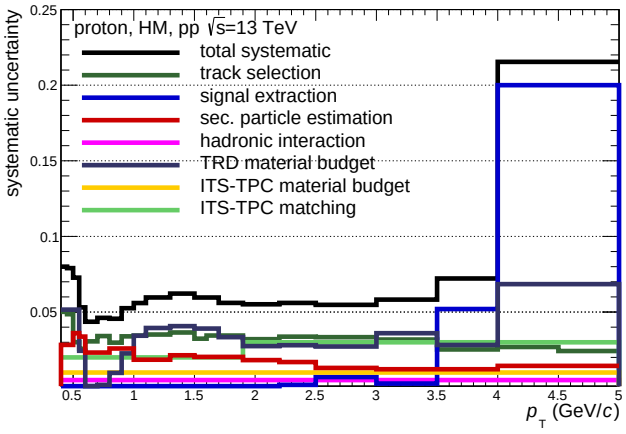

Figure 3.39: Total systematic uncertainty with the individual contributions of the proton p_T spectra in the HM event class.

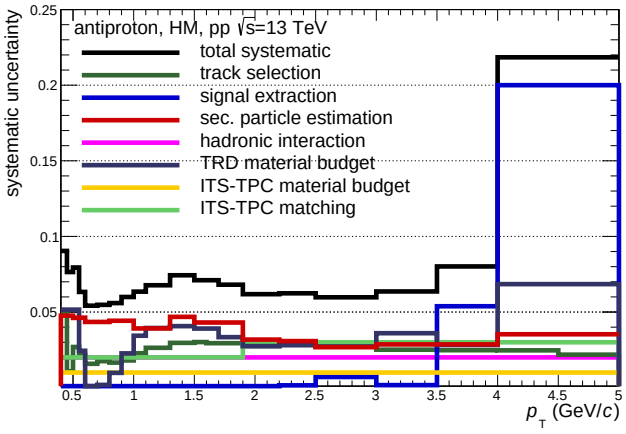

Figure 3.40: Total systematic uncertainty with the individual contributions of the antiproton p_T spectra in the HM event class.

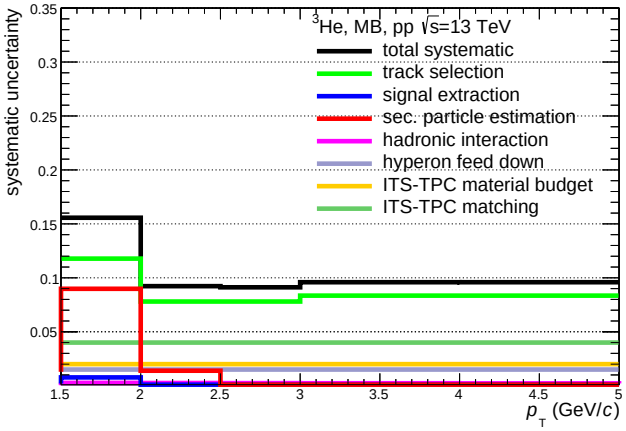

Figure 3.41: Total systematic uncertainty with the individual contributions of the ^{3}He p_T spectra in the MB event class.

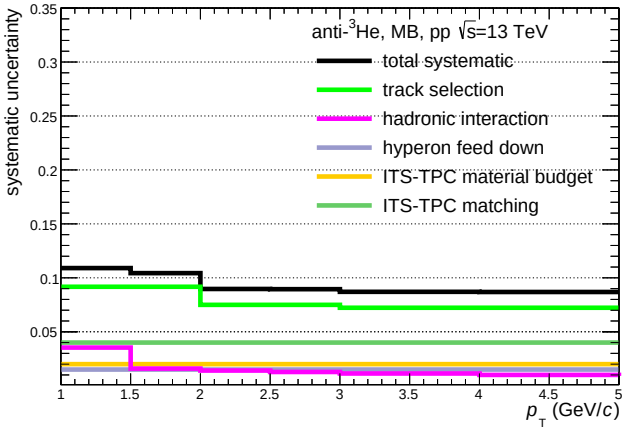

Figure 3.42: Total systematic uncertainty with the individual contributions of the anti-^{3}He p_T spectra in the MB event class.

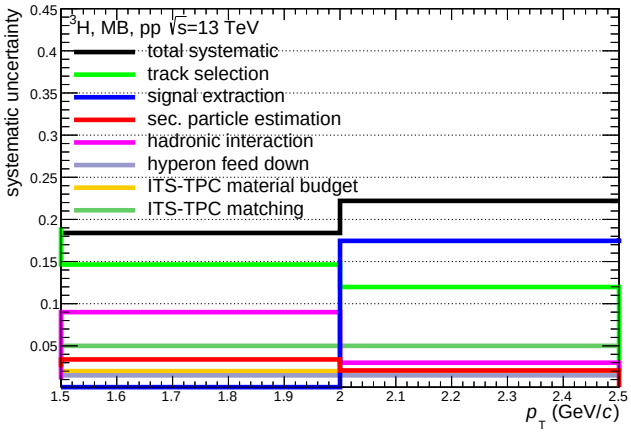

Figure 3.43: Total systematic uncertainty with the individual contributions of the ^{3}H p_T spectra in the MB event class.

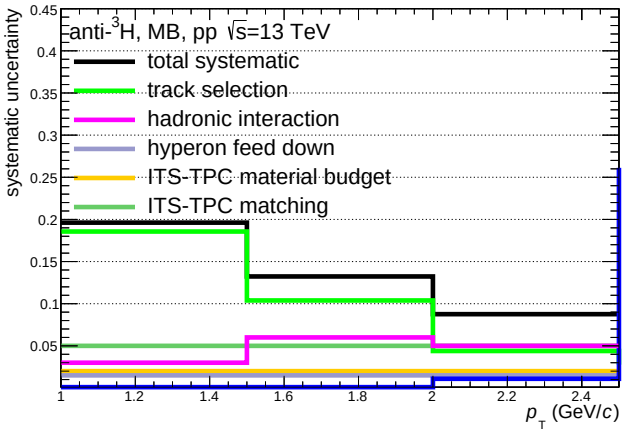

Figure 3.44: Total systematic uncertainty with the individual contributions of the anti-^{3}H p_T spectra in the MB event class.

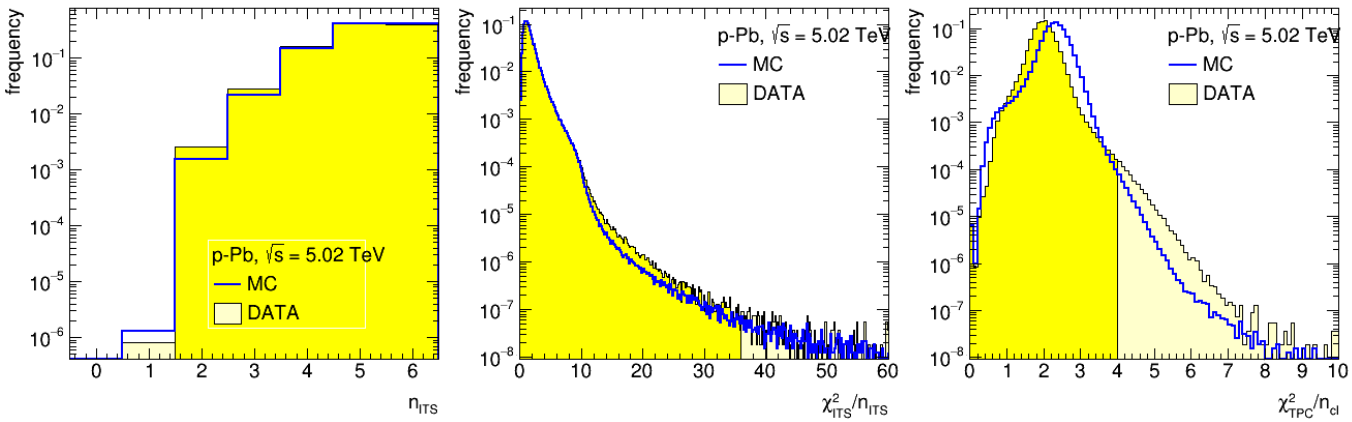

Figure 3.45: Self normalized track variable distribution of number of ITS clusters, χ^2 per number of ITS clusters, and χ^2 per number of TPC clusters in data and Monte Carlo for p-Pb at $\sqrt{s_{\mathrm{NN}}} = 5.02$ TeV and without applying any particle identification. The selection window is indicated with the brighter yellow.

correlation is not represented in the projections in figure 3.45. Therefore, the track selection criteria were simultaneously varied. The variation follows a random uniform distribution within the ranges summarized in table 3.4. The limits were chosen to be in a regime where the data and Monte Carlo distribution match reasonably well for the given parameter. The variation was repeated fifty times and fully corrected p_{T} spectra were evaluated. The relative difference to the nominal track selection setting is for each p_{T} bin filled into a distribution. Three of these distributions are shown in figure 3.46 for (anti)protons and 3.47 for helium. The distributions are interpolated with a Gaussian function and the extracted standard deviation is assigned as systematic uncertainty for this specific p_{T} interval. When the RMS of the distribution is used similar results are obtained.

track variable	lower limit	upper limit
$n_{\mathrm{clu}}^{\mathrm{TPC}}$	60	80
$n_{\mathrm{clu}}^{\mathrm{TPC}}$ for PID	40	70
$n_{\mathrm{row}}/n_{\mathrm{findable}}$	0.5	0.8
χ^2_{TPC}	3	5
$n_{\mathrm{clu}}^{\mathrm{ITS}}$	1	3
hit in SPD	none	any
DCA_{xy} (^{3}He,^{3}H)	0.1 cm	0.2 cm
DCA_{z} (^{3}He,^{3}H)	0.1 cm	0.2 cm
DCA_{xy} (p)	2.5σ	3.5σ
η	0.7	0.9

Table 3.4: Variation ranges of the track selection criteria to study systematic uncertainties.

This method was repeated for the proton, ^{3}He, and ^{3}H once for particle and once for antiparticle. Additionally, it was performed for the integrated MB multiplicity class and the integrated HM multiplicity class, assuming only a small multiplicity dependence within one specific trigger type.

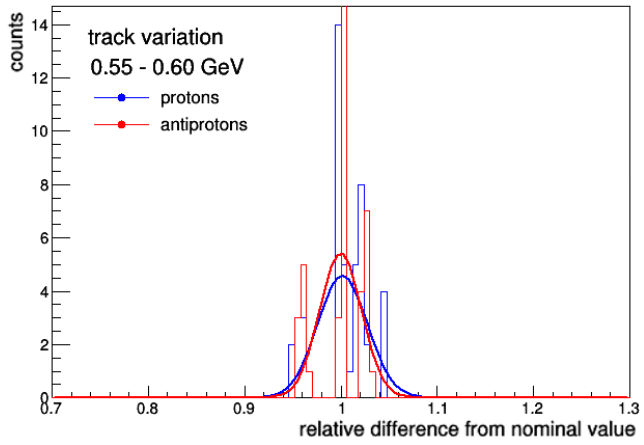

Figure 3.46: The track selection criteria were varied fifty times and the resulting differences from the nominal value are filled into the distributions in the $0.55 < p_{\mathrm{T}} < 0.6$ GeV/c range. The distributions are interpolated with a Gaussian and the width is taken as track selection systematic uncertainty.

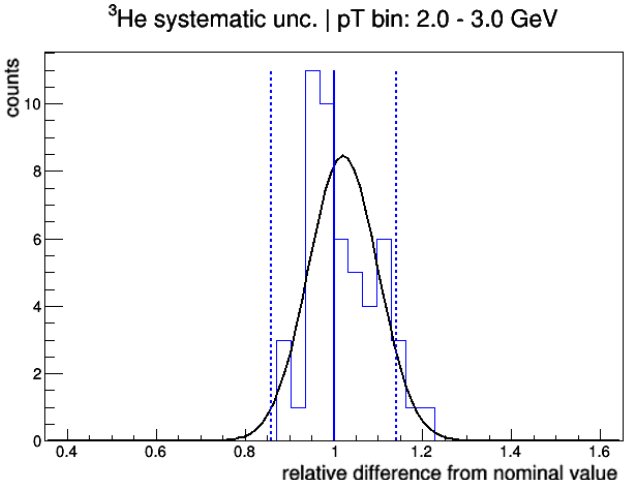

Figure 3.47: The track selection criteria for ^{3}He were varied fifty times and the resulting differences from the nominal value are filled into the distribution in the $2 < p_{\mathrm{T}} < 3$ GeV/c range and the integrated MB data sample. The distribution is interpolated with a Gaussian and the width is taken as track selection systematic uncertainty. The dashed lines show the statistical uncertainty in the corresponding p_{T} bin.

However, the simultaneous variation of track selection variables is not a flawless method to estimate systematic uncertainties on the track selection since it assumes full correlation of the track variables. In the future, an estimation method could be developed which instead of fully uncorrelated or fully correlated track selection variables takes partially correlated variables into account. The presented extreme cases assuming full correlation, however, give a conservative estimate of the systematic uncertainty and can, therefore, safely be used.

3.6.2 Particle identification systematic uncertainty

The particle identification method for proton, helium, and triton was discussed in section 3.3. Because the particle identification method changed for the proton analysis in comparison to the helium and triton analysis, the corresponding systematic uncertainties have to be evaluated separately and are, therefore, individually discussed in the next two subsections.

Proton identification systematic uncertainty

The systematic uncertainty due to the proton identification is directly linked to the sensitivity to the background contribution below the signal peak extracted in section 3.3, with figure 3.6 to 3.8 showing the method. The quality of the background description is probed by repeating the signal extraction in the integrated multiplicity class (V0M: 0-0.1%) with varied ranges for the background interpolation. For the estimation of the systematic uncertainty two cases were studied, shifting the interpolation range along the x-axis to the right or the left, that

is to higher or lower $n\sigma^{\mathrm{p}}_{\mathrm{TOF}}$ values, respectively. For the variation to the left, the fit was performed from -5.3 to 7.8 and for the variation to the right, it was performed from -4.7 to 8.3. The maximum difference from the nominal value in each p_{T} interval was taken as a systematic uncertainty. As expected from figure 3.6 the uncertainty is negligible in the low p_{T} range ($p_{\mathrm{T}} < 2.5$ GeV/c) and starts to rise to up to 5% for p_{T} equals 4 GeV/c. Since a slightly different background estimation was used in the 4 to 5 GeV/c p_{T} range (as described in section 3.3) also the systematic uncertainty was evaluated differently. The background estimation in this p_{T} bin is based on the average of many trails and the spread is taken as a systematic uncertainty. This results in a systematic uncertainty of about 20%.

Helium and triton identification systematic uncertainty

The helium and triton identification followed the same pattern so the corresponding systematic uncertainty on the particle identification was estimated using the same procedure. First, the effect on the PID selection criteria was investigated by choosing a tighter ($n\sigma^{^3\mathrm{He},^3\mathrm{H}}_{\mathrm{TPC}} > -2$) and looser ($n\sigma^{^3\mathrm{He},^3\mathrm{H}}_{\mathrm{TPC}} > -3$) selection of the possible candidates. The systematic uncertainty due to this variation is negligible with respect to the statistical fluctuations in the candidate signal, hence this contribution is dropped. The second source of systematic uncertainty studied is the shape of the background contaminating the signal. As discussed in section 3.3 and shown in figure 3.13 for helium and in figure 3.16 for triton candidates two cases were studied, that are a Gaussian and an exponential background shape. In figure 3.14 the momentum dependent correction factor for ^{3}He is shown for the two cases and the full difference is taken as a p_{T} dependent systematic uncertainty. This results in a systematic uncertainty of up to 20% for ^{3}He while the uncertainty is less than 1% for anti-^{3}He and (anti-)^{3}H.

3.6.3 Secondary-particle contamination systematic uncertainty

One of the main corrections to the final p_{T} spectra is the secondary-particle contamination. As discussed in section 3.4, the estimation method differs between the proton, helium, and triton analyses. Therefore, the systematic uncertainty related to the correction is evaluated with two different approaches discussed in the following subsection.

Proton contamination systematic uncertainty

The secondary-particle contamination for protons was estimated via template fits to the measured DCA$_{xy}$ distribution. As shown in figure 3.18 and 3.19 the used minimizer for the interpolation is sensitive to the DCA$_{xy}$ bin granularity. This is especially true for the region close to the primary proton peak. Therefore, variable bin edges were used with finer bins around zero and increasing bins size with increasing distance from zero. Additionally, the secondary contamination was evaluated four times with a different number of DCA$_{xy}$ bins, using 25, 31, 45, and 64 DCA$_{xy}$ bins in the $|\mathrm{DCA}_{xy}| < 1$ cm range. The correction is evaluated from the average of these variations and the assigned systematic uncertainty is given by the root mean square. The secondary contamination estimation for antiprotons only needs two input templates instead of the three used for the proton case. This improves the fit stability but the estimate does rely more

on the properly described DCA_{xy} shape in Monte Carlo. The systematic uncertainty for protons results in 2 to 4% and for antiprotons in 3 to 5% which indicates that the DCA_{xy} shape in MC does not perfectly match the shape in the measurement.

Helium and triton contamination systematic uncertainty

The estimate of the secondary-particle contamination from spallation processes for ^{3}He and for ^{3}H are described in section 3.4. The contamination was evaluated by interpolating the DCA distributions with different functions. The DCA_{xy}-DCA_z projection as well as the DCA_{xy} projection were interpolated with three functions listed in equation 3.7 to 3.9 (with $\mathrm{DCA}_z = 0$ in the one-dimensional case). The resulting six contamination estimates shown in figure 3.23 for ^{3}He and in figure 3.25 for ^{3}H are consistent with each other. Therefore, the two-dimensional Gaussian background shape result was used as correction and the root mean square of all results was assigned as a systematic uncertainty. This method was applied independently for the integrated minimum bias event class and the integrated high-multiplicity event class. The resulting systematic uncertainty amounts to maximal 20% for the low p_T range ($1.5 < p_\mathrm{T} < 1.75$ GeV/c) for the high-multiplicity triggered ^{3}He spectra and is in all cases negligible for p_T larger 2 GeV/c.
Since spallation processes in the detector material do not produce antimatter, no correction and hence no systematic uncertainty was applied for the antinuclei spectra.

Hypertriton feed down systematic uncertainty

As discussed in section 3.4 feed down from ${}^3_\Lambda\mathrm{H} \rightarrow {}^3\mathrm{H} + \pi^-$ (and charge conjugate) contaminates the (anti-)^{3}He spectra, and the ${}^3_\Lambda\mathrm{H} \rightarrow {}^3\mathrm{H} + \pi^0$ (and charge conjugate) contaminates the (anti-)^{3}H spectra. However, this contribution is expected to be negligible (based on the three arguments laid out in section 3.4) and, therefore, not corrected. Nevertheless, a systematic uncertainty due to the ${}^3_\Lambda$H feed down is estimated.
The estimate is based on the work in reference [64], where the ${}^3_\Lambda$H contamination and its uncertainty are estimated for p-Pb collisions at $\sqrt{s_\mathrm{NN}} = 5.02$ TeV. This study is based on the extrapolation of the (anti-)${}^3_\Lambda$H to (anti-)^{3}He ratio measured in Pb-Pb collisions at $\sqrt{s_\mathrm{NN}} = 2.76$ TeV [78] and results in a correction of 3.7% for ^{3}He and 1.9% for ^{3}H. The corresponding systematic uncertainty was estimated by shifting the data points used for the extrapolation up and down and before repeating the fit, which gave a relative uncertainty of 1.5% for ^{3}He and 0.75% for ^{3}H. These uncertainties are inherited here and serve as an estimate for the contamination systematic uncertainty.
In the future, this correction and its systematic uncertainty can be improved using precision measurements of the (anti-)${}^3_\Lambda$H to (anti-)^{3}He ratio in pp collisions.

3.6.4 Systematic uncertainty on the efficiency

In previous measurements of (anti)protons [147] and/or (anti)^{3}He [64] a systematic uncertainty due to the efficiency correction was estimated by comparing the predictions of different transport codes, typically GEANT3, GEANT4, or FLUKA [148]. Due to the quite different implementations of hadronic interaction cross sections in these transport codes, the resulting un-

certainties are relatively large (in the order of 4% for protons). In this analysis, a data-based correction method is applied to the hadronic inelastic interaction cross section implemented in GEANT4, which makes the previous method of comparing different transport codes obsolete while simultaneously improving the precision of the measurement.

The method, as well as the estimate for the systematic uncertainty, are explained in detail in section 3.5.1. For protons the systematic uncertainty is negligible, for antiprotons it is 0.5%, for ^{3}He it is negligible, and for anti-^{3}He it is less than 2%.

The measurement of the inelastic hadronic interaction cross section for anti-^{3}He on which the correction and the systemic uncertainty estimates are based on starts at a momentum of 1.5 GeV/c. The measurement presented in this work, however, starts at a p_{T} of 1 GeV/c. Therefore, an additional systematic uncertainty is considered accounting for the unknown momentum shape of the cross section at low momentum. It is estimated by the comparison of the interpolated GEANT3 and GEANT4 predictions to data in the low momentum region, as shown in figure 3.48. The maximum difference between the two predictions is propagated to the uncertainty on the efficiency using equation 3.14:

$$\begin{aligned}\frac{\Delta\epsilon}{\epsilon} &= \frac{e^{-\frac{\Delta x}{\lambda_{\mathrm{G4}}}} - e^{-\frac{\Delta x}{\lambda_{\mathrm{G3}}}}}{e^{-\frac{\Delta x}{\lambda_{\mathrm{G4}}}}} = \frac{e^{-\frac{\Delta x \rho N_A \sigma_{\mathrm{G4}}}{M}} - e^{-\frac{\Delta x \rho N_A \sigma_{\mathrm{G3}}}{M}}}{e^{-\frac{\Delta x \rho N_A \sigma_{\mathrm{G4}}}{M}}} = 1 - \exp\left(-\frac{\Delta x \rho N_A}{M}(\sigma_{\mathrm{G3}} - \sigma_{\mathrm{G4}})\right) \\ &= 1 - \exp\left(-\frac{\Delta x}{\lambda_{\mathrm{G4}}}\left(\frac{\sigma_{\mathrm{G3}} - \sigma_{\mathrm{G4}}}{\sigma_{\mathrm{G4}}}\right)\right)\end{aligned} \tag{3.18}$$

The factor $\frac{\Delta x}{\lambda_{\mathrm{G4}}}$ is taken form the GEANT4 simulation and it is about 0.3 for anti-^{3}He in case of a TPC only analysis. The final systematic uncertainty is shown in figure 3.49 for two cases. The first one is in the case of using only the TPC for the identification as applied in the presented analysis and the second one for using both TPC and TOF detectors for the identification. The second case is not used in the further analysis and is only added for completeness. In the TPC only case the uncertainty amounts to about 3% at $p = 900$ MeV/c. In the momentum regions without a σ_{inel} measurement this uncertainty is added in quadrature as an additional contribution to the already estimated uncertainties.

Unfortunately, the anti-^{3}H nucleus inelastic cross section is not measured and, therefore, it was not possible to apply the data-driven correction. So the uncertainty was estimated using the old method of comparing GEANT3 and GEANT4 transport codes. This results in a maximum systematic uncertainty of 10% for ^{3}H and 8% for anti-^{3}H.

3.6.5 ITS-TPC matching systematic uncertainty

The ITS-TPC matching efficiency is defined as the ratio of the number of tracks with clusters in ITS and TPC to the number of tracks with clusters only in the TPC. This ratio is not perfectly reproduced in Monte Carlo which leads to a systematic uncertainty on the tracking efficiency. The uncertainty can be estimated by comparing the ITS-TPC matching efficiencies in data and Monte Carlo, given as

$$\Delta\epsilon_{\text{ITS-TPC,match}} = \frac{\epsilon^{\text{Data}}_{\text{ITS-TPC,match}} - \epsilon^{\text{MC}}_{\text{ITS-TPC,match}}}{\epsilon^{\text{Data}}_{\text{ITS-TPC,match}}} \tag{3.19}$$

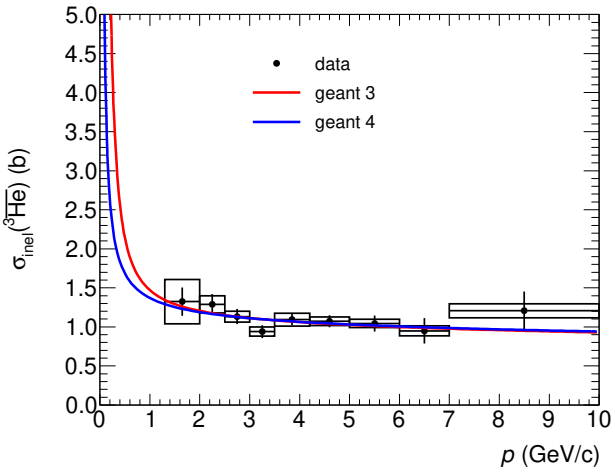

Figure 3.48: Prediction form GEANT3 and GEANT4 for the low momentum region for the hadronic interaction cross section. The high momentum region is scaled in both cases to fit the measurement.

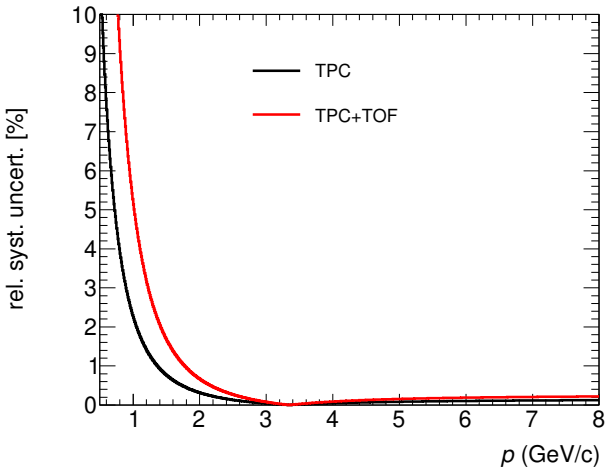

Figure 3.49: Relative systematic uncertainty on the anti-^{3}He spectra due to the assumed shape of the inelastic cross section at low momentum.

Since this uncertainty is independent of the physics analysis it is evaluated centrally by the ALICE data preparation group for each data-taking period. It varies between 3 and 4% for all data periods used in the presented work. A conservative approach is applied and a p_{T}-independent systematic uncertainty of 4% is assigned for all identified particle analyses.

3.6.6 Material budget systematic uncertainty

The material budget of ALICE is known only to a certain degree, which results in a systematic uncertainty on the tracking efficiency (see equation 3.16). The material budget systematic uncertainty of two parts of the ALICE detector is studied in two steps. First, only the systematic uncertainty allocated to the material up to the middle of the TPC is investigated, and second, the material allocated from the outer edge of the TPC to the TOF detector is addressed.

The material budget to the middle of the TPC is 10% in terms of radiation length with a relative uncertainty of 4.5% [117]. The corresponding systematic uncertainty of the transverse-momentum spectra is probed by varying the material bugged in dedicated Monte Carlo productions up and down by 4.5%, recalculating the resulting tracking efficiencies, and comparing them to the results using the nominal material setting. The first study performed using this technique was on pp data at $\sqrt{s} = 900$ GeV [149]. Later the effect on all other collision systems at the various center of mass energies was investigated. In all the cases the resulting systematic uncertainty was less than 2%.

The effect caused by the TRD material budget uncertainty on the reconstruction efficiency is discussed in section 3.5.2. A data-driven method was developed and used to reweight Monte Carlo predictions, based on the abortion of protons in the TRD detector. Two cases were examined relying on GEANT3 and GEANT4 simulations. The full difference between the two cases is assigned as systematic uncertainty on the (anti)proton p_{T} spectra, resulting in a with p_{T} increasing systematic uncertainties of 1 to 5%.

4 Results and Discussion

The results presented in this chapter have been published by the ALICE Collaboration in reference [150] and accepted for publication by the Journal of High Energy Physics. The publication is a combined effort in which this thesis contributed with the analysis of the proton, helium, and tritium nucleus. Luca Barioglio from the TU Munich contributed to the publication with the analysis of the deuteron, which uses the proton measurement as an important reference and will therefore also be presented in this chapter. Additionally, the theoretical calculations of the B_2 were performed by Bhawani Singh from TU Munich. The model predictions are compared to the measurements in section 4.3.2 and the equations are summarized in the appendix A.

4.1 Transverse-momentum spectra

The p_{T} spectra of (anti)proton, (anti-)^{3}H, and (anti-)^{3}He are calculated using the extracted raw signal and applying the corrections evaluated in chapter 3:

$$\frac{\mathrm{d}^2N}{\mathrm{d}y\mathrm{d}p_{\mathrm{T}}}(p_{\mathrm{T}}) = \frac{\epsilon^{\mathrm{trig}}}{N_{\mathrm{evt}}\,\Delta y\,\Delta p_{\mathrm{T}}} \cdot \frac{N(p_{\mathrm{T}}) \cdot c_{\mathrm{prim}}(p_{\mathrm{T}})}{\epsilon(p_{\mathrm{T}}) \cdot r_{\mathrm{int}}(p_{\mathrm{T}}) \cdot r_{\mathrm{TRD\text{-}mat}}(p_{\mathrm{T}})} \tag{4.1}$$

$N(p_{\mathrm{T}})$ is the number of signal candidates observed in each p_{T} bin, which is divided by the width of the transverse-momentum bin (Δp_{T}). The number of candidates are corrected for the fraction of primary particles $c_{\mathrm{prim}}(p_{\mathrm{T}})$ and the acceptance times reconstruction efficiency $\epsilon(p_{\mathrm{T}})$. The reconstruction efficiency itself is corrected for the hadronic interaction cross section $r_{\mathrm{int}}(p_{\mathrm{T}})$. In the case of TOF detector usage the TRD material budged correction $r_{\mathrm{TRD\text{-}mat}}(p_{\mathrm{T}})$ is also applied. Finally, the identified-particle p_{T} spectra are divided by the rapidity interval Δy and the total number of events N_{evt}, which are corrected for the trigger efficiency ϵ^{trig} in the corresponding multiplicity class. The transverse-momentum ranges covered by the measurements are summarized in table 4.1.

	Trigger class	p_{T} range
p ($\overline{\mathrm{p}}$)	HM	0.6 - 5.0 GeV/c
^{3}He ($^3\overline{\mathrm{He}}$)	MB	1.5 (1.0) - 5.0 GeV/c
	HM	1.5 (1.0) - 6.0 GeV/c
^{3}H ($^3\overline{\mathrm{H}}$)	MB & HM	1.5 (1.0) - 2.5 GeV/c

Table 4.1: Transverse-momentum ranges for all particle species. For ^{3}He and for ^{3}H the measurement starts at higher p_{T}, because of the dominant contribution from spallation which can not be corrected at the lowest p_{T}.

At LHC center-of-mass energies it is expected that equal amounts of matter and antimatter are produced. This expectation was confirmed in many measurements at the LHC for example in references [61, 60]. The antiparticle-to-particle yield ratio for the integrated high-multiplicity triggered event class is shown in the lower panel of figure 4.1 for protons on the left, for helium nuclei in the middle, and for triton on the right. For ^{3}He and ^{3}H antiparticle-to-particle ratios

fluctuate statistically around unity, while for protons the ratio agrees well with unity within uncertainties. Therefore, the particle and antiparticle spectra are presented according to $\mathrm{p} + \overline{\mathrm{p}}$, $\frac{^3\mathrm{He}+^3\overline{\mathrm{He}}}{2}$, and $\frac{^3\mathrm{H}+^3\overline{\mathrm{H}}}{2}$. However, for ^{3}He and ^{3}H in the $p_\mathrm{T} < 1.5$ GeV/c region only the antiparticle measurement is available.

The upper panel of figure 4.1 shows the particle and antiparticle p_T spectra with their assigned systematic uncertainties (shown as open boxes) and statistical uncertainties (shown as error bars) in the integrated high-multiplicity triggered event class, for protons on the left, helium nuclei in the middle, and triton on the right. Figure 4.2 shows the multiplicity differential measurements of the averaged p_T spectra with their assigned systematic uncertainties (shown as open boxes) and statistical uncertainties (shown as error bars) for protons, deuteron, helium nuclei, and triton. The proton, deuteron, and ^{3}He p_T spectra show a similar trend. The proton spectra have a maximum at around 0.8 GeV/c, the deuteron spectra have a maximum at around 1 GeV/c, and the helium spectra have their maximum at approximately 1.5 GeV/c. All three species fall off exponentially after the maximum. For the ^{3}H spectra no clear trend can be identified due to the limited p_T interval of the measurement.

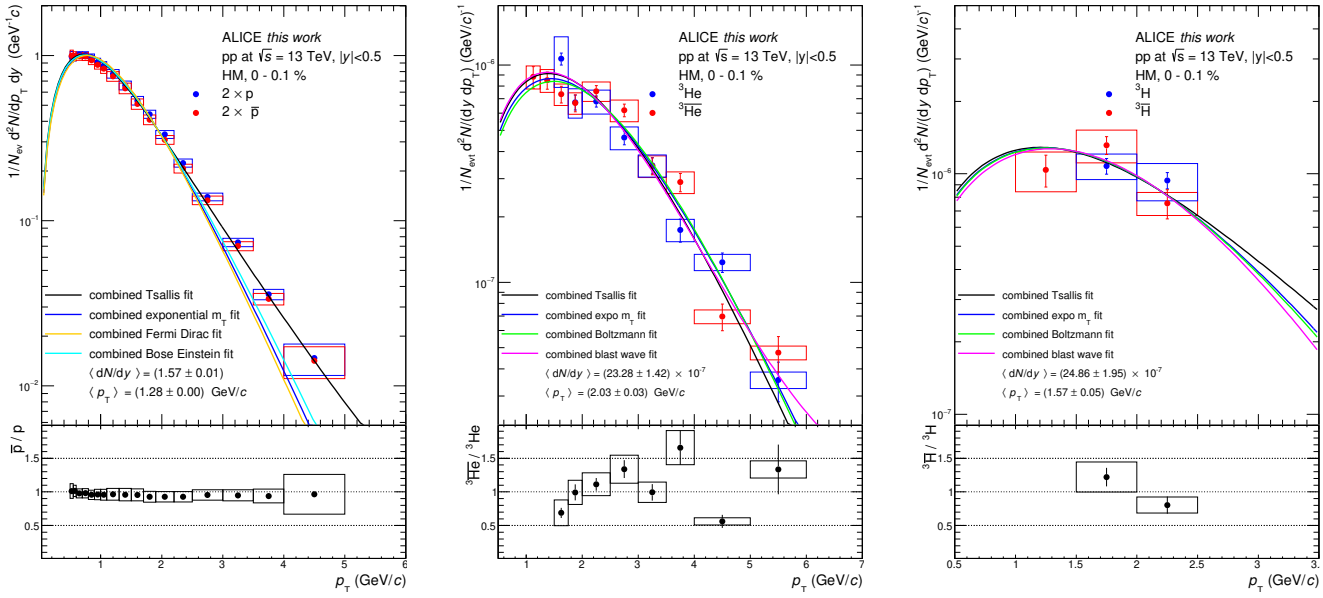

Figure 4.1: Proton (left), helium (middle), and triton (right) spectra for the integrated high-multiplicity triggered class (V0M: 0-0.1%) for particle in blue and antiparticle in red. The particle-to-antiparticle ratio is displayed in the lower panel. Systematic uncertainties are shown as open boxes and statistical uncertainties as error bars. Four different extrapolations are applied simultaneously particle + antiparticle p_T spectra.

Figure 4.2 also shows a Levy-Tsallis extrapolation. The deuteron spectra are added for completeness because they are published with the other presented results in reference [150] and the proton spectra serve as important references for the interpretation of the deuteron measurement. In figure 4.2 the proton and deuteron spectra which are measured in high-multiplicity triggered events (colored: Grey, red, orange, and yellow) complement the already published minimum bias results of protons in reference [147] and deuteron in reference [65]. The proton and deuteron spectra are scaled by a constant for better visibility. In the ^{3}He spectra, a harden-

ing with increasing multiplicity is visible, which can be better quantified when looking into the mean p_{T} as discussed in section 4.1.2.

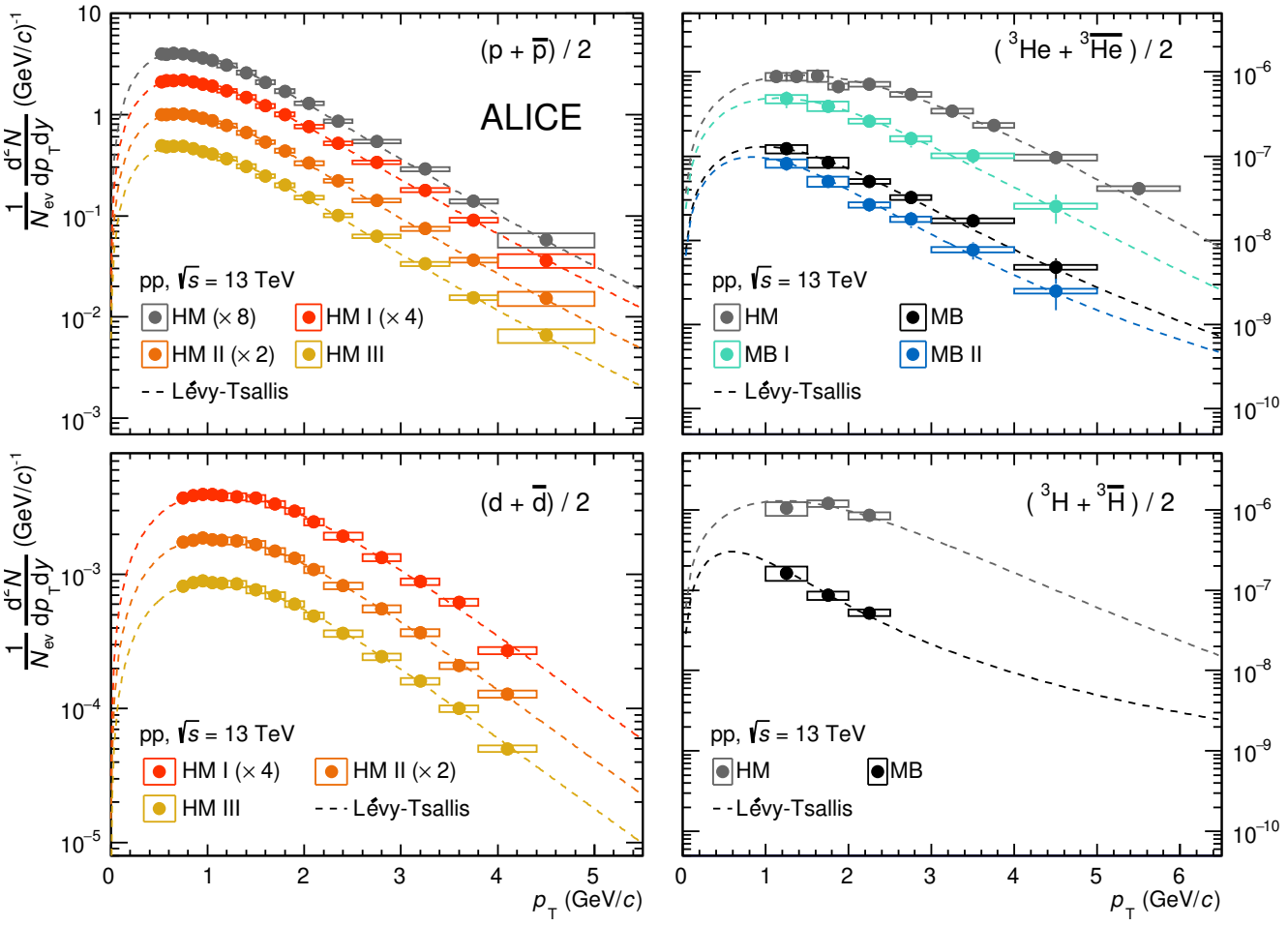

Figure 4.2: All measured identified nuclei p_{T} spectra in fine multiplicity intervals. Particle and antiparticle yields are averaged. For completeness, the deuteron spectra are added. The proton and deuteron spectra, which are measured in high-multiplicity (HM) triggered events, are scaled by a constant for better visibility. The V0M multiplicity classes are: MB 0-100%, MB I 0-10%, MB II 10-90%, HM 0-0.1%, HM I 0-0.01%, HM II 0.01-0.05%, and HM III 0.05-0.1%.

4.1.1 Spectra extrapolation

One of the key observables to extract from the identified particle p_{T} spectra are the total (p_{T}-integrated) yields and the mean p_{T}. Due to the transverse-momentum limitation of the measurements they can not be extracted immediately. Extrapolations down to zero p_{T} and high p_{T} are needed. For the parametrization of the p_{T} spectra, a wide range of different functions is available which have been developed over the last decades. The most common functions used are the Levy-Tsallis, blast-wave, m_{T} exponential, Boltzmann, and Bose-Einstein.

Levy-Tsallis parametrization is very commonly used and well established to describe the p_{T} spectrum created in a small collision system. The function has the following form [57]:

$$\frac{\mathrm{d}^2N}{\mathrm{d}p_{\mathrm{T}}dy} = \frac{\mathrm{d}N}{\mathrm{d}y} \cdot \frac{1}{p_{\mathrm{T}}} \cdot \frac{(n-1)(n-2)}{nC(nC+m_0(n-2))} \cdot \left(1 + \frac{m_{\mathrm{T}} - m_0}{nC}\right)^{-n} \tag{4.2}$$

where $m_{\mathrm{T}} = \sqrt{p_{\mathrm{T}}^2 + m_0^2}$ is the transverse mass, with m_0 being the rest mass. n, C, and $\frac{\mathrm{d}N}{\mathrm{d}y}$ are free fit parameters.

The blast-wave parametrization [57] is based on the assumption that particles are released from a local equilibrium with a common kinetic freeze-out temperature T_{kin} and common transverse velocity β_S. In small collision systems, like pp, this assumption does not necessarily hold. However, the interpolation nevertheless results in values for T_{kin} and β_S which evolve smoothly with multiplicity going from large to small collision systems. In reference [147], it was shown for a simultaneous blast-wave fit of multiple light-flavor particle spectra. Therefore, the blast-wave parametrization is considered as one of the options to extrapolate the p_{T} spectra in this work:

$$\frac{\mathrm{d}^2N}{\mathrm{d}p_{\mathrm{T}}\mathrm{d}y} \propto \int_0^R r\mathrm{d}r m_{\mathrm{T}} \cdot I_0\left(\frac{p_{\mathrm{T}}\sinh\rho}{T_{\mathrm{kin}}}\right) \cdot K_1\left(\frac{m_{\mathrm{T}}\cosh\rho}{T_{\mathrm{kin}}}\right) \tag{4.3}$$

The velocity profile ρ is given as:

$$\rho = \tanh^{-1}\beta = \tanh^{-1}\left(\beta_S\left(\frac{r}{R}\right)^n\right) \tag{4.4}$$

K_1 and I_0 are the modified Bessel functions, r the radial coordinate in the transverse plane, R the radius of the fireball, $\beta(r)$ the transverse velocity, and n the exponent of the velocity profile. The free fit parameters are a normalization parameter, T_{kin}, β_S, and n.

The third parametrization, also assumes the hadrons spectra to be produced in a common source at a given temperature. It is based on an exponential shape of the spectra:

$$\frac{\mathrm{d}^2N}{\mathrm{d}p_{\mathrm{T}}\mathrm{d}y} \propto p_{\mathrm{T}}\exp(-m_{\mathrm{T}}/T) \tag{4.5}$$

T is the inverse slope parameter and m_{T} is the transverse mass. Hence, this parameterization is referred to as exponential m_{T}. The free parameters are T and a normalization parameter.

A slightly modified version is the Boltzmann parametrization which factors in the transverse mass but otherwise follows the exponential m_{T}:

$$\frac{\mathrm{d}^2N}{\mathrm{d}p_{\mathrm{T}}\mathrm{d}y} \propto p_{\mathrm{T}}m_{\mathrm{T}}\exp(-m_{\mathrm{T}}/T) \tag{4.6}$$

The final function used to extrapolate the p_{T} spectra is the Bose-Einstein parametrization:

$$\frac{\mathrm{d}^2N}{\mathrm{d}p_{\mathrm{T}}\mathrm{d}y} \propto \frac{1}{\exp(m_{\mathrm{T}}/T)-1} \tag{4.7}$$

with m_{T} being the transverse mass. A normalization and the inverse slope parameter T are the model's free parameters. The Bose-Einstein parametrization, however, was only used to

extrapolate the proton spectra for a comparison to the proton measurement in minimum-bias collisions.

The models are used to extrapolate the measured p_{T} spectra in all multiplicity classes. Therefore, the measured particle and antiparticle spectra are averaged and a simultaneous fit is applied. Unfortunately, the triton spectra are very limited in their p_{T} range. To guarantee a stable fit, the free parameter, except for the normalization, were constrained with boundary conditions obtained from the fits performed to the helium spectra in the same multiplicity intervals. The triton fit parameters are allowed to be within a 5σ interval of the corresponding parameter from the helium fits. Figure 4.1 shows the extrapolations for the integrated high-multiplicity triggered event class for protons (left), helium (middle), and triton (right). The other multiplicity bins are shown in the appendix, figure B.15, B.16, and B.17 for protons, helium, and triton, respectively. All models describe the transverse-momentum spectra reasonably well and tend to agree with each other.

4.1.2 Integrated yield and mean transverse momentum

To extract the integrated yield of the nuclei, the models listed in equations 4.2, 4.3, 4.5, 4.6, and 4.7 are used to extrapolate the corresponding p_{T} spectra down to zero p_{T}. Additionally, the spectra are extrapolated to a maximum of 10 GeV/c after which the contribution to the total yield is less than one per mill due to the exponential shape of the p_{T} spectra. In the p_{T} region where the measurements are available, they were used to extract the integrated yield.

The statistical uncertainties of the spectra are propagated as fully uncorrelated uncertainties. The data points are distributed around their central yield value using a Gaussian distribution with the corresponding statistical uncertainty as standard deviation. The Gaussian sampling procedure is repeated a thousand times. The standard deviation of the resulting distribution containing the integrated yield and mean p_{T} of the smeared sample are assigned as statistical uncertainties for these quantities. For the propagation of the systematic uncertainty, a full correlation between the uncertainties in different p_{T} bins is assumed. The assumption of fully correlated uncertainties resembles an upper limit on the systematic uncertainty for the integrated yield. However, for the mean p_{T} the systematic uncertainty due to the interpolation might be underestimated. The systematic uncertainties are estimated by shifting the distribution up and down within by the systematic uncertainties and then reperforming the fit. The maximum deviation on the yield and the mean p_{T} are assigned as systematic uncertainties. This method is applied to all extrapolation models and the resulting yields and mean p_{T} values are shown as an example for (anti-)^{3}He in figure 4.3 and figure 4.4, respectively.

The average yield and the average mean p_{T} obtained from the different fit functions are taken as the final results with their root-mean-square added in quadrature as an additional systematic uncertainty. The relative systematic uncertainty from the fit function variation amounts up to 14% for the MB triton yield and it is the smallest for all the proton yields with around values 3%. The fraction of the yield which is obtained via the extrapolation also varies strongly for the different species and is 47% for the MB and 38% for the HM triton measurements, around 30% for the MB and 20% for the HM helium measurements, and 17% for the proton measurements. The integrated yields with their statistical and systematic uncertainties are summarized for all particle species and all measured multiplicity classes in table 4.2. Additionally, the extracted mean p_{T} for all measured particle species and multiplicity classes is listed in table 4.3.

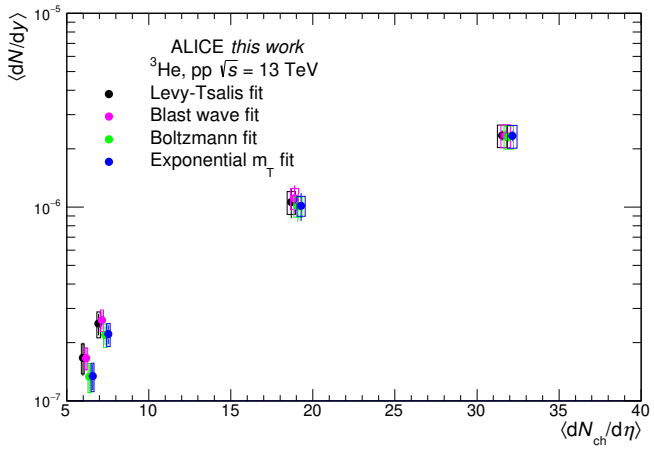

Figure 4.3: Integrated yield of (anti-)^{3}He nuclei obtained with the different models for extrapolation. The data points are sightly shifted along the x-axis for better visibility.

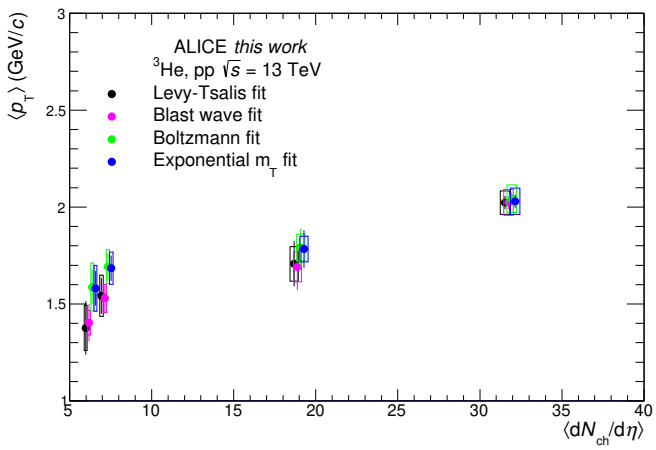

Figure 4.4: Mean p_T of (anti-)^{3}He nuclei obtained with the different models for extrapolation. The data points are sightly shifted along the x-axis for better visibility.

Multiplicity	$\langle dN_{ch}/d\eta \rangle$	dN/dy p	dN/dy ^{3}He	dN/dy ^{3}H
HM	31.5 ± 0.3	0.80 ± 0.01 ± 0.05	(23.3 ± 1 ± 3) ×10^{-7}	(25 ± 2 ± 4) ×10^{-7}
HM I	35.8 ± 0.5	0.91 ± 0.01 ± 0.05		
HM II	32.2 ± 0.4	0.83 ± 0.01 ± 0.05		
HM III	30.1 ± 0.4	0.77 ± 0.01 ± 0.04		
MB	6.9 ± 0.1		(2.4 ± 0.3 ± 0.4) ×10^{-7}	(1.7 ± 0.3 ± 0.4) ×10^{-7}
MB I	18.7 ± 0.3		(11 ± 2 ± 2) ×10^{-7}	
MB II	6.0 ± 0.2		(1.5 ± 0.2 ± 0.3) ×10^{-7}	

Table 4.2: Multiplicity classes for the different measurements, with the corresponding multiplicity $\langle dN_{ch}/d\eta \rangle_{|\eta_{lab}|<0.8}$, and p_T -integrated yields dN/dy for the different species (average for particle and antiparticle). The first uncertainty is statistical and the second is systematic.

Multiplicity	$\langle p_T \rangle$ (GeV/c) p	$\langle p_T \rangle$ (GeV/c) ^{3}He	$\langle p_T \rangle$ (GeV/c) ^{3}H
HM	1.28 ± 0.01 ± 0.03	2.03 ± 0.03 ± 0.08	1.57 ± 0.05 ± 0.10
HM I	1.32 ± 0.01 ± 0.03		
HM II	1.28 ± 0.01 ± 0.03		
HM III	1.26 ± 0.01 ± 0.03		
MB		1.61 ± 0.08 ± 0.12	1.22 ± 0.07 ± 0.12
MB I		1.74 ± 0.11 ± 0.14	
MB II		1.48 ± 0.10 ± 0.15	

Table 4.3: Extrapolated values for the mean p_T in the different measured multiplicity classes and for all particle species (average for particle and antiparticle). The first uncertainty is statistical and the second is systematic.

In figure 4.5 the mean p_{T} of helium nuclei is shown as a function of the average charged-particle multiplicity together with results measured in pp collisions at $\sqrt{s} = 7$ TeV [59], p-Pb collisions at $\sqrt{s_{\mathrm{NN}}} = 5.02$ TeV [64], Pb-Pb collisions at $\sqrt{s_{\mathrm{NN}}} = 2.76$ TeV [57], and preliminary results measured in Pb-Pb collisions at $\sqrt{s_{\mathrm{NN}}} = 5.02$ TeV. The results measured in this work follow the rising trend seen in the previous analysis. As for light-flavor hadrons the ^{3}He nucleus p_{T} spectra become harder with increasing multiplicity, which can be explained by an increased radial flow pushing the nuclei to higher p_{T}.

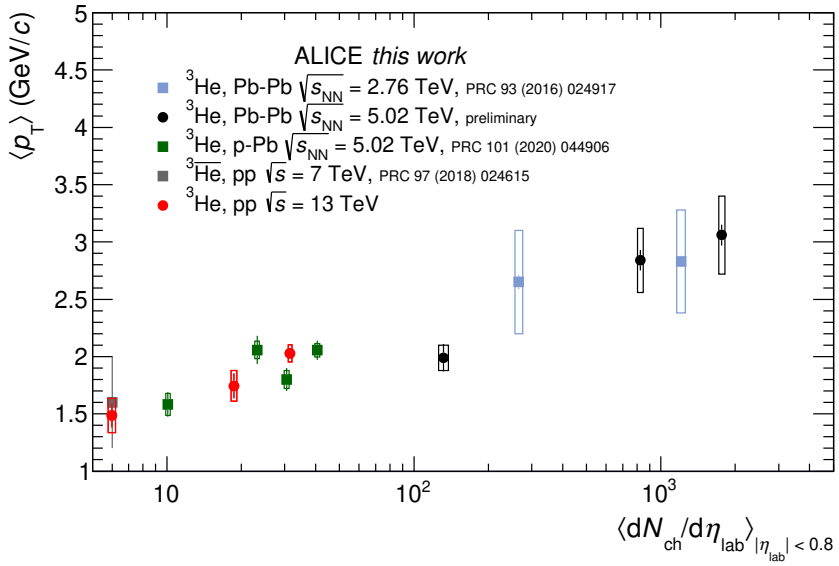

Figure 4.5: Mean p_{T} of ^{3}He nuclei as a function of charged-particle multiplicity. The red pints correspond to the measurement presented in this work. Results from pp collisions at $\sqrt{s} = 7$ TeV [59] (gray), p-Pb collisions at $\sqrt{s_{\mathrm{NN}}} = 5.02$ TeV [64] (green), Pb-Pb collisions at $\sqrt{s_{\mathrm{NN}}} = 2.76$ TeV [57] (blue), and preliminary results from Pb-Pb collisions at $\sqrt{s_{\mathrm{NN}}} = 5.02$ TeV (black) are also shown.

4.2 The ratio of integrated yields

The ratio of the integrated light nuclei yields to proton yields as a function of the average charged-particle multiplicity in a given event class is very interesting because it allows for probing the underlying production mechanism of the nuclei. Figure 4.6 shows the ratio of the integrated deuteron-to-proton yield on the left side and the ratio of the integrated helium-to-proton yield on the right side. The results obtained in this work are presented in the context of previous ALICE publications to broaden the physics picture. The deuteron-to-proton and/or helium-to-proton ratios were measured in MB pp collisions at 13 TeV [65], in p-Pb collisions at $\sqrt{s_{\mathrm{NN}}} = 5.02$ TeV [64, 62], and in Pb-Pb collisions at $\sqrt{s_{\mathrm{NN}}} = 2.76$ TeV [77]. Additionally, theoretical predictions are shown using different hadronization models. The black line corresponds to the canonical statistical hadronization model [87] (discussed in section 1.4.2). Two implementations are displayed, conserving charges over the correlation volume corresponding to one unit of rapidity or three units of rapidity, shown as dashed and full lines, respectively. The authors of the calculation mention that the correlation volume is not known a priori, and

they performed their calculations using two correlation volumes of $\mathrm{d}V/\mathrm{d}y$ and $3\mathrm{d}V/\mathrm{d}y$. In a more recent publication by the same authors in reference [92] they extent the correlation volume to $6\mathrm{d}V/\mathrm{d}y$ based on net proton fluctuations seen in central Pb-Pb collisions. The second model shown is an implementation of the advanced coalescence [55]. For B_3 the authors provide two different implementations of the coalescence approach with different underlying physics pictures. In green, the two-body coalescence is shown, which assumes the coalescence of helium nuclei to happen as a two-step process. First, two nucleons would coalesce into a deuteron which would then coalesce with the third nucleon to a ^{3}He in a separate process. The three-body coalescence, in contrast, shown in blue in the right figure, assumes the formation of a ^{3}He nucleus to happen as a one-step process where all nucleons coalesce at once. In the calculation presented in reference [55] the main difference between the two-body and three-body coalescence is a different radius of the formed helium nucleus. In the three-body coalescence only the helium radius ($r_{^3\mathrm{He}} = 1.76$ fm [151]) enters while for the two-body coalescence a larger radius is relevant, which is estimated by the distance between the proton and the center-of-mass of the deuteron inside the helium nucleus. The most interesting and striking

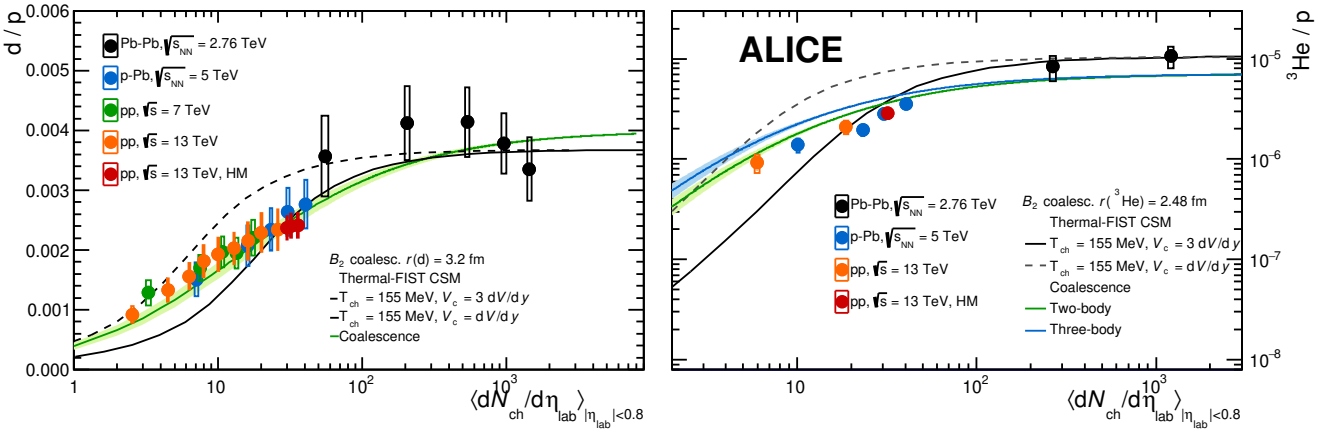

Figure 4.6: Ratio of integrated yields for deuteron-to-proton (left) and helium-to-proton (right) as a function of the average charged-particle multiplicity in the event class. For the deuteron-to-proton the red data points corespondent to the results presented in this work. For the helium-to-proton ratio the red and the orange data points were measured in this work. Additionally, coalescence [53] and canonical statistical hadronization model [87] predictions are shown.

message of figure 4.6 is the smooth transition from small (pp, p-Pb) to large systems (central Pb-Pb) in both ratios. It is better constrained in the deuteron-to-proton ratio due to the abundance of available measurements. The smooth evolution suggests that the nuclei production only scales with the average charged-particle multiplicity and that the underlying production mechanism continuously evolves going from small to large collision systems. Both presented advanced coalescence and canonical statistical hadronization models agree with the measured deuteron-to-proton ratio within the uncertainties. For the helium-to-proton ratio, however, a tension between models and data observed in p-Pb collisions at $\sqrt{s_{\mathrm{NN}}} = 5.02$ TeV [64] is confirmed by the presented measurement. Even though the two-body coalescence model agrees better with the data than the three-body coalescence model, both overestimate the measured ratio in pp and p-Pb collisions. The canonical statistical hadronization model also overshoots the data when using 3 units of rapidity as correlation volume. Here, the difference arises for the

measurement in the high-multiplicity triggered event class and for central p-Pb events, which corresponds to an average charged-particle multiplicity of around 30 particles. Additionally, a stronger systems size dependence for the helium-to-proton ratio is observed in comparison to the deuteron-to-proton ratio. In the coalescence picture, this difference is explained by the fact that the ^{3}He nucleus has three nucleons and, thus, is more sensitive to spatial distributions of the nucleons in the emission source [55].

4.2.1 Triton-to-helium ratio

Sun, Ko, and Dönigus showed in reference [55] that the canonical statistical hadronization and advanced coalescence models predict different values for the triton-to-helium yield ratio. For the statistical hadronization model, the ratio of the yields is given by $e^{-\Delta m/T_{\mathrm{ch}}}$, where Δm is the mass difference between the ^{3}He and ^{3}H nuclei and T_{ch} is the chemical freeze-out temperature of around 155 MeV. Due to the small mass difference $\Delta m \approx 19$ keV/c [152] the statistical hadronization model predicts a ratio very close to unity. In the case of coalescence, however, the radii of the formed nuclei enter the formation probability. The radii for helium and triton are $r_{^3\mathrm{He}} = 1.76$ fm and $r_{^3\mathrm{H}} = 1.59$ fm [151], respectively. Therefore, according to the coalescence model, the triton yield should be less suppressed than helium yield when going from large to small source sizes. The effect is most pronounced in pp and p-Pb collisions, while in Pb-Pb collisions the nuclei radii are small in comparison to the source size and, hence, the relative difference plays nearly no role.

Figure 4.7 shows the triton-to-helium yield ratio as a function of multiplicity. The coalescence predictions from reference [55] are also displayed, using the two-body and three-body coalescence picture. The two theory calculations differ for the lowest multiplicity bin ($\langle \mathrm{d}N_{\mathrm{ch}}/\mathrm{d}\eta \rangle \approx 7$). Figure 4.8 shows the triton-to-helium yield ratio as a function of p_{T} in the high-multiplicity triggered event class. Additionally to the already discussed theoretical models, also a recent

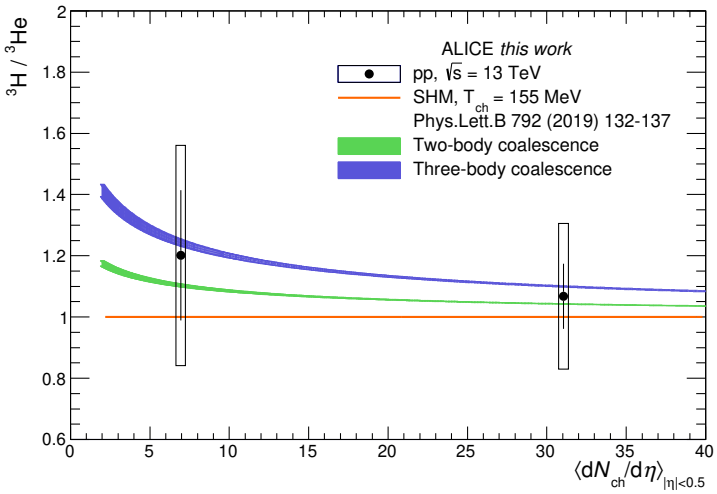

Figure 4.7: Triton-to-helium yield ratio as a function of multiplicity. The statistical uncertainties are displayed as error bars while the systematic uncertainties are shown as open boxes. A prediction from the statistical hadronization model as well as two coalescence predictions [55] are also shown assuming two-body or three-body coalescence.

implementation of the advanced coalescence [153] is displayed, which predicts the triton-to-helium ratio to be p_{T} dependent. In the study, the p_{T} dependence is obtained by implementing a so-called apparent source, which includes time and p_{T} dependence of the source size radius. In a simplified picture, high-momentum particles are produced earlier in the collision in the initial hard scattering process and, therefore, the corresponding emission source is smaller.

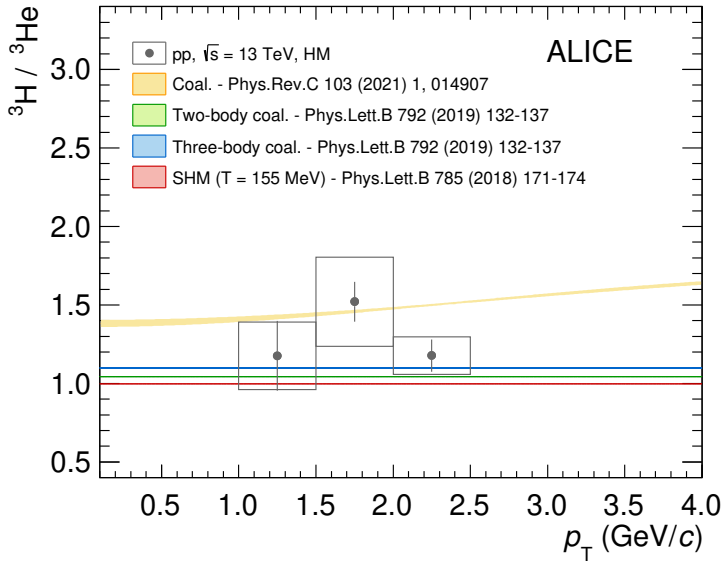

Figure 4.8: The ratio between the transverse-momentum spectra of triton and helium nuclei for the high-multiplicity triggered data sample. The statistical uncertainties are displayed as error bars while the systematic uncertainties are shown as open boxes. Three different coalescence predictions are presented [55, 153]. Additionally, the canonical statistical hadronization model prediction is shown [87].

Unfortunately, the measurement of the tritium nuclei is limited in statistical as well as systematic precision, due to the rare production rate of triton and their in p_{T} limited identification. Hence, the measured triton-to-helium yield ratio has not yet the needed precision to discriminate between the different models and the underlying physics pictures. With the upcoming LHC Run 3, however, ALICE will collect data at a much higher rate (expected 50 kHz for Pb-Pb collisions) and will, thus, have the needed data to perform the triton-to-helium yield ratio measurement with increased accuracy. The detector upgrades to achieve such an increase in performance are discussed in chapter 5. The projections for the LHC Run 3 are shown in section 5.1.3.

4.3 Coalescence parameter

As discussed in section 1.4.3, the key parameter of the coalescence model is the coalescence parameter B_A. Experimentally, it is accessible via equation 1.11 as the ratio of the nucleus spectrum to the proton spectrum to the power A, evaluated at the transverse momentum p_{T}/A. In this section, the parameters measured in this work will be presented and compared to coalescence predictions, first as a function of the average charged-particle multiplicity and second as a function of transverse momentum.

4.3.1 Coalescence parameter as a function of charged-particle multiplicity

Figure 4.9 shows the coalescence parameters B_2 on the left side and B_3 on the right side evaluated at a transverse momentum of $p_T/A = 0.75$ GeV/c in the case of B_2 and $p_T/A = 0.73$ GeV/c in the case of B_3 as a function of the average charged-particle multiplicity of the collision. In addition to the results obtained in this work previous measurements from the ALICE Collaboration are displayed. B_2 was measured in minimum bias pp collisions at $\sqrt{s} = 7$ TeV [61] and $\sqrt{s} = 13$ TeV [65], in p-Pb collisions at $\sqrt{s_{\mathrm{NN}}} = 5.02$ TeV [62], and in Pb-Pb collisions at $\sqrt{s_{\mathrm{NN}}} = 2.76$ TeV [77]. The B_3 was measured in pp collisions at $\sqrt{s} = 7$ TeV [59], in p-Pb collisions at $\sqrt{s_{\mathrm{NN}}} = 5.02$ TeV [64], and in Pb-Pb collisions at $\sqrt{s_{\mathrm{NN}}} = 2.76$ TeV [77]. The advanced coalescence prediction shown in figure 4.9 is taken from reference [53]. The model uses nuclei radii of $r_{\mathrm{d}} = 3.2$ fm and $r_{^3\mathrm{He}} = 2.48$ fm for the deuteron and helium nucleus, respectively. On top of that, two parameterizations for the emission source radius, labeled as A and B, are used. Parameterization A is obtained via a fit to ALICE femtoscopy measurements [99] of the source radius. The interpolation is realized with equation 1.17, which connects the source radius with the average charged-particle multiplicity in the event. Parametrization B, on the other hand, is obtained by fixing the relationship between the source radius and the multiplicity in such a way that B_2 in the most central (0-10%) Pb-Pb collisions at $\sqrt{s_{\mathrm{NN}}} = 2.76$ TeV is reproduced. The correlation between the source radius and the average charged-particle multiplicity is shown for both parameterizations in figure 1.15. The results obtained in pp collisions at $\sqrt{s} = 13$ TeV nicely confirm the trend which was observed in p-Pb collisions and thereby constrain the nuclei

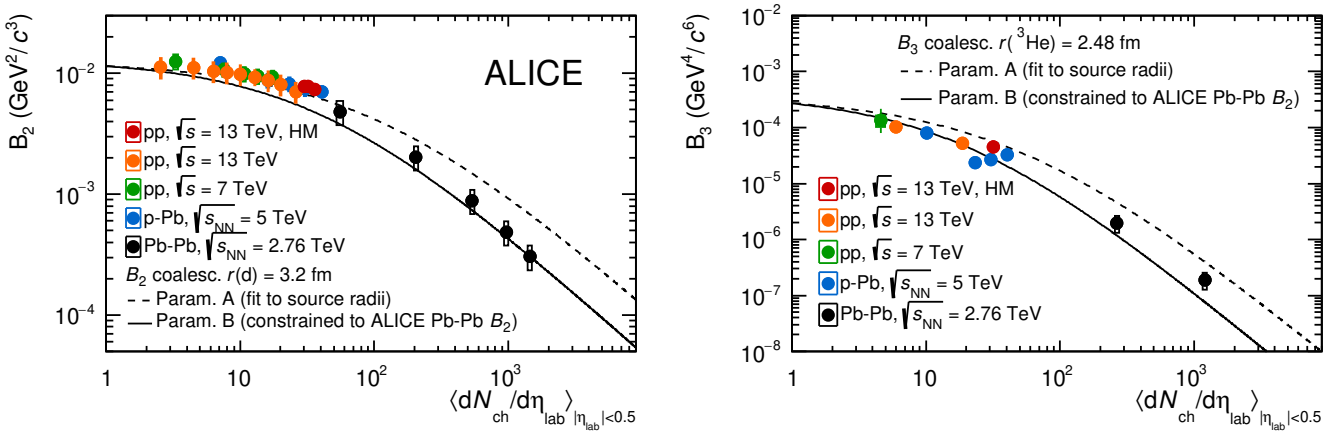

Figure 4.9: Coalescence parameters B_2 on the left side and B_3 on the right side as a function of the average charged-particle multiplicity in the collision. B_2 is evaluated at a fixed p_T/A of 0.75 GeV/c and measured in high-multiplicity triggered pp collisions at $\sqrt{s} = 13$ TeV in this work. Additional ALICE measurements are shown: in minimum bias pp collisions at $\sqrt{s} = 7$ TeV [61] and $\sqrt{s} = 13$ TeV [65], respectively, in p-Pb collisions at $\sqrt{s_{\mathrm{NN}}} = 5.02$ TeV [62], and in Pb-Pb collisions at $\sqrt{s_{\mathrm{NN}}} = 2.76$ TeV [77]. B_3 is evaluated at fixed p_T/A of 0.73 GeV/c and measured in minimum bias, as well as high-multiplicity triggered pp collisions at $\sqrt{s} = 13$ TeV as presented in this work. Additional measurements in p-Pb collisions at $\sqrt{s_{\mathrm{NN}}} = 5.02$ TeV [64], and in Pb-Pb collisions at $\sqrt{s_{\mathrm{NN}}} = 2.76$ TeV [77] are also shown. The coalescence predictions are taken from reference [53]. They rely on the same model with different parameterizations of the source radius.

formation models further. They also strengthen the idea of a continuously evolving underlying production mechanism going from small to large collision systems. The decreasing trend of the coalescence parameter with the average charged-particle multiplicity was already predicted by Scheibl and Heinz in 1999 [95] and can be explained by the increasing emission source radius which, according to equation 1.16, is inverse proportional to the coalescence parameter. With increasing source radius the average distance between the nucleons increases and, thus, the coalescence probability decreases. For B_2 and B_3 the coalescence model quantitatively describes the trend but struggles to describe the data over the full multiplicity range. A possible reason for the observed differences between data and model could be explained by the simplified connection between source size radius and the average charged-particle multiplicity. As shown in figure 1.14, the source radius and the charged-particle multiplicity density are only proportional in the first order. Instead, there seems to be a non-continuous transition when going from pp collisions to larger systems. Additionally, both coalescences parameters B_2 and B_3 significantly depend on p_{T} in fine multiplicity classes as shown in figure 4.10. The transverse-momentum dependence can be explained by assuming a smaller emission source with increasing transverse momentum [153], neither implemented in parameterization A or B. In the future, the measurement of the coalescence parameter as a function of multiplicity would benefit from more accurate and multiplicity differential measurements of the source size. This would further constrain B_A in the models and would allow for a comparison to data over the full multiplicity range.

4.3.2 Coalescence parameter as a function of transverse momentum

The coalescence parameters B_2 and B_3 are shown as a function of p_{T}/A in figure 4.10 for all available multiplicity classes. The multiplicity classes are listed in table 4.2. It is interesting to note that both coalescence parameters presented in figure 4.10 show a significant p_{T}/A dependence. Previous ALICE measurements indicated a constant B_2 in pp collisions at $\sqrt{s} = 7$ TeV [61] and $\sqrt{s} = 13$ TeV [65], and in p-Pb collisions at $\sqrt{s_{\mathrm{NN}}} = 5.02$ TeV [62] in fine multiplicity classes. It was also shown that the multiplicity integrated B_2 has a significant dependence on p_{T}/A [61, 65], which was explained by the hardening of the proton spectra within the integrated multiplicity class. The rise of the coalescence parameters seen in this work, however, can not be explained by the hardening of the proton spectra within one multiplicity class, due to the very narrowly chosen multiplicity intervals in the proton and deuteron analysis. This observed rise of the coalescence parameter rules out the simple coalescence model which assumes B_A to be momentum independent. As mentioned before, a possible physics explanation of the p_{T} dependence can be given by an apparent emission with a time-dependent source radius. It is not clear whether the formation of nuclei should happen at only one point in time during the evolution of the collision or whether the formation can happen continuously. A transverse-momentum dependent coalescence parameter suggests the latter. Also, the increase of the coalescence parameter as a function of p_{T} strengthens this picture because higher p_{T} particles are typically produced at earlier stages of the collisions, in which most of the hard (large momentum transfer) parton-parton interactions take place.

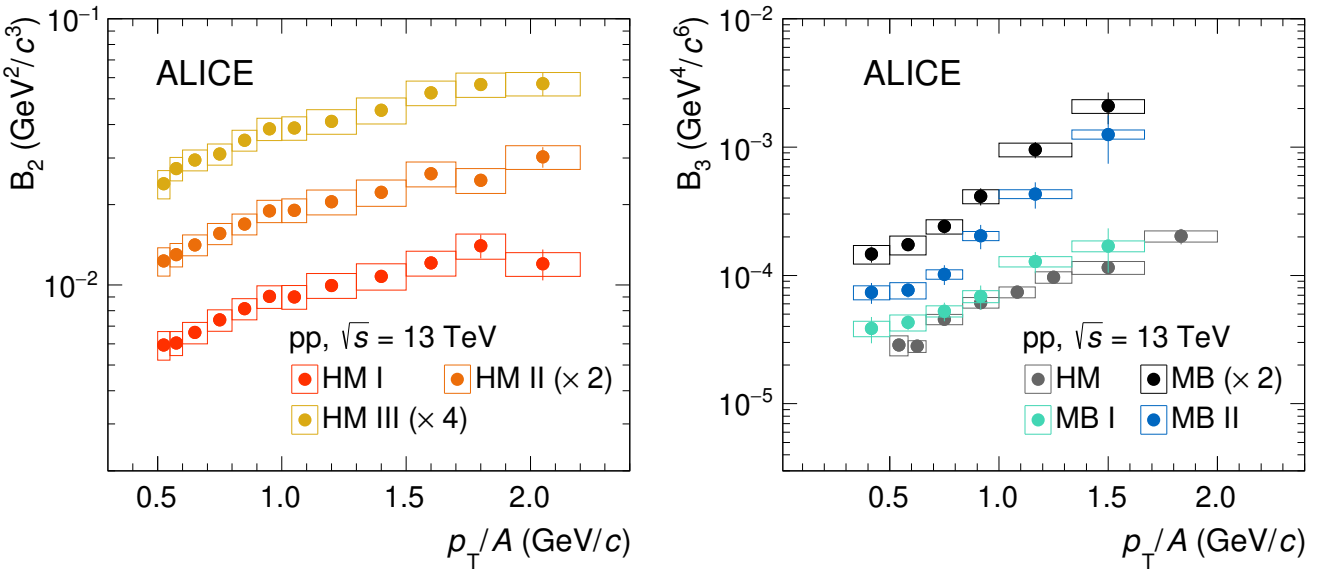

Figure 4.10: Coalescence parameters B_2 (left) and B_3 (right) as a function of p_T/A for different multiplicity classes, which are listed in the table 4.2. Error bars represent statistical uncertainties and open boxes depict the systematic uncertainties.

Deuteron and helium wave function

As shown in equation 1.23 for the deuteron and in equation 1.24 for generalized nuclei with the mass number A, the coalescence parameter is directly dependent on the wave function of the nuclei in the final state, which carries the information of the internal structure of the nucleus. Therefore, the wave function dependency of the coalescence parameter gives a direct way to test different wave functions within the coalescence picture. In figure 4.11, the measured coalescence parameter as a function of p_T/A is compared to theoretical predictions using different implementations for the wave function of the final-state nucleus.

In the left side of figure 4.11, the deuteron B_2 is shown in the 0-0.1% high-multiplicity triggered event class, with an advanced coalescence calculation using a single and double Gaussian [154], van Hulthen [95], and chiral effective field theory (χEFT) [155] wave function. The deviation of the measured coalescence parameter from the different deuteron wave functions as a function of the emission source radius is based on equation 1.23. The details of the calculations can be found in appendix A or alternatively in reference [150]. The right side of figure 4.11 shows the helium B_3 in the integrated high-multiplicity triggered event class, with only one coalescence prediction which uses a Gaussian helium wave function. The parameterization is based on equation 1.24, with $A = 3$ which was derived in reference [96]. In appendix figure A.1, the coalescence parameter as a function of the emission source radius is shown using different wave functions. The B_2, comparing four wave functions, shows large differences for small source radius (such as realized in pp or p-Pb collisions) and convergences towards the same value for large source radii. With increasing emission sources the coalescence parameter is less sensitive to the internal structure of the nucleus.

ALICE measured the emission source size radius in high-multiplicity triggered pp collisions at $\sqrt{s} = 13$ TeV in reference [156] using two-baryon correlations. Two source radii are reported

as a function of the transverse mass (m_T) of the correlated pair. The study includes a way to quantitatively account for strong resonance decay products, which leads to a universal emission source radius for p-p and p-Λ correlations. The corrected emission source radius R ranges from 0.85 to 1.3 fm and is parameterized as a function of m_T using

$$R(\langle m_T \rangle) = c_0 + \exp(c_1 + c_2 \langle m_T \rangle) \tag{4.8}$$

with c_0, c_1, and c_2 being free fit parameters. The transverse mass is calculated via $m_T = \sqrt{m_p^2 + (p_T/A)^2}$ with m_p being the proton rest mass.
In equation 1.23 and 1.24 for the calculation of the coalescence parameters also the nuclear size enters. For the deuteron and helium radii, the values $r_d = 3.2$ fm and $r_{^3He} = 2.48$ fm are used. All calculated coalescence parameters shown in figure 4.11 follow the with p_T/A increasing

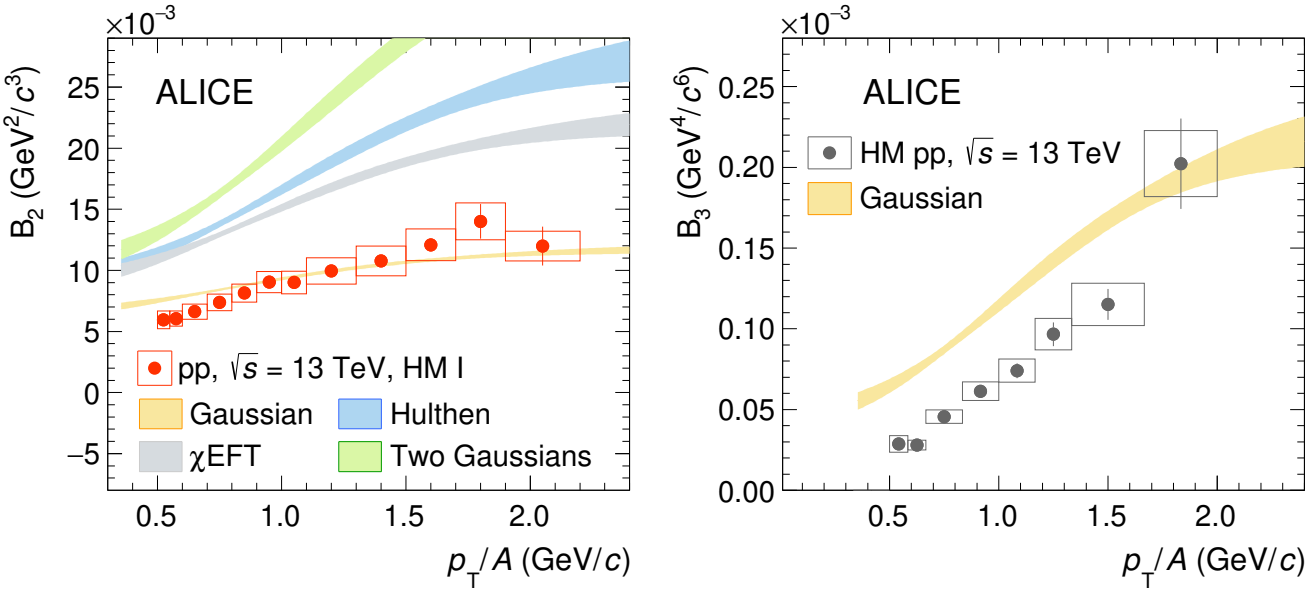

Figure 4.11: Theoretical predictions for the coalescence parameter B_2 for deuterons on the left side and B_3 for helium nuclei on the right side as a function of p_T/A. B_2 is compared to coalescence implementations using a Gaussian, van Hulthen, chiral effective field theory, or a two Gaussian wave function for the deuteron. B_3 is only compared to one prediction using a Gaussian wave function for the helium nucleus.

trend seen in the data. However, it is quite surprising and remarkable that only the Gaussian wave function implementation manages to describe the B_2 data quantitatively. The other three B_2 calculations using more complex wave functions, which are commonly used, overestimate the measured magnitude of B_2 by approximately a factor of two. In the case of B_3, only one calculation is available using a Gaussian wave function. In this case, however, the model also overestimates the measurement by roughly a factor of two, except for the last p_T bin.
Future application of this approach using more nuclear wave functions will allow for a systematic study of the helium wave function. Additionally, the internal structure of more exotic hypernuclei, which are not within the scope of this work, like hypertriton, can be studied within the coalescence approach using the presented method. This will become of relevance during LHC Run 3 when a large data sample will be collected and the hypertriton coalescence parameter can be measured precisely [157].

5 Outlook

5.1 LHC Run 3

With the transition from Long Shutdown 2 to LHC Run 3 in February 2022, the machine provides a substantially higher luminosity, with an expected integrated luminosity of 200 pb^{-1} for pp collisions by the end of LHC Run 3. To make full use of the higher collision rates the ALICE detector setup had to be upgraded. The two most important detector upgrades, employed for the kind of analysis presented in this work, will be presented briefly. The first key element of the upgrade is the replacement of the Inner Tracking System (ITS described in section 2.2.1) with a new silicon-based detector, using Monolithic Active Pixel Sensors (MAPS) [158]. The second key element is the upgrade of the TPC readout chambers from Multi-Wire Proportional Chamber (MWPC) to a Gas Electron Multiplier (GEM) detector, allowing the TPC to operate in continuous readout mode and handle the expected collision rate of 50 kHz in Pb-Pb collisions which will be delivered by the LHC [159]. Additionally, a new online and offline system (O^2) [160] will be installed to account for the new continuous readout and to cope with the expected data volume.

5.1.1 Monolithic Active Pixel Sensors based ITS

The main goal of the ITS upgrade was to improve the resolution of the primary event vertex as well as secondary decay vertices and to improve the detection capabilities for low p_{T} particles. Additionally, the detector has to keep up with a collision rate of 50 kHz in the case of Pb-Pb collisions. The three major design choices taken to achieve these goals are: first, a reduction of the beam-pipe radius from 29.8 mm to 18.2 mm, which allows the first ITS layer to be located at a radial distance of only 22.4-26.7 mm apart from the interaction point. Second, the granularity was increased by adding a seventh pixel layer to the ITS and, third, equipping all layers exclusively with Monolithic Active Pixel Sensors (MAPS), with a cell size of 29.24 µm × 26.88 µm. MAPS combine the sensitive volume and front-end readout logic in the same piece of silicon, allowing for a great reduction of material budget. The radiation length of the MAPS based ITS is 0.35% X_0 per layer for the innermost layers and to 1.0% X_0 for the outer layers [161]. The schematic layout of the ITS for LHC Run 3 is displayed in figure 5.1. More details of the ITS upgrade can be found in the technical design report in reference [158].

5.1.2 TPC upgrade with GEM-based readout chambers for a continues readout

The TPC operated by ALICE during LHC Run 1 and Run 2 is an almost ideal device for particle tracking and identification via the specific energy loss, as described in section 2.2.2. The old TPC had to be operated using a gating grid as explained in section 2.2.2. The gating grid prevented ion backflow from the amplification region in the readout chambers into the drift region of the detector, which causes a distortion of the electric field and, thus, reduces the tracking resolution. The operation of the gating grid limited the data-taking rate to 3 kHz because of long detector deadtimes. Roughly half of the time the gating grid was active prohibiting electrons to enter the

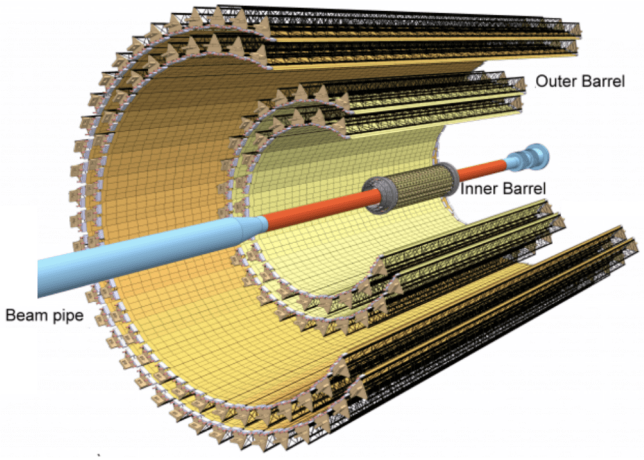

Figure 5.1: The schematic layout of the upgraded ITS during LHC Run 3 [158].

readout chambers. To benefit from the advantages of a TPC detector and the gain in luminosity from LHC Run 3 and beyond, the operation of a gating grid is not sustainable. Instead, a new electron amplification system was installed based on the Gas Electron Multiplier (GEM) [162] detector technology, which replaces the previous MWPCs. In the case of the TPC upgrade, GEMs are 50 µm thick foils with two copper layers sandwiching a polyimide insulator. In a photolithography process, the foils are pierced with small holes, which have an inner diameter of 50 µm (polyimide) and an outer diameter (copper) of 70 µm. The holes serve as open channels in which the amplification of the electrons is realized. During the detector operation, a nominal voltage between $230 \leq \Delta V_{GEM} \leq 320$ V will be applied to the conducting layers of the foil, creating a large electric field inside the holes. Drift electrons entering these holes are amplified in an electron avalanche. With the final ALICE TPC design, the ion backflow is less than 1% [159] because the ions are collected at the negatively charged foil layers. In figure 5.2 this effect is visible. The figure shows the dynamics of an electron in a GEM hole. The electron comes from the top and travels to the bottom. When entering the GEM hole the electron is accelerated and causes an electron avalanche, indicated with the light lines in the figure. All the free electrons move towards the bottom of the figure. The created ions on the other hand, indicated with dark lines, move along the electric field in opposite direction and most of them are collected at the upper negatively charged copper foil [163]. For the ALICE TPC in LHC Run 3, four layers of GEM foils are stacked to provide several amplification stages, as shown in figure 5.3. After applying the before mentioned potentials to the individual foils the amplification gain can be optimized while back drifting ions originating from subsequent layers can be efficiently blocked [159] by asymmetric transfer fields ($E_{T1} = 3500$ V/cm and $E_{T2} = 3500$ V/cm and low $E_{T3} = 100$ V/cm). To achieve a good signal-to-noise ratio the GEM stacks have to be operated at an effective gain of 2000, which results in a maximum of 20 ions drifting back into the drift volume. At the same time, the energy resolution for $\sigma(^{55}\text{Fe}) = 11.3\%$ at 5.9 keV is preserved. The signal is collected at the pad plane and readout by newly installed fronted electronics featuring continuous sampling with 10 bit resolution and 10 MHz.

Within this thesis work, I participated in the GEM foil testing and framing, as well as the chamber construction and quality assurance taking place in the GSI detector laboratory. Additionally, I took part in the dismounting of the previous TPC readout chambers at CERN, and the installa-

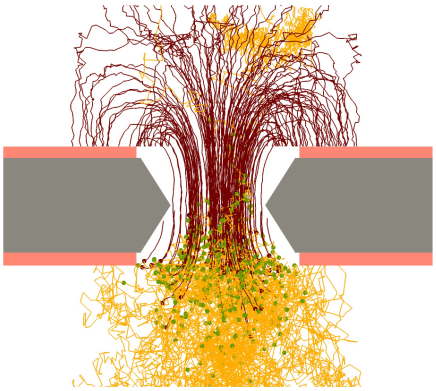

Figure 5.2: Simulation of a primary electron creating a electron avalanche in a GEM hole. The light lines indicate the electron path, while the dark lines show the path of the ions. The original electron comes from the top and creates a electron avalanche, leaving also free ions in the gas [163].

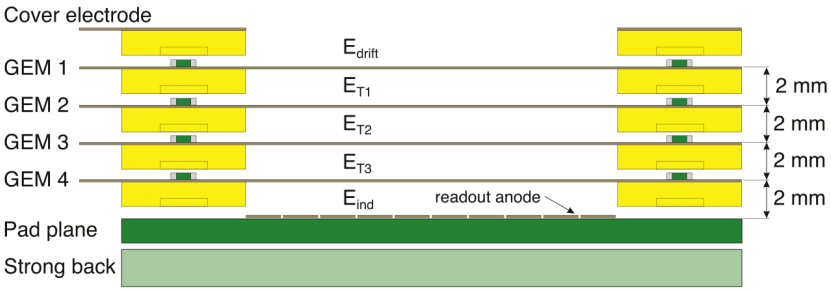

Figure 5.3: Set up of the GEM-based ALICE TPC readout chambers. Each GEM foil is glued onto a 2 mm thick support frame defining the gap between the four different GEM foils. The drift field E_{drift}, transfer fields E_{Ti}, and induction field E_{ind} are shown as well [164].

tion of the gas system, as well as the GEM chamber installation in the cleanroom at CERN LHC point 2. Additional information on the ALICE TPC upgrade can be found in reference [159].

5.1.3 Projection for LHC Run 3

As discussed in this work, measurements of (anti)(hyper)nuclei require large data samples, collected ideally with high tracking precision, excellent particle identification, and good secondary decay vertex resolution. The upgraded ALICE detector satisfies all these requirements. The expected integrated luminosity at the end of LHC Run 3 is 10 nb^{-1} for Pb-Pb collisions at $\sqrt{s_{\text{NN}}}$ = 5.5 TeV and 200 pb^{-1} in pp collisions at $\sqrt{s}$ =14 TeV in the case of nuclei, where a dedicated nuclei trigger will be applied. The trigger will look for events with a very high dE/dx track in the TPC detector. Figure 5.4 shows the expected raw yield of antinuclei on the left side and the expected significance for antihypernuclei on the right side. The yield is obtained in the range $2 < p_{\text{T}} < 10$ GeV/c for central Pb-Pb collisions and it is shown as a function of the integrated minimum-bias luminosity. The arrows indicate the integrated minimum-bias luminosity reached at the of LHC Run 2, while the dashed line indicates the anticipated integrated luminosity at the end of LHC Run 3. With the amount of anticipated (anti)(hyper)nuclei, precision measurements for $A \leq 3$ will be feasible, including the measurement of the mass difference between matter and antimatter for $A = 3$ nuclei, exploiting the TOF detector [56]. The measurement will allow for the testing of charge symmetry breaking due to the up and down quark differences. Additionally, elliptic flow measurements of $A = 3$ nuclei, as already performed for deuterons [58], might allow for the indirect study of the neutron flow by comparing ^{3}He to ^{3}H results. On top of that, the first observation of ${}^{4}_{\bar{\Lambda}}\overline{\text{He}}$ is expected at the LHC.

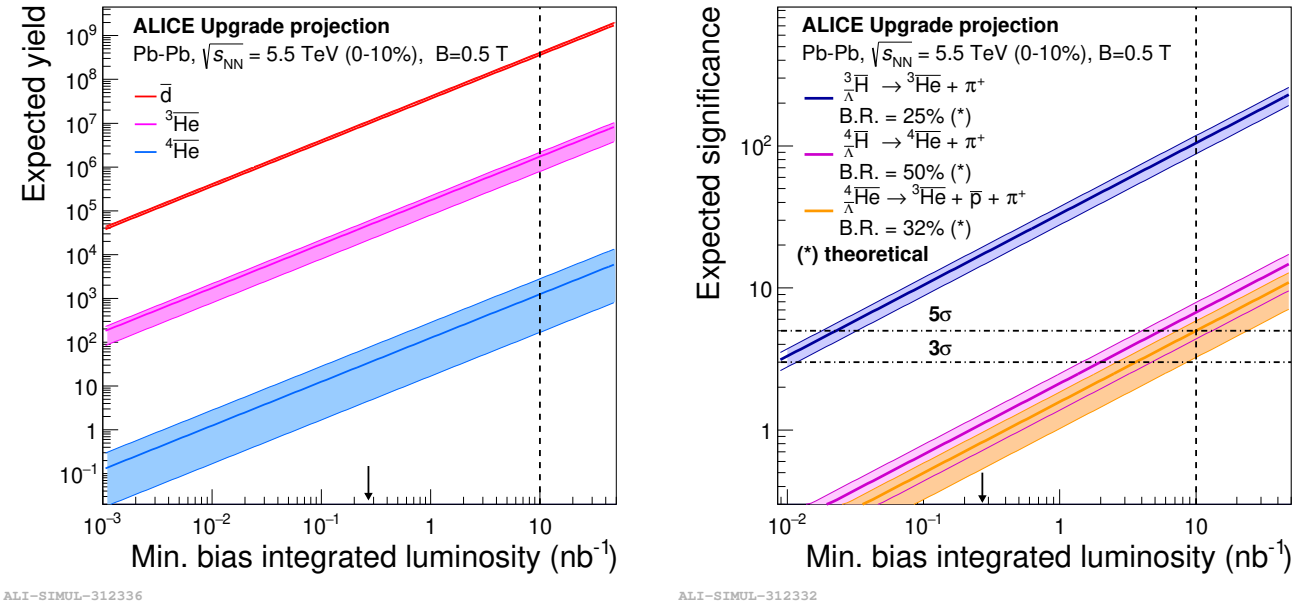

Figure 5.4: Expected raw yield of antinuclei in the $2 < p_{\mathrm{T}} < 10$ GeV/c interval (left) and expected significance of antihypernulcei (right), detectable in 0-10% central Pb-Pb collisions in LHC Run 3 and Run 4 with ALICE as a function of the integrated minimum-bias luminosity. The arrows represent the minimum-bias luminosity for the end of LHC Run 2 and the dashed lines show the expected integrated luminosity at the end of Run 3. The prediction uncertainties are shown as bands. The figure is taken form reference [157].

The data sample collected by the end of LHC Run 3 will also shed light on the underlying production mechanism of light nuclei and will be decisive in distinguishing between the statistical hadronization model (described in section 1.4.1) and coalescence model (described in section 1.4.3) as the relevant hadronization mechanism. To test the statistical hadronization model in terms of its description of the (anti)(hyper)nuclei formation, the capability of measuring light (anti)hypernuclei will be of special importance, since these objects are not produced via the strong decay of higher resonance states and, thus, are perfectly suited to constrain the chemical freeze-out temperature T_{ch} thermal-model fits. Testing coalescence and statistical hadronization models can be improved by using different observables, one of which is the difference in the production rate of ^{3}H and ^{3}He as discussed in section 4.2.1. Figure 5.5 shows the expected precision that will be achieved with 200 pb^{-1} integrated luminosity in pp collisions at the end of LHC Run 3. The expected charged-particle multiplicity is scaled to 14 TeV according to a power-law extrapolation of the measured multiplicities in 5 and 13 TeV. The systematic uncertainty is assumed to be reduced by a factor of four in the ratio with respect to the measurement presented in chapter 4. A factor of two to three is probably achievable for the individual particle yields due to the improved capabilities of the upgraded detector and with the implementation of a proper inelastic hadronic interaction cross section correction in the triton analysis. An additional improvement of the systematic uncertainty in the ^{3}H-to-^{3}He yield ratio can be obtained when taking correlated uncertainties into account. This was not done in the analysis presented in section 4.2.1, because with the current measurement the necessary statistical precision needed to distinguish between the models is not reached. As shown in figure 5.5 with LHC Run 3 the ratio will be sensitive to the difference between two-body, three-body coalescence,

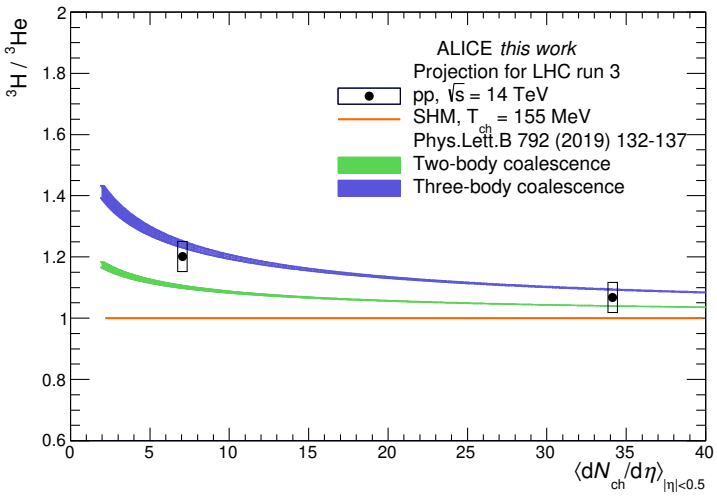

Figure 5.5: Expected precision of the triton-to-helium yield ratio as a function of multiplicity at the end of LHC Run 3. The data sample size will increase concerning its current size by approximately a factor of 1000. The systematic uncertainty is assumed to be reduced by a factor of four, exploiting the improved detector setup and canceling of correlated uncertainties in the ^{3}H-to-^{3}He yield ratio. Predictions from the statistical hadronization and coalescence models (assuming two-body or three-body coalescence) [55] are also shown.

and thermal-model predictions. The best observable at the end of LHC Run 3, however, to address the question of the underlying production mechanism will be the hypertriton-to-helium yield ratio. Due to its very large radius of about 10 fm and a comparable mass to the ^{3}He nucleus the thermal and coalescence model predictions differ by up to three orders of magnitude for small emission source radii [55].

The pp program planned for LHC Run 3 will play a critical role for cosmic ray and indirect dark matter searches via the precise measurement of the antinuclei coalescence parameter, which most cosmological-model calculations use as a fundamental baseline. The precision of B_3 will significantly improve, with an expected statistical uncertainty of the order of 0.1%, and, thus, further constrain the cosmic secondary antinuclei production rates. Additionally, the statistical precision of B_4 can be improved to the order of 10% [165], when using the planed dedicated (anti)nuclei trigger. This will help to interpret the preliminary AMS observation of anti-^{4}He nuclei (as discussed in section 1.5) should the AMS Collaboration confirm their measurement. All further opportunities at the LHC with Run 3 and 4 data are presented in a comprehensive report found in reference [165].

6 Summary and conclusions

Exploiting the full data sample collected in pp collisions at $\sqrt{s} = 13$ TeV at the end of LHC Run 2 it was possible to measure the rarely produced (anti-)^{3}He and (anti-)^{3}H nuclei. Thanks to the ALICE detector's excellent tracking and particle-identification capabilities the distributions of these nuclei were measured differentially for event multiplicity and transverse momentum. This is the first such measurement of $A = 3$ nuclei in pp collisions at top LHC energy. Additionally, the multiplicity and transverse-momentum differential (anti)proton spectra in high-multiplicity triggered pp events were measured complementing the already published minimum-bias result [147]. Due to the TPC's strong separation power of the $Z = 2$ helium nuclei, a TPC-only analysis delivered a solid identification. For protons and ^{3}H, on the other hand, the information from the TOF detector had to be added to ensure a clean sample. As discussed in chapter 3, the systematic precision of the proton measurement, as well as the nuclei measurements, were improved using a data-driven approach, which corrects the inelastic hadronic interaction cross section implemented in GEANT. Based on the same principles and under the inclusion of a recent ALICE measurement of the proton inelastic cross section a new correction for the TRD material budget was developed further improving the precision of the measurements.

The multiplicity differential deuteron-to-proton yield ratio, as well as the helium-to-proton yield ratio, were measured and compared to coalescence and thermal-model predictions. The multiplicity interval provided by the high-multiplicity trigger data sample overlaps with previous measurements using p-Pb collisions [64], while the minimum-bias sample extends the measurement to low multiplicities. In both ratios, a smooth evolution with multiplicity is observed. So the system size seems to be the driving factor. The deuteron-to-proton yield ratio as a function of multiplicity is well described by thermal as well as coalescence models, while some tension between the models and the helium-to-proton yield ratio as a function of multiplicity is observed at intermediate multiplicity ($\mathrm{d}N_{\mathrm{ch}}/\mathrm{d}\eta \approx 20$). The triton-to-helium yield ratio was also determined, which has a stronger discrimination power between the models and can additionally distinguish between two-body and three-body coalescence approaches. With the statistical and systematic precision achieved at the end of LHC Run 2, the measurement is not conclusive yet. With the upcoming LHC Run 3, however, this measurement will shed light on the underlying formation process of light nuclei, as discussed in chapter 5. Finally, the coalescence parameters B_2 and B_3 were determined as a function of multiplicity and transverse momentum. The multiplicity-dependent coalescence parameters show a decreasing trend, which is quantitatively described by the coalescence model via an increasing emission-source radius, which is typically obtained using femtoscopy measurements. Here, however, future measurements will certainly provide better constraints on the emission-source radius and multiplicity correlation. For the transverse-momentum dependent coalescence parameters an increasing trend with increasing p_{T} was observed, for both B_2 and B_3. This is in contradiction to the B_2 measurement performed using minimum-bias collisions at $\sqrt{s} = 13$ TeV [65] and the simple coalescence prediction, which assumes the coalescence process to be transverse-momentum independent. Also, for the B_3 this trend was observed for the first time. In chapter 4, a method was developed to test the nuclear wave function of the deuteron and helium nuclei using the coalescence approach. Surprisingly the best description of the B_2 was achieved under the assumption of a Gaussian wave function for the deuteron, while the results obtained using the more sophisticated Hulthen and

chiral-effective field theory nuclear wave function did not describe the data. The B_3, however, is overpredicted by a factor two using a Gaussian wave function for the helium nucleus in the coalescence approach, but the trend as a function of p_{T}/A is well reproduced. In the future, this method can also be applied to the helium nuclei using more sophisticated nuclear wave functions and can also be applied to hypernuclei like the hypertriton.

The B_3 measurement will also serve as an important benchmark of space-bound experiments searching for physics beyond the standard models via cosmic antinuclei fluxes. The measurement of the nuclei yields and the corresponding ratios are not able to give a conclusive statement on the light nuclei formation process. However, with the soon starting LHC Run 3, a new era will start allowing for more differential measurements while also providing higher precision. This will for example allow for the precise mass-difference measurements of anti-^{3}He and ^{3}He, the testing of the nuclei formation models using the ^{3}H-to-^{3}He yield ratio, or the access to the neutron flow via the comparison of ^{3}H and ^{3}He flow. Additionally, key measurements (e.g. yield, lifetime) will be possible in the hypernuclei sector with the potential first observation of a ${}^{4}_{\bar{\Lambda}}\overline{\mathrm{He}}$ nuclei.

7 Bibliography

[1] Particle Data Group, "Review of Particle Physics", *Physical Review D* **98** (Aug, 2018) 030001.

[2] L. Kreis, *Investigating the Initial State of Heavy-Ion Collisions through Measurements of Anisotropic Flow using Spectator Neutrons with ALICE at the LHC* . PhD thesis, Ruprecht-Karls-Universität Heidelberg, 2021.

[3] T. Aoyama, T. Kinoshita, and M. Nio, "Theory of the Anomalous Magnetic Moment of the Electron", *Atoms* **7** no. 1, (2019) 28.

[4] T. van Ritbergen, J. Vermaseren, and S. Larin, "The four-loop β-function in quantum chromodynamics", *Physics Letters B* **400** no. 3-4, (May, 1997) 379–384.

[5] D. d'Enterria, S. Kluth, S. Alekhin, *et al.*, "α_s(2019): Precision measurements of the QCD coupling", `arXiv:1907.01435 [hep-ph]`.

[6] Particle Data Group, "Review of Particle Physics", *Progress of Theoretical and Experimental Physics* **2020** no. 8, (08, 2020) . 083C01.

[7] H. D. Politzer, "Reliable Perturbative Results for Strong Interactions?", *Physical Review Letters* **30** (Jun, 1973) 1346–1349.

[8] D. J. Gross and F. Wilczek, "Ultraviolet Behavior of Non-Abelian Gauge Theories", *Physical Review Letters* **30** (Jun, 1973) 1343–1346.

[9] E. Eichten, K. Gottfried, T. Kinoshita, J. Kogut, K. D. Lane, and T. M. Yan, "Spectrum of Charmed Quark-Antiquark Bound States", *Physical Review Letters* **34** (Feb, 1975) 369–372.

[10] G. Parisi, R. Petronzio, and F. Rapuano, "A Measurement of the String Tension Near the Continuum Limit", *Physics Letters B* **128** (1983) 418–420.

[11] R. P. Feynman, "Very high-energy collisions of hadrons", *Physical Review Letters* **23** (Dec, 1969) 1415–1417.

[12] E. D. Bloom, D. H. Coward, H. DeStaebler, J. Drees, G. Miller, L. W. Mo, R. E. Taylor, M. Breidenbach, J. I. Friedman, G. C. Hartmann, and H. W. Kendall, "High-Energy Inelastic *e*-p Scattering at 6° and 10° ", *Physical Review Letters* **23** (Oct, 1969) 930–934.

[13] C. Gwenlan, "Combined HERA deep inelastic scattering data and NLO QCD fits", *Nuclear Physics B - Proceedings Supplements* **191** (Jun, 2009) 5–15.

[14] J. C. Collins and M. J. Perry, "Superdense Matter: Neutrons or Asymptotically Free Quarks?", *Physical Review Letters* **34** (1975) 1353.

[15] N. Cabibbo and G. Parisi, "Exponential Hadronic Spectrum and Quark Liberation", *Physics Letters B* **59** (1975) 67–69.

[16] Y. Aoki, G. Endrodi, Z. Fodor, S. D. Katz, and K. K. Szabo, "The Order of the quantum chromodynamics transition predicted by the standard model of particle physics", *Nature* **443** (2006) 675–678, `arXiv:0611014 [hep-lat]`.

[17] **STAR** Collaboration, M. M. Aggarwal *et al.*, "An Experimental Exploration of the QCD Phase Diagram: The Search for the Critical Point and the Onset of De-confinement", `arXiv:1007.2613 [nucl-ex]`.

[18] **CBM** Collaboration, T. Ablyazimov *et al.*, "Challenges in QCD matter physics -The scientific programme of the Compressed Baryonic Matter experiment at FAIR", *The European Physical Journal A* **53** no. 3, (Mar, 2017) 60.

[19] A. Bazavov, H.-T. Ding, P. Hegde, O. Kaczmarek, F. Karsch, N. Karthik, E. Laermann, A. Lahiri, R. Larsen, S.-T. Li, *et al.*, "Chiral crossover in QCD at zero and non-zero chemical potentials", *Physics Letters B* **795** (Aug, 2019) 15–21.

[20] S. Borsanyi, Z. Fodor, J. N. Guenther, R. Kara, S. D. Katz, P. Parotto, A. Pasztor, C. Ratti, and K. K. Szabó, "QCD Crossover at Finite Chemical Potential from Lattice Simulations", *Physical Review Letters* **125** no. 5, (Jul, 2020) 052001.

[21] F. Karsch, "Lattice QCD at high temperature and density", *Lecture Notes in Physics* **583** (2002) 209–249, arXiv:0106019 [hep-lat].

[22] F. Karsch and E. Laermann, "Thermodynamics and in medium hadron properties from lattice QCD", arXiv:0305025 [hep-lat].

[23] R. Hagedorn, "Statistical thermodynamics of strong interactions at energies", *Nuovo Cimento* **3** (1965) 147–186. http://cds.cern.ch/record/346206.

[24] A. Bazavov, T. Bhattacharya, C. DeTar, *et al.*, "Equation of state in (2+1)-flavor QCD", *Physical Review D* **90** no. 9, (Nov, 2014) 094503.

[25] R. Sahoo, "Possible Formation of QGP-droplets in Proton-Proton Collisions at the CERN Large Hadron Collider", *AAPPS Bulletin* **29** no. 4, (2019) 16–21, arXiv:1908.10566 [nucl-ex].

[26] U. Heinz, "The Little Bang: searching for quark–gluon matter in relativistic heavy-ion collisions", *Nuclear Physics A* **685** no. 1-4, (Mar, 2001) 414–431.

[27] **ALICE** Collaboration, B. Abelev *et al.*, "Centrality determination of Pb-Pb collisions at $\sqrt{s_{\mathrm{NN}}} = 2.76$ TeV with ALICE", *Physical Review C* **88** no. 4, (Oct, 2013) 044909.

[28] M. L. Miller, K. Reygers, S. J. Sanders, and P. Steinberg, "Glauber Modeling in High-Energy Nuclear Collisions", *Annual Review of Nuclear and Particle Science* **57** no. 1, (Nov, 2007) 205–243.

[29] S. Donnachie, H. G. Dosch, O. Nachtmann, and P. Landshoff, *Pomeron physics and QCD*, vol. 19. Cambridge University Press, 12, 2004.

[30] **CMS** Collaboration, V. Khachatryan *et al.*, "Measurement of diffractive dissociation cross section in pp collisions at $\sqrt{s} = 7$ TeV", *Physical Review D* **92** no. 1, (Jul, 2015) 012003.

[31] S. Navin, "Diffraction in Pythia", arXiv:1005.3894 [hep-ph].

[32] P. Bartalini and J. R. Gaunt, *Multiple parton interactions at the LHC*. Advanced series on directions in high energy physics, 1793-1339; vol. 29. World Scientific, 2018.

[33] S. Acharya *et al.*, "Underlying event properties in pp collisions at $\sqrt{s} = 13$ TeV", *Journal of High Energy Physics* **2020** no. 4, (Apr, 2020) 192.

[34] **ATLAS** Collaboration, G. Aad *et al.*, "Observation of Long-Range Elliptic Azimuthal Anisotropies in $\sqrt{s} = 13$ and 2.76 TeV pp Collisions with the ATLAS Detector", *Physical Review Letters* **116** no. 17, (Apr, 2016) 172301.

[35] **PHOBOS** Collaboration, B. Alver *et al.*, "System size dependence of cluster properties from two-particle angular correlations in Cu+Cu and Au+Au collisions at $\sqrt{s_{\mathrm{NN}}} =$ 200 GeV", *Physical Review C* **81** no. 2, (Feb, 2010) 024904.

[36] **CMS** Collaboration, S. Chatrchyan *et al.*, "Long-range and short-range dihadron angular correlations in central Pb-Pb collisions at $\sqrt{s_{\mathrm{NN}}} = 2.76$ TeV", *Journal of High Energy Physics* **2011** no. 7, (Jul, 2011) 76.

[37] S. Acharya *et al.*, "Kaon femtoscopy in Pb-Pb collisions at $\sqrt{s_{\mathrm{NN}}} = 2.76$ TeV", *Physical Review C* **96** no. 6, (Dec, 2017) 064613.

[38] T. Matsui and H. Satz, "J/ψ suppression by quark-gluon plasma formation", *Physics Letters B* **178** no. 4, (1986) 416–422.

[39] **NA50** Collaboration, B. Alessandro *et al.*, "A new measurement of J/ψ suppression in Pb-Pb collisions at 158 GeV per nucleon", *The European Physical Journal C* **39** no. 3, (Feb, 2005) 335–345.

[40] **NA60** Collaboration, R. Arnaldi *et al.*, "J/ψ production in Indium-Indium collisions at 158 GeV per nucleon", *Physical Review Letters* **99** (Sep, 2007) 132302.

[41] **PHENIX** Collaboration, A. Adare *et al.*, "J/ψ Production versus centrality, transverse momentum, and rapidity in Au+Au collisions at $\sqrt{s_{\mathrm{NN}}} = 200$ GeV", *Physical Review Letters* **98** (Jun, 2007) 232301.

[42] **STAR** Collaboration, B. Abelev *et al.*, "J/ψ production at high transverse momenta in p+p and Cu+Cu collisions at $\sqrt{s_{\mathrm{NN}}} = 200$ GeV", *Physical Review C* **80** no. 4, (Oct, 2009) 041902.

[43] B. Abelev *et al.*, "Centrality, rapidity and transverse momentum dependence of J/Ψ suppression in Pb-Pb collisions at $\sqrt{s_{\mathrm{NN}}} = 2.76$ TeV", *Physics Letters B* **734** (2014) 314–327, `arXiv:1311.0214 [nucl-ex]`.

[44] P. Braun-Munzinger and J. Stachel, "The quest for the quark-gluon plasma", *Nature* **448** (07, 2007) 302–309.

[45] **ALICE** Collaboration, S. Acharya *et al.*, "Transverse momentum spectra and nuclear modification factors of charged particles in pp, p-Pb and Pb-Pb collisions at the LHC", *Journal of High Energy Physics* **2018** no. 11, (Nov, 2018) 13.

[46] **ALICE** Collaboration, S. Acharya *et al.*, "Transverse-momentum spectra and nuclear modification factors of charged particles in Xe–Xe collisions at $\sqrt{s_{\mathrm{NN}}} = 5.44$ TeV ", *Physics Letters B* **788** (Jan, 2019) 166–179.

[47] K. Eskola, H. Paukkunen, and C. Salgado, "EPS09 — A new generation of NLO and LO nuclear parton distribution functions", *Journal of High Energy Physics* **2009** no. 04, (Apr, 2009) 065–065.

[48] **CMS** Collaboration, Y. Go, "Nuclear modification factor of isolated prompt photons in pp and Pb-Pb collisions at $\sqrt{s_{\mathrm{NN}}} = 5.02$ TeV with the CMS detector", *Nuclear Physics A* **1005** (2021) 121824. The 28th International Conference on Ultra-relativistic Nucleus-Nucleus Collisions: Quark Matter 2019.

[49] M. Habib, "Transverse-momentum distribution of primary charged particles measured in p-Pb collisions using ALICE", Master's thesis, Technische Universität Darmstadt, 2017.

[50] H. Garcilazo, "Pion-Deuteron Breakup in the Region of the (3,3) Resonance", *Physical Review Letters* **48** (Mar, 1982) 577–580.

[51] S. Bass, M. Belkacem, M. Bleicher, M. Brandstetter, L. Bravina, C. Ernst, L. Gerland, M. Hofmann, S. Hofmann, J. Konopka, G. Mao, L. Neise, S. Soff, C. Spieles, H. Weber, L. Winckelmann, H. Stöcker, W. Greiner, C. Hartnack, J. Aichelin, and N. Amelin, "Microscopic models for ultrarelativistic heavy ion collisions", *Progress in Particle and*

Nuclear Physics **41** (1998) 255–369.

[52] A. Andronic, P. Braun-Munzinger, K. Redlich, and J. Stachel, "Decoding the phase structure of QCD via particle production at high energy", *Nature* **561** no. 7723, (Sep, 2018) 321–330.

[53] F. Bellini and A. P. Kalweit, "Testing production scenarios for (anti-)(hyper-)nuclei and exotica at energies available at the CERN Large Hadron Collider", *Physical Review C* **99** no. 5, (May, 2019) 054905.

[54] J. Steinheimer, K. Gudima, A. Botvina, I. Mishustin, M. Bleicher, and H. Stöcker, "Hypernuclei, dibaryon and antinuclei production in high energy heavy ion collisions: Thermal production vs. coalescence", *Physics Letters B* **714** no. 1, (Jul, 2012) 85–91.

[55] K.-J. Sun, C. M. Ko, and B. Dönigus, "Suppression of light nuclei production in collisions of small systems at the Large Hadron Collider", *Physics Letters B* **792** (May, 2019) 132–137.

[56] **ALICE** Collaboration, J. Adam *et al.*, "Precision measurement of the mass difference between light nuclei and anti-nuclei", *Nature Physics* **11** no. 10, (2015) 811–814, arXiv:1508.03986 [nucl-ex].

[57] **ALICE** Collaboration, J. Adam *et al.*, "Production of light nuclei and anti-nuclei in pp and Pb-Pb collisions at energies available at the CERN Large Hadron Collider", *Physical Review C* **93** (Feb, 2016) 024917.

[58] **ALICE** Collaboration, S. Acharya *et al.*, "Measurement of deuteron spectra and elliptic flow in Pb-Pb collisions at $\sqrt{s_{\rm NN}} = 2.76$ TeV at the LHC", *European Physical Journal* **C77** no. 10, (2017) 658, arXiv:1707.07304 [nucl-ex].

[59] **ALICE** Collaboration, S. Acharya *et al.*, "Production of deuterons, tritons, ^{3}He nuclei and their antinuclei in pp collisions at $\sqrt{s} = 0.9$, 2.76 and 7 TeV", *Physical Review* **C97** no. 2, (2018) 024615, arXiv:1709.08522 [nucl-ex].

[60] **ALICE** Collaboration, S. Acharya *et al.*, "Production of ^{4}He and $^4\overline{\rm He}$ in Pb-Pb collisions at $\sqrt{s_{\rm NN}} = 2.76$ TeV at the LHC", *Nuclear Physics* **A971** (2018) 1–20, arXiv:1710.07531 [nucl-ex].

[61] **ALICE** Collaboration, S. Acharya *et al.*, "Multiplicity dependence of (anti-)deuteron production in pp collisions at $\sqrt{s} = 7$ TeV", *Physics Letters B* **794** (2019) 50–63, arXiv:1902.09290 [nucl-ex].

[62] **ALICE** Collaboration, S. Acharya *et al.*, "Multiplicity dependence of light (anti-)nuclei production in p-Pb collisions at $\sqrt{s_{\rm NN}} = 5.02$ TeV", *Physics Letters B* **800** (2020) 135043, arXiv:1906.03136 [nucl-ex].

[63] **ALICE** Collaboration, S. Acharya *et al.*, "Measurement of the (anti-)^{3}He elliptic flow in Pb-Pb collisions at $\sqrt{s_{\rm NN}} = 5.02$ TeV", *Physics Letters* **B805** (2020) 135414, arXiv:1910.09718 [nucl-ex].

[64] **ALICE** Collaboration, S. Acharya *et al.*, "Production of (anti-)He3 and (anti-)H3 in p-Pb collisions at $\sqrt{s_{\rm NN}}$=5.02 TeV", *Physical Review C* **101** no. 4, (Apr, 2020) 044906.

[65] **ALICE** Collaboration, S. Acharya *et al.*, "(Anti-)deuteron production in pp collisions at $\sqrt{s} = 13$ TeV", *European Physical Journal* **C80** no. 9, (2020) 889, arXiv:2003.03184 [nucl-ex].

[66] **ALICE** Collaboration, S. Acharya *et al.*, "Elliptic and triangular flow of (anti)deuterons in Pb-Pb collisions at $\sqrt{s_{\rm NN}} = 5.02$ TeV", *Physical Review C* **102** no. 5, (Nov, 2020) 055203.

[67] **E878** Collaboration, M. J. Bennett *et al.*, "Light nuclei production in relativistic Au + nucleus collisions", *Physical Review C* **58** (Aug, 1998) 1155–1164.

[68] **E802** Collaboration, L. Ahle *et al.*, "Proton and deuteron production in Au + Au reactions at 11.6/A-GeV/c", *Physical Review C* **60** (1999) 064901.

[69] **E864** Collaboration, T. A. Armstrong *et al.*, "Measurements of light nuclei production in 11.5 AGeV/c Au+Pb heavy-ion collisions", *Physical Review C* **61** no. 6, (May, 2000) 064908.

[70] **E864** Collaboration, T. Armstrong *et al.*, "Anti-deuteron yield at the AGS and coalescence implications", *Physical Review Letters* **85** (2000) 2685–2688, arXiv:0005001 [nucl-ex].

[71] **STAR** Collaboration, C. Adler *et al.*, "$\overline{\mathrm{d}}$ and $^3\overline{\mathrm{He}}$ production in $\sqrt{s_{\mathrm{NN}}}$ = 130 GeV Au + Au collisions", *Physical Review Letters* **87** (Dec, 2001) 262301.

[72] **PHENIX** Collaboration, S. S. Adler *et al.*, "Deuteron and antideuteron production in Au + Au collisions at 200 GeV", *Physical Review Letters* **94** (2005) 122302, arXiv:0406004 [nucl-ex].

[73] **BRAHMS** Collaboration, I. Arsene *et al.*, "Rapidity dependence of deuteron production in Au+Au collisions at $\sqrt{s_{\mathrm{NN}}}$ = 200 GeV", *Physical Review C* **83** no. 4, (Apr, 2011) 044906.

[74] **STAR** Collaboration, H. Agakishiev *et al.*, "Observation of the antimatter helium-4 nucleus", *Nature* **473** (2011) 353, arXiv:1103.3312 [nucl-ex]. [Erratum: Nature 475 (2011) 412].

[75] **STAR** Collaboration, A. K. Bhati *et al.*, "Measurement of elliptic flow of light nuclei at $\sqrt{s_{\mathrm{NN}}}$ = 200, 62.4, 39, 27, 19.6, 11.5, and 7.7 GeV at the BNL Relativistic Heavy Ion Collider", *Physical Review C* **94** no. 3, (2016) 034908, arXiv:1601.07052 [nucl-ex].

[76] **STAR** Collaboration, J. Adam *et al.*, "Beam energy dependence of (anti-)deuteron production in Au + Au collisions at the BNL Relativistic Heavy Ion Collider", *Physical Review C* **99** no. 6, (2019) 064905, arXiv:1903.11778 [nucl-ex].

[77] **ALICE** Collaboration, J. Adam *et al.*, "Production of light nuclei and anti-nuclei in pp and Pb-Pb collisions at energies available at the CERN Large Hadron Collider", *Physical Review C* **93** no. 2, (Feb, 2016) 024917.

[78] **ALICE** Collaboration, J. Adam *et al.*, "H^3_Λ and $\bar{\mathrm{H}}^3_{\bar{\Lambda}}$ production in Pb–Pb collisions at $\sqrt{s_{\mathrm{NN}}}$ =2.76 TeV", *Physics Letters B* **754** (2016) 360–372.

[79] **ALICE** Collaboration, B. Abelev *et al.*, "Centrality dependence of π, K, and p production in Pb-Pb collisions at $\sqrt{s_{NN}} = 2.76$ TeV", *Physical Review C* **88** (Oct, 2013) 044910.

[80] **ALICE** Collaboration, J. Adam *et al.*, "Measurement of pion, kaon and proton production in proton–proton collisions at $\sqrt{s} = 7$ TeV", *The European Physical Journal C* **75** no. 5, (May, 2015) 226.

[81] E. Fermi, "High Energy Nuclear Events", *Progress of Theoretical Physics* **5** no. 4, (07, 1950) 570–583.

[82] F. Becattini, J. Manninen, and M. Gaździcki, "Energy and system size dependence of chemical freeze-out in relativistic nuclear collisions", *Physical Review C* **73** (Apr, 2006) 044905.

[83] A. Andronic, P. Braun-Munzinger, J. Stachel, and M. Winn, "Interacting hadron resonance gas meets lattice QCD", *Physics Letters B* **718** no. 1, (Nov, 2012) 80–85.

[84] S. Wheaton, J. Cleymans, and M. Hauer, "THERMUS—A thermal model package for ROOT", *Computer Physics Communications* **180** no. 1, (Jan, 2009) 84–106.

[85] G. Torrieri, S. Steinke, W. Broniowski, W. Florkowski, J. Letessier, and J. Rafelski, "SHARE: Statistical hadronization with resonances", *Computer Physics Communications* **167** (2005) 229–251, arXiv:0404083 [nucl-th].

[86] A. Andronic, P. Braun-Munzinger, B. Friman, P. M. Lo, K. Redlich, and J. Stachel, "The thermal proton yield anomaly in Pb-Pb collisions at the LHC and its resolution", *Physics Letters B* **792** (May, 2019) 304–309.

[87] V. Vovchenko, B. Dönigus, and H. Stoecker, "Multiplicity dependence of light nuclei production at LHC energies in the canonical statistical model", *Physics Letters B* **785** (Oct, 2018) 171–174.

[88] F. Becattini, "A thermodynamical approach to hadron production in e^+e^- collisions", *Zeitschrift für Physik C Particles and Fields* **69** (1995) 485–492.

[89] F. Becattini and U. Heinz, "Thermal hadron production in pp and $p\bar{p}$ collisions", *Zeitschrift für Physik C Particles and Fields* **76** no. 2, (Oct, 1997) 269–286.

[90] V. Vovchenko, M. I. Gorenstein, and H. Stoecker, "Finite resonance widths influence the thermal-model description of hadron yields", *Physical Review C* **98** no. 3, (Sep, 2018) 034906.

[91] P. Castorina and H. Satz, "Causality constraints on hadron production in high energy collisions", *International Journal of Modern Physics E* **23** no. 04, (Apr, 2014) 1450019.

[92] V. Vovchenko, B. Dönigus, and H. Stoecker, "Canonical statistical model analysis of pp, p-Pb, and Pb-Pb collisions at energies available at the CERN Large Hadron Collider", *Phys. Rev. C* **100** (Nov, 2019) 054906.

[93] S. T. Butler and C. A. Pearson, "Deuterons from High-Energy Proton Bombardment of Matter", *Physical Review* **129** (Jan, 1963) 836–842.

[94] J. I. Kapusta, "Mechanisms for deuteron production in relativistic nuclear collisions", *Physical Review C* **21** (Apr, 1980) 1301–1310.

[95] R. Scheibl and U. Heinz, "Coalescence and flow in ultrarelativistic heavy ion collisions", *Physical Review C* **59** no. 3, (Mar, 1999) 1585–1602.

[96] K. Blum and M. Takimoto, "Nuclear coalescence from correlation functions", *Physical Review C* **99** no. 4, (Apr, 2019) 044913.

[97] R. Hanbury Brown and R. Q. Twiss, "A Test of a new type of stellar interferometer on Sirius", *Nature* **178** (1956) 1046–1048.

[98] **ALICE** Collaboration, J. Adam *et al.*, "Two-pion femtoscopy in p-Pb collisions at $\sqrt{s_{\mathrm{NN}}}$=5.02 TeV", *Physical Review C* **91** no. 3, (Mar, 2015) 034906.

[99] **ALICE** Collaboration, B. Abelev *et al.*, "Charged kaon femtoscopic correlations in pp collisions at $\sqrt{s_{\mathrm{NN}}}$=TeV", *Physical Review D* **87** no. 5, (Mar, 2013) 052016.

[100] **ALICE** Collaboration, J. Adam *et al.*, "Two-pion femtoscopy in p-Pb collisions at $\sqrt{s_{\mathrm{NN}}}$=5.02 TeV", *Physical Review C* **91** no. 3, (Mar, 2015) 034906.

[101] **ALICE** Collaboration, J. Adam *et al.*, "Centrality dependence of pion freeze-out radii in Pb-Pb collisions at $\sqrt{s_{\mathrm{NN}}}$=2.76 TeV", *Physical Review C* **93** no. 2, (Feb, 2016) 024905.

[102] D. Abercrombie, N. Akchurin, E. Akilli, J. A. Maestre, B. Allen, B. A. Gonzalez, J. Andrea, A. Arbey, G. Azuelos, P. Azzi, *et al.*, "Dark Matter benchmark models for early

LHC Run-2 Searches: Report of the ATLAS/CMS Dark Matter Forum", *Physics of the Dark Universe* **27** (Jan, 2020) 100371.

[103] N. P. Topchiev, A. M. Galper, V. Bonvicini, I. V. Arkhangelskaja, A. I. Arkhangelskiy, *et al.*, "High-energy gamma-ray studying with GAMMA-400", arXiv:1707.04882 [astro-ph.IM].

[104] F. Halzen and S. R. Klein, "Invited Review Article: IceCube: An instrument for neutrino astronomy", *Review of Scientific Instruments* **81** no. 8, (2010) 081101.

[105] **AMS** Collaboration, S. Ahlen *et al.*, "An Antimatter spectrometer in space", *Nuclear Instruments and Methods in Physics Research Section A* **350** (1994) 351–367.

[106] **ALICE** Collaboration, S. Acharya *et al.*, "Measurement of the Low-Energy Antideuteron Inelastic Cross Section", *Physical Review Letters* **125** no. 16, (Oct, 2020) 162001.

[107] V. Poulin, P. Salati, I. Cholis, M. Kamionkowski, and J. Silk, "Where do the AMS-02 antihelium events come from?", *Physical Review D* **99** no. 2, (Jan, 2019) 023016.

[108] K. Blum, K. C. Y. Ng, R. Sato, and M. Takimoto, "Cosmic rays, antihelium, and an old navy spotlight", *Physical Review D* **96** no. 10, (Nov, 2017) 103021, arXiv:1704.05431 [astro-ph.HE].

[109] **AMS** Collaboration, S. Ting, "Latest Results from the AMS Experiment on the International Space Station",. https://cds.cern.ch/record/2320166.

[110] N. Saffold, T. Aramaki, R. Bird, M. Boezio, S. Boggs, V. Bonvicini, D. Campana, W. Craig, P. von Doetinchem, E. Everson, *et al.*, "Cosmic antihelium-3 nuclei sensitivity of the GAPS experiment", *Astroparticle Physics* **130** (2021) 102580.

[111] P. von Doetinchem, T. Aramaki, S. Boggs, W. Craig, H. Fuke, F. Gahbauer, C. Hailey, J. Koglin, N. Madden, I. Mognet, K. Mori, R. Ong, T. Yoshida, T. Zhang, and J. Zweerink, "The General Antiparticle Spectrometer (GAPS) - Hunt for dark matter using low-energy antideuterons", arXiv:1012.0273 [astro-ph.IM].

[112] P. v. Doetinchem, K. Perez, T. Aramaki, S. Baker, S. Barwick, R. Bird, M. Boezio, S. Boggs, M. Cui, A. Datta, *et al.*, "Cosmic-ray antinuclei as messengers of new physics: status and outlook for the new decade", *Journal of Cosmology and Astroparticle Physics* **2020** no. 08, (Aug, 2020) 035–035.

[113] E. Mobs, "The CERN accelerator complex - 2019. Complexe des accelerateurs du CERN - 2019",. https://cds.cern.ch/record/2684277. General Photo.

[114] L. R. Evans and P. Bryant, "LHC Machine", *Journal of Instrumentation* **3** (2008) S08001. 164 p. This report is an abridged version of the LHC Design Report (CERN-2004-003).

[115] **ATLAS** Collaboration, K. Sliwa *et al.*, "ATLAS Overview and Main Results", arXiv:1305.4551 [hep-ex].

[116] **CMS** Collaboration, S. Chatrchyan *et al.*, "The CMS Experiment at the CERN LHC", *Journal of Instrumentation* **3** (2008) S08004.

[117] **ALICE** Collaboration, B. Abelev *et al.*, "Performance of the ALICE experiment at the CERN LHC", *International Journal of Modern Physics A* **29** no. 24, (Sep, 2014) 1430044.

[118] **LHCb** Collaboration, A. A. Alves *et al.*, "The LHCb Detector at the LHC", *Journal of Instrumentation* **3** (2008) S08005. Also published by CERN Geneva in 2010.

[119] P. Braun-Munzinger and J. Wambach, "The Phase Diagram of Strongly-Interacting Matter", *Reviews of Modern Physics* **81** (2009) 1031–1050, arXiv:0801.4256 [hep-ph].

[120] **ALICE** Collaboration, S. Acharya *et al.*, "Calibration of the photon spectrometer PHOS of the ALICE experiment", *Journal of Instrumentation* **14** no. 05, (May, 2019) P05025–P05025.

[121] **ALICE** Collaboration, G. Dellacasa *et al.*, *ALICE time projection chamber: Technical Design Report*. Technical design report. ALICE. CERN, Geneva, 2000. https://cds.cern.ch/record/451098.

[122] W. R. Leo, *Techniques for Nuclear and Particle Physics Experiments*. Springer, 1994.

[123] H. Bethe, "Zur Theorie des Durchgangs schneller Korpuskularstrahlen durch Materie", *Annalen der Physik* **397** no. 3, (Jan, 1930) 325–400.

[124] **ALICE** Collaboration, S. Acharya *et al.*, "The ALICE Transition Radiation Detector: Construction, operation, and performance", *Nuclear Instruments and Methods in Physics Research Section A* (Feb, 2018) 88–127.

[125] **ALICE** Collaboration, A. Akindinov *et al.*, "Performance of the ALICE Time-Of-Flight detector at the LHC", *European Physical Journal Plus* **128** (2013) 44.

[126] **ALICE** Collaboration, E. Abbas *et al.*, "Performance of the ALICE VZERO system", *Journal of Instrumentation* **8** no. 10, (Oct, 2013) P10016–P10016.

[127] **ALICE** Collaboration, S. Acharya *et al.*, "The ALICE definition of primary particles",. https://cds.cern.ch/record/2270008.

[128] **ALICE** Collaboration, S. Acharya *et al.*, "Pseudorapidity distributions of charged particles as a function of mid and forward rapidity mutiplicities in pp collisions at $\sqrt{s}$ = 5.02, 7 and 13 TeV", arXiv:2009.09434 [nucl-ex].

[129] **ALICE** Collaboration, J. Adam *et al.*, "Pseudorapidity and transverse-momentum distributions of charged particles in proton–proton collisions at $\sqrt{s}$=13 TeV", *Physics Letters B* **753** (Feb, 2016) 319–329.

[130] T. Sjöstrand, "The Pythia event generator: Past, present and future", *Computer Physics Communications* **246** (Jan, 2020) 106910.

[131] **GEANT4** Collaboration, S. Agostinelli *et al.*, "Geant4—a simulation toolkit", *Nuclear Instruments and Methods in Physics Research Section A* **506** no. 3, (2003) 250 – 303.

[132] M. Knichel, *Transverse momentum distributions of primary charged particles in pp, p–Pb and Pb–Pb collisions measured with ALICE at the LHC*. PhD thesis, Technische Universität Darmstadt, 2014.

[133] S. Ahmed, *Physics and Engineering of Radiation Detection*. Elsevier, 2014.

[134] R. Brun, F. Bruyant, M. Maire, A. C. McPherson, and P. Zanarini, *GEANT 3: user's guide Geant 3.10, Geant 3.11; rev. version*. CERN, Geneva, 1987. https://cds.cern.ch/record/1119728.

[135] R. Barlow and C. Beeston, "Fitting using finite Monte Carlo samples", *Computer Physics Communications* **77** (Jun, 1993) 219–228. 16 p. https://cds.cern.ch/record/249779.

[136] H. Kamada, J. Golak, K. Miyagawa, H. Witała, and W. Glöckle, "π-mesonic decay of the hypertriton", *Physical Review C* **57** no. 4, (Apr, 1998) 1595–1603.

[137] K.-J. Sun, C. M. Ko, and B. Dönigus, "Suppression of light nuclei production in collisions of small systems at the Large Hadron Collider", *Physics Letters B* **792** (May, 2019) 132–137.

[138] J. Jaros, A. Wagner, L. Anderson, O. Chamberlain, R. Z. Fuzesy, J. Gallup, W. Gorn, L. Schroeder, S. Shannon, G. Shapiro, and H. Steiner, "Nucleus-nucleus total cross sections for light nuclei at 1.55 and 2.89 GeV/c per nucleon", *Physical Review C* **18** (Nov, 1978) 2273–2292.

[139] B. M. Bobchenko *et al.*, "Measurement of total inelastic cross-sections from proton interactions with nuclei in the momentum range from 5 GeV/c to 9 GeV/c and π-meson with nuclei in the momentum range from 1.75 GeV/c to 6.5 GeV/c ", *Soviet Journal of Nuclear Physics* **30** (1979) 805.

[140] P. Schwaller, M. Pepin, B. Favier, C. Richard-Serre, D. Measday, and R. P.U., "Proton total cross sections on 1H, 2H, 4He, 9Be, C and O in the energy range 180 to 560 MeV", *Nuclear Physics A* **316** no. 3, (1979) 317–344.

[141] W. Bauhoff, "Tables of reaction and total cross sections for proton-nucleus scattering below 1 GeV", *Atomic Data and Nuclear Data Tables* **35** no. 3, (1986) 429–447.

[142] K. Olive, "Review of particle physics", *Chinese Physics C* **38** no. 9, (Aug, 2014) 090001.

[143] F. Balestra, S. Bossolasco, M. Bussa, *et al.*, "Inelastic interaction of antiprotons with 4He nuclei between 200 and 600 MeV/c", *Physics Letters B* **165** no. 4, (1985) 265–269.

[144] V. F. Kuzichev, Y. B. Lepikhin, and V. A. Smirnitsky, "The Anti-proton - nuclei annihilation cross-section at the momentum range from 0.70 GeV/c to 2.5 GeV/c", *Nuclear Physics A* **576** (1994) 581–602.

[145] K. Nakamura, J. Chiba, T. Fujii, H. Iwasaki, T. Kageyama, S. Kuribayashi, T. Sumiyoshi, T. Takeda, H. Ikeda, and Y. Takada, "Absorption and Forward Scattering of Antiprotons by C, Al, and Cu Nuclei in the Region 470-880 MeV/c", *Physical Review Letters* **52** (Feb, 1984) 731–734.

[146] V. Ashford, M. E. Sainio, M. Sakitt, J. Skelly, R. Debbe, W. Fickinger, R. Marino, and D. K. Robinson, "Low energy antiproton nuclear absorption cross sections", *Physical Review C* **31** (Feb, 1985) 663–665.

[147] **ALICE** Collaboration, S. Acharya *et al.*, "Multiplicity dependence of π, K, and p production in pp collisions at $\sqrt{s} = 13$ TeV", *The European Physical Journal C* **80** no. 8, (Aug, 2020) 693. 20 p, arXiv:2003.02394.

[148] A. Ferrari, P. R. Sala, A. Fasso, and J. Ranft, "FLUKA: A multi-particle transport code (Program version 2005)",. https://cds.cern.ch/record/898301.

[149] **ALICE** Collaboration, K. Aamodt *et al.*, "Transverse momentum spectra of charged particles in proton-proton collisions at $\sqrt{s} = 900$ GeV with ALICE at the LHC", *Physics Letters B* **693** no. 2, (Sep, 2010) 53–68.

[150] **ALICE** Collaboration, S. Acharya *et al.*, "Production of light (anti)nuclei in pp collisions at $\sqrt{s} = 13$ TeV", arXiv:2109.13026 [nucl-ex].

[151] G. Fäldt and U. Tengblad, "Erratum: Coulomb-nuclear interference in pion-nucleus bremsstrahlung [Physical Review C 79, 014607 (2009)]", *Physical Review C* **87** (Feb, 2013) 029903.

[152] E. Tiesinga, P. J. Mohr, D. B. Newell, and B. N. Taylor, "CODATA recommended values of the fundamental physical constants: 2018", *Reviews of Modern Physics* **93** (Jun, 2021) 025010.

[153] F. Bellini, K. Blum, A. P. Kalweit, and M. Puccio, "Examination of coalescence as the origin of nuclei in hadronic collisions", *Physical Review C* **103** (Jan, 2021) 014907.

[154] M. Kachelrieß, S. Ostapchenko, and J. Tjemsland, "Alternative coalescence model for deuteron, tritium, helium-3 and their antinuclei", *The European Physical Journal A* **56** no. 1, (Jan, 2020) 4.

[155] D. R. Entem, R. Machleidt, and Y. Nosyk, "High-quality two-nucleon potentials up to fifth order of the chiral expansion", *Physical Review C* **96** (Aug, 2017) 024004.

[156] **ALICE** Collaboration, S. Acharya *et al.*, "Search for a common baryon source in high-multiplicity pp collisions at the LHC", *Physics Letters B* **811** (Dec, 2020) 135849.

[157] **ALICE** Collaboration, S. Acharya *et al.*, "ALICE upgrade physics performance studies for 2018 Report on HL/HE-LHC physics",. `http://cds.cern.ch/record/2661798`.

[158] **ALICE** Collaboration, B. Abelev *et al.*, "Technical Design Report for the Upgrade of the ALICE Inner Tracking System", *Journal of Physics G* **41** no. 8, (Jul, 2014) 087002.

[159] **ALICE TPC** Collaboration, J. Adolfsson *et al.*, "The upgrade of the ALICE TPC with GEMs and continuous readout", *Journal of Instrumentation* **16** no. 03, (Mar, 2021) P03022.

[160] P. Buncic, M. Krzewicki, and P. Vande Vyvre, "Technical Design Report for the Upgrade of the Online-Offline Computing System", tech. rep., CERN, Apr, 2015. `https://cds.cern.ch/record/2011297`.

[161] **ALICE** Collaboration, D. Colella, "ALICE ITS upgrade for LHC Run 3: commissioning in the laboratory", `arXiv:2106.16168 [physics.ins-det]`.

[162] F. Sauli, "GEM: A new concept for electron amplification in gas detectors", *Nuclear Instruments and Methods in Physics Research Section A* **386** no. 2, (1997) 531–534.

[163] F. V. Böhmer, M. Ball, S. Dorheim, C. Höppner, B. Ketzer, I. Konorov, S. Neubert, S. Paul, J. Rauch, and M. Vandenbroucke, "Space-Charge Effects in an Ungated GEM-based TPC", `arXiv:1209.0482 [physics.ins-det]`.

[164] **ALICE TPC** Collaboration, C. Lippmann, "A continuous read-out TPC for the ALICE upgrade", *Nuclear Instruments and Methods in Physics Research A* **824** (2016) 543–547. 5 p.

[165] Z. Citron, A. Dainese, J. F. Grosse-Oetringhaus, J. M. Jowett, Y. J. Lee, U. A. Wiedemann, *et al.*, "Future physics opportunities for high-density QCD at the LHC with heavy-ion and proton beams", `arXiv:1812.06772 [hep-ph]`.

[166] U. Laha and J. Bhoi, "Two-nucleon Hulthen-type interactions for few higher partial waves", *Pramana* **84** no. 4, (2015) 555–567.

[167] R. Machleidt, "High-precision, charge-dependent Bonn nucleon-nucleon potential", *Physical Review C* **63** no. 2, (Jan, 2001) 024001.

Appendices

A Theoretical predictions for the deuteron coalescence parameter

In the following, the coalescence parameters using different deuteron wave functions as displayed in figure 4.11 are derived. The calculations are based on equation 1.23 which was obtained in reference [96]:

$$B_2 = \int \mathrm{d}^3 p D(\vec{q}) C_2^{\mathrm{PRF}}(\vec{p},\vec{q}) \tag{A.1}$$

with $D(\vec{q})$, being the Wigner density of the deuteron and $C_2^{\mathrm{PRF}}(\vec{p},\vec{q})$ the two-particle correlation function int the two-particle rest frame. Additionally, a homogeneous emission source is assumed, which simplifies the correlation function in equation 1.21 to:

$$C_2^{\mathrm{PRF}}(\vec{p},\vec{q}) = \exp\left(-R^2 q^2\right) \tag{A.2}$$

Four different deuteron wave functions (Φ_d) were studied: single and double Gaussian [154], Hulthen [95], and chiral effective field theory (χEFT) [155]. The following calculations were performed by Bhawani Singh.

The single Gaussian wave function, also known as harmonic oscillator, is the simplest available wave function to describe a deuteron with a nuclear radius of $d = 3.2$ fm.

$$\Phi_\mathrm{d}(r) = \frac{e^{-\frac{r^2}{2d^2}}}{(\pi d^2)^{3/4}} \tag{A.3}$$

When inserting the wave function into equation 1.20 the Wigner density is given as

$$D(\vec{q}) = e^{-\frac{q^2 d^2}{4}} \tag{A.4}$$

This results in the coalescence parameter as a function of the source size radius to be

$$B_2(R) = \frac{3\pi^2}{2m\left(R^2 + (\frac{d}{2})^2\right)^{\frac{3}{2}}} \tag{A.5}$$

The second deuteron wave function used is the Hulthen wave function, which is successfully used in nuclear physics to describe the deuteron binding energy as well partial wave nucleon–nucleon potentials [166].

$$\Phi_\mathrm{d} = \sqrt{\frac{\alpha\beta(\alpha+\beta)}{2\pi(\alpha-\beta)^2}} \frac{e^{-\alpha r} - e^{-\beta r}}{r} \tag{A.6}$$

Here $\alpha = 0.2\ \mathrm{fm}^{-1}$ and $\beta = 1.56\ \mathrm{fm}^{-1}$ are two parameters with values taken from reference [95]. After inserting the wave function into equation 1.23 the coalescence parameter is:

$$B_2(R) = \frac{3\pi^2}{R^2} \frac{\alpha\beta(\alpha+\beta)}{(\alpha-\beta)^2} \left[e^{4\alpha^2 R^2} \mathrm{erfc}(2\alpha R) - 2e^{(\alpha+\beta)^2 R^2} \mathrm{erfc}((\alpha+\beta)R) + e^{4\beta^2 R^2} \mathrm{erfc}(2\beta R) \right] \tag{A.7}$$

The third tested wave function is obtained from a chiral effective field theory calculation (χEFT) of the N^{4}LO, which uses a cut off at $\Lambda_c = 500$ MeV. The wave function is taken form reference [155] and its normalization is based on the work presented in reference [167]. The deuteron wave function is given as:

$$\phi_{\mathrm{d}}(\vec{r}) = \frac{1}{\sqrt{4\pi}\, r}\left[u(r) + \frac{1}{\sqrt{8}}\, w(r)\, S_{12}(\hat{r})\right]\chi_{1m} \tag{A.8}$$

with $S_{12}(\hat{r})$ being the spin tensor, χ_{1m} a spinor, and $u(r)$ and $w(r)$ being radial wave functions. Therefore, the spin-averaged density of the deuteron nucleus can be rewritten as

$$|\phi_{\mathrm{d}}(r)|^2 = \frac{1}{4\pi\, r^2}\left(u^2(r) + w^2(r)\right) \tag{A.9}$$

Inserting again into the Wigner density (equation 1.20) and into equation 1.23, the coalescence parameter turns out to be

$$B_2(R) = \frac{6\pi}{m}\int_0^{\Lambda_c} \mathrm{d}q \int_0^{\infty} \mathrm{d}r\, q\left[u(r)^2 + w(r)^2\right]\frac{\sin(qr)}{r}\, e^{-R^2q^2} \tag{A.10}$$

After a final integration over q the coalescence parameter is given as:

$$\begin{aligned} B_2(R) = &\frac{3\pi}{mR^2}\int_0^{\infty} \frac{\mathrm{d}r}{r}\left[u^2(r) + w^2(r)\right] \\ &\cdot\left(e^{-\Lambda_c^2R^2}\sin(\Lambda_c r) + \frac{\sqrt{\pi}r}{4R}\, e^{-\frac{r^2}{4R^2}}\left[\mathrm{erf}\left(\frac{ir + 2R^2\Lambda_c}{2R}\right) - \mathrm{erf}\left(\frac{ir - 2R^2\Lambda_c}{2R}\right)\right]\right) \end{aligned} \tag{A.11}$$

The last wave function tested is a combination of two Gaussian functions fitted to a Hulthen wave function.

$$\phi_{\mathrm{d}}(r) = \pi^{-3/4}\left[\frac{\Delta^{1/2}}{d_1^{3/2}} e^{-r^2/(2d_1^2) + e^{i\alpha}}\frac{(1-\Delta)^{1/2}}{d_2^{3/2}} e^{-r^2/(2d_2^2)}\right] \tag{A.12}$$

with $\Delta = 0.581$, $d_1 = 3.979$ fm and $d_1 = 0.890$ fm. This leads to a Wigner density of

$$|\phi_{\mathrm{d}}(r)|^2 = \pi^{-3/2}\left[\frac{\Delta}{d_1^3} e^{-r^2/d_1^2} + \frac{1-\Delta}{d_2^3} e^{-r^2/d_2^2}\right] \tag{A.13}$$

Inserting the result into equation 1.23 the B_2 can be written as

$$B_2(R) = \frac{24\pi^{5/2}}{m}\int_0^{\infty} \mathrm{d}q \int_0^{\infty} \mathrm{d}r\, |\phi_d(r)|^2 \sin(qr)\, r\, q\, e^{-R^2q^2} \tag{A.14}$$

and after integrating over q and r the coalescence parameter is:

$$B_2(R) = \frac{3\pi^{3/2}}{2mR^3}\left[\Delta\left(1 + \frac{d_1^2}{4R^2}\right)^{-3/2} + (1-\Delta)\left(1 + \frac{d_2^2}{4R^2}\right)^{-3/2}\right] \tag{A.15}$$

The coalescence parameters B_2 as a function of the source radius are shown in the left panel of figure A.1 for the different wave functions. For small source radii ($R < 3$ fm) the different B_2 predictions differ, while for large source radii the predictions agree with each other. This means the relative effect from the nuclear structure on the coalescence parameter becomes less and less important with increasing emission source radius. For completeness, the right side of the figure shows the B_3 as a function of R using a Gaussian wave function only.

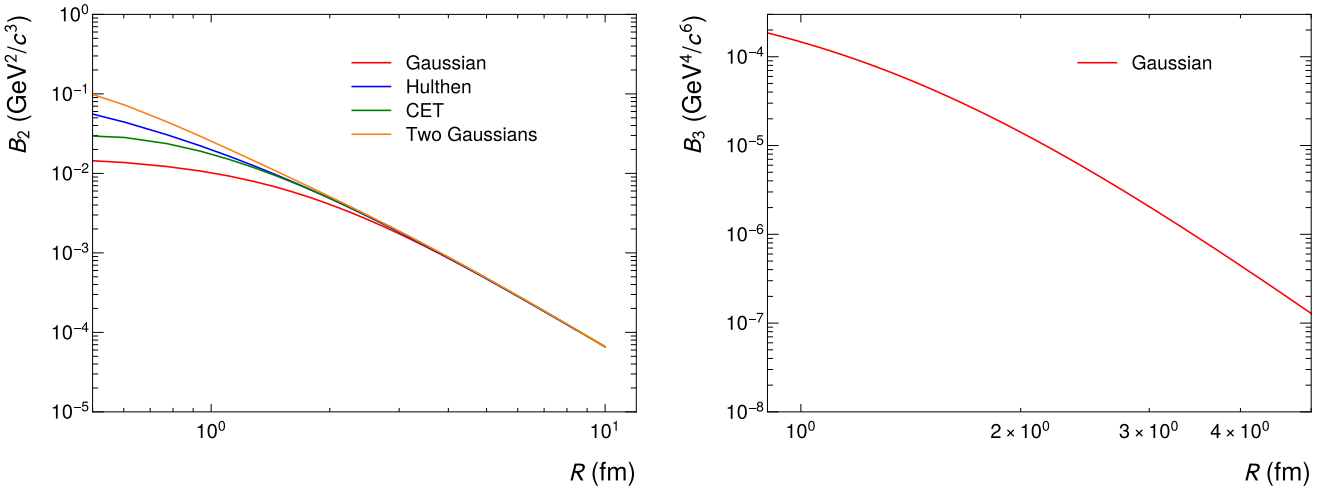

Figure A.1: Coalescence parameters B_2 (left) and B_3 (right) as a function of the source radius R calculated for different wave nucleus functions.

B Additional analysis figures

B.1 Multiplicity differential signal extraction

Multiplicity differential proton signal extraction

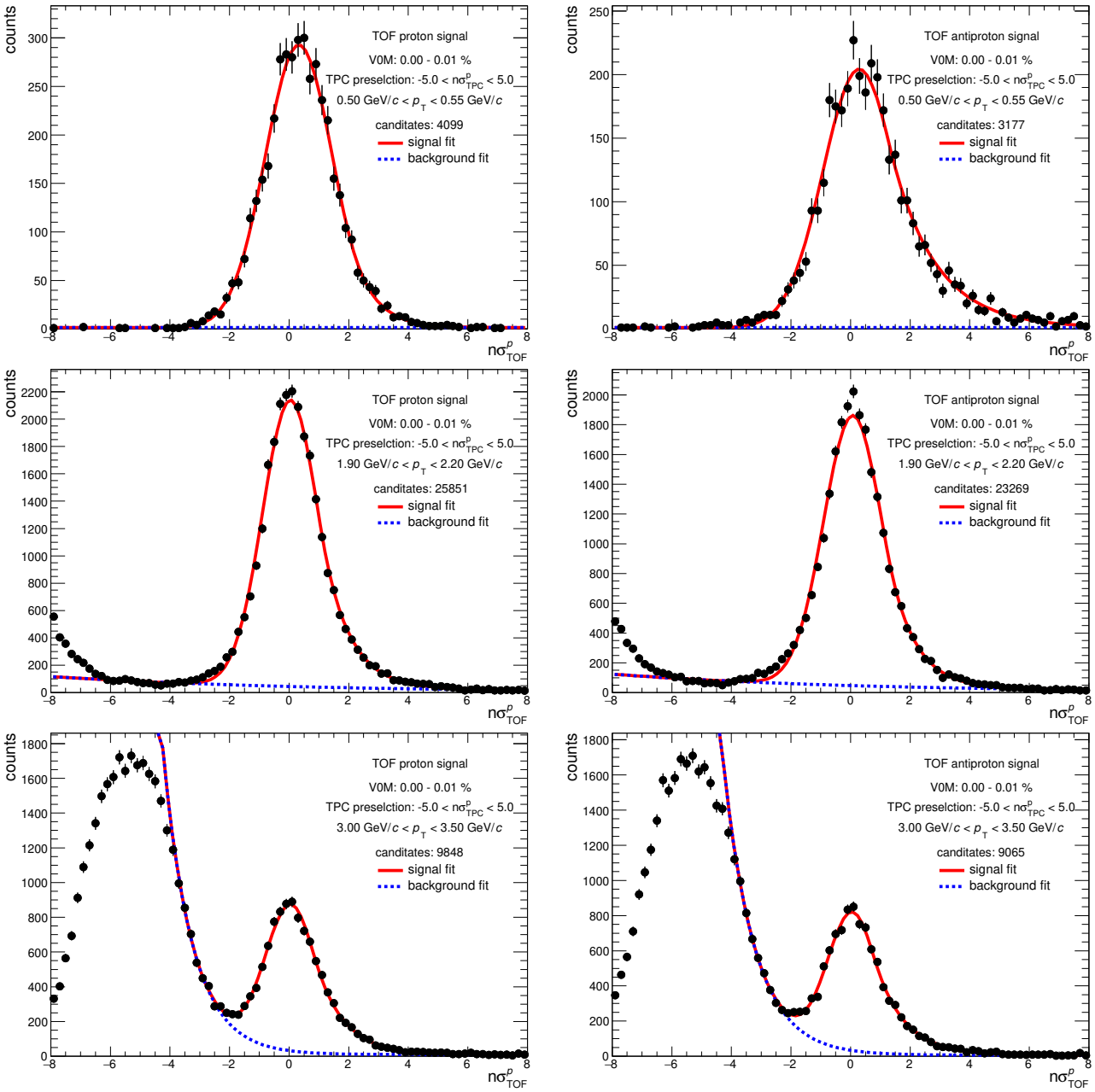

Figure B.1: Proton TOF signal extraction for the integrated multiplicity class (V0M: 0-0.01%). Protons on the left side and antiprotons on the right. The displayed momentum bins are from top to bottom $0.5 \leq p_{\mathrm{T}} < 0.55$ GeV/c, $1.9 \leq p_{\mathrm{T}} < 2.2$ GeV/c, and $3.0 \leq p_{\mathrm{T}} < 3.5$ GeV/c.

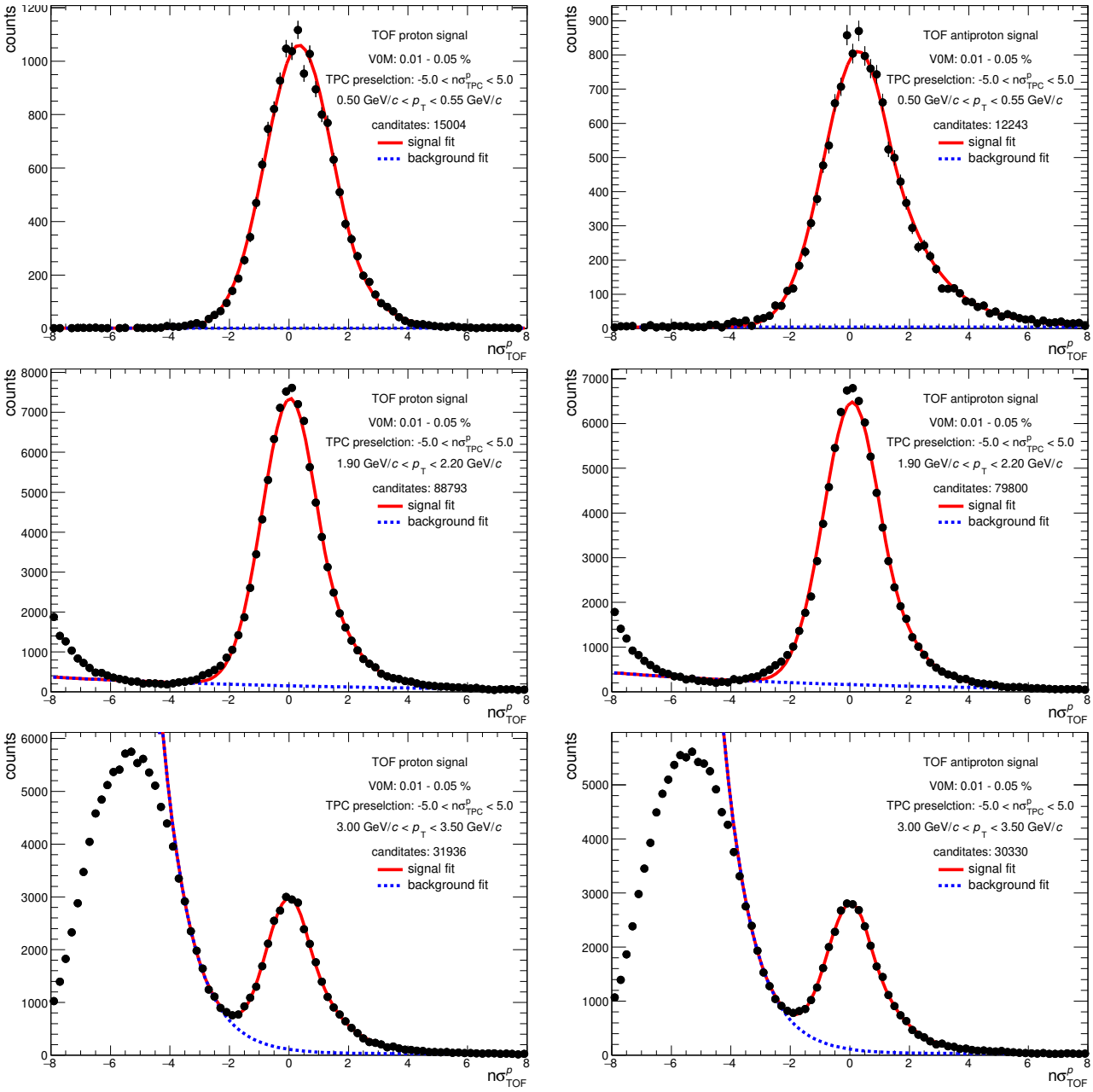

Figure B.2: Proton TOF signal extraction for the integrated multiplicity class (V0M: 0.01-0.05%). Protons on the left side and antiprotons on the right. The displayed momentum bins are from top to bottom $0.5 \leq p_{\mathrm{T}} < 0.55$ GeV/c, $1.9 \leq p_{\mathrm{T}} < 2.2$ GeV/c, and $3.0 \leq p_{\mathrm{T}} < 3.5$ GeV/c.

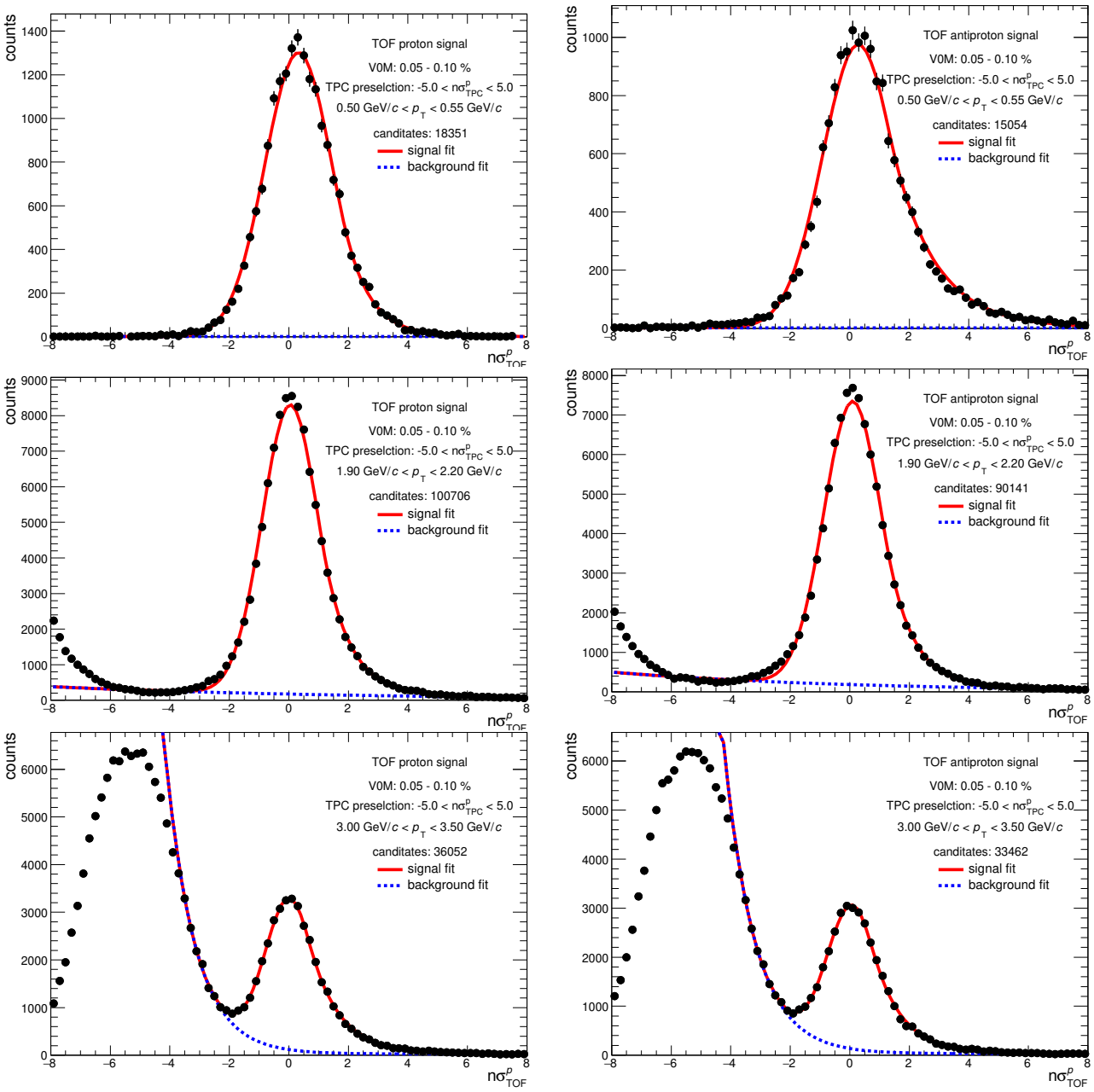

Figure B.3: Proton TOF signal extraction for the integrated multiplicity class (V0M: 0.05-0.1%). Protons on the left side and antiprotons on the right. The displayed momentum bins are from top to bottom $0.5 \leq p_{\mathrm{T}} < 0.55$ GeV/c, $1.9 \leq p_{\mathrm{T}} < 2.2$ GeV/c, and $3.0 \leq p_{\mathrm{T}} < 3.5$ GeV/c.

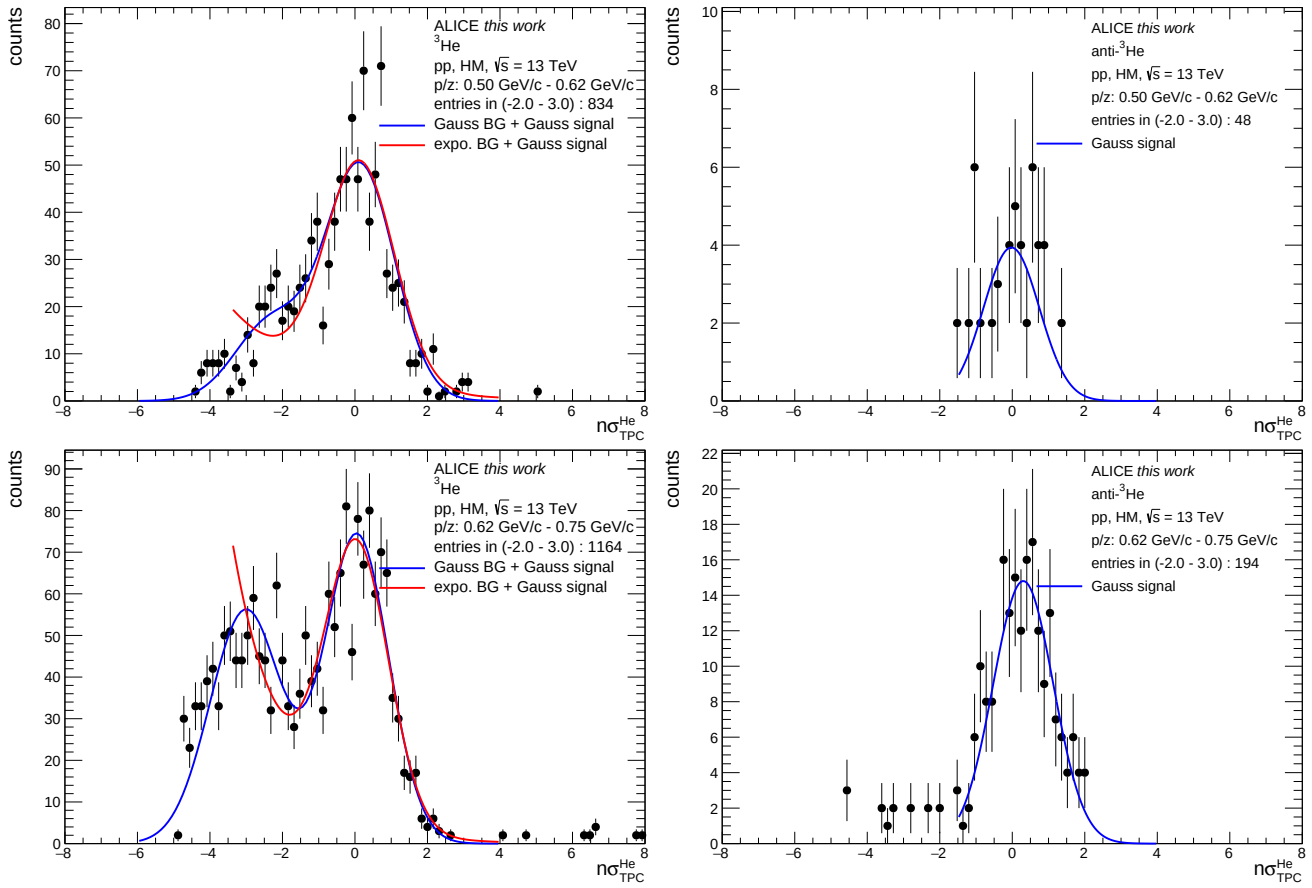

Figure B.4: TPC signal extraction for ^{3}He (left) and anti-^{3}He (right) for the integrated high multiplicity triggered event class in the 0.5-0.625 GeV/c (top) and 0.625-0.75 GeV/c (bottom) rigidity intervals, with a signal plus background interpolation. The interpolation is not used for anti-^{3}He.

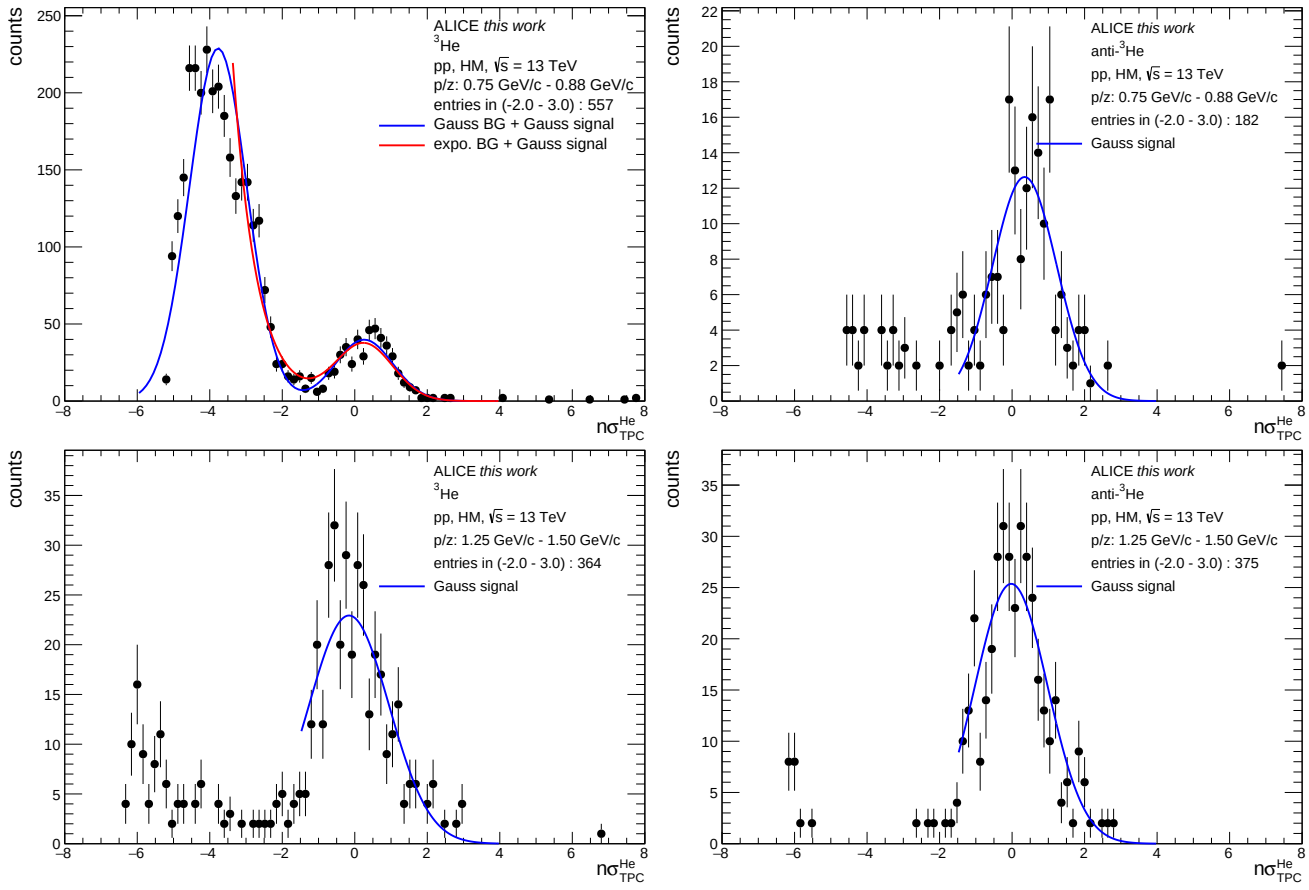

Figure B.5: TPC signal extraction for ^{3}He (left) and anti-^{3}He (right) for the integrated high multiplicity triggered event class in the 0.75-0.88 GeV/c (top) and 1.25-1.5 GeV/c (bottom) rigidity intervals, with a signal plus background interpolation. The interpolation is not used for anti-^{3}He.

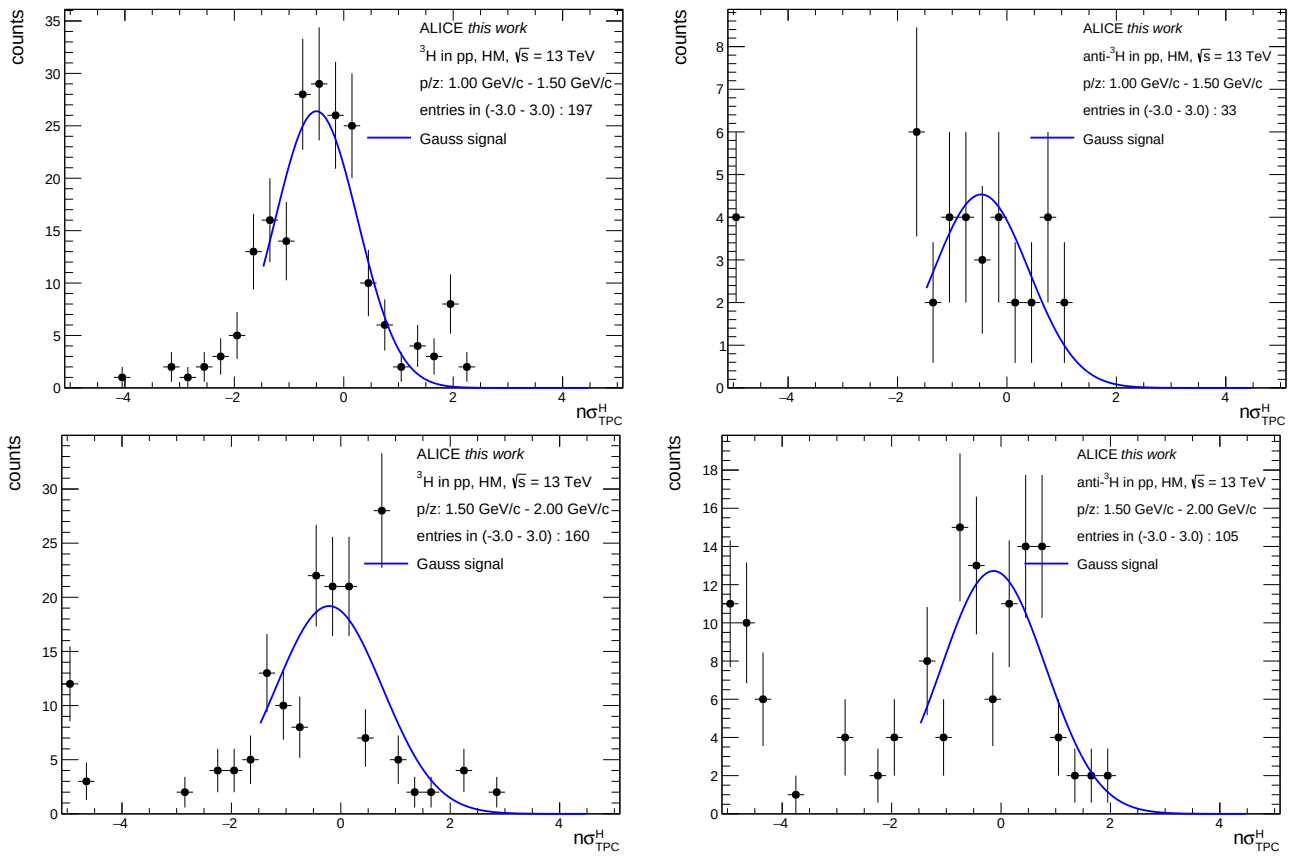

Figure B.6: TPC only signal extraction for triton candidates with low momentum ($p \leq 2$ GeV/c) in the high multiplicity triggered event class. The left side shows particle while the right one shows anti-particle.

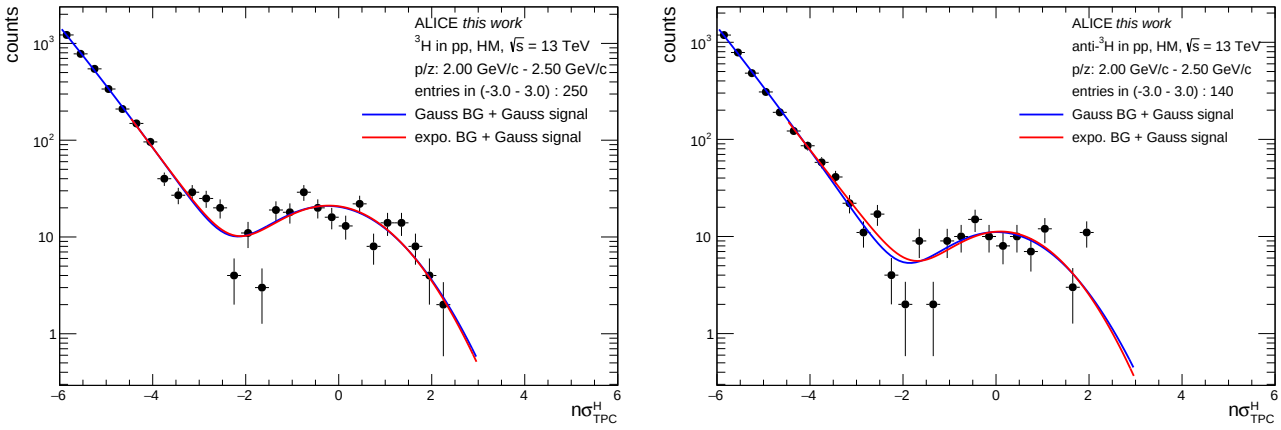

Figure B.7: Expected TPC triton signal after applying a TOF preselection ($|n\sigma^{^3\mathrm{H}}_{\mathrm{TOF}}| < 3$) for the momentum bin $2 < p < 2.5$ GeV/c in the high multiplicity triggered event class. The left side shows particle while the right one shows anti-particle.

B.2 Multiplicity differential secondary correction

Secondary correction factor for protons in fine multiplicity bins

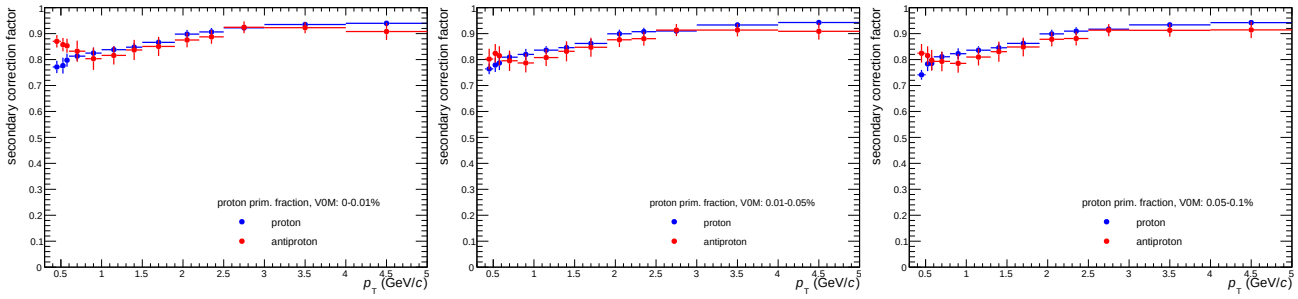

Figure B.8: Primary fraction of (anti)proton in the 0-0.01%, 0.01-0.05%, and 0.05-0.1% V0M multiplicity interval going from left to right.

Primary fraction for helium and triton in the HM trigger event class

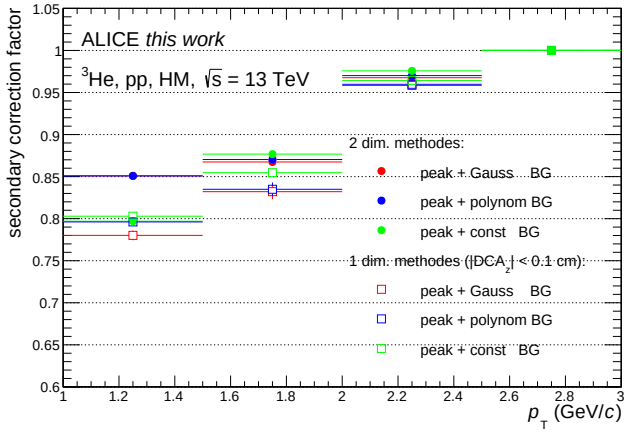

Figure B.9: p_T -dependent ^{3}He secondary particle contamination estimated with different background assumptions shown for the HM (V0M 0-0.1%) multiplicity class.

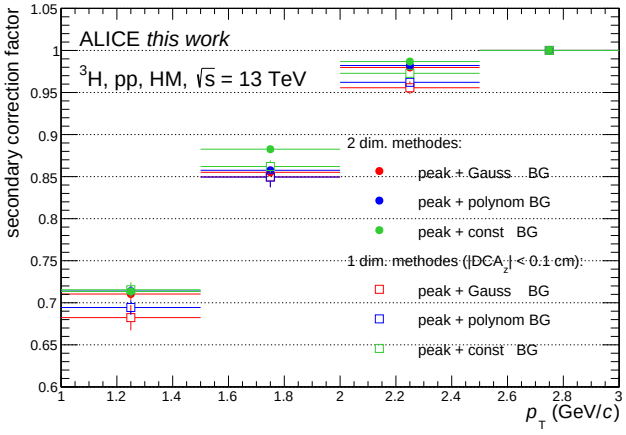

Figure B.10: p_T -dependent ^{3}H secondary particle contamination estimated with different background assumptions shown for the HM (V0M 0-0.1%) multiplicity class.

B.3 Systematic uncertainties for helium and triton in the HM trigger event class

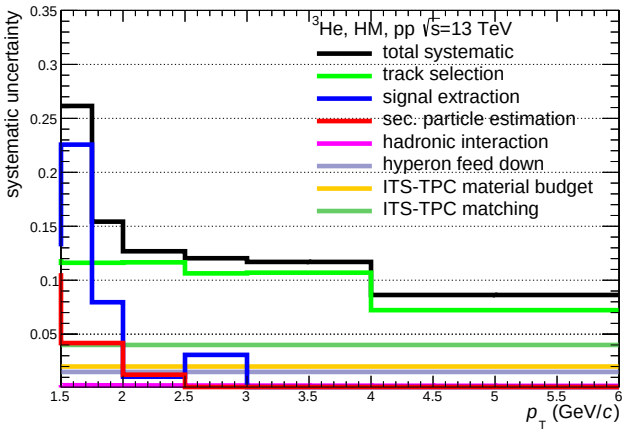

Figure B.11: Total systematic uncertainty with the individual contributions of the ^{3}He p_T spectra in the HM event class.

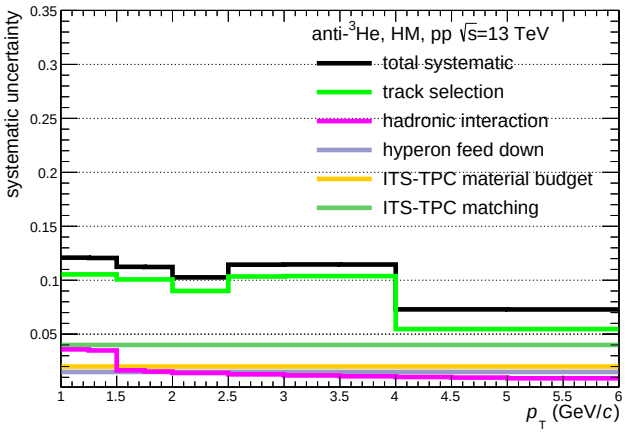

Figure B.12: Total systematic uncertainty with the individual contributions of the anti-^{3}He p_T spectra in the HM event class.

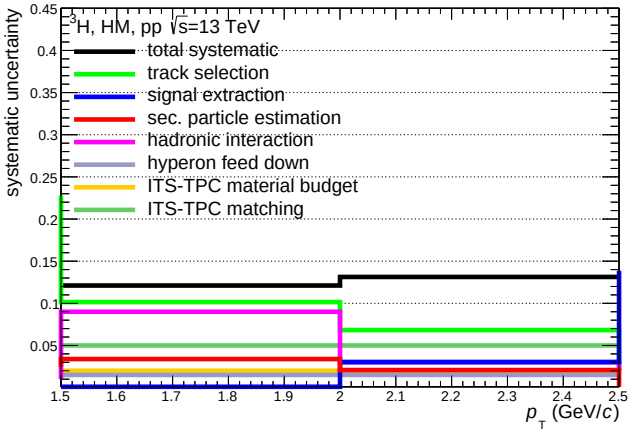

Figure B.13: Total systematic uncertainty with the individual contributions of the ^{3}H p_T spectra in the HM event class.

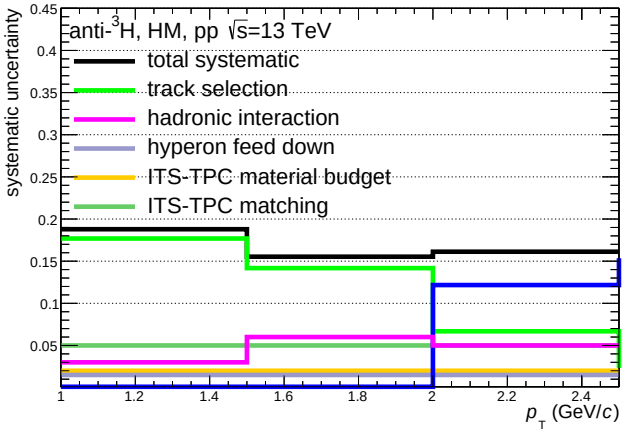

Figure B.14: Total systematic uncertainty with the individual contributions of the anti-^{3}H p_T spectra in the HM event class.

B.4 Transverse-momentum spectra interpolation in finite multiplicity intervals

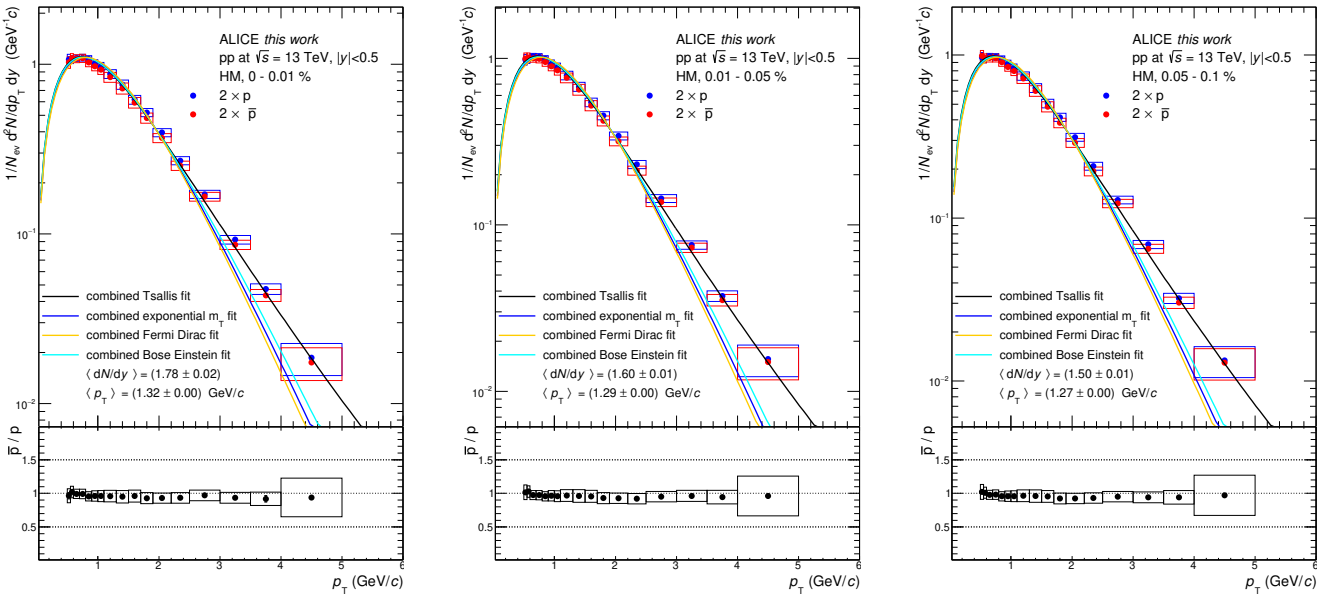

Figure B.15: Proton spectra for three high multiplicity triggered event classes with the p to anti-p ratio in the lower panel. The multiplicity classes are going from left to right: V0M: 0-0.01%, V0M: 0.01-0.05%, and V0M: 0.05-0.1%. Systematic uncertainties are shown as open boxes and statistical as error bars. Four different interpolations are applied to the combined (p + $\overline{\text{p}}$) p_{T} spectra.

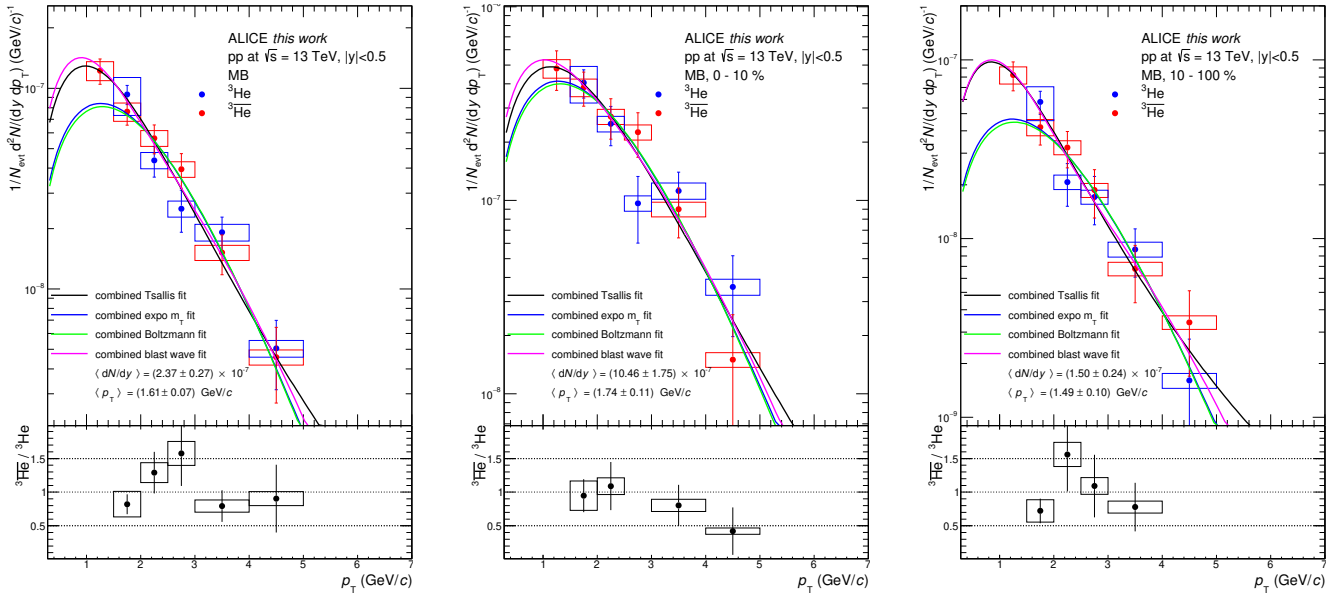

Figure B.16: Helium spectra for the minimum bias triggered classes with the ^{3}He to $^3\overline{\text{He}}$ ratio in the lower panel. The multiplicity classes are going from left to right: V0M: 0-100%, V0M: 0-10%, and V0M: 10-100%. Systematic uncertainties are shown as open boxes and statistical as error bars. Four different interpolations are applied to the combined $(0.5 \cdot (^3\text{He} + ^3\overline{\text{He}}))$ p_{T} spectra.

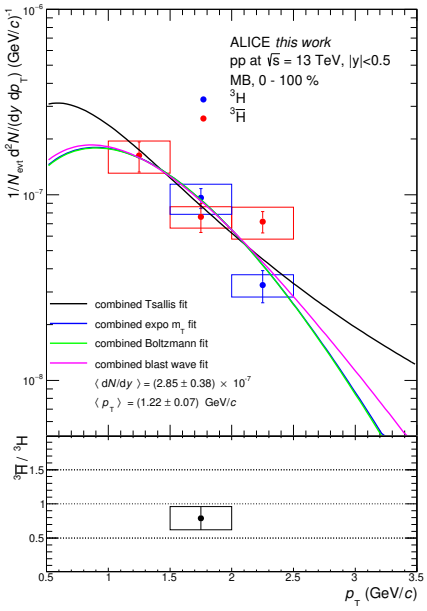

Figure B.17: Triton spectra for the integrated minimum bias triggered class (V0M: 0-100%) with the ^{3}H to $^3\overline{\text{H}}$ ratio in the lower panel. Systematic uncertainties are shown as open boxes and statistical as error bars. Four different interpolations are applied to the combined $(0.5 \cdot (^3\text{H} + ^3\overline{\text{H}}))$ p_{T} spectra.

Acknowledgment

I like to take the opportunity and give thanks to the people who supported me over the last few years. First, I want to thank my supervisor Prof. Dr. Tetyana Galatyuk, for allowing me to start a Ph.D. on such an exciting research topic and for the excellent support during the project. I want to thank Dr. Ralf Averbeck for the countless physics discussions and for proofreading the thesis. I also want to thank Dr. Alberto Caliva and Dr. Luca Barioglio for their immense efforts in the publication process and help during the data analysis. A special thanks to Prof. Dr. Anton Andronic, who introduced me to the field of heavy-ion physics and caught me with his passion and enthusiasm. Thanks to Dr. Dariusz Miskowiec and Dr. Chilo Garabatos for allowing me to participate in the unique and stunning TPC upgrade project. I am also thankful to Prof. Dr. Silvia Masciocchi for welcoming me to the ALICE group and helping me whenever needed. Being part of this warm and joyful environment was a very great experience. So, I want to thank all my colleagues at GSI for the fun discussions during the lunch breaks, the wonderful and relaxing group retreats, and the supportive attitude.

Erklärung zur Dissertation

Hiermit versichere ich, die vorliegende Dissertation ohne Hilfe Dritter nur mit den angegebenen Quellen und Hilfsmitteln angefertigt zu haben. Alle Stellen, die aus Quellen entnommen wurden, sind als solche kenntlich gemacht. Diese Arbeit hat in gleicher oder ähnlicher Form noch keiner Prüfungsbehörde vorgelegen.

Darmstadt, den 14.11.2021

(Michael Habib)